

AD-A038 457

ARMY MISSILE RESEARCH DEVELOPMENT AND ENGINEERING LAB--ETC F/6 20/11  
FRACTURE MECHANICS DESIGN HANDBOOK.(U)  
DEC 76 D G SMITH, B R MULLINIX

UNCLASSIFIED

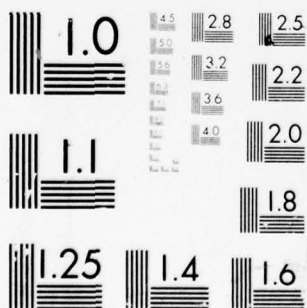
RL-77-5

NL

1 OF 3  
AD  
A038457



1 OF 3  
D  
A038457





AD A 038457



TECHNICAL REPORT RL-77-5

**FRACTURE MECHANICS DESIGN HANDBOOK**

Department of Engineering Science  
Tennessee Technological University  
Cookeville, Tennessee 38501  
and

Ground Equipment and Material Directorate  
US Army Missile Research Development and Engineering Laboratory  
US Army Missile Command  
Redstone Arsenal, Alabama 35809

16 December 1976

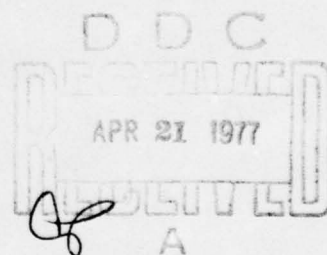
Approved for public release; distribution unlimited.



**U.S. ARMY MISSILE COMMAND**

**Redstone Arsenal, Alabama 35809**

DDC FILE COPY,



#### **DISPOSITION INSTRUCTIONS**

**DESTROY THIS REPORT WHEN IT IS NO LONGER NEEDED. DO NOT  
RETURN IT TO THE ORIGINATOR.**

#### **DISCLAIMER**

**THE FINDINGS IN THIS REPORT ARE NOT TO BE CONSTRUED AS AN  
OFFICIAL DEPARTMENT OF THE ARMY POSITION UNLESS SO DESIGNATED  
BY OTHER AUTHORIZED DOCUMENTS.**

#### **TRADE NAMES**

**USE OF TRADE NAMES OR MANUFACTURERS IN THIS REPORT DOES  
NOT CONSTITUTE AN OFFICIAL INDORSEMENT OR APPROVAL OF  
THE USE OF SUCH COMMERCIAL HARDWARE OR SOFTWARE.**

UNCLASSIFIED

SECURITY CLASSIFICATION OF THIS PAGE (When Data Entered)

REPORT DOCUMENTATION PAGE		READ INSTRUCTIONS BEFORE COMPLETING FORM
1. REPORT NUMBER RL-77-5	2. GOVT ACCESSION NO.	3. RECIPIENT'S CATALOG NUMBER
4. TITLE (and Subtitle) FRACTURE MECHANICS DESIGN HANDBOOK		5. TYPE OF REPORT & PERIOD COVERED Technical Report
7. AUTHOR(s) Dallas G. Smith and Bobby R. Mullinix		6. PERFORMING ORG. REPORT NUMBER
9. PERFORMING ORGANIZATION NAME AND ADDRESS Commander US Army Missile Command Attn: DRSMI-RL Redstone Arsenal, Alabama 35809		8. CONTRACT OR GRANT NUMBER(s)
11. CONTROLLING OFFICE NAME AND ADDRESS Commander US Army Missile Command Attn: DRSMI-RPR Redstone Arsenal, Alabama 35809		10. PROGRAM ELEMENT, PROJECT, TASK AREA & WORK UNIT NUMBERS
14. MONITORING AGENCY NAME & ADDRESS (if different from Controlling Office)		12. REPORT DATE 16 December 1976
		13. NUMBER OF PAGES 233
		15. SECURITY CLASS. (of this report) Unclassified
16. DISTRIBUTION STATEMENT (of this Report) Approved for public release; distribution unlimited.		15a. DECLASSIFICATION/DOWNGRADING SCHEDULE
17. DISTRIBUTION STATEMENT (of the abstract entered in Block 20, if different from Report)		
18. SUPPLEMENTARY NOTES		
19. KEY WORDS (Continue on reverse side if necessary and identify by block number) Fracture mechanics Design manual Homogeneous materials Applications		
20. ABSTRACT (Continue on reverse side if necessary and identify by block number) This design manual is directed toward the needs of practicing engineers and stress analysts. Basic information on the history, philosophy, and theory of fracture mechanics including such topics as common definitions, elastic solutions, plastic zone effects, and both plane strain and plane stress fracture toughness testing are included. However, the major emphasis is placed on applications. A large number of the most applicable solutions presently available for use in fracture mechanics are documented with details covering their application and accuracy.		

DD FORM 1 JAN 73 1473 EDITION OF 1 NOV 65 IS OBSOLETE

UNCLASSIFIED

SECURITY CLASSIFICATION OF THIS PAGE (When Data Entered)

**SECURITY CLASSIFICATION OF THIS PAGE(When Data Entered)**

SECURITY CLASSIFICATION OF THIS PAGE(When Data Entered)



## CONTENTS

	Page
Chapter 1. INTRODUCTION . . . . .	1
1.1 History. . . . .	1
1.2 Philosophy and Purpose . . . . .	2
1.3 Energy Rate Analysis of Crack Extension and Its Measurement. . . . .	2
1.4 Experimental Correlation . . . . .	5
1.5 Size Effect. . . . .	6
1.6 Loading Modes. . . . .	7
1.7 Summary. . . . .	8
Chapter 2. THE CRACK-TIP STRESS FIELDS. . . . .	9
2.1 Westergaard Stress Function. . . . .	9
2.2 Mode I - Stresses and Displacements. . . . .	11
2.3 Mode II - Stresses and Displacements . . . . .	18
2.4 Mode III - Stresses and Displacements. . . . .	20
2.5 Characteristics of the Elastic Crack-Tip Stress Field . . . . .	22
2.6 Meaning of the Stress Intensity Factor . . . . .	24
2.7 Dimensional Considerations for the Classical Problems of Cracks in Infinite Plates . . . . .	25
2.8 Correlation of Stress Intensity Factor with Stress Concentration Factor . . . . .	27
2.9 Equivalence of Energy Rate and Stress Intensity Factor Approaches. . . . .	28
Chapter 3. STRESS INTENSITY FACTOR SOLUTIONS. . . . .	31
3.1 Examples of Crack-Tip Solutions Using the Westergaard Stress Function. . . . .	31
3.2 Crack-Tip Solutions Using the Method of Muskhelishvili . . . . .	33
3.3 Influence of Local Boundaries Other Than Crack Surfaces . . . . .	40
3.4 Three-Dimensional Considerations . . . . .	48
3.5 Estimation of the Stress Intensity Factor. . . . .	54
Chapter 4. EFFECTS OF CRACK-TIP PLASTICITY. . . . .	57
4.1 Introduction . . . . .	57
4.2 Mode III - Elasto-Plastic Solution . . . . .	60
4.3 Strip Yield Model. . . . .	63
4.4 Limitations of the Crack-Tip Stress Field Theory . . .	68

	Page
Chapter 5. FRACTURE TOUGHNESS TESTING . . . . .	73
5.1 Characteristics of the Critical Stress Intensity Factor . . . . .	73
5.2 Plane Strain Fracture Toughness Testing. . . . .	76
5.3 Plane-Stress and Transistional Fracture - Toughness Testing. . . . .	79
5.4 Fatigue Crack Propagation. . . . .	83
5.5 Stress Corrosion Cracking. . . . .	90
Chapter 6. DESIGN APPLICATIONS OF FRACTURE MECHANICS. . . . .	93
6.1 Residual Strength of a Center-Cracked Panel. . . . .	93
6.2 Strength of a Bracket with Cracks Emanating from a Hole. . . . .	95
6.3 Cracked Bar Loaded in Bending. . . . .	99
6.4 Evaluation of Materials Based on $K_{IC}$ Data and Design Requirements - Surface Flaw . . . . .	101
6.5 Eccentric Crack Growing from a Rivet Hole. . . . .	105
6.6 Crack in a Stiffened Panel . . . . .	109
6.7 Fatigue Life of an Edge Crack. . . . .	116
Chapter 7. COMPENDIUM OF STRESS INTENSITY FACTORS . . . . .	120
7.1 Two-Dimensional Solutions for Cracks in Infinite Plates . . . . .	121
7.2 Two-Dimensional Solutions for Cracks in Semi-Infinite Plates . . . . .	145
7.3 Two-Dimensional Solutions for Cracks in Long Strips . . . . .	152
7.4 Two-Dimensional Solutions for Finite Specimens . . . . .	166
7.5 Shafts with Circumferential Cracks . . . . .	178
7.6 Large Stiffened Plates with Cracks . . . . .	181
7.7 Three-Dimensional Solutions for Surface Flaws, Embedded Flaws, and Through Flaws. . . . .	191
7.8 Flaws Loaded by Stress Waves and Impact Loads. . . . .	213
LIST OF SYMBOLS. . . . .	218
REFERENCES . . . . .	222
RECOMMENDED BIBLIOGRAPHY . . . . .	230

## PREFACE

This work has two purposes: (1) to provide an introduction to the fundamentals of fracture mechanics, and (2) to provide a convenient source of fracture design information. The presentation, limited to isotropic, homogeneous materials, is aimed at practicing engineers rather than those engaged in fracture mechanics research. In the past 20 years, a great volume of material has been written on research results in fracture mechanics but it seems that there has been too little effort devoted to distilling and summarizing this information and in disseminating it to designers. Consequently, engineers, attempting to gain an overview of the subject, are frequently lead into a bewildering maze of technical papers, ASTM special technical publications, proceedings of conferences, and the like. Practicing designers have little time for this; therefore, an effort has been made here to present the fundamentals of fracture mechanics in compact form in a single volume. At the same time a substantial, but edited, compendium of solutions for fracture analysis has been included.

Chapters 1, 2, and 3 cover background information dealing with the history, philosophy, fundamental concepts, and basic theory needed for a general understanding of fracture mechanics. The effects of the plastic zone in the region of the crack tip are considered in Chapter 4. Techniques for both plane stress and plane strain fracture toughness testing are briefly discussed in Chapter 5. Chapter 6 contains several example solutions to some commonly encountered problems in the application of fracture mechanics. Solutions for the stress intensity factors for several different types of problems are compiled in Chapter 7. The stress analyst or engineer who already has a fundamental knowledge of fracture mechanics should find Chapters 6 and 7 the most useful.

It is expected that a stress analyst or engineer will supplement the solutions presented with other solutions commonly needed in his specific work and that a tabulation of toughness data for the materials will be available. The Damage Tolerant Design Handbook listed in the references is the best single source available for fracture data for metals.

In keeping with the above aims, information was gathered from many sources, including the book by Wilhelm, the handbook by Tada, the book on three-dimensional problems by Parmeter, ASTM STP 381, the seven volume series edited by Liebowitz, and various technical papers by many other eminent scientists too numerous to individually acknowledge here. It is hoped, though, that due credit has been given at the appropriate places in the text.

The authors are especially grateful to Professor C. W. Smith, an outstanding scholar and teacher of Virginia Polytechnic Institute and State University, who encouraged the author's interest in fracture mechanics and guided their first research efforts in that subject.

For the administrative and contractual support of this project during the summer of 1976, the authors gratefully acknowledge the scientific services program of the Army Research Office.



## Chapter 1. INTRODUCTION

### 1.1 History

As early as 1920, A. A. Griffith [1] published his concept of crack propagation. The concept stated that an existing crack will propagate if, in so doing, the total energy of the system is lowered. The stress analysis used to calculate the stored elastic energy was based on a 1913 solution by Inglis [2] for an elliptical hole in an infinite plane under uniaxial tension. Griffith, in his work on glass, postulated the existence of flaws prior to loading, which were large compared to atomic or molecular distances. In 1945 Orowan [3] noted extensive plastic deformation on fracture surfaces of materials which had failed in a brittle fashion. Then, in 1948, Irwin [4] pointed out that the Griffith type energy balance must be between the strain energy stored in the specimen and the surface energy plus the work of plastic deformation. The same arguments were stated by Orowan [5], who showed that the Griffith condition, when modified to account for plastic work, was a necessary and sufficient condition for predicting brittle fracture.

Then in 1955, Irwin [6] suggested and in 1957 [7] he showed that the energy approach is equivalent to a stress intensity approach according to which fracture occurs when a critical stress distribution, characteristic of the material, is reached. This discovery, shifting fracture mechanics from the energy approach to the stress approach, placed fracture mechanics on a basis more familiar to the practicing engineer, and was largely responsible for the subsequent development and application of the new discipline.

The need for increased knowledge of brittle fracture mechanics was clear. The spectacular failures, by breaking in half, of the liberty ships in the 1940's, the repeated brittle fracture failures of the Polaris missile at stresses below the design level, and the accelerating demand for lightweight structures provided considerable impetus for study of the subject.

By 1959 the so-called Griffith-Irwin concept of sharp crack mechanics had become well known and the ASTM Special Committee on Fracture Testing of High Strength Materials was formed to launch a broad assault on fracture. By then, the need to design, and test specimens with severe artificial flaws was recognized and there, followed much experimental plane strain fracture toughness testing. In addition to the experimental work, considerable analytical work was performed, seeking to clarify the state of stress around flaws of various shapes under various loading conditions.

In summary, the history of fracture mechanics shows development along both theoretical and experimental lines. From a theoretical point of view, the subject is founded upon linear, small strain elasticity insofar as the stress field which controls the crack is concerned. For a given material crack propagation occurs when the intensity of the stress field reaches a certain critical value, determined experimentally.

## 1.2 Philosophy and Purpose

The basic, underlying philosophy in fracture mechanics lies in the assumption that the elastic stress field in the neighborhood of the crack root controls the crack behavior. The influence of this stress field can be measured in terms of the so-called stress intensity factor (referred to as  $K$  or as SIF), or alternatively, from a strain energy approach, in terms of the strain energy release rate  $g$ . An understanding of these quantities and their correlation is basic to an understanding of this approach. In addition, it is assumed that of all flaws in a given specimen or structural component, only one of the flaws plays a major role in inducing fracture. In other words, the mechanism requiring a coalescence of voids into a nucleus out of which a crack is created is not included in the mathematical modeling which follows. This is done to permit comparison with controlled experiments on precracked materials and also because fracture of a structural component is complete when only one crack propagates across it.

It must be further emphasized that the subsequent analysis will be accurate only for brittle fracture resulting from sharp cracks. When applied to notches with root radii large compared to, say, the grain size, the plastic zone preceding the crack root may not be small relative to the elastic zone which is influenced by the notch root. In such cases, the elastic stress field surrounding the plastic zone may not govern; such is the case with ductile cracking. However, as already pointed out, the energy of plastic work is not negligible in technologically important brittle fracture situations, as was originally assumed by Griffith.

## 1.3 Energy Rate Analysis of Crack Extension and Its Measurement

Before proceeding further, it seems appropriate to present an elementary analysis together with a qualitative explanation of a quantity called the "strain energy release rate  $g$ ," or alternatively the "crack extension force." This quantity represents a concept which may be new to some engineers, and although the interpretation of this quantity will become more sophisticated in later chapters, the following quasiheuristic elementary discussion will serve to provide the basic concepts involved.

Consider a linearly elastic body which contains a through crack (here defined as two planar mating surfaces which are stress free but are initially separated by an infinitesimally small distance). The body is in a deformed equilibrium position under the action of load  $P$ , which causes an extension  $\Delta$  under the load point. The energy rate (that is, energy per unit of new crack area generated),  $g$ , available for an increment of crack extension,  $da$ , is provided from work done by the force,  $Pd\Delta$ , and the release,  $-dV$ , in the total strain energy,  $V$ , stored in the body. In other words, part of the work  $Pd\Delta$ , results in an increase in strain energy and part is used in creating new fracture surface. Expressed mathematically

$$g = P \frac{d\Delta}{da} - \frac{dV}{da} \quad (1.1)$$

$g$  = strain energy release per unit increase in fracture surface area ( $\frac{\text{in.-lb}}{\text{in.}^2}$ )

$V$  = total strain energy stored in the body (in.-lb) as indicated in Figure 1.1. (There is no provision in this explanation to account for plasticity but this is a detail to be dealt with later.)

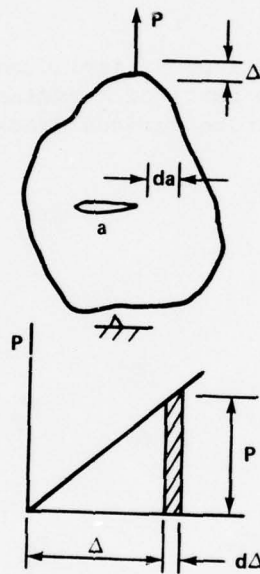


Figure 1.1. Cracked body under load.

Measurement of  $g$  is accomplished by the definition of compliance,  $\lambda = \Delta/P$ , an inverse spring constant. In Equation (1.1),  $V = \frac{1}{2} P\Delta = \frac{1}{2} P^2 \lambda$ . Thus,

$$\frac{dV}{da} = P \frac{\partial P}{\partial a} \lambda + \frac{P^2}{2} \frac{\partial \lambda}{\partial a}$$

and

$$\frac{d\Delta}{da} = \frac{\partial P}{\partial a} \lambda + \frac{\partial \lambda}{\partial a} P;$$

then by substituting into Equation (1.1)

$$g = P \left( \frac{\partial P}{\partial a} \lambda + \frac{\partial \lambda}{\partial a} P \right) - P \left( \frac{\partial P}{\partial a} \lambda + \frac{P}{2} \frac{\partial \lambda}{\partial a} \right)$$

or

$$g = \frac{P^2}{2} \left( \frac{\partial \lambda}{\partial a} \right) \quad (1.2)$$

Since the quantity  $\frac{\partial P}{\partial a}$  cancels from Equations (1.2),  $g$  is independent of the type of test fixture, whether fixed cross head or fixed load. This fact will be useful later.

In a compliance calibration, a displacement gage is mounted on the specimen. A calibration curve of  $\lambda$  versus  $a$  is prepared by obtaining  $\Delta$  -  $P$  curves for a specimen with various crack lengths  $a$  (Figure 1.2).

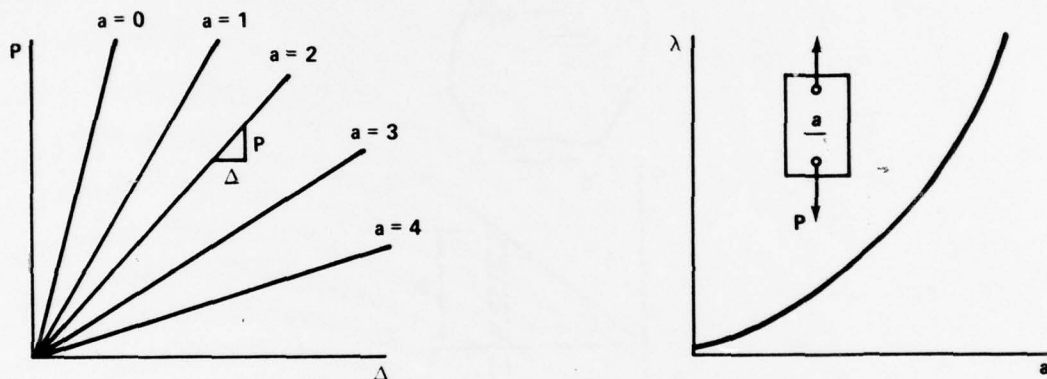


Figure 1.2. Compliance calibration curves.

The  $P$  -  $\Delta$  curve is linear and its reciprocal slope is the  $\lambda$  for that particular crack length. The  $\lambda$  -  $a$  curve, however, is nonlinear. For a specimen with a given crack length or area, the quantity  $\partial \lambda / \partial a$  can be determined from the  $\lambda$  -  $a$  curve. Using this with a known load  $P$  in Equation (1.2), the strain energy release rate  $g$  becomes known.

Although Griffith's fracture criterion was originally stated a slightly different way, essentially, crack extension occurs when  $g$  approaches a critical value, e.g.,  $g_c$ , equal to the total solid state surface tension,  $T$ . That is, when

$$g = g_c = T \quad (1.3)$$

then crack extension occurs.



Instead of measuring  $g$  as explained previously, from Griffith's work [1,8], one can calculate  $g$  for the plane stress condition and the geometry shown, Figure 1.3. For that case,

$$g = \frac{2\pi\sigma^2 a}{E} \quad (1.4)$$

where  $E$  is Young's modulus and  $\sigma$  is the applied stress.

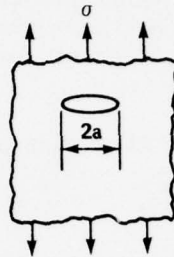


Figure 1.3. Large thin plate containing a crack of length  $2a$ .

An incremental crack extension of  $da$  on each end of the crack creates a new surface area of  $4da$ ; hence in Equation (1.3) let  $T = 4U$ , where  $U$  is the surface tension per unit area. Using Equation (1.3), a gross critical (or fracture) stress can be obtained.

$$\sigma_c = \sqrt{\frac{2E}{\pi a}} \quad (1.5)$$

It is noted that the fracture stress is inversely proportional to the square root of crack length. As noted before, Irwin and Orowan discovered that for most materials the energy balance is primarily between the elastic energy release and the plastic work in crack propagation, and have suggested the addition of a plastic work factor (which is large compared to  $U$ ) to the surface tension  $U$ .

#### 1.4 Experimental Correlation

It has already been mentioned that the fracture theory is based upon linear small strain elasticity. This is feasible if Griffith's assumption regarding the finiteness of the crack length in size relative to the molecular dimensions holds. It further permits one to ignore atomic inhomogeneities in formulation of the theory. Consequently, except for the obvious presence of a stress singularity at the tip of a sharp crack, the theory will be in many ways similar to those for dealing with deep notches.

This means that experimental models which must be tested for correlation of theory with reality will be much the same as models one might fabricate for choosing theoretical elastic solutions for deep grooves, (i.e., ordinary continuum theory is assumed to apply). However, there is one important difference. In the groove problem, no stress singularity exists, and, if the experiment can be carefully performed for one material without exceeding the elastic range, exact correlation with theory should result and it may be assumed to hold for all materials. In the case of a sharp crack, a plastic zone will develop due to the stress singularity in the experiment. (One can only insure this by precracking the specimen, since any artificial crack may not have the appropriate sharpness.) Since the plastic behavior is different for different materials, tests must be run for each material.

Specimen configuration and size must also be considered, together with the loading mode.

### 1.5 Size Effect

Irwin and McClintock [9] have identified an order of magnitude size scale appropriate to the analysis of crack behavior phenomena as shown in Figure 1.4 (all dimensions in cm).

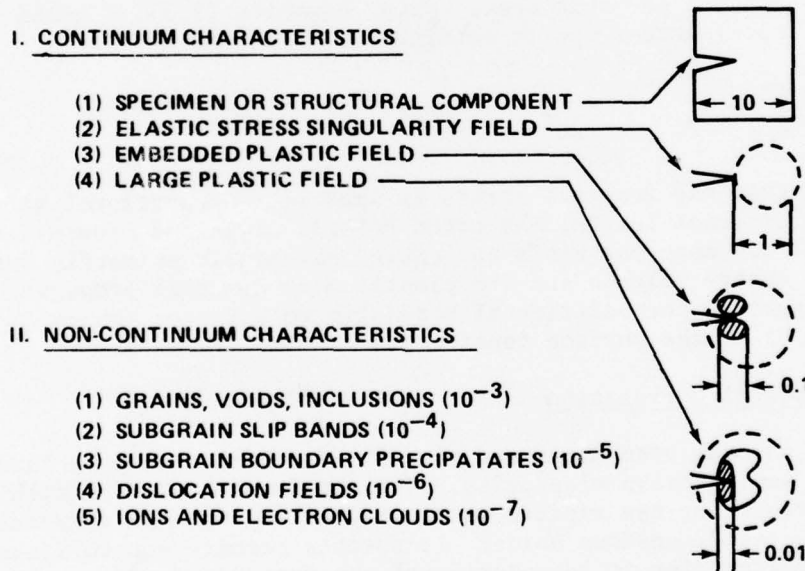


Figure 1.4. Size effect associated with cracks.

Until model 9 can be analyzed by means of wave mechanics and the results integrated through this order of magnitude, it will be necessary to consider a series of different models, each of which is appropriate to its own level of investigation (i.e., size range).

Boundary conditions must be obtained from the next largest and next smallest scales. The smaller the model size, the broader the range of conditions which can be predicted or correlated from given experimental data. From whatever level one starts, test data must be used in place of the lack of knowledge at the smaller size levels. Note that the local stress field surrounding an elastic singularity would contain on the order of  $(10^6)^2$  or  $10^{12}$  separate dislocation fields where one field is regarded as the largest size which would be sensitive to a single dislocation.

#### 1.6 Loading Modes

Stress fields near crack tips can be divided into three basic types, each of which is associated with a local mode of deformation. They are known as Modes I, II, and III, respectively (Figure 1.5).

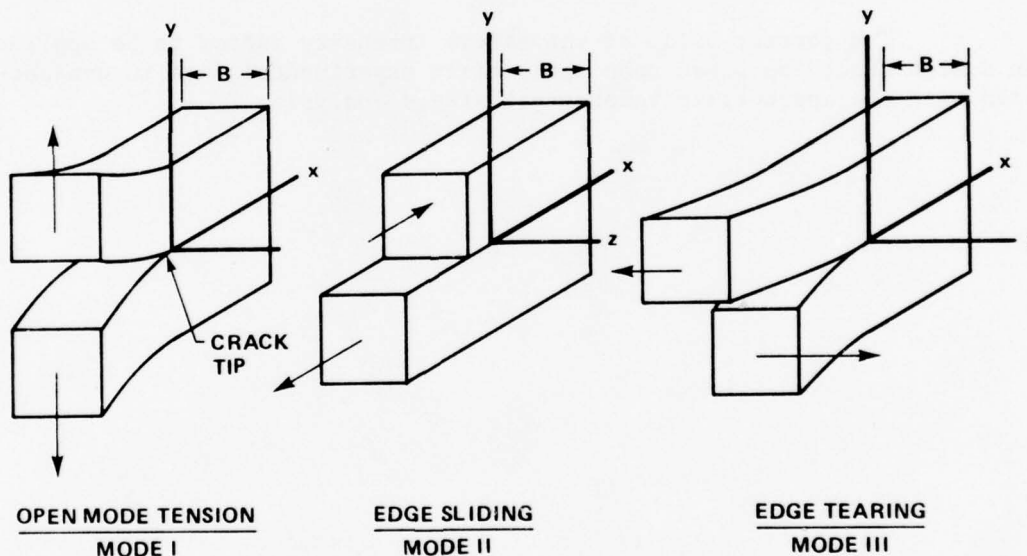


Figure 1.5. Modes of crack tip deformation.

Modes II and III bear a certain analogy to edge and screw dislocations respectively in the sense that displacement discontinuities exist along the crack surface behind the crack tips. However, the components of the stress vector must also vanish on the crack surfaces whereas for dislocation they take on continuous non-zero values.

The superposition of these three modes is sufficient to describe the most general case of local crack tip stress and deformation fields. Furthermore, it is clear from elasticity theory that if the specimen width  $B$  is small and the loads are distributed uniformly or symmetrically over  $B$ , then Modes I and II would essentially conform to plane stress fields but if  $B$  is large, the states of deformation of these modes might be more nearly plane strain. Mode III is clearly neither one.

#### 1.7 Summary

From the foregoing introduction, the following points may be made:

a) The theoretical foundation for fracture mechanics may be soundly based upon the linear small strain theory of elasticity, regardless of the phenomena occurring within the plastic zone at the crack tip which precipitates fracture.

b) The failure criterion may be based upon a limiting intensity of the local elastic stress field in the neighborhood of the crack tip. This limit can be specified in terms of a single material parameter (not yet shown). This parameter was initially recognized historically to be the so-called strain energy release rate and was later shown to be related to the stress intensity factor.

c) The correct value of the stress intensity factor to be applied in design should be based upon appropriate experimental data in conjunction with the appropriate theoretical stress analysis.



## Chapter 2. THE CRACK-TIP STRESS FIELDS

### 2.1 Westergaard Stress Function

The most direct approach to the determination of the stress and displacement fields associated with the three modes of loading of the crack is based upon the use of the Westergaard Stress Function [10,11]. Modes I and II can be analyzed as plane strain problems which are symmetric and skew-symmetric, respectively, with respect to the crack plane. Mode III can be regarded as the pure shear or torsion problem (antiplane strain). The Westergaard Stress Function will be defined and then used in defining the stress intensity factor. Correlation with the stress concentration factor and the energy rate analysis will follow.

It is known in elasticity theory [12] that any stress function  $\Phi(x,y)$  defined by

$$\sigma_{xx} = \frac{\partial^2 \Phi}{\partial y^2}, \sigma_{yy} = \frac{\partial^2 \Phi}{\partial x^2}, \tau_{xy} = -\frac{\partial^2 \Phi}{\partial x \partial y} \quad (2.1)$$

will satisfy the equilibrium equations of elasticity. Furthermore, if the function satisfies  $\nabla^4 \Phi = 0$  at every point in the body and on the boundary, then the function  $\Phi$  is said to be the solution to the associated plane strain problem. The stress components are shown in Figure 2.1.

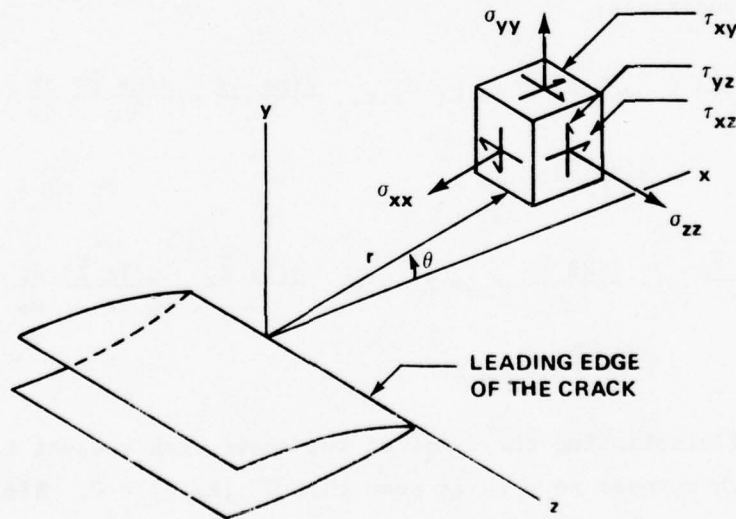


Figure 2.1. Coordinates measured from the leading edge of the crack and the stress components in the neighborhood of the crack tip.

It is further noted that any harmonic function  $\psi(x,y)$  can be made bi-harmonic by multiplying by  $x$  or  $y$ . Accordingly, one may write:

$$\Phi = \psi_1 + x \psi_2 + y \psi_3 \quad (2.2)$$

where  $\psi_1$ ,  $\psi_2$ , and  $\psi_3$  are harmonic functions and  $\Phi$  is an Airy stress function. Consider now the analytic function (Westergaard Stress Function),  $\bar{Z}$ , and its derivatives:

$$\begin{aligned} \bar{Z} &= \frac{d\bar{Z}}{dz} \\ Z &= \frac{d^2\bar{Z}}{dz^2} = \frac{d\bar{Z}}{dz} \\ Z' &= \frac{d^3\bar{Z}}{dz^3} = \frac{dZ}{dz} \end{aligned} \quad (2.3)$$

where  $z = x + iy$  is a complex coordinate.

If these functions are analytic, then due to the Cauchy-Riemann conditions, each will have harmonic real and imaginary parts. These give certain relationships between the derivatives of the real and imaginary parts. If, for example  $\bar{Z} = \text{Re } \bar{Z} + i \text{Im } \bar{Z}$  then from the Cauchy-Riemann conditions:

$$\begin{aligned} \frac{\partial(\text{Re } \bar{Z})}{\partial x} &= \frac{\partial(\text{Im } \bar{Z})}{\partial y} = \text{Re } Z; \quad \text{i.e.,} \quad \frac{\partial(\text{Re } \bar{Z})}{\partial x} = \frac{d(\text{Re } \bar{Z})}{dz} \frac{dz}{dx} \\ &= \frac{d(\text{Re } \bar{Z})}{dz} = \text{Re } Z \\ \frac{\partial(\text{Im } \bar{Z})}{\partial x} &= - \frac{\partial(\text{Re } \bar{Z})}{\partial y} = \text{Im } Z; \quad \text{i.e.,} \quad \frac{\partial(\text{Im } \bar{Z})}{\partial x} = \frac{d(\text{Im } \bar{Z})}{dz} \frac{dz}{dx} \\ &= \frac{d(\text{Im } \bar{Z})}{dz} = \text{Im } Z \end{aligned} \quad (2.4)$$

Now by differentiating the first of the above with respect to  $x$  and the second with respect to  $y$  it is seen that  $\nabla^2 (\text{Re } Z) = 0$ . Similarly,  $\nabla^2 (\text{Im } Z) = 0$ . The above equations will be used in evaluating the derivatives of the  $Z$  functions in the following paragraph.

## 2.2 Mode I - Stresses and Displacements

For Mode I deformations, in order to free the crack surface of  $\tau_{xy}$ , consider the following special form of Equations (2.2).

$$\Phi_I = \text{Re } \bar{\bar{Z}}_I + y \text{Im } \bar{Z}_I \quad (2.5)$$

where the functions  $\text{Re } \bar{\bar{Z}}_I$  and  $\text{Im } \bar{Z}_I$  are harmonic. The subscript "I" refers to Mode I. To get the stresses use

$$\begin{aligned} \sigma_{xx} &= \frac{\partial^2 \Phi_I}{\partial y^2} \\ \frac{\partial \Phi_I}{\partial y} &= \frac{\partial(\text{Re } \bar{\bar{Z}}_I)}{\partial y} + \text{Im } \bar{Z}_I + y \frac{\partial(\text{Im } \bar{Z}_I)}{\partial y} \\ &= -\text{Im } \bar{Z}_I + \text{Im } \bar{Z}_I + y \text{Re } Z_I \\ &= y \text{Re } Z_I \\ \frac{\partial^2 \Phi_I}{\partial y^2} &= \text{Re } Z_I + y \frac{\partial(\text{Re } Z_I)}{\partial y} \\ &= \text{Re } Z_I - y \text{Im } Z_I' \end{aligned}$$

Hence

$$\sigma_{xx} = \text{Re } Z_I - y \text{Im } Z_I'$$

Proceeding similarly one obtains

$$\begin{aligned} \sigma_{xx} &= \text{Re } Z_I - y \text{Im } Z_I' \\ \sigma_{yy} &= \text{Re } Z_I + y \text{Im } Z_I' \\ \tau_{xy} &= -y \text{Re } Z_I' \end{aligned} \quad (2.6)$$

Thus the choice of the form of  $\Phi_I$  above provides that  $\tau_{xy} = 0$  everywhere  $y = 0$ . Furthermore, using Hooke's Law for a state of plane strain,

$$\begin{aligned}
e_{xx} &= \frac{\partial u_x}{\partial x} = \frac{\sigma_{xx} - \nu(\sigma_{yy} + \sigma_{zz})}{E} \\
e_{yy} &= \frac{\partial u_y}{\partial y} = \frac{\sigma_{yy} - \nu(\sigma_{xx} + \sigma_{zz})}{E} \\
e_{xy} &= \frac{1}{2} \left( \frac{\partial u_x}{\partial y} + \frac{\partial u_y}{\partial x} \right) = \frac{2(1+\nu)}{E} \tau_{xy} \\
e_{zz} &= 0 = \frac{\sigma_{zz} - \nu(\sigma_{xx} + \sigma_{yy})}{E}
\end{aligned} \tag{2.7}$$

where  $u_x$  and  $u_y$  are the displacements in the x and y directions, respectively; E is Young's modulus and  $\nu$  is Poisson's ratio.

In order to obtain expressions for the displacements, substitute Equations 2.6 into Equations 2.7 and integrate as indicated. For example

$$\frac{\partial u_y}{\partial y} = \frac{\sigma_{yy} - \nu(\sigma_{xx} + \sigma_{zz})}{E}$$

and since  $\sigma_{zz} = \nu(\sigma_{xx} + \sigma_{yy})$

$$\begin{aligned}
\frac{\partial u_y}{\partial y} &= \frac{1}{E} \left[ (1 - \nu^2) \sigma_{yy} - \nu(1 + \nu) \sigma_{xx} \right] = \frac{1 + \nu}{E} \left[ (1 - \nu) \sigma_{yy} - \nu \sigma_{xx} \right] \\
&= \frac{1 + \nu}{E} \left[ (1 - \nu) (\text{Re } Z_I + y \text{ Im } Z_I') - \nu (\text{Re } Z_I - y \text{ Im } Z_I') \right] \\
&= \frac{1 + \nu}{E} \left[ (1 - 2\nu) \text{Re } Z_I + y \text{ Im } Z_I' \right]
\end{aligned}$$

Integrate by parts and use Equation (2.4)

$$\begin{aligned}
u_y &= \frac{1 + \nu}{E} \left[ (1 - 2\nu) \text{Im } \bar{Z}_I + y(-\text{Re } Z_I) + \int \text{Re } Z_I dy \right] \\
&= \frac{1 + \nu}{E} \left[ (1 - 2\nu) \text{Im } \bar{Z}_I + y(-\text{Re } Z_I) + \text{Im } \bar{Z}_I \right] \\
u_y &= \frac{1 + \nu}{E} \left[ 2(1 - \nu) \text{Im } \bar{Z}_I - y \text{Re } Z_I \right] \quad .
\end{aligned} \tag{2.8}$$

Similarly,

$$u_x = \frac{1+\nu}{E} \left[ (1-2\nu) \operatorname{Re} \bar{Z}_I - y \operatorname{Im} Z_I \right] . \quad (2.9)$$

When a straight through-the-thickness crack lies on the x axis in an infinite plate and loads are applied remote from the crack so as to produce the symmetric Mode I deformation near the crack tip, one may take

$$\Phi_I = \operatorname{Re} \bar{Z}_I + \operatorname{Im} \bar{Z}_I .$$

Whence,

$$\sigma_{yy} = \operatorname{Re} Z_I + y \operatorname{Im} Z_I'$$

$$\tau_{xy} = -y \operatorname{Re} Z_I' .$$

Thus,  $\tau_{xy} = 0$  along  $y = 0$ . One must also require that  $\operatorname{Re} Z_I$  vanish on the crack surface in order to make  $\sigma_{yy} = 0$  there.

In addition, note that (a) stress singularities must exist at the ends of the crack, and (b)  $u_y$  must be double valued along the crack surface. When a function is analytic and single-valued in a domain except along one line along which it becomes double- or multi-valued and discontinuous, that line is called a branch cut. If one takes

$$Z_I = \frac{g(z)}{[(z+b)(z-a)]^{1/2}}$$

then for a crack extending from  $x = -b$  to  $x = +a$  as in Figure 2.2 stress singularities exist at  $x = -b$  and  $x = +a$ . If one requires that  $g(z)$  is well behaved (no singularities, etc.) in the neighborhood of the crack tip, then the crack surface can be thought of as a branch cut. It is also required that  $\operatorname{Im} g(x) = 0$  for  $-b < x < a$  so that  $\operatorname{Re} Z_I = 0$  in that range (i.e., consider as a special case of  $g(z) = u(x,y) + iv(x,y)$ ,  $g = iz$ ). Then, along  $y = 0$  for  $-b < x < a$ , the denominator of  $Z_I$  above is imaginary; also  $g = ix$  is imaginary, so  $Z_I$  is real and  $\neq 0$ . Thus,  $\sigma_{yy} \neq 0$ . So one must have  $\operatorname{Im} g(x) = 0$ .

Moving the origin to the crack tip at  $x = a$ , introduce  $\xi = z - a$  (Figure 2.2). Now



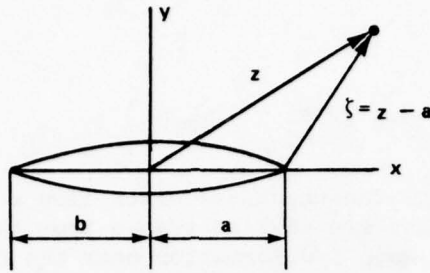


Figure 2.2. A crack in a large plate.

$$Z_I = \frac{g(\zeta + a)}{[(\zeta + a + b) \zeta]^{1/2}}$$

which can be written as

$$Z_I = \frac{f(\zeta)}{\zeta^{1/2}}$$

where  $f(\zeta)$  is also well behaved so that when  $\zeta \rightarrow 0$ ,  $f(\zeta)$  remains finite. Such a well-behaved analytic function may be expanded into a MacLaurin series about the new origin,

$$f(\zeta) = f(0) + \sum_{n=1}^{\infty} f^{(n)}(0) \zeta^n$$

write the results as

$$Z_I = \frac{K_I/\sqrt{2\pi} + a_1 \zeta + a_2 \zeta^2 + \dots}{\zeta^{1/2}}$$

where  $f(0) = K_I/\sqrt{2\pi}$  (the  $\sqrt{2\pi}$  is arbitrary), and  $a_n$  is  $f^{(n)}(0)$ . Thus

$$Z_I \Big|_{\zeta \rightarrow 0} = \frac{K_I}{(2\pi\zeta)^{1/2}} \quad (2.10)$$

All crack tip stress functions reduce to the above form. The functional forms of the local elastic stress and displacement fields may be obtained by substituting the above into the stress and displacement field equations.

For example, for  $\sigma_{xx}$  it is seen that  $\text{Re } Z_I$  and  $\text{Im } Z_I'$  are required. Introduce polar coordinates  $r$  and  $\theta$  and consider the origin to be at the right crack tip. i.e.,

$$Z_I \Big|_{|\zeta| \rightarrow 0} = \frac{K_I}{\sqrt{2\pi} \zeta^{1/2}} = \frac{K_I}{\sqrt{2\pi}} \zeta^{-1/2} .$$

Use

$$\zeta^{-1/2} = r^{-1/2} e^{-i \theta/2} = r^{-1/2} \left\{ \cos \frac{\theta}{2} - i \sin \frac{\theta}{2} \right\} .$$

Then

$$Z_I \Big|_{r \rightarrow 0} = \frac{K_I}{\sqrt{2\pi} r^{1/2}} \left( \cos \frac{\theta}{2} - i \sin \frac{\theta}{2} \right) .$$

Therefore,

$$\operatorname{Re} Z_I = \frac{K_I}{\sqrt{2\pi} r^{1/2}} \cos \frac{\theta}{2}$$

$$\operatorname{Im} Z_I = - \frac{K_I}{\sqrt{2\pi} r^{1/2}} \sin \frac{\theta}{2} .$$

Now

$$Z_I' = \frac{dZ}{d\zeta} = - \frac{K_I}{2\sqrt{2\pi}} \zeta^{-3/2}$$

$$Z_I' = - \frac{K_I}{2\sqrt{2\pi} r^{3/2}} \left( \cos \frac{3\theta}{2} - i \sin \frac{3\theta}{2} \right)$$

and

$$\operatorname{Im} Z_I' = \frac{K_I}{2\sqrt{2\pi} r^{3/2}} \sin \frac{3\theta}{2} .$$

Now use  $y = r \sin \theta$ . Then

$$y \operatorname{Im} Z_I' = \frac{K_I}{2\sqrt{2\pi} r^{1/2}} \sin \theta \sin \frac{3\theta}{2} .$$

Substituting into the expression for  $\sigma_{xx}$ , Equations (2.6)

$$\sigma_{xx} = \frac{K_I}{\sqrt{2\pi} r^{1/2}} \left( \cos \frac{\theta}{2} - \frac{1}{2} \sin \theta \sin \frac{3\theta}{2} \right) .$$

By using  $\frac{1}{2} \sin \theta = \sin \frac{\theta}{2} \cos \frac{\theta}{2}$ , the stress  $\sigma_{xx}$  can be written in the desired form. Stresses  $\sigma_{yy}$  and  $\tau_{xy}$  follow in a similar manner:

$$\begin{aligned} \sigma_{xx} &= \frac{K_I}{\sqrt{2\pi r}} \cos \frac{\theta}{2} \left( 1 - \sin \frac{\theta}{2} \sin \frac{3\theta}{2} \right) \\ \sigma_{yy} &= \frac{K_I}{\sqrt{2\pi r}} \cos \frac{\theta}{2} \left( 1 + \sin \frac{\theta}{2} \sin \frac{3\theta}{2} \right) \\ \tau_{xy} &= \frac{K_I}{\sqrt{2\pi r}} \cos \frac{\theta}{2} \sin \frac{\theta}{2} \cos \frac{3\theta}{2} \\ \sigma_{zz} &= \nu(\sigma_{xx} + \sigma_{yy}) \quad \tau_{xz} = \tau_{yz} = 0 \end{aligned} \tag{2.11}$$

where  $K_I$  is the stress intensity factor for Mode I deformation. The quantity  $K_I$  is a constant for a given loading condition and a given specimen geometry and crack length; it will be discussed in more detail later.

Displacements are calculated from Equations (2.8) and (2.9). For example, for  $u_x$ , it is seen that  $\text{Re } \bar{Z}_I$  and  $\text{Im } Z_I$  are required. Obtain first  $\text{Re } \bar{Z}_I$

$$\begin{aligned} Z_I &= \frac{K_I}{\sqrt{2\pi} \zeta^{1/2}} \\ \bar{Z}_I &= \frac{K_I}{\sqrt{2\pi}} \int \zeta^{-1/2} d\zeta = \frac{2K_I}{\sqrt{2\pi}} \zeta^{1/2} \\ \bar{Z}_I &= \sqrt{\frac{2}{\pi}} K_I r^{1/2} \left( \cos \frac{\theta}{2} + i \sin \frac{\theta}{2} \right) . \end{aligned}$$



Therefore,

$$\operatorname{Re} \bar{Z}_I = \sqrt{\frac{2}{\pi}} K_I r^{1/2} \cos \frac{\theta}{2} .$$

Now  $\operatorname{Im} Z_I$  was noted during the calculation of the stress fields

$$\operatorname{Im} Z_I = - \frac{K_I}{\sqrt{2\pi} r^{1/2}} \sin \frac{\theta}{2} .$$

Use  $y = r \sin \theta$  to obtain

$$y \operatorname{Im} Z_I = - \frac{K_I}{\sqrt{2\pi}} r^{1/2} \sin \frac{\theta}{2} \sin \theta .$$

Substituting  $\operatorname{Re} \bar{Z}_I$  and  $y \operatorname{Im} Z_I$  into Equation (2.9) yields

$$u_x = \frac{2(1+\nu)}{E} \frac{K_I r^{1/2}}{\sqrt{2\pi}} \left[ (1-2\nu) \cos \frac{\theta}{2} + \frac{1}{2} \sin \frac{\theta}{2} \sin \theta \right] .$$

The displacement  $u_y$  would be obtained similarly. In order to write  $u_x$  in its final form use

$$\sin \theta = 2 \sin \frac{\theta}{2} \cos \frac{\theta}{2}$$

and

$$G = \frac{E}{2(1+\nu)} .$$

Finally,

$$\begin{aligned} u_x &= \frac{K_I r^{1/2}}{\sqrt{2\pi} G} \cos \frac{\theta}{2} \left[ 1 - 2\nu + \sin^2 \frac{\theta}{2} \right] \\ u_y &= \frac{K_I r^{1/2}}{\sqrt{2\pi} G} \sin \frac{\theta}{2} \left[ 2(1-\nu) - \cos^2 \frac{\theta}{2} \right] \end{aligned} \quad (2.12)$$

$$u_z = 0 \quad (\text{for plane strain}) .$$

Equations (2.12) give the displacements associated with Mode I deformation. Again, it is pointed out that different  $Z_I$ 's change only the intensity of the displacement fields so long as first mode deformation is maintained.

Note also that the obtained values of  $u_x$  and  $u_y$  involve symmetric and unsymmetric forms of  $\theta/2$  and so they do indeed describe opening mode deformations, i.e.,  $u_y \propto \sin \theta/2$  and  $u_x \propto \cos \theta/2$  and so are unsymmetric and symmetric, respectively (when unsymmetric forms are squared, as  $\sin^2 \theta/2$ , the unsymmetric effects vanish).

### 2.3 Mode II - Stresses and Displacements

Just as Equation (2.5) leads to the proper stress and displacement form for Mode I deformation, one can, by a judicious choice of  $\Phi_{II}$ , obtain the appropriate forms for a Mode II deformation. Once  $\Phi_{II}$  has been chosen, the procedure followed is the same as that followed in the development just completed for Mode I displacements. Consequently, instead of developing the results in detail, only an outline of procedure with the results will be given. Assume,

$$\Phi_{II} = -y \operatorname{Re} \bar{Z}_{II} \quad . \quad (2.13)$$

The stresses in terms of  $Z_{II}$  become

$$\left. \begin{aligned} \sigma_{xx} &= 2 \operatorname{Im} Z_{II} + y \operatorname{Re} Z'_{II} \\ \sigma_{yy} &= -y \operatorname{Re} Z'_{II} \\ \tau_{xy} &= \operatorname{Re} Z_{II} - y \operatorname{Im} Z'_{II} \end{aligned} \right\} \quad (2.14)$$

This frees the  $y = 0$  surface of  $\sigma_{yy}$ . The displacements in terms of  $Z_{II}$  are

$$\begin{aligned} u_x &= \frac{1+\nu}{E} \left[ 2(1-\nu) \operatorname{Im} \bar{Z}_{II} + y \operatorname{Re} Z_{II} \right] \\ u_y &= \frac{1+\nu}{E} \left[ (2\nu-1) \operatorname{Re} \bar{Z}_{II} - y \operatorname{Im} Z_{II} \right] \quad . \end{aligned} \quad (2.15)$$

Next, taking

$$Z_{II} \Big|_{|\zeta| \rightarrow 0} = \frac{K_{II}}{(2\pi\zeta)^{1/2}} \quad (2.16)$$

where  $\zeta = re^{i\theta}$ , and using the same reasoning as before, one obtains

$$\begin{aligned} \sigma_{xx} &= - \frac{K_{II}}{\sqrt{2\pi} r^{1/2}} \sin \frac{\theta}{2} (2 + \cos \frac{\theta}{2} \cos \frac{3\theta}{2}) \\ \sigma_{yy} &= \frac{K_{II}}{\sqrt{2\pi} r^{1/2}} \cos \frac{\theta}{2} \sin \frac{\theta}{2} \cos \frac{3\theta}{2} \\ \tau_{xy} &= \frac{K_{II}}{\sqrt{2\pi} r^{1/2}} \cos \frac{\theta}{2} (1 - \sin \frac{\theta}{2} \sin \frac{3\theta}{2}) \end{aligned} \quad (2.17)$$

$$\sigma_{zz} = \nu(\sigma_{xx} + \sigma_{yy}), \quad \tau_{xz} = \tau_{yz} = 0 \text{ (plane strain)}$$

and

$$\begin{aligned} u_x &= \frac{K_{II} r^{1/2}}{\sqrt{2\pi} G} \sin \frac{\theta}{2} (2 - 2\nu + \cos^2 \frac{\theta}{2}) \\ u_y &= \frac{K_{II} r^{1/2}}{\sqrt{2\pi} G} \cos \frac{\theta}{2} (1 - 2\nu + \sin^2 \frac{\theta}{2}) \\ u_z &= 0 \text{ (plane strain)} \end{aligned} \quad (2.18)$$

where  $K_{II}$  is the stress intensity factor for Mode II deformation.

Equations (2.18) show that  $u_x$  is an unsymmetric function of  $\theta/2$  and  $u_y$  is a symmetric function of  $\theta/2$ , which is in accordance with the Mode II deformation.

Due to the forms exhibited by  $\Phi_I$  and  $\Phi_{II}$ , Equations (2.5) and (2.13), the results from the first and second modes may be directly superimposed since  $\Phi_I + \Phi_{II}$  is also an admissible form of Equation (2.2). It follows that the stresses and displacements resulting from individual values of  $\Phi_I$  and  $\Phi_{II}$  may also be directly superimposed.

#### 2.4 Mode III - Stresses and Displacements

The antiplane strain problem or two-dimensional problem of pure shear may be specified as follows:

$$\begin{aligned} u_x &= 0 \\ u_y &= 0 \\ u_z &= u_z(x, y). \end{aligned} \tag{2.19}$$

Applying the strain-displacement equations and Hooke's Law, one finds

$$\begin{aligned} 2 e_{xz} &= \frac{\partial u_z}{\partial x} + \frac{\partial u_x}{\partial z} = \frac{\tau_{xz}}{G} \\ 2 e_{yz} &= \frac{\partial u_z}{\partial y} + \frac{\partial u_y}{\partial z} = \frac{\tau_{yz}}{G} \end{aligned} \tag{2.20}$$

so that

$$\begin{aligned} \tau_{xz} &= G \frac{\partial u_z}{\partial x} \\ \tau_{yz} &= G \frac{\partial u_z}{\partial y} . \end{aligned} \tag{2.21}$$

All other components of strain and stress vanish, and the single resulting equilibrium equation is

$$\frac{\partial \tau_{xz}}{\partial x} + \frac{\partial \tau_{yz}}{\partial y} = 0 . \tag{2.22}$$

Substituting Equations (2.21) into Equation (2.22), there results

$$\nabla^2 u_z = 0 . \tag{2.23}$$

The function

$$u_z = \frac{1}{G} \operatorname{Im} \bar{Z}_{III} \tag{2.24}$$

where  $\bar{Z}_{III}$ , being analytic and harmonic, satisfies the governing equation, Equation (2.23). Now, following the same reasoning as before, the

function  $Z_{III}$  for a crack along the x axis must take the following form near the crack tip:

$$Z_{III} \Big|_{\zeta \rightarrow 0} = \frac{K_{III}}{(2\pi \zeta)^{1/2}} \quad (2.25)$$

where  $K_{III}$  is the Mode III stress intensity factor. Now, substituting Equation (2.25) into Equations (2.21), where  $\zeta = re^{i\theta}$ , and proceeding as before one obtains

$$\begin{aligned} \tau_{xz} &= \frac{-K_{III}}{\sqrt{2\pi} r^{1/2}} \sin \frac{\theta}{2} \\ \tau_{yz} &= \frac{K_{III}}{\sqrt{2\pi} r^{1/2}} \cos \frac{\theta}{2} \end{aligned} \quad (2.26)$$

$$\sigma_{xx} = \sigma_{yy} = \sigma_{zz} = \tau_{xy} = 0$$

and

$$\begin{aligned} u_z &= \frac{K_{III}}{G} \sqrt{\frac{2}{\pi}} r^{1/2} \sin \frac{\theta}{2} \\ u_x &= u_y = 0 \end{aligned} \quad (2.27)$$

Having now obtained the expressions for the stresses and displacements in terms of the stress intensity factors  $K_I$ ,  $K_{II}$ ,  $K_{III}$  for Modes I, II, and III loading, it is pointed out that one is able to do this only because the crack surfaces are the dominating influence on the stress distributions in the neighborhood of the cracks, and the specimen boundaries and loads affect only the intensity and not the form of the local elastic stress and displacement fields.

The stress Equations (2.11) and displacement Equations (2.12) for the Mode I deformation and the stress Equations (2.17) and displacement Equations (2.18) for Mode II deformation have been written for the case of plane strains (i.e.,  $u_z = 0$ ) but by setting  $\sigma_{zz} = 0$  and replacing Poisson's ratio  $\nu$  with  $\nu/(1+\nu)$  ( $G$  is not changed) in the displacement equations, field equations for plane stress may be obtained.



## 2.5 Characteristics of the Elastic Crack-Tip Stress Field

The dominant mathematical feature of the three stress fields is the  $1/r^{1/2}$  singularity. All three sets of stresses (Modes I, II, and III) were obtained by neglecting the higher order terms in  $r$  in the MacLaurin expansion of  $Z$ ; thus, the stresses can be regarded as good approximations when  $r$  is small compared to the other planar dimensions ( $x - y$  plane) of the body, such as crack length, and mathematically exact as  $r$  approaches zero. The  $1/r^{1/2}$  singularity predicts that the stresses approach infinity as  $r$  approaches zero. Crack-tip plasticity prevents this in a way which is discussed in Chapter 4. Equations (2.11), (2.17), and (2.26) also predict that the stresses approach zero as  $r$  becomes large. This is because the higher order terms in the MacLaurin expansion were omitted. Physically, for large  $r$ , the stresses would approach those values in the body that would exist due to remote loads even if the crack were not present.

It is instructive to take a more detailed look at the nature of the crack-tip stress field represented by Equations (2.11) for the opening mode. The various stress quantities have been summarized by Williams [13] as shown in Figure 2.3. It is seen that a state of hydrostatic tension exists in the material along the crack plane ( $y = 0$ ) ahead of the crack tip: i.e.,

$$\frac{\sigma_{xx}(x,0)}{\sigma_{yy}(x,0)} = 1 \quad . \quad (2.28)$$

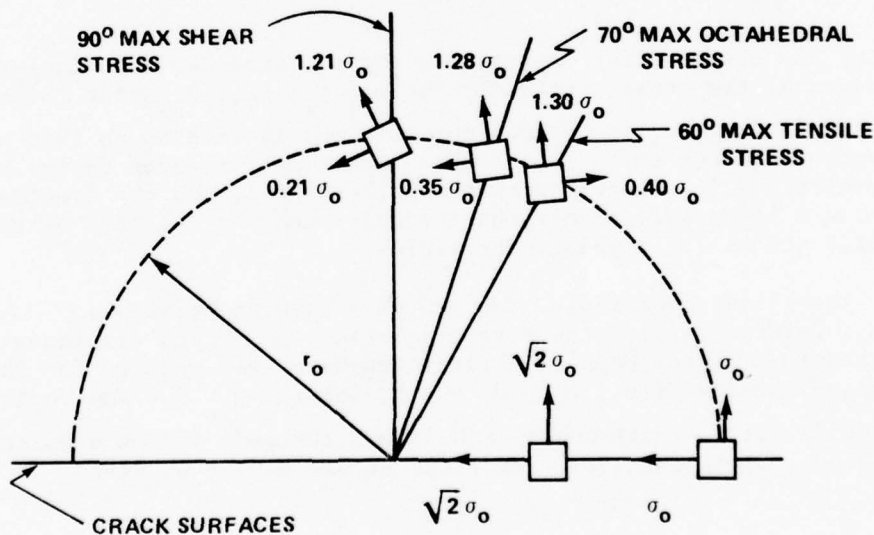


Figure 2.3. Opening mode stresses.

This indicates a decreased tendency for yielding at the base of the crack. At the same time a large amount of distortion is indicated off to the sides of the crack ( $\theta = \pm 70$  degrees). The maximum shear stress occurs at  $\theta = 90$  degrees. The maximum tensile stress occurs not ahead of the crack as one might expect but at  $\theta = 60$  degrees.

The stress components near the crack tip in polar coordinates (Figure 2.4) can be calculated by substitution of Equation (2.11) into stress transformation expressions such as

$$\sigma_{\theta} = \sigma_{xx} \sin^2 \theta + \sigma_{yy} \cos^2 \theta - 2\tau_{xy} \sin \theta \cos \theta \quad .$$

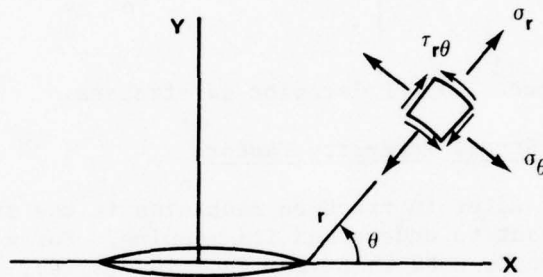


Figure 2.4. Stress components in polar coordinates.

For the opening mode, Figure 2.5 shows a sketch of the variation of these stresses with the angle  $\theta$ . The location of maximum  $\sigma_{\theta}$  is important in determining the direction of crack propagation, and Yoffee [14] assumed propagation would occur along a line normal to maximum  $\sigma_{\theta}$ . For the opening mode, maximum  $\sigma_{\theta}$  occurs at  $\theta = 0$  degrees. For a mixture of Modes I and II, maximum  $\sigma_{\theta}$  would occur at  $\theta \neq 0$  degrees.

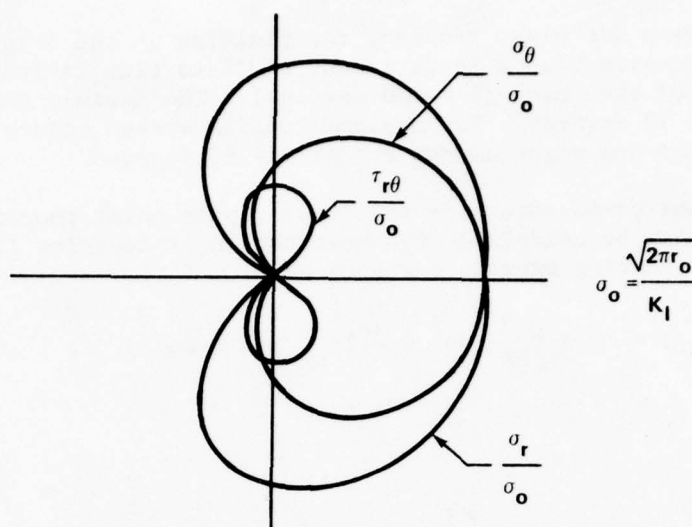


Figure 2.5. Polar plot of stresses.

## 2.6 Meaning of the Stress Intensity Factor

The primary parameter in fracture mechanics is the stress intensity factor; it is important to understand its meaning. For a given Westergaard stress function  $Z_I$  note that from Equation (2.10),

$$K_I = \lim_{|z| \rightarrow 0} (2\pi |z|)^{1/2} Z_I \quad (2.29)$$

with similar equations for  $K_{II}$  and  $K_{III}$ . It is pointed out that while  $K_I$  will be different for different  $Z_I$ 's, the form of the stresses, Equation (2.11), for any Mode I problem will be the same. The only result will be that the intensity or magnitude of the stresses in the neighborhood of the crack tip will be altered. In other words,  $K_I$  is the strength of the  $1/r^{1/2}$  stress singularity, and it is not a function of coordinates  $r$  and  $\theta$ .

It is important to distinguish here between the stress concentration factor and the stress intensity factor. The stress concentration factor is defined as the maximum stress at the tip of, say, a notch divided by the nominal stress. Since the opening mode stresses of Equations (2.11) mathematical approach infinity at the crack tip, the stress concentration factor for a crack would be infinite while the stress intensity factor is a finite constant (for a given specimen geometry and load). This constant is multiplied times the form of the stress field. While the stress concentration and stress intensity factors are different quantities, mathematically, they are related in a useful way (Art. 2.8).



Finally, from dimensional considerations of the stress Equations (2.11), (2.17), and (2.26), it is clear that the stress intensity factors vary linearly with the applied loads (for linearly elastic bodies) and also depend upon the geometric configuration, including the crack size. The dimensions on  $K_I$ ,  $K_{II}$ , and  $K_{III}$  are (stress)  $\times$  (length)<sup>1/2</sup>.

An aspect of the stress intensity factor which has caused considerable confusion must be explained. As a holdover from the formulative period of fracture mechanics, there exists another definition of  $K$  - call it  $K^*$  - which differs from the present definition by the factor  $\sqrt{\pi}$ . That is,  $K = \sqrt{\pi} K^*$ . When the  $K^*$  definition is used then the singularity of the stress fields, Equations (2.11), (2.17), and (2.26) are written in the form  $\frac{1}{\sqrt{2r}}$  rather than  $\frac{1}{\sqrt{2\pi r}}$ . Unfortunately, many authors do not explain which definition is being used, and one must examine the form of the author's stress field for clarification. To avoid an error of  $\sqrt{\pi}$  when using stress intensity factor solutions from the literature one must be careful to determine which definition the author used.

## 2.7 Dimensional Considerations for the Classical Problems of Cracks in Infinite Plates

In Figure 2.6(a) only two characteristic dimensions are present,  $\sigma$  and  $a$ . Furthermore, this configuration is symmetric with respect to the crack plane. Due to this symmetry with respect to the x-z plane, one notes that only Mode I deformation is present. This leads to Equation (2.11) for stress. Since, in Equation (2.11),  $\sigma_y \propto K/r^{1/2}$ , one sees from dimensional considerations that

$$K_I = c_1 \sigma a^{1/2} \quad (2.30)$$

Also, due to symmetry,  $K_{II} = K_{III} = 0$ . For this case the complete Westergaard stress function is available so that the exact stresses ahead of the crack can be computed. The exact stresses can then be compared with the fracture mechanics stress Equations (2.11) to determine the constant  $c_1$ . For the case of part (a), the Westergaard stress function is,

$$Z = \frac{\sigma z}{(z^2 - a^2)^{1/2}} \quad (2.31)$$

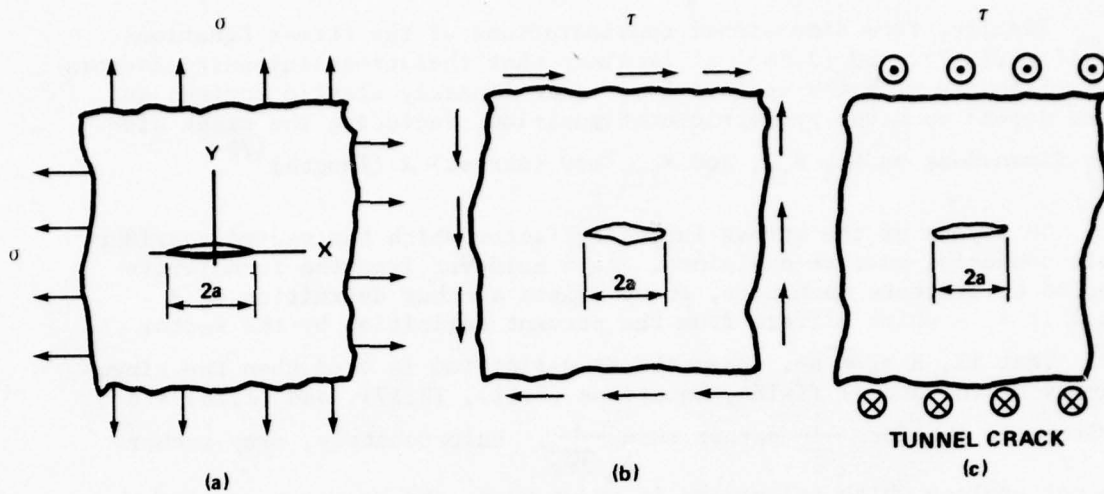


Figure 2.6. Crack in an infinite plate - various modes.

From Equation (2.6),

$$\sigma_{yy} = \operatorname{Re} Z_I + y \operatorname{Im} Z_I'.$$

Along  $y = 0$

$$\sigma_{yy}|_{y=0} = \operatorname{Re} Z_I = \frac{\sigma(\zeta + a)}{[(\zeta + a)^2 - a^2]^{1/2}}$$

where  $\zeta$  is a complex coordinate centered at the right crack tip.

$\zeta = re^{i\vartheta}$  and for  $y = 0$ ,  $\vartheta = 0$  and  $\zeta = r$ . Therefore,

$$\sigma_{yy}|_{\vartheta=0} = \frac{\sigma(r + a)}{[(r + a)^2 - a^2]^{1/2}} = \frac{\sigma(r + a)}{[r^2 + 2ar]^{1/2}} \quad (2.32)$$

is the exact stress. From Equations (2.11), the fracture mechanics stress is

$$\sigma_{yy}|_{\vartheta=0} = \frac{K_I}{(2\pi r)^{1/2}} \quad (2.33)$$

By requiring that the approximate stress, Equation (2.33) equals the exact stress, Equation (2.32), as  $r \rightarrow 0$

$$\lim_{r \rightarrow 0} \left[ \frac{K}{(2\pi r)^{1/2}} - \frac{\sigma(r+a)}{(r+2a)^{1/2} r^{1/2}} \right] = 0$$

there results

$$K_I = \sigma (\pi a)^{1/2} \quad . \quad (2.34)$$

Comparing Equation (2.34) with Equation (2.30), it is seen that

$$C_I = \sqrt{\pi} \quad .$$

## 2.8 Correlation of Stress Intensity Factor with Stress Concentration Factor

Many solutions are already available in the literature which provide stress concentration type solutions for various kinds of notches. It is then a distinct advantage to be able to relate the stress concentration solutions for a notch to the stress intensity factor for a crack. Consider a symmetrically loaded notch for which the tips are embedded in a Mode I stress field. For this case, it is known from Equation (2.34) that  $K_I = \sigma (\pi a)^{1/2}$ . From Equation (2.11) the stress  $\sigma_{yy}$  directly ahead of a crack ( $\theta = 0$ ) is  $\sigma_{yy} = K_I / (2\pi r)^{1/2}$ . Suppose one used this form to approximate the stress near a notch with a root radius  $\rho$  and root stress  $\sigma_m$  (this is accurate only when  $\rho \rightarrow 0$ ). Then in order to have the proper units on  $\sigma_{yy}$  one must pick

$$K_I \approx c' \sigma_m \rho^{1/2} \quad . \quad (2.35)$$

Now by expressing  $\sigma_m$  in terms of  $\sigma$  from the notch solution and letting  $\rho \rightarrow 0$ , in the limit one obtains an expression for  $K_I$  in terms of  $\sigma$  and  $a$ . By equating this new expression to a known case Equation (2.34),  $c'$  can be evaluated. Consider the notch solution for an elliptical hole under uniform tension,

$$\sigma_m = \sigma \left[ 1 + 2 \left( \frac{a}{\rho} \right)^{1/2} \right] \quad (2.36)$$

where  $a$ , the semiminor axis, becomes the root radius as  $\rho$  becomes small. Using Equation (2.35) as  $\rho$  becomes small

$$K_I = \lim_{\rho \rightarrow 0} \left\{ c' \sigma \left[ 1 + 2 \left( \frac{a}{\rho} \right)^{1/2} \right] \rho^{1/2} \right\} = 2 c' \sigma a^{1/2} .$$

Equating this to Equation (2.34), it is seen that

$$c' = \frac{\sqrt{\pi}}{2}$$

or that  $K_I$  for a crack under Mode I loading can be computed from a corresponding notch solution by

$$K_I = \lim_{\rho \rightarrow 0} \frac{\sqrt{\pi}}{2} \sigma_m \rho^{1/2} . \quad (2.37)$$

A converse relationship also exists for determining stress concentration factors for notches from stress intensity factor solutions for cracks [15].

A similar line of reasoning may be used to identify the problems of Figure 2.6(b) and (c) with Modes II and III, respectively, so that:

Figure 2.6(b), Mode II:

$$K_{II} = \tau(\pi a)^{1/2} \quad (2.38)$$

$$K_I = K_{III} = 0 .$$

Figure 2.6(c), Mode III:

$$K_{III} = \tau(\pi a)^{1/2} \quad (2.39)$$

$$K_I = K_{II} = 0 .$$

## 2.9 Equivalence of Energy Rate and Stress Intensity Factor Approaches

It was shown in Chapter 1 that  $g$  is independent of the load type or grip condition. Thus, for convenience, in the discussion which follows, the fixed grip situation may be employed with no loss in generality of results.

If an elastic body is loaded and the grips (load point displacements) are then fixed, the strain energy change  $dV/da$  will be the only contribution to  $g$ . In this case, the work required to close a small segment of the crack  $\delta a$ , from the opened position (Figure 2.7(a)) to the closed position (Figure 2.7(b)) is identical to the strain energy released

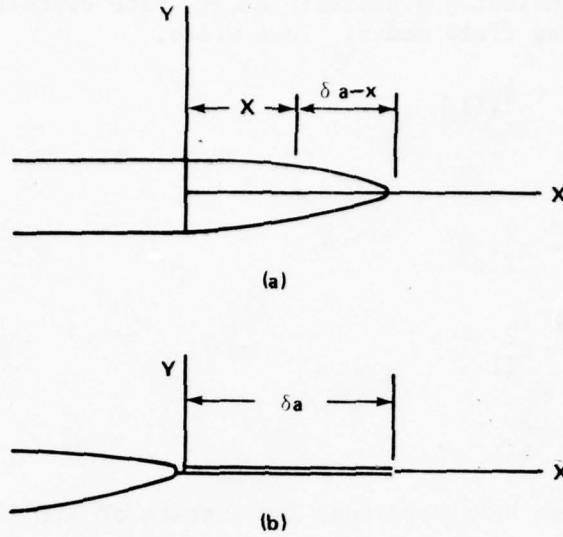


Figure 2.7. Closing of a crack by crack-surface tractions.

upon its opening (for linear, elastic behavior). The work can be computed as the crack-surface tractions required to close the crack times their closing displacements times one-half. The tractions will be those along  $\delta a$  for case (b) of Figure 2.7. The displacements will be those along  $\delta a$  in case (a) of Figure 2.7.

The strain energy release per unit area of crack extension is:

$$g = - \left. \frac{dV}{da} \right|_{\text{fixed grips}} = \lim_{\delta a \rightarrow 0} \frac{2}{\delta a} \int_0^{\delta a} \left( \frac{\sigma_{yy} u_y}{2} + \frac{\tau_{xy} u_x}{2} + \frac{\tau_{yz} u_z}{2} \right) dx . \quad (2.40)$$

The negative sign is properly accounted for because the crack opening displacements which are used here are negative to the crack closing displacements. The factor of 2 preceding the integral is necessary because displacements occur on both sides of the crack plane. The stresses for Modes I, II, and III, Equations (2.11), (2.17), and (2.26), are evaluated at  $\theta = 0$  and  $r = x$ . The displacements for the three modes are evaluated at  $\theta = \pi$  and  $r = \delta a - x$ . Working out the details, the strain energy release rate becomes,

$$g = \frac{1 - \nu^2}{E} K_I^2 + \frac{1 - \nu^2}{E} K_{II}^2 + \frac{1 + \nu}{E} K_{III}^2 . \quad (2.41)$$



Equation (2.41) indicates a separate energy rate contribution from each of the three stress field modes. Then write,

$$g = g_I + g_{II} + g_{III} \quad (2.42)$$

where

$$\begin{aligned} g_I &= \frac{1 - \nu^2}{E} K_I^2 \\ g_{II} &= \frac{1 - \nu^2}{E} K_{II}^2 \\ g_{III} &= \frac{1 + \nu}{E} K_{III}^2 \end{aligned} \quad (2.43)$$

Equations (2.43) has been developed for a state of plane strain. They can be converted to the plane stress case by discarding the  $1 - \nu^2$  term in the first two equations.

Thus, for isotropic materials, Equations (2.43) permit the conversion of a measured  $g$  into a  $K$  without knowledge of the stress function for the problem at hand. It was assumed in obtaining Equations (2.43) that the crack extends straight ahead along a plane. For combined-mode loading, cracks do not extend in a plane fashion and therefore results obtained using the approach taken to obtain Equations (2.43) would be divergent from reality. Equations (2.43) do serve, though, to show the general equivalency of the energy rate and stress intensity factor approach.

It was discussed briefly in Chapter 1 that fracture is assumed to occur when the strain energy release rate  $g$  approaches a critical value which depends upon the material; i.e., when  $g \rightarrow g_c$ . It can now be seen that this is equivalent to assuming that fracture occurs when the stress intensity factor approaches a critical value. Then the fracture criterion is that as

$$K \rightarrow K_c, \quad (2.44)$$

crack propagation occurs.

### Chapter 3. STRESS INTENSITY FACTOR SOLUTIONS

The relationship of the stress intensity factor to the Westergaard Stress Function was described in Chapter 2. The discussion will begin here by considering some examples of solutions by the Westergaard method. Its limitations will be noted, and a more general approach, based upon the method of Muskhelishvili will be developed for plane problems. Finally, a brief discussion will be included, noting the results of other technologically important solutions.

#### 3.1 Examples of Crack-Tip Solutions Using the Westergaard Stress Function

Consider a crack of length  $2a$  in a uniform biaxial stress field (Figure 3.1). This problem was treated from a dimension viewpoint in Chapter 2. The Westergaard Stress Function for this case is given by [10,11]

$$Z_1 = \frac{\sigma z}{(z^2 - a^2)^{1/2}} \quad (3.1)$$

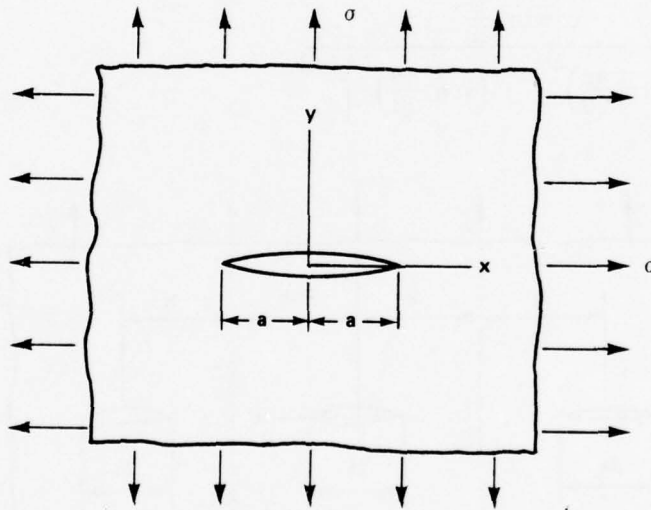


Figure 3.1. Crack in a uniform, biaxial stress field.

Use now  $z = \zeta + a$  to write

$$z_I^2 = \frac{\sigma (\zeta + a)}{(\zeta + 2a)^{1/2} \zeta^{1/2}} \quad (3.1)$$

and use Equation (2.29) to yield

$$K_I = \lim_{|\zeta| \rightarrow 0} (2\pi\zeta)^{1/2} \frac{\sigma (\zeta + a)}{(\zeta + 2a)^{1/2} \zeta^{1/2}} .$$

There results

$$K_I = \sigma(\pi a)^{1/2} \quad (3.2)$$

which was found previously in Equation (2.34).

Consider next an infinite periodic array of cracks along a line in a field of uniform tension (Figure 3.2). The half period is  $b$  and the half crack length is  $a$ . The stress function that solves this problem has been provided by Westergaard [10,11] as:

$$z_I = \frac{\sigma \sin \frac{\pi z}{2b}}{\left[ \left( \sin \frac{\pi z}{2b} \right)^2 - \left( \sin \frac{\pi a}{2b} \right)^2 \right]^{1/2}} \quad (3.3)$$

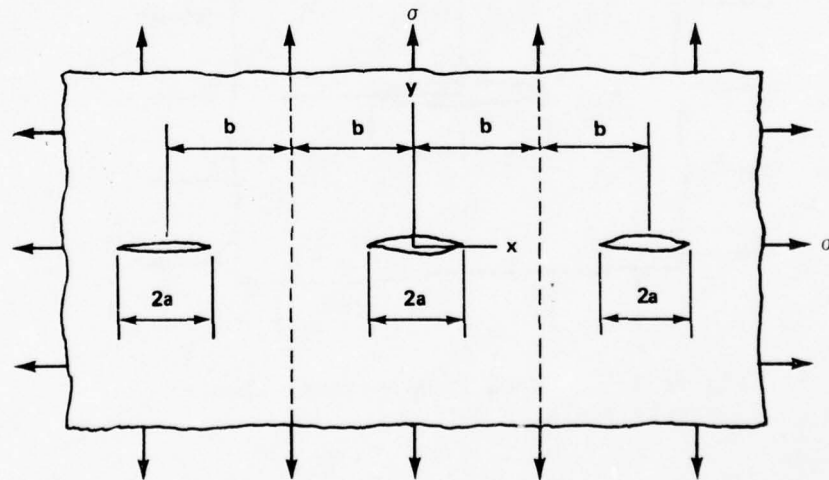


Figure 3.2. Periodic array of cracks along a line.

Again using Equation (2.29) with  $z = \zeta + a$  one finds

$$K_I = \sigma(\pi a)^{1/2} \left( \frac{2b}{\pi a} \tan \frac{\pi a}{2b} \right)^{1/2} \quad (3.4)$$

This formula, sometimes referred to as the tangent solution, has been widely used in fracture toughness testing. It is a good example of how solutions for infinite bodies can sometimes be usefully applied to finite shapes. Consider the following.

The dotted lines on the plate in Figure 3.2 represent axes of symmetry and so they are free of shear stress. Now if  $a \ll b$ , then one may remove the horizontal stress field at infinity leaving only small self-equilibrating stresses  $\sigma_{xx}$  along these axes. This will not alter the value of  $K_I$  since  $K_I$  depends only upon  $\sigma_{yy}$ . Consequently, one may regard it as permissible to cut the sheet along the axes of symmetry and to consider the above  $K_I$  as an approximate solution for finite width strips with central cracks provided  $a < b/2$ . Results of Isida [16] and Kobayashi [17,18] indicate that, even for  $a > b/2$ , the error in this practice is less than 7 percent.

Furthermore, if one slices the body along the y-axis (or corresponding axes) the above  $K_I$  may be regarded as an approximate solution for double-edge-notched strips which is within 2 percent according to Bowie [19] if  $a > b/2$ .

Both the center-cracked and double edge-cracked specimens have been used in fracture toughness testing. Finally, note that for  $b \gg a$  the results found here, Equation (3.4), reduce to the case of a single crack in an infinite plate, Equation (3.2).

### 3.2 Crack-Tip Solutions Using the Method of Muskhelishvili

Westergaard stress functions have been used to solve many problems, but there are limitations to the scope of the method. The method is restricted to infinite two-dimensional bodies with cracks along one or more straight lines. The complex function approach developed by Muskhelishvili [20] and others [11] has some advantages over the Westergaard method by treating a broader class of plane problems.

As noted in Chapter 2, an Airy stress function  $\phi$  must satisfy  $\nabla^4 \phi = 0$  together with the boundary conditions of the problem. It is known from elasticity theory (see Timoshenko and Goodier [12]) that  $\phi$  can be written as

$$\phi = \text{Re}[\bar{z}^2 \psi(z) + \chi(z)] \quad (3.5)$$

where  $\Psi(z)$  and  $\chi(z)$  are suitably chosen complex functions known as Goursat functions and  $\bar{z}$  is the conjugate of the complex variable  $z$ . It is further known that the stress invariant  $\sigma_{xx} + \sigma_{yy}$  is given by

$$\sigma_{xx} + \sigma_{yy} = 4 \operatorname{Re}[\Psi'(z)] \quad (3.6)$$

where  $\Psi'(z)$  represents  $d\Psi(z)/dz$ . Introduce now the concept of the complex stress intensity factor

$$K = K_I - i K_{II} \quad (3.7)$$

Now adding the first two of Equations (2.11) to the first two of Equations (2.17) one obtains

$$\sigma_{xx} + \sigma_{yy} = \frac{2K_I}{(2\pi r)^{1/2}} \cos \frac{\theta}{2} - \frac{2K_{II}}{(2\pi r)^{1/2}} \sin \frac{\theta}{2} \quad (3.8)$$

Now consider the function

$$\sqrt{\frac{2}{\pi \zeta}} K = \sqrt{\frac{2}{\pi r}} \left( \cos \frac{\theta}{2} - i \sin \frac{\theta}{2} \right) (K_I - i K_{II}) \quad (3.9)$$

It is seen that

$$\operatorname{Re} \sqrt{\frac{2}{\pi \zeta}} K = \sqrt{\frac{2}{\pi r}} \left( K_I \cos \frac{\theta}{2} - K_{II} \sin \frac{\theta}{2} \right) \quad (3.10)$$

which is the same as the right-hand side of Equation (3.8). Therefore,

$$\sigma_{xx} + \sigma_{yy} = \operatorname{Re} \left\{ \frac{\sqrt{2}}{(\pi \zeta)^{1/2}} K \right\} \quad (3.11)$$

Now let

$$\zeta = z - z_1 \quad (3.12)$$

where  $z_1$  is the location of the crack tip (Figure 3.3). Now substituting Equation (3.11) into Equation (3.10) one obtains

$$\sigma_{xx} + \sigma_{yy} = \operatorname{Re} \left\{ \frac{\sqrt{2} K}{\sqrt{\pi} (z - z_1)^{1/2}} \right\} \quad (3.13)$$



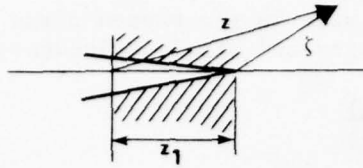


Figure 3.3. Complex coordinates at the crack tip.

But from Equation (3.6)

$$\sigma_{xx} + \sigma_{yy} = 4 \operatorname{Re}[\psi'(z)] .$$

Now it is known that when the real parts of two analytic complex functions are the same, then the functions themselves can differ by only a real constant times  $i$ . It is also known from elasticity theory that in a singly connected body, the form of the complex stress function  $\psi'$  for a unique stress state can only be specified to within a real constant times  $i$ . For unique displacements, even this constant must vanish. By restricting consideration to the neighborhood of the crack tip (i.e., a singly connected region) one may write, without loss of the above prescribed extent of uniqueness,

$$\lim_{z \rightarrow z_1} \left[ \frac{\sqrt{2}}{\sqrt{\pi}} \frac{K}{(z - z_1)^{1/2}} = 4\psi'(z) \right] .$$

Therefore,

$$K = 2\sqrt{2\pi} \lim_{z \rightarrow z_1} \left[ \psi'(z) \cdot (z - z_1)^{1/2} \right] . \quad (3.13)$$

The technique of conformal mapping, to map holes into cracks, has been used by Sih, Paris, and Erodogan [21], Muskhelishvili [20], and others to determine the function  $\psi(z)$  for an extensive variety of crack problems.

Consider the mapping functions:

$$z = \omega(\gamma) \quad (3.14)$$

where  $\eta$  is the complex variable in the mapped plane and the usual restrictions as to analyticity and single valuedness apply. Then

$$\Psi'(z) = \frac{d\Psi}{d\eta} \cdot \frac{d\eta}{dz} = \frac{\Psi'(\eta)}{\omega'(\eta)}$$

and Equation (3.13) becomes

$$K = 2\sqrt{2\pi} \lim_{\eta \rightarrow \eta_1} \left\{ \omega(\eta) - \omega(\eta_1) \right\}^{1/2} \frac{\Psi'(\eta)}{\omega'(\eta)} \quad (3.15)$$

Now, corresponding to a crack tip at  $z_1$  in the  $z$ -plane, there will be a crack tip at  $\eta_1$  in the  $\eta$  plane. In order to transform a straight crack of length  $2a$  in the  $x$ -direction, located centrally at the origin in the  $z$ -plane, into a circular hole of unit radius in the  $\eta$  plane, consider the mapping function:

$$z = \frac{a}{2} \left[ \eta + \frac{1}{\eta} \right] \quad (3.16)$$

or in terms of mapped variables  $u$  and  $v$  (Figure 3.4),

$$x + iy = \frac{a}{2} \left[ u + iv + \frac{1}{u + iv} \right] \quad (3.17)$$

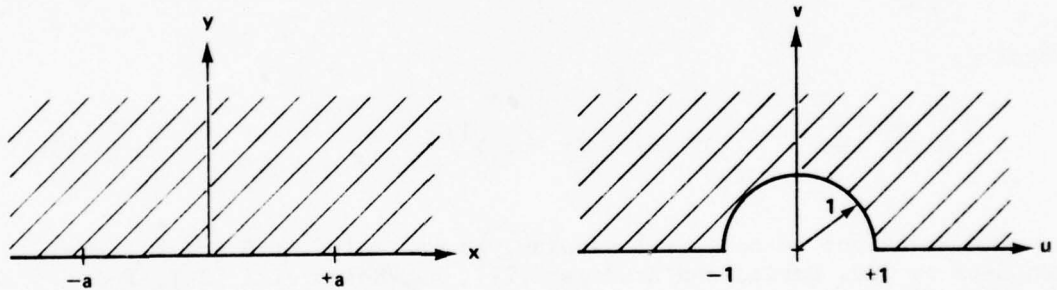


Figure 3.4. Mapping a crack into a unit circle.

Separating Equation (3.17) into real and imaginary parts, one obtains

$$\begin{aligned} x &= \frac{a}{2} \left[ u + \frac{u}{u^2 + v^2} \right] \\ y &= \frac{a}{2} \left[ v - \frac{v}{u^2 + v^2} \right] \end{aligned} \quad (3.18)$$

The boundary  $y = 0$  is transformed as follows. Let  $y = 0$  in the second of Equations (3.18).

$$0 = \frac{av}{2} [u^2 + v^2 - 1] \quad .$$

Solutions are:

$v = 0$ , a line of  $v = 0$ , and

$$u^2 + v^2 - 1 = 0,$$

a circle of unit radius, as shown in Figure 3.4.

To locate the right crack tip in the mapped plane let  $z \rightarrow z_1 = a$  in Equation (3.16). Then,

$$a = \frac{a}{2} \left( \eta_1 + \frac{1}{\eta_1} \right) \quad .$$

solving

$$\eta_1 = 1 \quad ,$$

i.e.,  $u = 1$ , and  $v = 0$ . Similar reasoning shows that the left crack tip  $z = -a$  maps into the point  $\eta_1 = 1$  or  $u = -1$ , and  $v = 0$ .

Now using the mapping function, Equations (3.16) in (3.15),

$$K = 2\sqrt{2\pi} \lim_{\eta \rightarrow \eta_1} \left\{ \frac{a}{2} \left( \eta + \frac{1}{\eta} \right) - \frac{a}{2} \left( \eta_1 + \frac{1}{\eta_1} \right) \right\}^{1/2} \frac{\Psi'(\eta)}{\frac{a}{2} \left( 1 - \frac{1}{\eta^2} \right)} \quad .$$

Letting,  $\eta_1 = 1$  and taking the limit as  $\eta \rightarrow \eta_1$ , one finally finds

$$K = 2\sqrt{\frac{\pi}{a}} \Psi'(1) \quad . \quad (3.19)$$

Thus, it is noted that stress intensity factors may be found simply from a knowledge of  $\Psi'(\eta)$  in the vicinity of the crack tip. While only  $\Psi(\eta)$  is used in Equation (3.19), it should be pointed out that in the course of solving a new problem both  $\Psi(\eta)$  and  $X(\eta)$  would be needed in satisfying the boundary conditions.

As an application of Equation 3.19 consider the problem shown in Figure 3.5. For this case Muskhelishvili [20] has given the stress function as

$$\Psi(\eta) = \frac{\sigma a}{8} \left( \eta + \frac{2e^{2i\beta} - 1}{\eta} \right) .$$

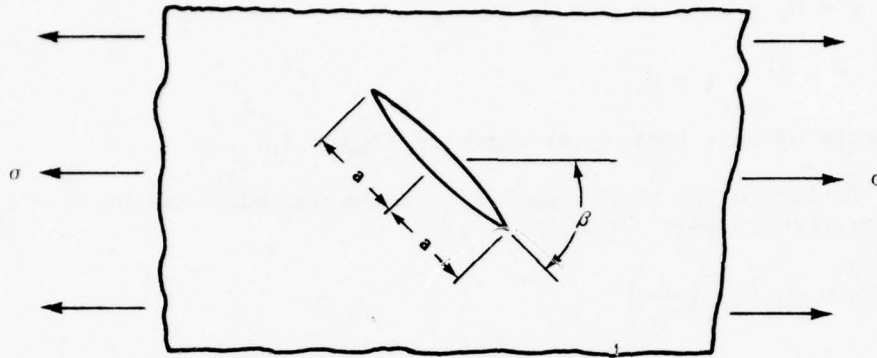


Figure 3.5. Skewed crack in a uniaxial tensile field.

Taking the derivative

$$\Psi'(\eta) = \frac{\sigma a}{8} \left( 1 - \frac{2e^{2i\beta} - 1}{\eta^2} \right) .$$

Evaluating at  $\eta = 1$

$$\Psi'(1) = \frac{\sigma a}{4} (1 - e^{i2\beta})$$

or

$$\Psi'(1) = \frac{\sigma a}{4} (1 - \cos 2\beta - i \sin \beta) .$$

Using Equation (3.19) together with the identity  $1 - \cos 2\beta = 2\sin^2 \beta$  and separating into real and imaginary parts, one finds,

$$K_I = \sigma \sqrt{\pi a} \sin^2 \beta$$

$$K_{II} = \sigma \sqrt{\pi a} \sin \beta \cos \beta .$$

(3.20)

Another important example of a problem solved by the method of Muskhelishvili is that of a straight crack with a concentrated load as shown in Figure 3.6. For this case, Sih, Paris, and Erdogan [21] found the stress function to be

$$\Psi(\eta) = \frac{Fa}{4\pi(a^2 - b^2)^{1/2}} \left\{ -\frac{1}{\eta} + \left( \frac{\eta_0}{\eta_0 - \eta} \right) \left[ \left( \eta + \frac{1}{\eta} \right) - \left( \eta_0 + \frac{1}{\eta_0} \right) \right] + \left( \eta_0 + \frac{1}{\eta_0} \right) \left[ \frac{\kappa}{1 + \kappa} \log \eta - \log (\eta_0 - \eta) \right] \right\} \quad (3.21)$$

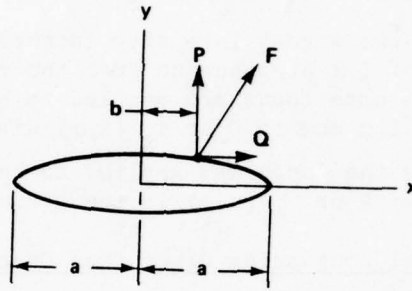


Figure 3.6. Straight crack with a concentrated force.

where

$$F = P - iQ$$

$\eta_0$  corresponds to  $z = b$

$\kappa =$  an elastic constant  $3 - 4\nu$  for plane strain and  $(3 - \nu)/(1 + \nu)$  for plane stress ( $\nu =$  Poisson's ratio).

Applying Equation (3.19), one obtains,

$$\begin{aligned} K_I &= \frac{1}{2} \left( \frac{1}{\pi a} \right)^{1/2} \left[ P \left( \frac{a+b}{a-b} \right)^{1/2} + Q \left( \frac{\kappa-1}{\kappa+1} \right) \right] \\ K_{II} &= \frac{1}{2} \left( \frac{1}{\pi a} \right)^{1/2} \left[ -P \left( \frac{\kappa-1}{\kappa+1} \right) + Q \left( \frac{a+b}{a-b} \right)^{1/2} \right] \end{aligned} \quad (3.22)$$

Equations (3.22) are important because they become the Green influence functions for solving any single straight crack problem in an infinite plane from a knowledge of the stresses on the prospective crack surface with the crack absent; i.e.,  $\sigma_{yy}(x,0)$  and  $\tau_{xy}(x,0)$ . The procedure is to



solve the infinite plate problem without a crack for the above stresses at the prospective crack surface location. Then superimpose tractions equal and opposite to those computed on the crack surface location. The result can be written directly from Equations (3.22) as:

$$\left. \begin{aligned} K_I &= \frac{1}{(\pi a)^{1/2}} \int_{-a}^{+a} \sigma_{yy}(x,0) \left( \frac{a+x}{a-x} \right)^{1/2} dx \\ K_{II} &= \frac{1}{(\pi a)^{1/2}} \int_{-a}^{+a} \tau_{xy}(x,0) \left( \frac{a+x}{a-x} \right)^{1/2} dx \end{aligned} \right\} \quad (3.23)$$

Equations (3.23) give the stress intensity factors at the right crack tip. The multiplier of  $1/2$  disappeared from the results of Equations (3.22) because in this case loads are applied to both crack surfaces. The shearing contribution due to  $Q$  or  $\tau_{xy}(x,0)$  disappeared from the first equation because the force was applied to both surfaces - similarly for the contribution of  $P$  or  $\sigma_{yy}(x,0)$  in the second equation.

### 3.3 Influence of Local Boundaries Other than Crack Surfaces

Thus far, only cases where the crack location was remote from the external boundaries of the body have been considered so that infinite body solutions were acceptable. One may separate problems where boundaries other than the crack surface boundaries are also local into two categories:

- a) Edge cracks in semi-infinite bodies.
- b) Cracks in infinite strips.

**Edge Cracks in Semi-Infinite Bodies** - It was implied in the previous article that good approximations could be obtained to problems involving cracks in semi-infinite bodies ( $b/a \gg 1$ ) by slicing infinite body problems along axes of symmetry. The accuracy of such solutions has been evaluated by comparison with analytical solutions by Bowie [19], Wigglesworth [22], and Irwin [23,24]. Although dimensional analysis of the problem in Figure 3.7 would lead one again to Equation (2.9),

$K_I = C_I \sigma (a)^{1/2}$  with  $C_I$  unknown, formidable analytical methods are required to obtain the effects of the free surface of the semi-infinite body. In general, the method of Muskhelishvili is employed, in which the mapping function takes the form of a series and the use of Green's influence function lead to dual integral equations. Since these methods have already been developed and illustrated by means of simple problems, the results only will be written here for the problem of Figure 3.7:

$$\begin{aligned}
 K_I &= 1.12 \sigma (\pi a)^{1/2} \\
 K_{II} &= K_{III} = 0
 \end{aligned}
 \tag{3.24}$$

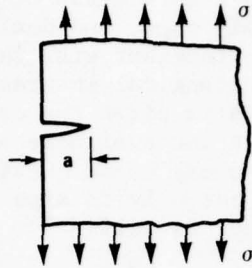


Figure 3.7. An edge crack under Mode I loading.

Recalling Equation (3.2)  $K_I = \sigma(\pi a)^{1/2}$  which was developed for an internal crack in an infinite body, one may conclude that the free surface correction factor for edge notches perpendicular to a field of uniform tension is 1.12. On the other hand, note the results of Sih [25] for an edge crack (Figure 3.8) under a mode III deformation; his results

$$\begin{aligned}
 K_{III} &= \tau (\pi a)^{1/2} \\
 K_I &= K_{II} = 0
 \end{aligned}
 \tag{3.25}$$

are identical with those for an internal crack in an infinite body and therefore no free surface correction is required for this case.

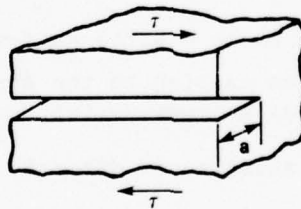


Figure 3.8. An edge crack under Mode III loading.

Since the free surface would normally be a loaded surface in the infinite plate with Mode II loading, it is concluded that there is no Mode II case directly analogous to the Mode II case in the infinite plate corresponding to the cases discussed above.

**Cracks in Infinite Strips** - This class of problems, including plate strips with transverse internal, edge, and dual colinear edge cracks under normal tension has been, together with the same configurations under plane bending, of great practical interest in connection with fracture toughness testing. As is often the case, however, closed form solutions for such problems are not available and many of the approximate solutions in the literature may be of questionable accuracy. Consequently, it seems important not only to cite available results but to give estimates of their accuracy as well.

The limitations on Equation (3.4)

$$K_I = \sigma(\pi a)^{1/2} \left( \frac{2b}{\pi a} \tan \frac{\pi a}{2b} \right)^{1/2}$$

(for a row of colinear cracks in an infinite plate) when it is applied to cracks in strips was discussed in the first of the chapter. These limitations were compared with solutions resulting from direct attack upon strip type problems.

One of the most useful approaches to this class of problems appears to be the work of Isida [16]. Isida has extensively developed mapping functions for strip problems for the determination of stress concentrations at the tips of round-ended cracks of end radius  $\rho$ . His results are presented in the form [16],

$$\sigma_{\max} = \frac{2 \sigma a^{1/2}}{\rho^{1/2}} f\left(\frac{a}{b}\right) \quad (3.26)$$

where  $a$  = crack half-length, and  $b$  = strip half-width.  $f\left(\frac{a}{b}\right)$  is determined by applying power series mapping to the stress function variable  $z$  and  $\phi$  is itself expressed as a power series.

Equation (3.26) may be substituted directly into Equation (2.37),

$$K_I = \lim_{\rho \rightarrow 0} \left\{ \frac{\pi^{1/2}}{2} \sigma_{\max} \rho^{1/2} \right\}$$

The resulting stress intensity factors can be computed to any degree of accuracy by Isida's methods, provided the power series employed in the analysis converge, which they do for relatively large variations in  $a/b$ . Within this minor limitation, Isida's results are expected to yield accuracies of  $\pm 2$  percent. Isida [16] has computed results in the form of Equation (3.26) for a number of problems of special interest in fracture testing. Consider, for example, the problem of Figure 3.9.

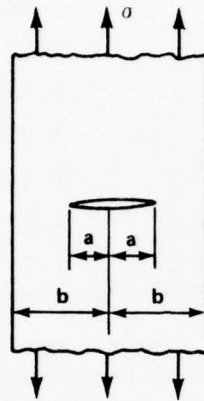


Figure 3.9. Center cracked infinite strip.

Substituting Equation (3.26) into Equation (2.37).

$$K_I = \sigma \rightarrow 0 \left[ \frac{\pi^{1/2}}{2} \frac{2\sigma a^{1/2}}{1/2} f\left(\frac{a}{b}\right) \sigma^{1/2} \right] \quad (3.27)$$

$$K_I = \sigma(\pi a)^{1/2} f\left(\frac{a}{b}\right)$$

Thus  $f\left(\frac{a}{b}\right)$  becomes the free surface correction factor for the finite width strip, the approximate form for which is given by Equation (3.4). The two solutions are compared in Table 3.1.

Frequently in design situations, approximate solutions must be employed, and sometimes solutions for a certain class of problems must be adapted to cases for which they do not exactly apply. The comparison in Table 3.1 gives an idea of the kind of approximations one can make for a given amount of error. For example, for  $a/b$  as large as 0.410 the approximate tangent formula gives results to within 5 percent. Differences for larger  $a/b$  values result from the fact that lines of symmetry in the infinite plate are subject to larger local stress distributions.

TABLE 3.1. FREE EDGE CORRECTION  
FACTORS FOR CENTER CRACKED  
INFINITE STRIPS

$a/b$	$f\left(\frac{a}{b}\right)$	$\left(\frac{2b}{\pi a} \tan \frac{\pi a}{2b}\right)^{1/2}$
0.074	1.00	1.00
0.207	1.03	1.02
0.275	1.05	1.03
0.337	1.09	1.05
0.410	1.13	1.08
0.466	1.18	1.11
0.535	1.25	1.15
0.592	1.33	1.20

Buechner [29] has developed integral equation procedures and solved a number of crack problems including the solution to a strip with a single edge notch subjected to pure bending (Figure 2.10).

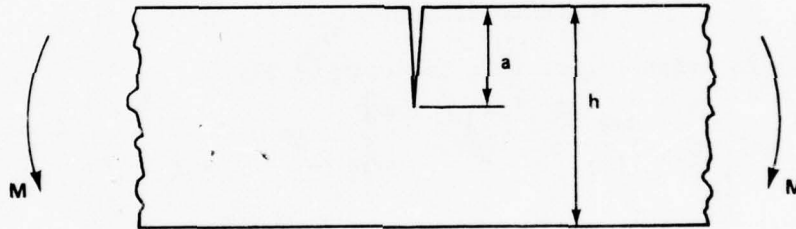


Figure 3.10. Strip with single  
edge crack subjected to pure  
bending.

His results are given by

$$K_I = \sigma(h - a)^{1/2} f\left(\frac{a}{h}\right)$$

$$K_{II} = K_{III} = 0$$
(3.28)



where  $\sigma = \frac{6M}{(h-a)^2}$ , and  $f\left(\frac{a}{h}\right)$  is given in Table 3.2. One sees a large variation in  $f(a/h)$  for small  $a/h$ . For larger values of  $(a/h)$ ,  $f(a/h)$  tends to become constant, approaching the value it would have for a deep notch, [30].

TABLE 3.2. STRESS INTENSITY FACTORS FOR A SINGLE-EDGE CRACKED STRIP LOADED IN BENDING

a/h	0.05	0.10	0.20	0.30	0.40	0.50	0.60 (and larger)
$f\left(\frac{a}{h}\right)$	0.36	0.49	0.60	0.66	0.69	0.72	0.73

Bowie developed polynomial mapping functions for use with the complex stress function technique to solve plane problems, such as cracks emanating from circular holes [31] and the double-edge-cracked strip in tension [19]. The latter example (Figure 3.11) may be compared with the tangent formula, Equation (3.4). This comparison may be achieved by introducing a correction factor,  $f(a/b)$ , into Equation (3.3). Thus one has

$$K_I = \sigma(\pi a)^{1/2} \left( \frac{2b}{\pi a} \tan \frac{\pi a}{2b} \right)^{1/2} f\left(\frac{a}{b}\right) \quad (3.29)$$

$$K_{II} = K_{III} = 0$$

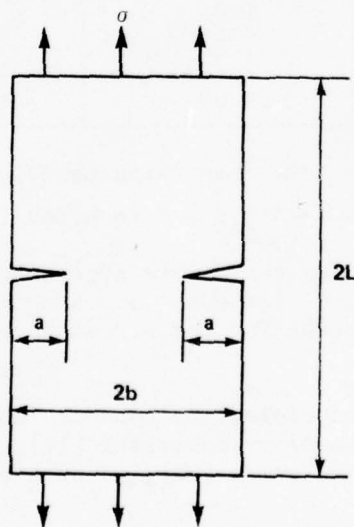


Figure 3.11. Double-edge-cracked strip loaded in tension.

The results are shown in Table 3.3. From this table, one sees that, for low  $a/b$  values, the correction factor of 1.12 for a crack emanating from a free surface, as noted in Equation (3.24), is present. As  $a/b$  increases, its effect disappears and the correction factor becomes 1.00. The values in the last column represent the correction factors which would have to be applied to the solution for a single internal crack in an infinite plate to account for the two deep cracks in a finite width strip.

TABLE 3.3. STRESS INTENSITY SOLUTION  
FOR A DOUBLE-EDGE-CRACKED STRIP  
LOADED IN TENSION

$a/b$	$f\left(\frac{a}{b}\right)$ $L/b = 1.00$	$f\left(\frac{a}{b}\right)$ $L/b = 1.00 \begin{cases} \text{same} \\ \text{as} \\ \infty \end{cases}$	$\left(\frac{2b}{\pi a} \tan \frac{\pi a}{2b}\right)^{1/2} f\left(\frac{a}{b}\right)$ $L/b \rightarrow \infty$
0.1	1.13	1.12	1.12
0.2	1.13	1.11	1.12
0.3	1.19	1.09	1.13
0.4	1.16	1.06	1.14
0.5	1.14	1.02	1.15
0.6	1.10	1.01	1.22
0.7	1.02	1.00	1.34
0.8	1.01	1.00	1.57
0.9	1.00	1.00	2.09

The foregoing shows that when using Equation (3.24),  $K_I = 1.12 \sigma(\pi a)^{1/2}$ , for  $a/b < 0.5$  and Equation (3.4),  $K_I = \left[ \frac{2b}{\pi a} \tan \frac{\pi a}{2b} \right] \sigma(\pi a)^{1/2}$ , for  $a/b > 0.5$  for the double-edge-cracked problem, the error will be less than 3 percent for  $L/b > 3$ . Such information can frequently be of help in estimating the stress intensity factor for design problems.

Numerical methods involving the boundary collocation of the stress function have been developed by Kobayashi [18] and Gross. Srawley [32] and by Wilson [33] and by Newman [34], to name a few.

Kobayashi [18] treated the infinite strip with a central crack using Muskhelishvili's complex stress functions, and collocating equally spaced points in the sides and ends of the strip.

Gross [32] solved the single-edge-cracked strip using the Williams [13] eigen function representation of the Airy stress function. His results are given in the usual form

$$K_I = \sigma(\pi a)^{1/2} f\left(\frac{a}{b}\right)$$

$$K_{II} = K_{III} = 0$$
(3.30)

where the single edge cracked strip is shown in Figure 3.12. Gross' [32] numerical results are compared with Bowie's [19] solution for the double- and single-edge-cracked strip in Table 3.4. This table shows how the stress intensity factor is increased due to bending in the single-edge-cracked strip. When the double-edge-cracked strip is cracked half way across ( $a/b = 0.5$ ), the correction factor is approximately 1.15, whereas when the single-edge-cracked strip is cracked halfway across ( $a/b = 1.0$ ), the correction factor is 2.82 — over twice as great.

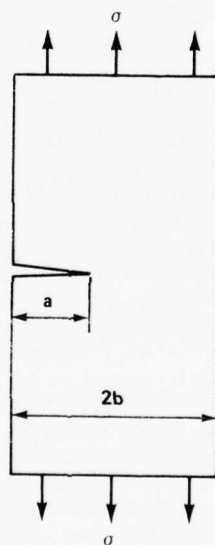


Figure 3.12. The single-edge cracked strip loaded in tension.

TABLE 3.4. CORRECTION FACTORS FOR THE SINGLE-EDGE-CRACKED STRIP COMPARED WITH THE DOUBLE-EDGE-CRACKED STRIP

a/b	$\frac{a}{2b}$	Single-Edge Cracked f(a/b) Gross [32]	Double-Edge-Cracked $\left[ \frac{2b}{\pi a} \tan \frac{\pi a}{2b} \right]^{1/2} f(a/b)$ Bowie [19]	Single-Edge-Cracked f(a/b) Bowie [19]
0.10	0.05	1.14	1.12	1.15
0.20	0.10	1.19	1.12	1.20
0.30	0.15	1.29	1.13	1.29
0.40	0.20	1.37	1.14	1.37
0.50	0.25	1.50	1.15	1.51
0.60	0.30	1.66	1.22	1.68
0.70	0.35	1.87	1.34	1.89
0.80	0.40	2.12	1.57	2.14
0.90	0.45	2.44	2.09	2.46
1.00	0.50	2.82	-	2.86

### 3.4 Three-Dimensional Considerations

The discussion thus far has only dealt with the two-dimensional case. In practical applications of results though it should be remembered that all bodies are really three dimensional. It is not unusual to treat certain problems as two dimensional, analytically, and by correlating with experiment, to assess the three-dimensional effects in the real problem. The implication here is that the three-dimensional effects are always present, and are yet often justifiably negligible. Other problems undeniably call for a three-dimensional approach. Such is the case of, say, an elliptical flaw embedded in a body.

Consider the stresses in the neighborhood of the curved crack border shown in Figure 3.13 Kassir and Sih [35] have shown that if the stresses are expressed in terms of a set of polar coordinates  $r$  and  $\theta$  defined in a plane normal to the edge of the crack that the angular distribution and universal square-root stress singularity of the plane problem (Equations 2.11, 2.17, and 2.26) are preserved. This means that the local elastic stress field can be described in terms of the three stress intensity factors, and that the concepts already discussed for two dimensional problems apply here also. In the presence of all three modes the following fracture criterion in three dimensions was postulated by Kassir and Sih [35]

$$f(K_I, K_{II}, K_{III}) = f_{cr}$$

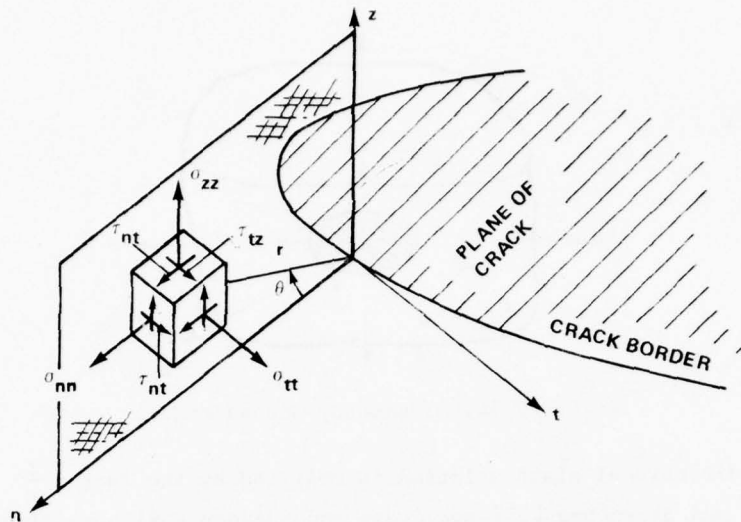


Figure 3.13. Stresses and coordinates in a plane normal to a crack edge.

This equation shows that the crack propagation will occur when some combination of  $K_I$ ,  $K_{II}$  and  $K_{III}$  reaches a critical value. In many three dimensional problems; however, only Mode I may be present.

Using a method employing Fourier Transforms, Snaddon [36] solved the problem of a circular "penny shaped" internal crack loaded with an internal pressure on the crack boundaries (Figure 3.14). The resulting stresses and displacements were given as sets of integral equations. Upon superimposing a dilatational field to negate the pressure distribution in the crack,

$$\sigma_{zz} = \sigma; \sigma_{rr} = \sigma_{\theta\theta} = \sigma$$

The solution for a circular crack under opening mode tension was obtained. For this case, it was found that:

$$\begin{aligned} K_I &= \frac{2}{\pi} \sigma (\pi a)^{1/2} \\ K_{II} &= K_{III} = 0 \end{aligned} \quad (3.31)$$



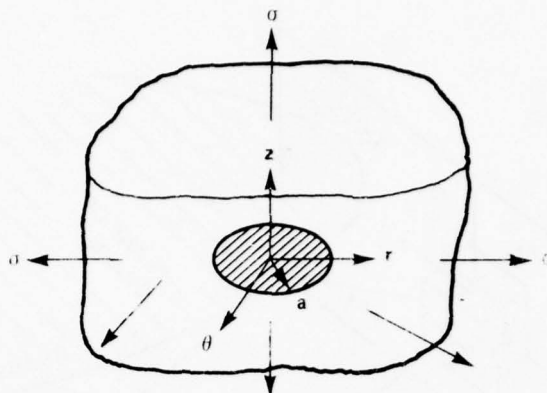


Figure 3.14. The penny-shaped crack.

The two-dimensional plate solution is modified by the factor  $\frac{2}{\pi}$ .

Sadowsky and Sternburg [37] and Green and Sneddon [38] have discussed the problem of stresses in an infinite body near an elliptical cavity. When the cavity is degenerated into a crack, certain difficulties arise in the computation of the stresses at the edge of the crack. Irwin [39] subsequently computed the stress intensity factor at any location on the crack border, described by the angle  $\beta$  (Figure 3.15) by comparing the displacements obtained by Green and Sneddon with Equations (2.12). His results showed that:

$$K_I = \frac{\sigma(\pi a)^{1/2}}{E(k)} \left[ \sin^2 \beta + \left( \frac{a}{b} \right)^2 \cos^2 \beta \right]^{1/4} \quad (3.32)$$

$$K_{II} = K_{III} = 0$$

where

$$E(k) = \int_0^{\pi/2} [1 - (k^2) \sin^2 \vartheta]^{1/2} d\vartheta$$

is the complete elliptic integral of the second kind and

$$k^2 = 1 - \frac{b^2}{a^2}.$$

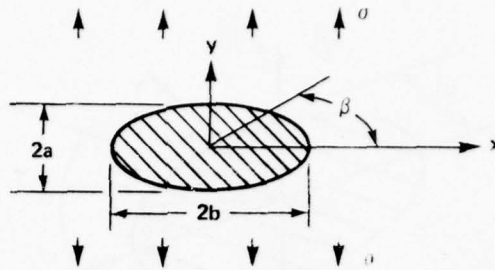


Figure 3.15. Elliptical crack.

Now for very large  $b$  (i.e.,  $b \rightarrow \infty$ ),

$$E(k) = \int_0^{\pi/2} \cos \phi \, d\phi = 1$$

and if

$$K_I = \pi/2, K_{II} = \sigma(\pi a)^{1/2}$$

which is identical with Equation (2.34) for a through crack of length  $2a$  in an infinite plate. In effect, the above may be thought of as extending the thickness of an infinite plate to infinity. On the other hand, if one sets  $b = a$ , then

$$E(k) = \frac{\pi}{2}$$

and

$$K_I = \frac{2}{\pi} \sigma(\pi a)^{1/2}$$

which is the same as Equation (3.31) for the circular crack.

The companion problem of the above, the case of a flat elliptical crack in an infinite medium loaded with an arbitrary shear load (Figure 3.16), was solved by Kassir and Sih [35]. The solution for a stress-free crack under uniform loads in an infinite medium can be obtained as the superposition of the stresses for uniform loads at infinity on a uncracked medium and the stresses due to the negative of the uniform loads applied directly to the crack surface. Consequently, for purposes of calculating the form of the singular stresses it suffices to apply the loads in question directly to the crack surface, as shown in Figure 3.16.

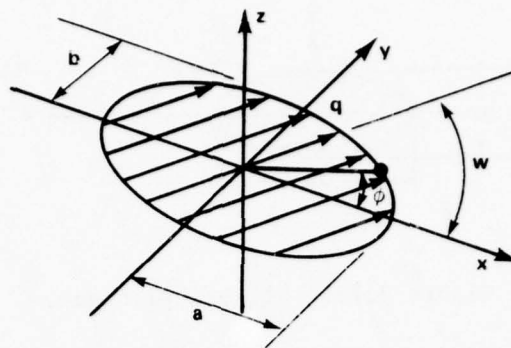


Figure 3.16. Elliptical crack under uniform shear.

The stresses  $\tau_{nt}$  and  $\tau_{tz}$  (Figure 3.13) contained only the tearing mode influence,  $K_{III}$ , but all other components exhibited a combination of  $K_I$  and  $K_{II}$ . In general, the  $K$ 's were a complicated function of  $\nu, \phi, \omega$ , and  $a/b$ .

**Semi-Elliptic Surface Flaw** - The surface flaw is important for two reasons: (a) it has caused a number of well-documented service failures, and (b) it has been used extensively in fracture toughness testing. In service the surface flaw occurs by fatigue growth of such things as a tool scratch, or an arc strike. This flaw, illustrated in Figure 3.17, was first analyzed by Irwin [39]. By modifying the elliptic flaw solution, Equation (3.32), Irwin suggested that at the deepest point of the flaw

$$K_I = \frac{1.1 \sigma \sqrt{\pi a}}{\left[ E^2 - 0.212 \left( \frac{\sigma}{\sigma_{ys}} \right)^2 \right]^{1/2}} \quad (3.33)$$

where  $\sigma_{ys}$  is the yield strength of the material. At the deepest point of the flaw,  $\beta = 90$ , it is noted that the bracketed factor in Equation (3.32) is 1. The negative factor in Equation (3.33) is a correction for crack tip plasticity (See Chapter 4), and the factor of 1.1 is an approximate correction for the bisecting free surface which transforms the elliptic flaw into a semi-elliptic flaw. The factor of 1.1 is approximately equal to the edge crack correction factor of 1.12 previously presented. Since Equation (3.33) contains no correction for the free back surface of the plate the range of validity of Equation (3.33) is restricted to  $a/T < 0.5$ .

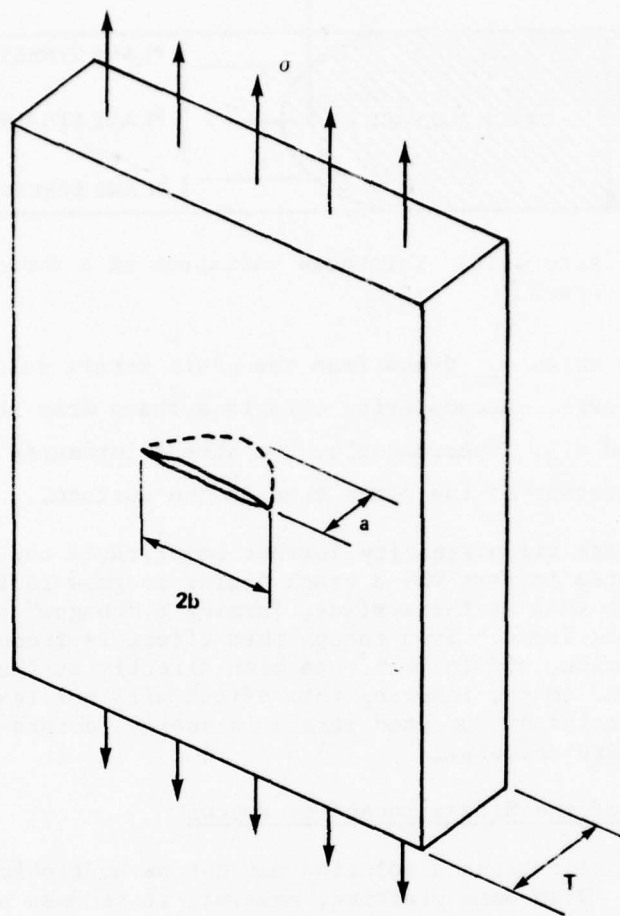


Figure 3.17. Semi-elliptic surface flaw.

Recently, numerical techniques have been applied in order to obtain more refined solution to the surface flaw problem. Some of these results are given in Chapter 7. Because of its importance, the surface crack was the subject of a special symposium of the 1977 Annual Meeting of ASME [40].

Most two-dimensional problems exhibit three-dimensional effects. Consider the problem of a sheet of finite thickness with a through crack (Figure 3.18). For an infinitely thick sheet, a plane strain analysis would apply. For a vanishingly thin sheet, a plane stress analysis would apply. But with a finite thickness, a mixed situation of plane stress near the surface of the plate and plain strain in the interior occurs in the crack tip stress field. Consequently, the stress intensity factors computed for plane problems represent only values averaged through the plate thickness. Recent results by Leven [41] and Cruse and Van Buren [42] reveal a thin boundary layer on the plate surfaces

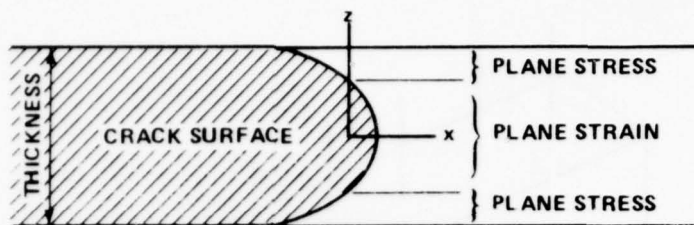


Figure 3.18. Thickness variation of a through crack.

(Figure 3.18) in which  $\sigma_{zz}$  drops from the plain strain value of  $\nu(\sigma_{xx} + \sigma_{yy})$  to zero. Accompanying this is a sharp drop in the in-plane stresses,  $\sigma_{xx}$  and  $\sigma_{yy}$ . Consequently, the stress intensity factor is greater in the interior of the plate than on the surface.

Although crack tip plasticity further complicates the situation, the above indicates in part why a crack begins to grow in the interior of a plate rather than at the surface, forming a "tongue" or "thumb nail" shaped crack front. Even though this effect is frequently observed in practice, and in fact, has been directly utilized in the so called "pop-in" tests, ignoring this effect will not lead to significant inaccuracies of computed stress intensity factors for use in developing fracture criteria.

### 3.5 Estimation of the Stress Intensity Factor

In design applications a solution may not be available for the problem at hand. With some practice, however, it becomes possible to estimate the stress intensity factor for cases of practical interest. Consider the following example from Paris and Sih [11]. The crack has an arbitrary shape, shown in Figure 3.19, and is subjected to a uniform tension,  $\sigma$ , normal to the crack plane. Separate regions of the crack are denoted by  $K_I$ ,  $K_2$ , etc. For this case  $K_{II} = K_{III} = 0$ . Using the results for the penny-shaped crack,

$$K_I = \frac{2}{\sqrt{\pi}} \sigma (\pi a)^{1/2},$$

and the tunnel crack,

$$K_I = \sigma (\pi a)^{1/2},$$



one can guess the Mode I stress intensity factor  $K_I$  for the different labeled portions of the crack border. Guess, e.g.,

$$k_1 \approx 0.75 \sigma (\pi a_1)^{1/2}$$

$$k_2 \approx 0.85 \sigma (\pi a_1)^{1/2}$$

$$k_3 \approx 1.05 \sigma (\pi a_3)^{1/2}$$

$$k_4 \approx 0.75 \sigma (\pi a_4)^{1/2} .$$

These estimates, it is believed, are accurate to within 10 percent and probably even 5 percent.

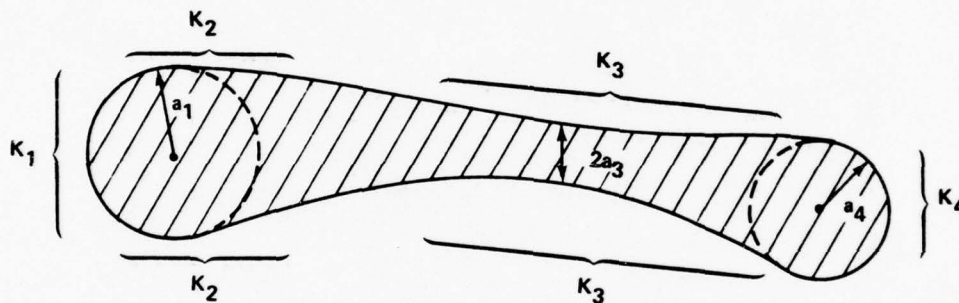


Figure 3.19. An arbitrary shaped crack loaded in tension.

## Chapter 4. EFFECTS OF CRACK-TIP PLASTICITY

Up to this point, the entire effort has been devoted to the establishment and use of a linear elastic theory for the local stress field around the tip of the crack. The discussion will start here by considering the general features of small scale plastic yielding at the crack tip. Two analytical models will be reviewed and their results compared. Some remarks will be made concerning the limitations of the crack-tip stress theory.

### 4.1 Introduction

The local elastic stresses predicted by Equations (2.11), (2.17), and (2.26) approach infinity at the tip of the crack. For a real material it is known that the stress does not become infinite. This means that yielding must occur which eliminates the crack-tip stress singularity. In the study of brittle fracture, this yielding is what is normally referred to as small scale, meaning that the crack-tip plastic zone is small compared to the elastic stress field within which it is embedded. The size and shape of this plastic zone has been studied analytically and experimentally by several researchers. Due to the complex analysis required for Modes I and II, an exact solution has been obtained for the Mode III case only.

For the Mode I case, an estimate can be made, following McClintock and Irwin [9]. Figure 4.1 shows the locus,  $R$ , of points at which the Mises yield criterion would be exceeded if the elastic stress distribution were unaffected by yielding, assuming Poisson's ratio to be  $1/3$ . The difference in the plane-strain and plane-stress loci is not due to the in-plane stress components, which are identical, but to the presence or absence of transverse constraint. It is remembered that for plane stress  $\sigma_{zz} = 0$ , whereas for plane strain,  $\sigma_{zz} = \nu(\sigma_{xx} + \sigma_{yy})$ . The presence of  $\sigma_{zz}$  causes a state of triaxial stress which inhibits plastic flow for the plane-strain case. The above results are estimates only since yielding affects the stress distribution outside the plastic zone and thus modifies the shape of the plastic zone itself. Material work hardening also affects the shape of the plastic zone and the extent of yielding.

From Figure 4.1, it is noticed that the radius  $R$  of the plastic zone is proportional to  $(K_I/\sqrt{\pi} \sigma_{ys})^2$ . The plastic zone size is normally stated by giving its radius  $R_y$  ahead of the crack (i.e., at  $\theta = 0$ ). For this dimension the commonly assumed values are

$$R_y = \frac{1}{2\pi} \left( \frac{K_I}{\sigma_{ys}} \right)^2 \quad (\text{plane stress})$$

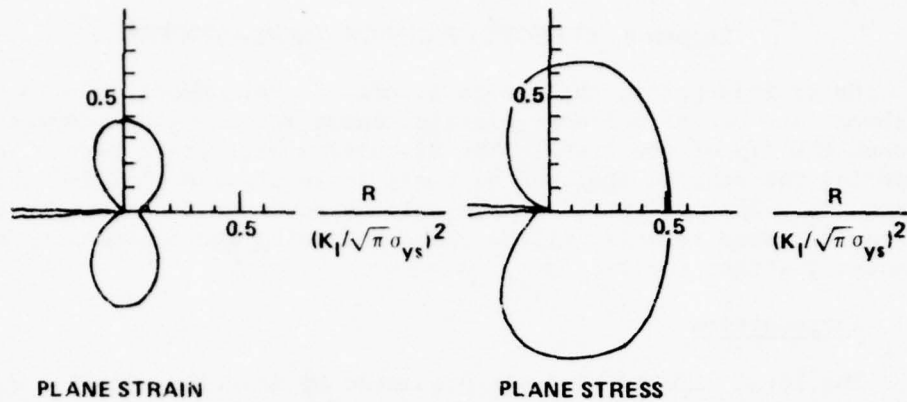


Figure 4.1. The shape of the Mode I plastic zone determined from miss yield criterion, with  $\nu = 1/3$ .

$$R_y = \frac{1}{6\pi} \left( \frac{K_I}{\sigma_{ys}} \right)^2 \quad (\text{plane strain}) \quad (4.1)$$

where  $\sigma_{ys}$  is the yield stress of the material. Since the yielding causes a redistribution of stresses ahead of the crack, the actual diameter is estimated at twice the above, i.e.,  $2 R_y$ .

Liu [43] proposed a model which shows the plane-stress, plane-strain transition of a plastic zone in a finite-thickness plate. The model, indicating the relative sizes of the plastic zones, is shown in Figure 4.2.

Based on the work of Hahn and Rosenfield [44], Wilhelm [45] summarized the effect of work hardening as follows:

- a) Large work hardening: Dumbell or circular zones are formed (Figure 4.2).
- b) Small work hardening: Slip is concentrated ahead of the crack and yielding is confined to a thin wedge ahead of the crack.

Before proceeding to a more detailed study of plastic yielding, it is appropriate to note how a simple plasticity correction can be made in fracture analysis. It will be shown in Article 4.2, for Mode III yielding, that the elastic stress field in the presence of a plastic zone is the same as the elastic case where the crack tip has been moved forward by half the width of the plastic zone. Irwin [46] proposed using an effective crack length determined by replacing  $a$  with  $a + R_y$ . Then expressions for  $K$  of the form

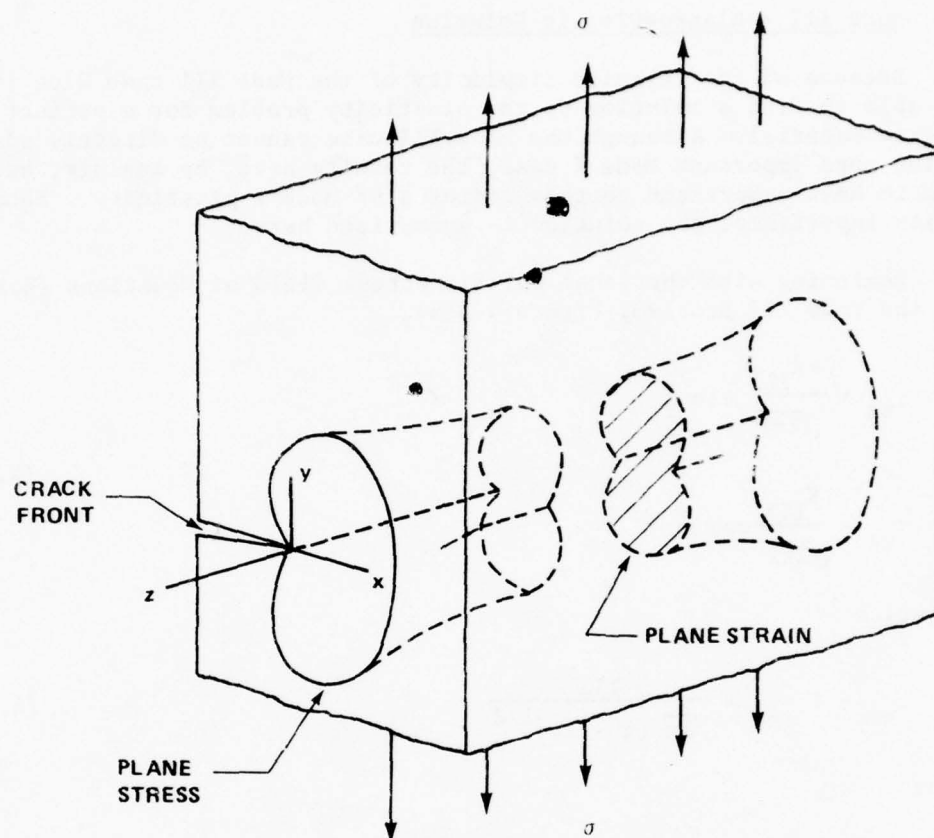


Figure 4.2. Model of through-the-thickness plastic zone as first visualized by Liu.

$$K = \sigma f(\sqrt{a})$$

become

$$K = \sigma f(\sqrt{a + R_y})$$

This was the basis of the plasticity correction, which appeared in the surface flaw solution Equation (3.33). As mentioned previously, the commonly used values of  $R_y$  are those given by Equations (4.1). This approach was once used widely in fracture toughness testing, but has now been largely replaced by the use of compliance techniques, which determine the effective crack length. In fracture analysis, the approximate technique of replacing "a" with  $a + R_y$  is still used although for many materials and situations  $R_y$  is sufficiently small to neglect. Indeed, for high accuracy it is necessary to have  $R_y$  small enough to neglect entirely. For low accuracy calculations of larger-scale yield problems, the practice of replacing "a" with  $a + R_y$  is regarded as a reasonable, approximate method; the accuracy depends upon the extent of yielding, though results of such calculations must be interpreted with judgement.

#### 4.2 Mode III - Elasto-Plastic Solution

Because of the relative simplicity of the Mode III case Rice [47] was able to find a solution to the plasticity problem for a perfectly plastic material. Although the Mode III case cannot be directly adapted to the more important Mode I case, the results have, by analogy, been used to help understand certain features of Mode I plasticity. Because of its importance, the solution is summarized here.

Beginning with the local elastic stress field of Equations (2.26), for the Mode III problem, Figure 4.3(a),

$$\begin{aligned}\tau_{xz} &= \frac{-K_{III}}{\sqrt{2\pi r}} \sin \frac{\theta}{2} \\ \tau_{yz} &= \frac{K_{III}}{\sqrt{2\pi r}} \cos \frac{\theta}{2}\end{aligned}\tag{4.2}$$

and write

$$\tau_{yz} - i \tau_{xz} = \frac{K_{III}}{\sqrt{2\pi} (x - iy)^{1/2}}\tag{4.3}$$

since

$$\frac{\cos \frac{\theta}{2} + i \sin \frac{\theta}{2}}{\sqrt{r}} = \frac{e^{i\frac{\theta}{2}}}{\sqrt{r}} = \frac{1}{\sqrt{r} e^{-i\frac{\theta}{2}}} = \frac{1}{\sqrt{x - iy}}.$$

Now seek solutions to the elasto-plastic problem by specifying that the stress approaches the value of Equation (4.3) asymptotically as  $|x - iy| \rightarrow \infty$ .

Define a dimensionless stress by,

$$\xi = \frac{\tau_{yz}}{\tau_{yp}} - i \frac{\tau_{xz}}{\tau_{yp}}\tag{4.4}$$

where  $\tau_{yp}$  is the yield stress in shear. Now from Equation (4.3) one can write

$$x - iy = \frac{K_{III}^2}{2\pi \tau_{yp}^2 \xi^2}.\tag{4.5}$$



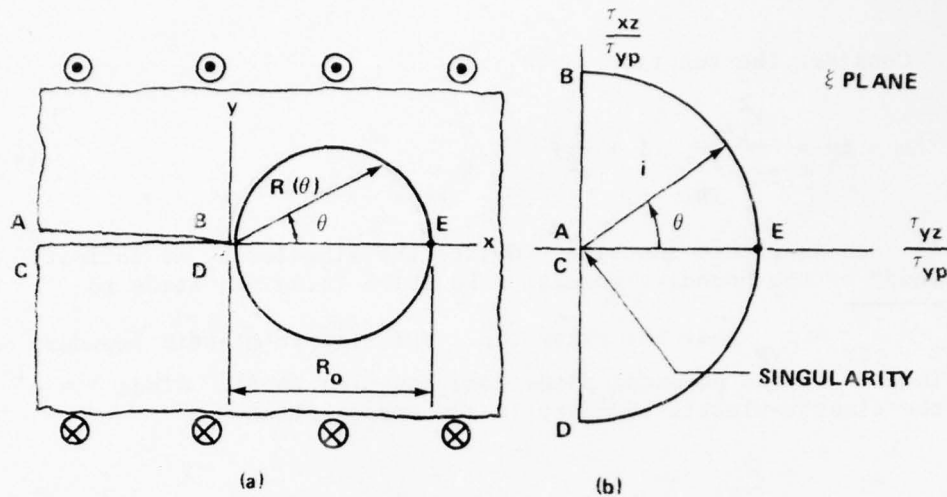


Figure 4.3. Small-scale yielding solution for elastic - perfectly plastic Mode III deformation (a) physical plane (b) map of elastic region of physical plane onto interior of unit semicircle in stress plane.

One can now visualize  $x - iy$  as a function of  $\xi$ . The asymptotic boundary condition can then be stated as either

$$\tau_{yz} - i \tau_{xz} \rightarrow \frac{K_{III}}{\sqrt{2\pi} (x - iy)^{1/2}} \text{ as } |x - iy| \rightarrow \infty$$

or

$$x - iy \rightarrow \frac{K_{III}^2}{2\pi \tau_{yp}^2 \xi^2} \text{ as } |\xi| \rightarrow 0 \quad (4.6)$$

The map of the physical plane into the  $\xi$  plane is shown in Figure 4.3. The elastic-plastic boundary maps into a unit semicircle. Points at infinity map into the origin and the crack surfaces map into the imaginary  $\xi$  axis.

In the neighborhood of the crack tip (i.e., within the plastic zone), the stress is at the yield level,

$$\sqrt{\tau_{xz}^2 + \tau_{yz}^2} = \tau_{yp}$$

or

$$|\xi| = 1 \text{ as } |x - iy| \rightarrow 0 \quad (4.7)$$

Consider the function

$$x - iy = \frac{K_{III}^2}{2\pi \tau_{yp}^2} \left\{ 1 + \frac{1}{\xi^2} \right\} \quad (4.8)$$

It is seen that this function provides the singularity at infinity demanded by the boundary condition Equation (4.6) and leads to

$\sqrt{\tau_{yz}^2 + \tau_{xz}^2} = \tau_{yp}$  near the crack tip. The elastic-plastic boundary may be located in the physical plane from Equation (4.8). Since  $\xi = e^{i\theta}$ , on the elastic-plastic boundary in the stress plane

$$x - iy = \frac{K_{III}^2}{2\pi \tau_{yp}^2} \{ 1 + \cos 2\theta - i \sin 2\theta \} \quad (4.9)$$

which is the path in the physical plane corresponding to BED in the stress plane in Figure 4.3. Separating the real and imaginary parts, one has

$$\begin{aligned} x &= \frac{K_{III}^2}{2\pi \tau_{yp}^2} (1 + \cos 2\theta) \\ y &= \frac{K_{III}^2}{2\pi \tau_{yp}^2} \sin 2\theta \end{aligned} \quad (4.10)$$

These are the parametric equations of a circle. Thus, the elastic-plastic boundary is a circle as already shown in Figure 4.3(a).

The diameter,  $R_o$ , of the plastic zone is given by  $x$  at  $\theta = 0$  in Equation (4.10). Thus,

$$R_o = x_{\theta=0} = \frac{1}{\pi} \left( \frac{K_{III}}{\tau_{yp}} \right)^2 \quad (4.11)$$

is the Mode III plastic zone diameter.

Solving for the stresses from Equation (4.8),

$$x - \frac{K_{III}^2}{2\pi \tau_{yp}^2} - iy = \frac{K_{III}^2}{2\pi \tau_{yp}^2} \left( \frac{1}{z} \right)$$

or

$$z = \frac{K_{III}}{\tau_{yp} \sqrt{2\pi} \left[ x - \frac{K_{III}^2}{2\pi \tau_{yp}^2} - iy \right]^{1/2}}$$

Therefore,

$$\tau_{yz} - i \tau_{xz} = \frac{K_{III}}{\sqrt{2\pi} \left[ x - \frac{K_{III}^2}{2\pi \tau_{yp}^2} - iy \right]^{1/2}} \quad (4.12)$$

are the stresses in the elastic region. Comparing Equation (4.12) with Equation (4.3), it can be seen that the effect of yielding is to create a stress field identical to the elastic stress field, but shifted ahead by half the plastic zone size (i.e., by  $K_{III}^2/2\pi \tau_{yp}^2$ ), as if the crack

tip were at the center of the plastic zone. This fact, first noted by Irwin [46] and Koskinen [48], lends support to the practice in Mode I fracture of increasing the physical crack length by one-half the plastic zone size. Furthermore, from Equation (4.11), the plastic zone size  $R_0$  depends only upon  $K_{III}$  and  $\tau_{yp}$ . Thus it is established that for small-scale yielding, the plastic zone size depends upon  $K_{III}$ , the elastic stress intensity factor.

#### 4.3 Strip Yield Model

In lieu of an exact analysis of the elasto-plastic problem for Mode I loading, a simple model was proposed by Dugdale [49]. This model, called a strip-yield model, provides a known plastic zone shape by assuming that yielding is confined to a thin layer of material directly ahead of the crack tip. Then the model of the elastic-plastic problem becomes the one pictured in Figure 4.4. While a model such as this cannot be expected to yield detailed features of the plastic deformation near the crack tip, one can expect reasonable predictions of such things as plastic zone size, functional dependence of plasticity effects upon external loads and geometry, and unloading-reloading behavior.

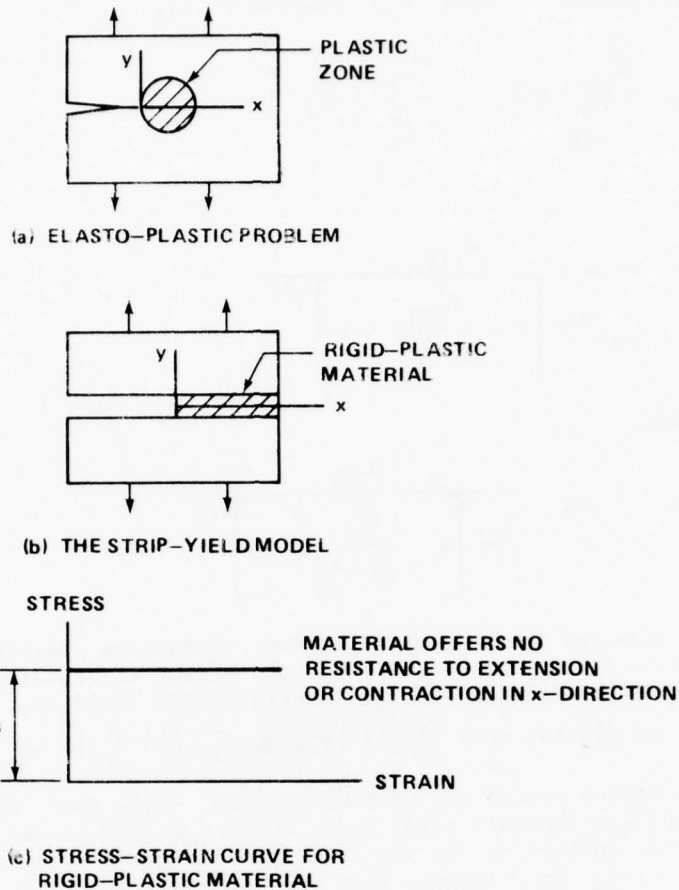


Figure 4.4. Strip-yield modeling of the crack-tip plastic zone.

Consider, as an example, the finite crack in an infinite plate shown in Figure 4.5. In that figure, the portion of the rigid plastic material which has yielded has been removed and replaced by the yield-stress  $\sigma_{ys}$  on the boundary of the extended portion of the crack  $w$ .

Since the rigid plastic material was assumed to offer no resistance to extension or contraction in the  $x$ -direction, the solutions to the elastic regions of the model in Figure 4.5 may be obtained by taking the usual elastic solutions and replacing  $a$  by  $a + w$ , and then adding the  $\sigma_{yp}$  distribution as an additional external loading.

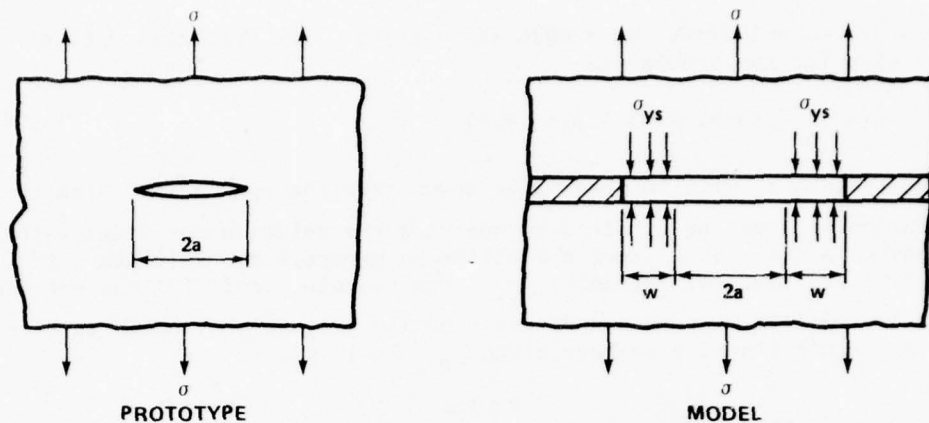


Figure 4.5. Strip yield model for a finite crack in an infinite plate.

The problem thus formulated can be solved not just for this specific example but in general terms which will cover all possible Mode I loadings for cracks in infinite plates. Let

$K_e(a)$  = Elastic stress intensity factor for the crack problem

$Z_e(z,a)$  = Westergaard stress function for the crack problem

$K_p(w,a)$  = Elastic stress intensity factor for the  $\sigma_{ys}$  load

$Z_p(z,w,a)$  = Westergaard stress function for the  $\sigma_{ys}$  load

where the subscript I for Mode I has been dropped.

Since one is concerned here only with the superposition of two sets of elastic solution, the fact that the physical cracks for the "p" solution will have one side of the crack running into the other will be of no consequence in the model. The size of the plastic zone,  $w$ , is determined by the condition that the stresses should be bounded at the outer edges of the plastic zone. This means that the stress intensity factors due to the external loadings (with  $a$  replaced by  $a + w$ ) and due to the  $\sigma_{ys}$  loadings, should sum to zero, and thus for the two problems considered  $w$  is the solution of:

$$K_e(a + w) + K_p(a + w) = 0 \quad (4.13)$$



in order to annihilate the stress singularity. The Westergaard Stress Function for the problem is

$$Z(z) = Z_e(z-w, a+w) + Z_p(z, w, a) \quad (4.14)$$

The function  $Z_e$  will in general be known from the appropriate elastic solution.  $Z_p$  may be obtained by applying the solution for wedging force loads on a crack as a Green's Function to generate the solution for distributed loads of intensity  $\sigma_{ys}$ . For example, Irwin [7] has provided the appropriate Westergaard Stress Function (Figure 4.6) which is used as a Green's Function in generating  $Z_p$ . Irwin gives:

$$Z = \frac{2Pa^2}{\pi(z^2 - b^2)} \left[ \frac{1 - (b/a')^2}{1 - (a'/z)^2} \right]^{1/2} \quad (4.15)$$

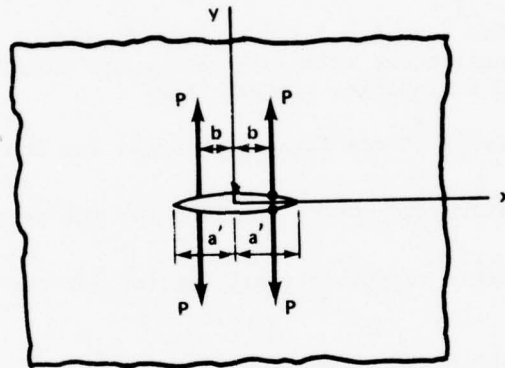


Figure 4.6. Wedging force on a crack.

By replacing  $a'$  with  $a + w$ , shifting the origin to the right " $a$ ," and replacing  $P$  by  $-\sigma_{ys} dz$  with  $z$ , the distance along  $x$  from the new origin to  $-\sigma_{ys}$ , the Green's Function for generating  $Z_p$  is obtained. After integrating from  $z = 0$  to  $z = w$  one has

$$Z_p = -\sigma_{ys} \left[ 1 - \frac{2}{\pi} \sin^{-1} \left( \frac{a}{a+w} \right) \right] \frac{z' + a}{[(z' + a)^2 - (a+w)^2]^{1/2}} + \sigma_{ys} \left\{ 1 - \frac{2}{\pi} \tan^{-1} \left[ \left( \frac{a}{a+z'} \right) \left( \frac{(z' + a)^2 - (a+w)^2}{(a+w)^2 - a^2} \right)^{1/2} \right] \right\} \quad (4.16)$$

where  $z'$  is a complex coordinate measured from the physical crack tip  $x = a'$ . Now to find  $K_p$  apply Equation (2.29),

$$K_p = \lim_{z' \rightarrow w} \sqrt{2\pi} (z' - w)^{1/2} \sigma_p \quad (4.17)$$

One then obtains

$$K_p = -\sigma_{ys} \sqrt{\pi(a+w)} \left[ 1 - \frac{2}{\pi} \sin^{-1} \left( \frac{a}{a+w} \right) \right] \quad (4.18)$$

Substituting into Equation (4.13) and rearranging one finds

$$\sin^{-1} \left( \frac{a}{a+w} \right) = - \frac{\sqrt{\pi} K_e}{2\sigma_{ys} \sqrt{a+w}} + \frac{\pi}{2}$$

or

$$\cos^{-1} \left( \frac{a}{a+w} \right) = \frac{\sqrt{\pi} K_e}{2\sigma_{ys} \sqrt{a+w}}$$

or

$$\sec^{-1} \left( \frac{a+w}{a} \right) = \frac{\sqrt{\pi} K_e}{2\sigma_{ys} \sqrt{a+w}}$$

and finally solving for  $w$

$$w = a \left\{ \sec \left( \frac{\sqrt{\pi} K_e}{2\sigma_{ys} \sqrt{a+w}} \right) - 1 \right\} \quad (4.19)$$

where it is understood that  $K_e$  must be determined for a crack of length  $a+w$ . For the problem at hand, Figure 4.5,  $K_e = \sigma \sqrt{\pi(a+w)}$ , Equation (2.34). Thus, for a finite crack in an infinite plate,

$$w = a \left[ \sec \left( \frac{\pi}{2} \frac{\sigma}{\sigma_{ys}} \right) - 1 \right] \quad (4.20)$$

which is an exact solution to the strip yield model, since no assumption has been made regarding the plastic zone size.

By assuming that the yielding is small scale, a general result can be obtained for the plastic zone size  $w$  in terms of  $K_e$  and  $\sigma_{yp}$ . Simplify Equation (4.19) by replacing the secant term with the first two terms of its expansion, i.e.,

$$\sec x = 1 + \frac{x^2}{2} + \frac{5}{24} x^4 + \frac{61}{720} x^6 + \dots$$

Equation (4.19) becomes

$$w = \frac{\pi}{8} \frac{K_e^2}{\sigma_{ys}^2} \left( \frac{a}{a+w} \right) \quad (4.21)$$

Assuming  $w \ll a$  and neglecting all  $w/a$  terms in comparison to unity, one has  $K_e(a+w) \approx K_e(a) = K_e$  and Equation (4.21) reduces to

$$w = \frac{\pi}{8} \frac{K_e^2}{\sigma_{ys}^2} \quad (4.22)$$

Recall that for Mode III,  $R_o = \frac{1}{\pi} \frac{K_{III}^2}{\sigma_{yp}^2}$ . Thus, again one sees that for

small-scale plasticity (i.e., small zone size), the plastic zone size depends on the loading and geometry only through the elastic stress intensity factor.

Equation (4.22) was derived from stress fields for cracks in infinite planes. These results, however, will be valid for finite planes, provided that the plastic zone size is negligible not only in comparison to crack length but also to all planar dimensions of the cracked body. An important feature of the strip yield model, as just illustrated, is the fact that the methods of analysis are essentially the same as those used in the conventional elastic treatment of crack problems.

#### 4.4 Limitations of the Crack-Tip Stress Field Theory

A certain amount of nonlinear deformation, including plastic yielding, can occur without grossly affecting the surrounding elastic crack-tip stress field. Moreover, such nonlinearities, if embedded in identical stress fields, will likewise be identical and self-compensating in fracture toughness testing. Thus, it is important to determine the

relative sizes of nonlinear zones which can be tolerated within the crack-tip stress fields. This size is, in turn, related to the relative size in which the field equations (2.11), (2.17), and (2.26) apply. Before proceeding, it seems wise to further place into perspective some limitations of the elastic crack-tip stress field theory. This will be done by consideration of two dissimilar problems.

For a finite crack in an infinite plate under uniform tension (Figure 4.7), the approximate stress ahead of the crack is obtained by substituting  $K_I = \sigma(\pi a)^{1/2}$  into Equation (2.11) for  $\theta = 0$ .

$$\sigma_{yy} \Big|_{\theta=0} = \frac{\sigma(a)^{1/2}}{(2r)^{1/2}} \quad (4.23)$$

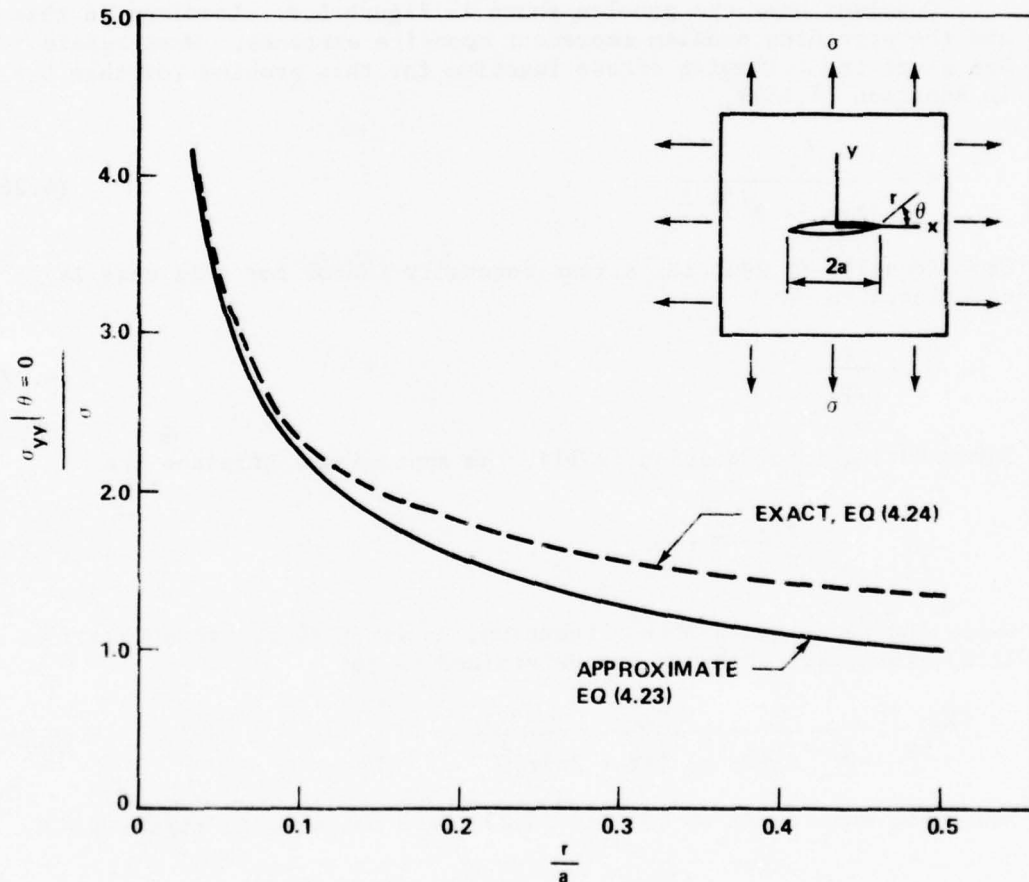


Figure 4.7. Comparison of approximate and exact solutions for a finite crack in an infinite plate.

As  $r$  becomes larger, Equation (4.23) becomes more and more approximate. The exact stress may be obtained from the Westergaard Stress Function [see Equation (2.32)]

$$\sigma_{yy}\bigg|_{\theta=0} = \frac{\sigma(r+a)}{(r^2 + 2ar)^{1/2}} \quad (4.24)$$

A comparison of Equations (4.23) and (4.24) is given in Figure 4.7. The increasing inaccuracy in the approximate stresses is apparent as  $r$  increases. It will be useful in the following to have the ratio of the approximate and exact stresses. Namely,

$$\frac{\sigma_{yy}(\text{approx})}{\sigma_{yy}(\text{exact})} = \frac{(1 + \frac{r}{2a})^{1/2}}{1 + r/a} \quad (4.25)$$

Consider next the problem shown in Figure 4.8. Loadings in this and the preceding problem represent opposite extremes. Westergaard has given the following stress function for this problem (or take  $b = 0$  in Equation (4.15)),

$$Z = \frac{P}{\pi z(z^2 - a^2)^{1/2}} \quad (4.26)$$

From Equation (2.29), the stress intensity factor for this case is calculated to be

$$K_I = \frac{P}{\sqrt{\pi a}} \quad (4.27)$$

Substituting into Equation (2.11), the approximate stresses are

$$\sigma_{yy}\bigg|_{\theta=0} = \frac{P}{\pi} \frac{1}{(2ar)^{1/2}} \quad (4.28)$$

Using the Westergaard Stress Function, Equation (4.26) into Equations (2.6), the exact stresses are determined to be

$$\sigma_{yy}\bigg|_{\theta=0} = \frac{P}{\pi(r+a) [(r+2a)r]^{1/2}} \quad (4.29)$$

These two equations, (4.28) and (4.29), are compared in Figure 4.8.



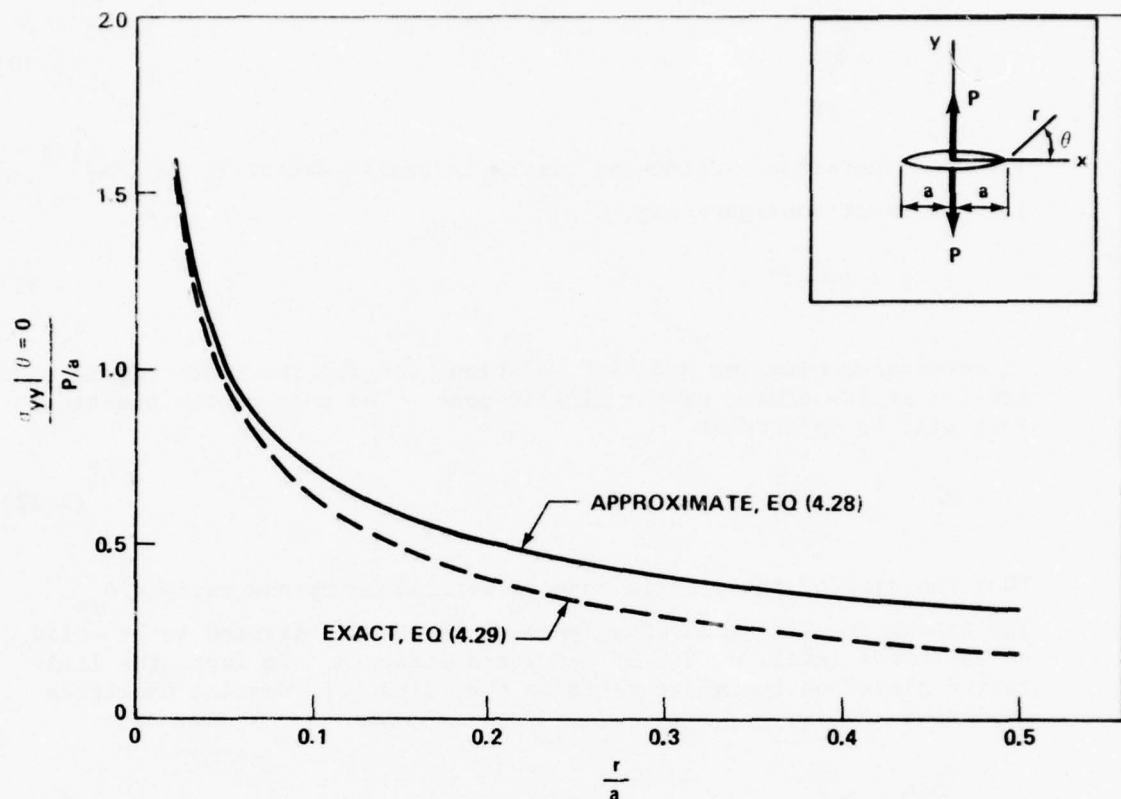


Figure 4.8. Comparison of approximate and exact solutions for wedging forces on a finite crack.

Both configurations (Figures 4.7 and 4.8) illustrate the accuracy of the stresses when  $r$  is small and the departure from accuracy as  $r$  increases. For the two problems, results indicate similar deviations of the approximate stresses from the exact. Thus, if the tolerable plastic zone size can be determined for one problem it should be applicable to others.

While for brittle problems, the usefulness of the approximate stresses for predicting fracture behavior is not questioned, Figures 4.7 and 4.8 contain strong implications pertaining to certain experimental techniques. For example, in using photoelasticity, moiré, etc. measurements must be made very near the crack tip before favorable comparison with the approximate stresses could be expected.

Returning to the question of the tolerable plastic zone size, recall the results of the Mode III solution (the strip-yield results were comparable),

$$R_o = \frac{K_I^2}{\pi \sigma_{ys}^2} \quad (4.30)$$

in Mode I notation. Using the stress intensity factor  $K_I = \sigma(\pi a)^{1/2}$  for the first configuration,

$$R_o/a = \left(\frac{\sigma}{\sigma_{ys}}\right)^2 \quad (4.31)$$

In accordance with the Mode III solution, imagine the crack tip to be located at the center of the plastic zone. The edge of the plastic zone will be located at

$$R_y = \frac{1}{2} \left(\frac{\sigma}{\sigma_{ys}}\right)^2 a \quad (4.32)$$

Thus the size of the plastic zone is determined by the ratio  $\sigma/\sigma_{ys}$ . The linear fracture mechanics approach is usually assumed to be valid up to stress levels of 0.8 of the yield strength. In fact, the limitation placed on the above ratio in the fifth ASTM Special Committee Report was

$$\frac{\sigma_{net}}{\sigma_{ys}} \leq 0.8$$

Substituting the upper limit of stress  $\sigma = 0.8 \sigma_{ys}$  into Equation (4.32), the relative size  $R_y/a$  for reasonable accuracy is about 0.3. From Equation (4.25), the actual stresses deviate about 20 percent from the approximate stresses. It thus appears that the plastic zone at a crack tip may be fairly large without grossly disturbing the usefulness of the elastic stress field approach. It is pointed out that this is only a rough estimate intended to illustrate the usefulness of the elastic stress approach in the presence of a given amount of yielding. Requirements on the plastic zone size for obtaining valid plane-strain fracture toughness data are much more stringent than the above would seem to indicate. This is necessary in order to obtain fracture toughness values which are independent of specimen dimensions (see Chapter 5).

## Chapter 5. FRACTURE TOUGHNESS TESTING

The purpose of fracture toughness testing is to determine the critical stress intensity factor for a given material in a given environment. The basic procedure is to load a precracked specimen to failure, observe the failure load and crack length, and use the appropriate solution for the test specimen to calculate the value of the critical stress intensity factor. Other tests are aimed at determining the rate of crack growth under cyclic loads and the fracture toughness under long-term sustained loads in a corrosive environment. Though conceptually simple, there are numerous considerations of basic material behavior and experimental procedure which must be accounted for in order to obtain useful fracture data. A comprehensive collection of fracture data have been tabulated in the Damage Tolerant Design Handbook [50]. ASTM specifications [51] now control the method of test for plain-strain fracture toughness testing. A review of developments leading to the adoption of the ASTM specifications is included in the ASTM Special Technical publications STP 410 [52] and STP 463 [53]. Fatigue crack growth data and additional fracture toughness testing are included in the publications, STP 513 [54] and STP 514 [55], Part I and Part II, respectively, of the proceedings of the 1971 National Symposium on Fracture Mechanics. Since test methods are described in detail elsewhere, only a summary of basic ideas is presented here.

### 5.1 Characteristics of the Critical Stress Intensity Factor

Because of its technological importance, most fracture toughness testing has been directed to the Mode I case. The value of the stress intensity factor at which crack propagation occurs is known as  $K_{Ic}$ . Irwin [56] determined that  $K_{Ic}$  (or, alternatively, the critical strain energy release rate  $g_{Ic}$ ) varied with plate thickness. His results, taken from Reference [57], for tests on plates of 7075-T6 aluminum are shown in Figure 5.1. The  $g_{Ic}$  curve shows a decreasing toughness for plates of increasing thickness, while the fracture surface makes a transition from full slant to nearly square (Figure 5.2). For thin specimens the state of stress at the crack tip approaches that of plane stress ( $\sigma_{zz} = 0$ ). In the absence of  $\sigma_{zz}$  the state of stress is biaxial permitting the formation of a relatively large plastic zone (see Chapter 4). The ability to yield thus increases the fracture toughness. Since, for thin specimens the state of stress is approximately biaxial,  $\sigma_{xx} = \sigma_{yy}$ , the maximum shear stress occurs on a plane at approximately 45 degrees to the crack plane and a slant (or V-slant) fracture results (i.e.,  $P = 0$ ) as illustrated by Figure 5.2 and as shown by the dotted line in Figure 5.1. Focusing attention on the crack tip for this case, it can be seen that failure occurs by a combination of opening mode and edge tearing or a combination of Modes I and III. As the specimen

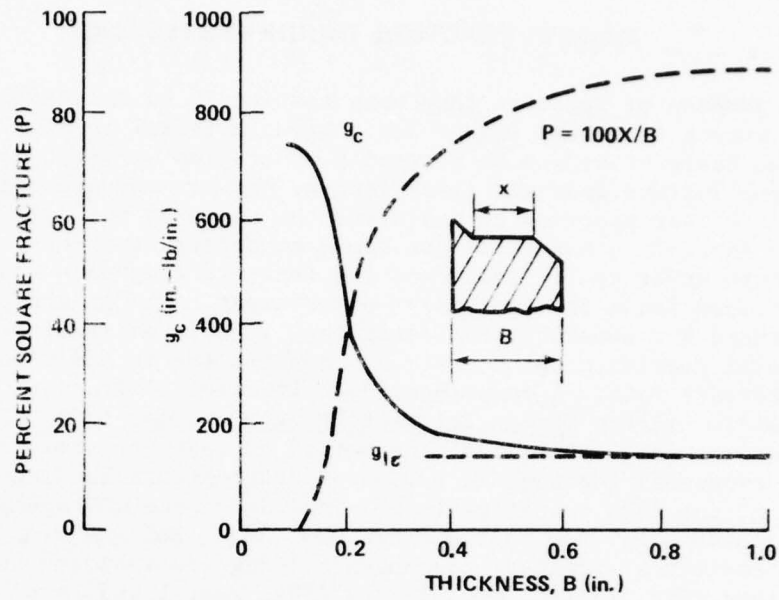


Figure 5.1. Appearance of fracture surface and effect of plate thickness on fracture toughness.

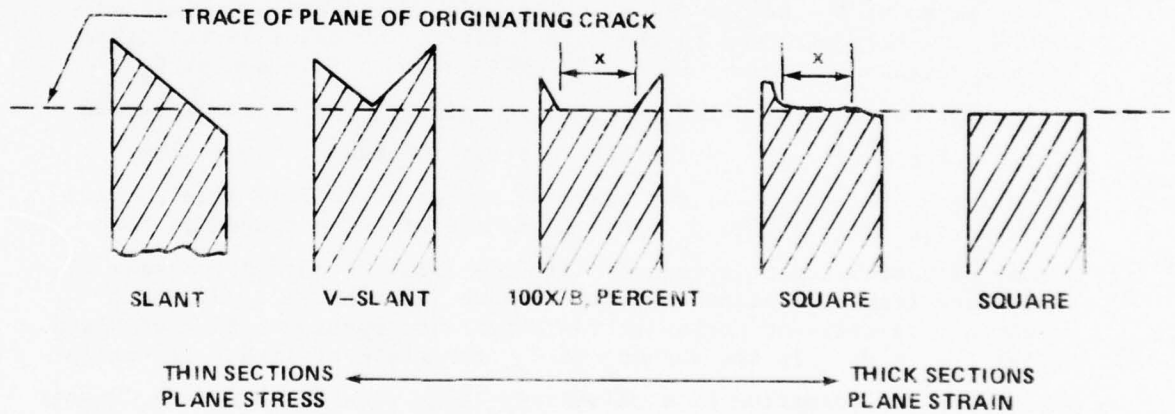


Figure 5.2. Types of fracture surfaces illustrated by section views taken normal to direction of crack propagation.

thickness increases, the state of stress along the crack front approaches that of plain strain,  $\sigma_{zz} = \nu(\sigma_{xx} + \sigma_{yy})$ , resulting in a state of tri-axial tension; plastic flow is inhibited and the fracture toughness decreases while the fracture surface becomes more nearly square. A state of plane stress still exists on the plate surface, and shear lips form there as shown in the section view of Figure 5.1. Figure 5.2 gives a pictorial representation of the thin-to-thick fracture surface transition.

As the specimen thickness is increased further, the  $g_c$  curve levels out and approaches a constant value. This value is designated as the plane-strain fracture toughness  $K_{IC}$  (historically  $g_{IC}$ ).  $K_{IC}$ , when determined in accordance with ASTM specifications, is taken to be a material constant characteristic only of the given material.

Following Wilhelm [45], the variation of the critical stress intensity factor with thickness for several materials is shown in Figure 5.3. The values are nominal values only and are shown to illustrate behavior. Some materials, 7075-T6 and Ti-B120VCA, quickly approach a constant value of  $K_{IC}$  while others require greater thicknesses.

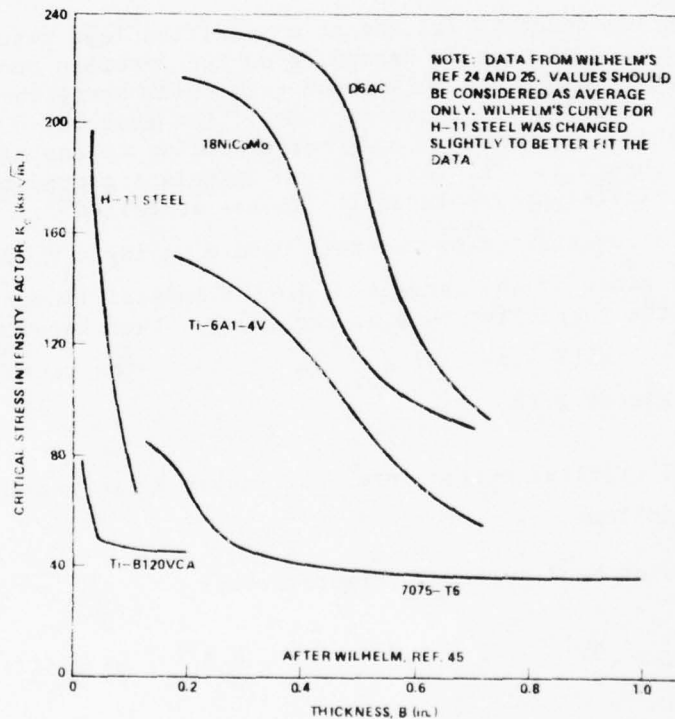


Figure 5.3. Nominal critical stress intensity factors for several materials as a function of thickness.



## 5.2 Plane Strain Fracture Toughness Testing

Numerous specimen designs have been used in the past to obtain fracture toughness data, but only two specimens are now recognized as ASTM standards [51]. They are the three-point-bend specimen and the compact-tension specimen. These are shown in Figure 5.4. Each specimen contains a crack-starter notch. The chevron notch is shown in Figure 5.4, but several forms are acceptable. The notch must terminate with a fatigue crack of at least 0.05 inch in length. The fatigue cracking load must be limited to a relatively low value to insure a suitably sharp crack with a small crack-tip plastic zone. The curvature of the fatigue crack front must also be within certain limits. The original crack length is measured after fracture at three locations: (a) at the center of the crack front, (b) midway between the center, and (c) the end of the crack front on each side. The average of these three is then used as the crack length,  $a$ , in subsequent calculations. The dimensions of the specimens are controlled by the crack-tip plastic zone size. The crack length,  $a$ , and the thickness,  $B$ , must exceed  $2.5 \left( \frac{K_{IC}}{\sigma_{ys}} \right)^2$ , where  $\sigma_{ys}$  is the 0.2 percent offset yield strength of the material. This is approximately 50 times the plane-strain plastic zone size.

The specimen is loaded to failure at a specified load rate either in three-point bending or tension depending on the specimen configuration used. During loading, a displacement gage which spans the notch measures the crack opening displacement (COD). The load and COD are recorded autographically, resulting in a curve similar to one of the three shown in Figure 5.5. The load used to calculate a conditional value  $K_Q$  of the critical stress intensity factor is called  $P_Q$ . A secant line  $OP_5$  is constructed on the test record having a slope of 95 percent of the slope of the tangent  $OA$  to the initial linear part of the record. For the respective type of record,  $P_Q$  then becomes the value indicated in Figure 5.5. For a valid  $K_{IC}$  test, the ratio  $P_{max}/P_Q$  must not exceed 1.10.

A conditional critical stress intensity factor  $K_Q$  in  $\text{psi-in.}^{1/2}$  is calculated as follows:

a) Three-point bend specimen (Figure 5.4a):

$$K_Q = \frac{P_Q S}{B w^{3/2}} \left[ 2.9 \left( \frac{a}{w} \right)^{1/2} - 4.6 \left( \frac{a}{w} \right)^{3/2} + 21.8 \left( \frac{a}{w} \right)^{5/2} - 37.6 \left( \frac{a}{w} \right)^{7/2} + 38.7 \left( \frac{a}{w} \right)^{9/2} \right] \quad (5.1)$$

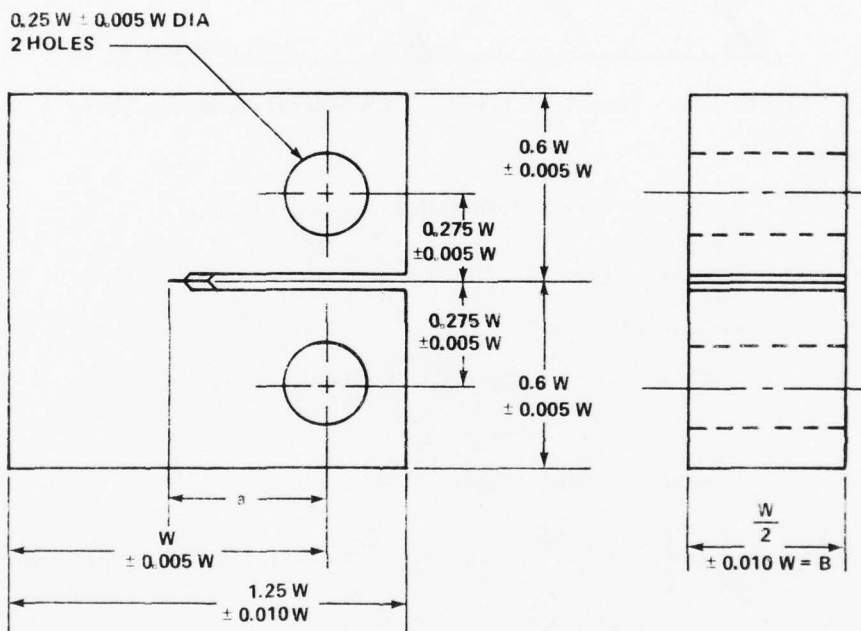
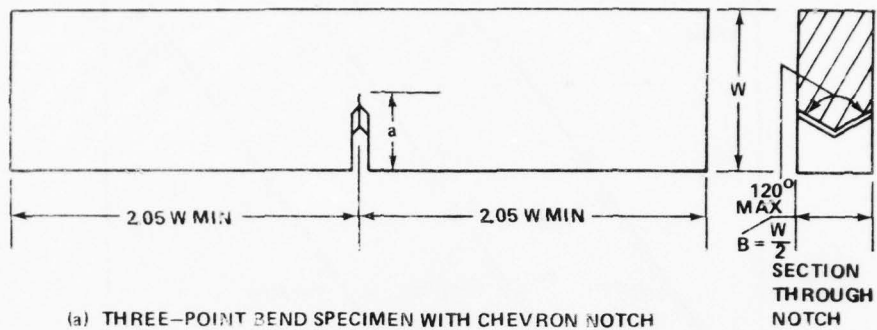


Figure 5.4 Standard ASTM  $K_{IC}$  specimens.

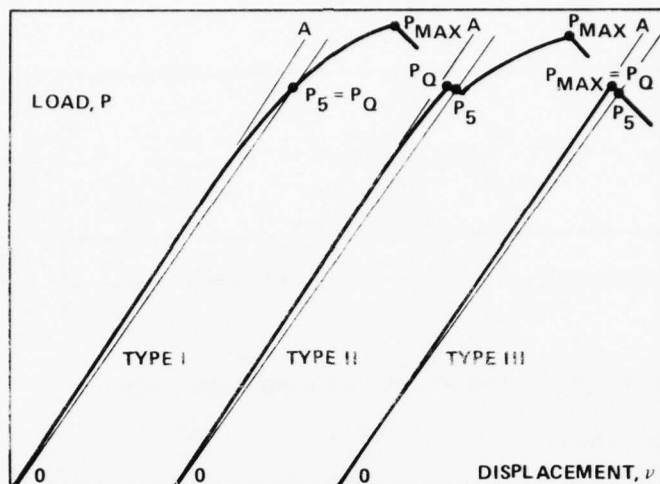


Figure 5.5. Principal types of load-displacement records.

where

$P_Q$  = load from load - deformation curve, pounds

$B$  = specimen thickness, inches

$S$  = span length, inches

$w$  = width (depth) of specimen, inches

$a$  = crack length, inches

b) Compact specimen (Figure 5.4b):

$$K_Q = \frac{P_Q}{Bw^{1/2}} \left[ 29.6 \left( \frac{a}{w} \right)^{1/2} - 185.5 \left( \frac{a}{w} \right)^{3/2} + 655.7 \left( \frac{a}{w} \right)^{5/2} - 1017 \left( \frac{a}{w} \right)^{7/2} + 638.9 \left( \frac{a}{w} \right)^{9/2} \right] \quad (5.2)$$

Only after the test has been shown to satisfy all of the requirements, such as minimum specimen size (in comparison with  $2.5 \frac{K_Q^2}{\sigma_{ys}} \frac{a}{w}$ ), fatigue cracking load level, and crack-tip shape does the test become a valid test. Then the conditional value  $K_Q$  becomes  $K_{IC}$ , the plane

strain fracture toughness. Plane-strain fracture toughness testing is unusual in that the test requirements (specimen size, etc.) depend upon  $K_{IC}$ , the quantity to be determined. Therefore, there is no advance assurance that a valid  $K_{IC}$  will be determined in a particular test.

The range of application of the ASTM test method is restrictive. The method does not apply, for example, to brittle materials having a thickness less than 0.25 inch. Also, since specimen size increases proportional  $(K_{IC}/\sigma_{ys})^2$ , then for low-strength, high-toughness materials the method leads to specimens of a prohibitively large size. Nor is it possible to determine  $K_{IC}$  if any dimension of the available stock of material is insufficient to provide a specimen of the required size. By giving due consideration to the principles involved in the development of the standard method, it is sometimes possible for the investigator to design a useful fracture toughness specimen. For a good example of this see Kendall and Hussain [58].

The value  $K_{IC}$  determined in accordance with Reference 51 can be considered to be a material constant. It can serve the following purposes:

- a) In research and development to assess the effects of metallurgical variables such as heat treatment or of fabrication operations such as welding on the fracture toughness of new or existing materials.
- b) In design applications or service, evaluation to establish the suitability of a material for a given specific application where the load level and maximum flaw size are known.
- c) For specifications of acceptance and manufacturing quality control.

### 5.3 Plane-Stress and Transitional Fracture - Toughness Testing

Currently, no ASTM standard exists for determining plane-stress or transitional values of  $K_c$ . Development of a standard method has been hampered by the degree to which crack tip plasticity and associated stable crack extension occurs prior to fracture. Consequently, considerable emphasis must be directed to monitoring the slow, stable tearing portion of the fracture process to determine an effective critical crack length. A number of experimental guidelines have been developed, as explained in Reference 50, and were used as a criteria in selecting  $K_c$  data for inclusion in that handbook.

In 1970 a research program was initiated at the Naval Research Laboratories (NRL) for developing a standard testing procedure for determining  $K_c$  values for thin sheets [59]. This research has resulted in a proposed standardized test for screening purposes using the center-cracked tensile (CCT) sheet specimen. Some of the details of this method differ from those summarized in Reference 50. Because of the extensive research conducted in arriving at the method proposed in Reference [59], the general features of that method are summarized here.

The CCT specimen of thickness B and width W is shown in Figure 5.6. The recommended length L is:

$$L = 2W, W \leq 12 \text{ in.}$$

$$L = 1.5 W, W > 12 \text{ in.}$$

where L is measured between the innermost grip pins (grips are detailed in Reference [59]). The recommended final crack length  $2a_c$  is approximately 0.333 W. (The original crack length  $2a_o$  will be smaller.) The starter slot ideally should be subtended by fatigue cracks although in some cases a slot with a root radius of approximately 0.001 to 0.002 inch will effectively simulate a fatigue crack. For specimens thinner than 0.123 inch, crack buckling is suppressed by the use of rigid, lubricated face plates attached to the central portion of the specimen.

To determine the dimensions of the specimen the plastic zone size is estimated as

$$R_y = \frac{1}{2\pi} \left( \frac{K_c}{\sigma_{ys}} \right)^2 \quad (5.3)$$

Then the minimum width is

$$W_{\min} = 27 R_y \quad (5.4)$$

A suitable crack length is then

$$2a_c = 0.333W \quad (5.5)$$

However, the critical crack length is a function of the initial crack length,  $a_o$ ,

$$\frac{a_o}{a_c} = \frac{0.882}{\beta(0.1026)} \quad (5.6)$$



where  $\beta = (K_c / \sigma_{ys})^2 / \beta$ . This provides the starter slot length. The above proportioning of the specimen, Equations (5.4) through (5.6), limits the plastic zone size relative to the plate dimensions.

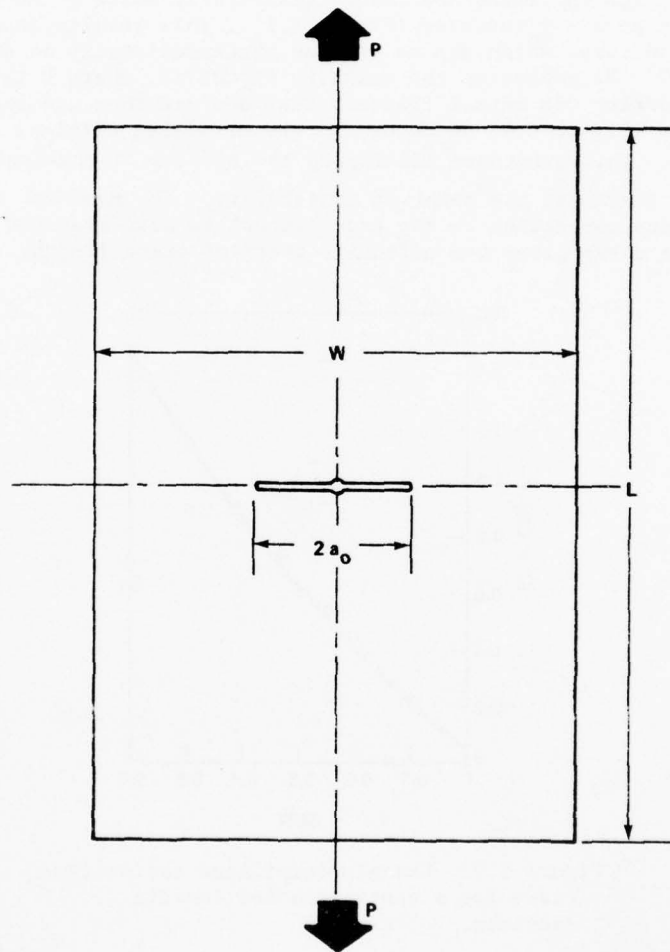


Figure 5.6. The center-cracked tensile (CCT) specimen.

During the fracture test a COD gage is used to measure crack opening (similar to plane-strain testing) as the load is applied. The effective crack length  $2a_c$  is determined after the test, not by measuring but from a compliance calibration curve. To determine the compliance calibration curve, specimens are prepared with slot lengths varying through a range of values of  $2a_0/w$  such as 0.1, 0.2, 0.3, 0.4, 0.5, 0.6. The specimens are loaded elastically while  $P$  and COD are graphed by an  $x - y$  recorder (Figure 2.1). This results in a compliance calibration curve which can be plotted nondimensionally as shown in Figure 5.7. By measuring the quantity  $EB[COD]/P$ , where  $E$  is Young's modulus, during the actual fracture test one can then use the compliance curve (Figure 5.7) to determine the effective critical crack length  $a_c$ . This procedure eliminates the problem of physically measuring the crack length at the point of instability. The need for adding a plastic zone correction to the crack length is also bypassed since the compliance curve gives the effective critical crack length.

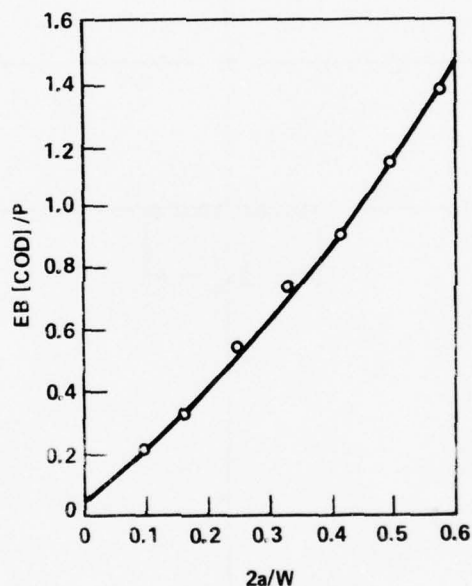


Figure 5.7. Example compliance calibration curve for a center-cracked tensile specimen.

Figure 5.8 shows two types of load-displacement curves for a plane-stress fracture test. In curve A, the curve rises linearly to a given point before crack growth starts, then continues to rise with accompanying crack growth until final instability occurs. After the maximum load is reached on Curve B, the crack continues to grow under constant load until final separation.

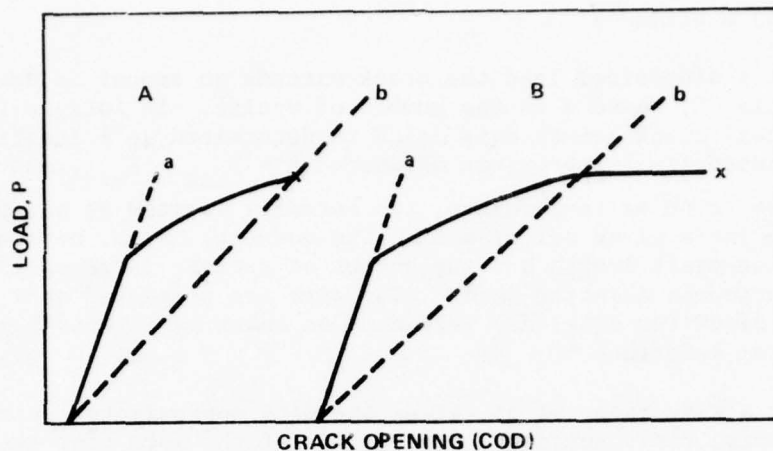


Figure 5.8. Load - COD curves showing two types of crack growth response.

To find  $K_c$ , both curves are analyzed in the same way. A straight line (a) is drawn through the linear portion of the curve. The value of  $EB[COD]/P$  is calculated and compared with the value known for  $2a_0/w$  from the compliance curve (Figure 5.7), and the difference is noted. There will be a slight difference due to variations of alignment, etc. A secant line (b) is then drawn to the first point of maximum load value;  $EB[COD]/P$  is calculated for this line and corrected by the difference noted above. The corrected value of  $EB[COD]/P$  is then used on the appropriate calibration curve (Figure 5.7) to determine the effective critical crack length  $a_c$ . Finally,  $K_c$  is calculated from the following formula:

$$K_c = \sigma \sqrt{a_c} (1.77) \left[ 1 - 0.1 \left( \frac{2a_c}{w} \right) + \left( \frac{2a_c}{w} \right)^2 \right] . \quad (5.7)$$

The above is only a summary of plane stress testing, and for further details the reader is referred to the handbook [50], and the paper by Sullivan and Stoop [59].

#### 5.4 Fatigue Crack Propagation

The rate of growth of a fatigue crack under a time-varying load is influenced by a number of variables, including stress level, crack length, specimen geometry, load frequency, material, environment, and temperature. The effects of stress level, crack lengths, and specimen geometry can be properly accounted for by means of the stress intensity factor. For a fatigue loading, the applied stress varies with time and since the stress intensity factor is proportional to stress then the stress intensity factor exhibits the same kind of variation with time. That is,  $K$  has the form

$$K(t) \propto \sigma(t) \sqrt{\pi a} \quad (5.8)$$

For a sinusoidal load the crack extends an amount  $\Delta a$  during each load cycle  $\Delta N$ , where  $N$  is the number of cycles. In fatigue testing the incremental crack growth rate  $\Delta a/\Delta N$  is determined as a function of the stress intensity factor range  $\Delta K$  where  $\Delta K = K_{\max} - K_{\min}$ , and the other variables, such as temperature, are normally treated as parameters, constant for a given set of data. The quantity  $\Delta a/\Delta N$ , determined by monitoring crack length and the number of cycles, is generally written as a continuous quantity  $da/dN$ . The data are presented as a log-log plot of  $da/dN$  (or  $d(2a)/dN$ ) versus  $\Delta K$  as shown by Figures 5.9 and 5.10, taken from Reference 50.

For a wide range of  $\Delta K$  values the data approximate a straight line. Noting this, Paris suggested a power law of the form (for example, see References 60 and 61),

$$\frac{da}{dN} = C(\Delta K)^n \quad (5.9)$$

where  $c$  depends upon the load ratio,  $R = \sigma_{\min}/\sigma_{\max}$ , the material, and other test parameters. Instead of the stress ratio, Paris used the relative mean load  $\gamma$  defined in the present notation by  $\gamma = \sigma_{\text{mean}}/\Delta\sigma$ .

For several materials with  $\gamma = 0.5$  ( $R = 0$ ), a value of  $n = 4$  gave a reasonably accurate fit to the data, as shown by Figures 5.11 (a), (b), and (c) from Reference 60. In fact, based on Figure 5.12 for steels loaded with  $\gamma = 0.5$ , Irwin and Paris [62], recommended for estimation purposes

$$\frac{da}{dN} = C(\Delta K)^4 \quad (5.10)$$

where

$$C = 1.0 \times 10^{-12} \quad (\text{for mean data on medium-strength and low strength steel})$$

$$C = 1.6 \times 10^{-12} \quad (\text{for mean data on all steel})$$

$$C = 2.0 \times 10^{-12} \quad (\text{for conservative estimating of fastest rates on all steels})$$

and

$$da/dN = \text{inches per cycle}$$

$$K = \text{ksi-inch}^{1/2}.$$

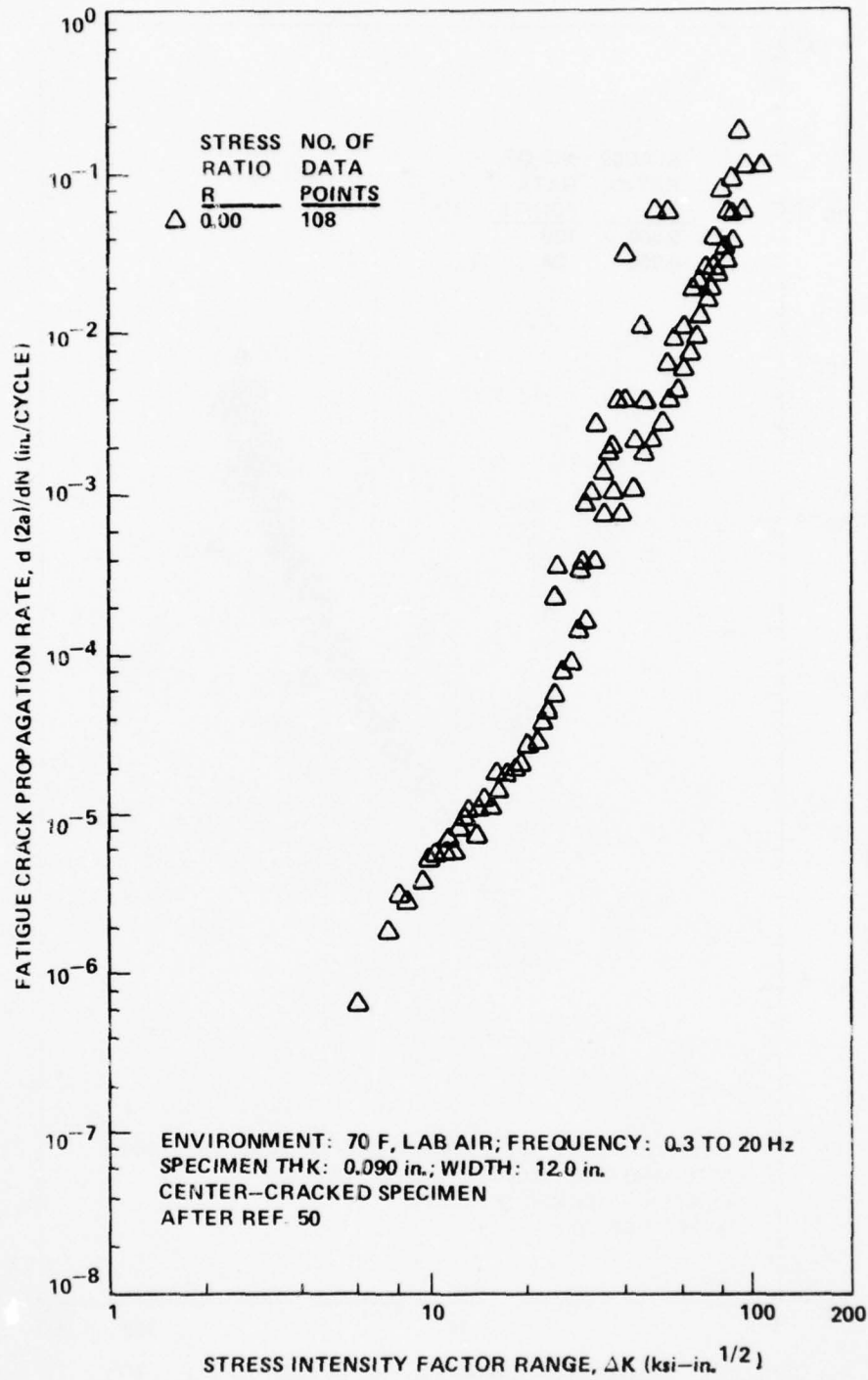


Figure 5.9. Variation of fatigue-crack-growth rate with  $\Delta K$  for 2024-T3 alloy.



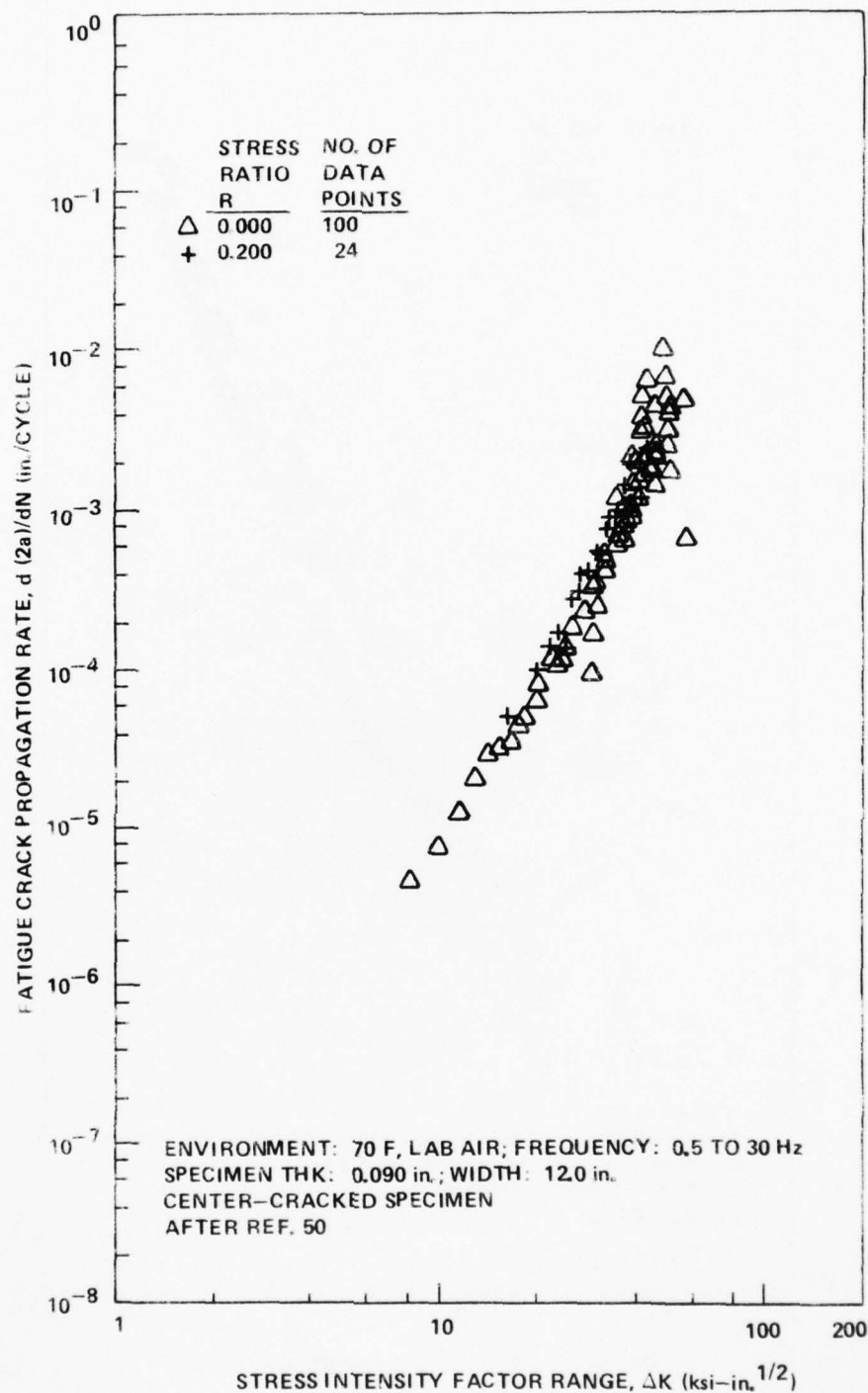
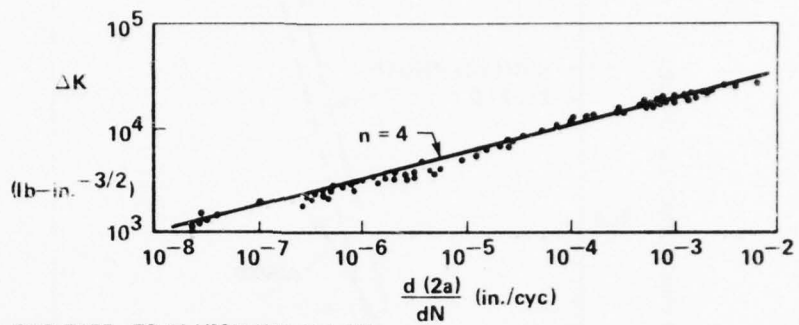
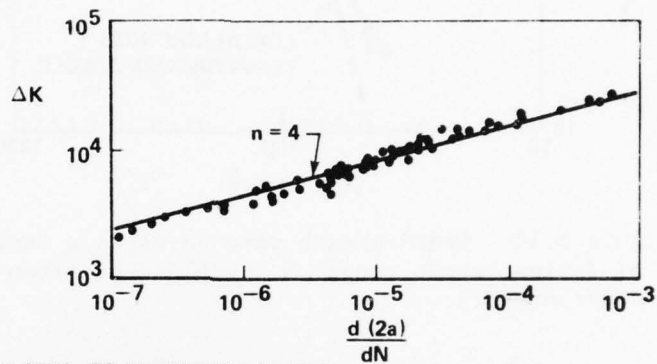


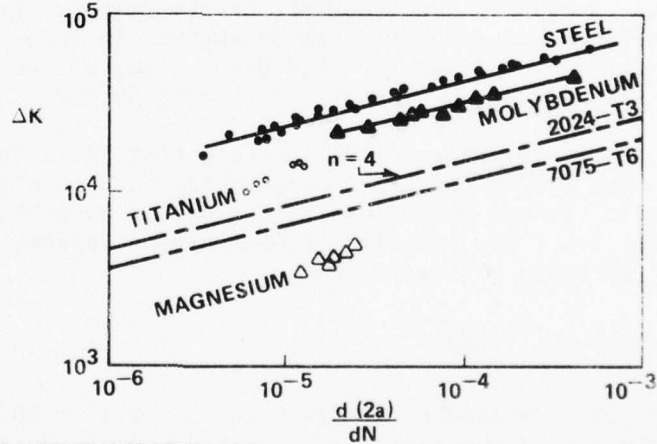
Figure 5.10. Variation of fatigue-crack-growth rate with  $\Delta K$  for 7075-T6 alloy



(a) DATA FOR 7075-T6 ALUMINUM ALLOY



(b) DATA FOR 2024-T3 ALUMINUM ALLOY



(c) DATA FOR VARIOUS MATERIALS

Figure 5.11. The exponential equation of Paris fitted to the data for various materials (Figures from Reference 60).

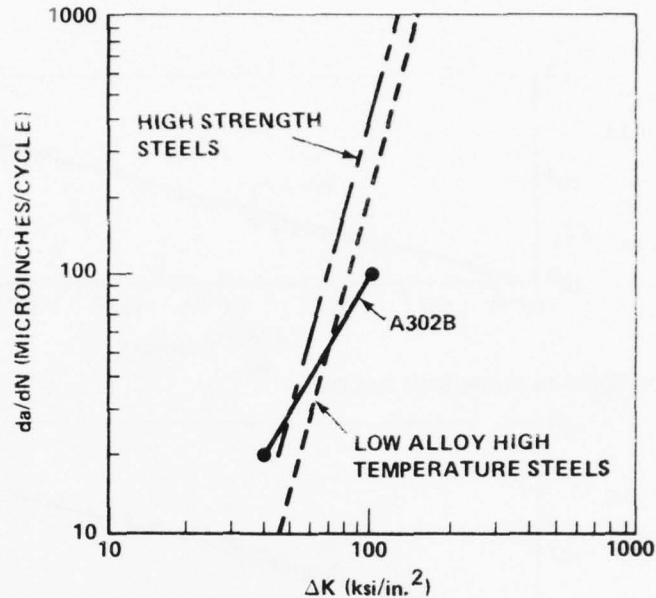


Figure 5.12. Crack-growth rate  $da/dN$  as a function of fatigue cycle range  $\Delta K$ . A302B data (from Reference 62).

Equation (5.10) is a crude relationship, not containing the effects of load ratio, frequency, environment, or temperature, etc. Hence, it is only recommended for estimates of whether fatigue-crack growth is a real problem or not for an anticipated flaw, and not recommended for actual estimates of the fatigue life of structures.

Recent results by Barsom [63] indicate that, at a low stress intensity factor range, the crack propagation rate in high yield strength steels conform more closely to a second power law than to a fourth power law. The equation recommended by Barsom, which was verified for 19 types of steels, is

$$\frac{da}{dN} = 0.66 \times 10^{-8} (\Delta K)^{2.25} \quad (5.11)$$

For the steel D6AC, values of  $n = 2.55$  and  $C = 1.97 \times 10^{-9}$  were recently found by Paris [64]. Much earlier, Liu [65] had, in fact, claimed, based on deduction, a value of  $n = 2$ . It seems clear though that the data fail to support any fundamental value of  $n$ . Thus, Equation (5.9) must continue to be viewed as an empirical relationship, useful nevertheless.

Equation (5.9) does not account for two important effects: the variation in the crack growth rate due to the load ratio,  $R$ , and the instability of the crack growth when the stress intensity factor approaches the  $K_c$  value for the material. To account for these, Forman et al. [66] proposed the following equation:

$$\frac{da}{dN} = \frac{C (\Delta K)^n}{(1 - R) K_c - \Delta K} \quad (5.12)$$

For 2024-T3 and 7075-T6 aluminum and  $n = 3$ , Forman's equation gave good correlation with data for several values of  $R$ . For the same two materials, Hudson [67] further verified Forman's equation by showing that it produced an excellent fit for a wide range of  $R$  ratios. In theory, for any problem for which there is an analytical expression for  $K$ , Equation (5.12) can be integrated to determine the crack length (or, alternatively,  $K$ ) after a given number of cycles. In practice, for most cases, numerical integration must be resorted to due to complex expressions for  $K$ , especially if the fatigue load is nonuniform, i.e., if  $R$  and  $\Delta\sigma$  are not constant.

As a special case, Forman illustrated the case of an infinite plate containing a crack of length  $2a$ . Then

$$\Delta K = \Delta\sigma \sqrt{\pi a} \quad (5.13)$$

For constant  $R$  and  $\Delta\sigma$ , it is possible to substitute Equation (5.13) into (5.12) and integrate Equation (5.12) exactly. For  $n = 3$ , results are

$$N_f - N_o = \frac{2(1 - R) K_c}{C(\Delta\sigma\sqrt{\pi})^3} \left[ \frac{1}{\sqrt{a_o}} - \frac{1}{\sqrt{a_f}} \right] + \frac{1}{C(\Delta\sigma\sqrt{\pi})^2} \left[ \ln a_o - \ln a_f \right] \quad (5.14)$$

where  $a_o$  and  $N_o$  are the initial values of crack length and number of cycles, respectively, and  $a_f$  and  $N_f$  are the final values. Using  $\Delta\sigma = (1 - R) \sigma$ , Equation (5.14) can be simplified to

$$N_f - N_o = \frac{2}{\pi C(1 - R)^2 \sigma^2} \left[ \frac{K_c}{K_o} - \frac{K_c}{K_f} - \ln \frac{K_f}{K_o} \right] \quad (5.15)$$

Upon letting  $K_f = K_c$ , Equation (5.15) can be used to determine the number of cycles  $N_c$  required for crack instability. Results are

$$N_c - N_o = \frac{2}{\pi C(1 - R)^2 \sigma^2} \left[ \frac{K_c}{K_o} - 1 - \ln \frac{K_c}{K_o} \right] \quad (5.16)$$

AD-A038 457

ARMY MISSILE RESEARCH DEVELOPMENT AND ENGINEERING LAB--ETC F/G 20/11  
FRACTURE MECHANICS DESIGN HANDBOOK.(U)  
DEC 76 D G SMITH, B R MULLINIX

UNCLASSIFIED

RL-77-5

NL

2 OF 3  
AD  
A038457



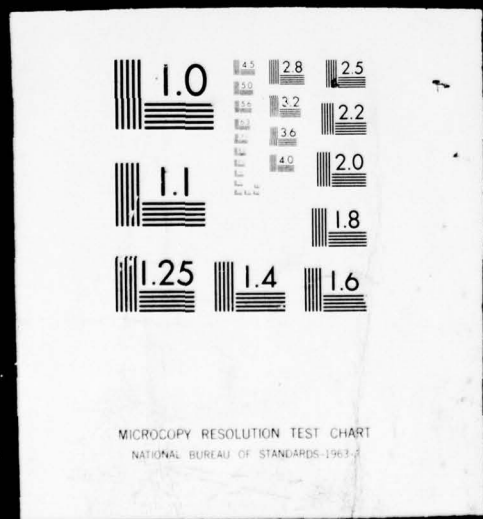


IFIED

2 OF 3

AD

A038457



While equations such as (5.9) and (5.12) represent the trend of fatigue data it must be kept in mind that environmental, material, temperature, and frequency effects all are lumped into the constants  $C$  and  $n$ . Moreover, for some materials and loading conditions, other phenomena require attention. Paris [68] has investigated the idea of threshold stress intensity, value of  $\Delta K$  below which the crack propagation rate becomes vanishingly small. For values of  $R < 0$ , crack closure can, for some materials, cause additional fatigue damage resulting in increased crack growth rates. This has been observed by Elber [69] and Hudson [67] among others. For additional information on recent fatigue crack testing, the reader is referred to ASTM STP 486 [70], and ASTM STP 513 [54]. For those interested specifically in D6AC steel the report, "Crack Behavior in D6AC Steel - An Evaluation of Fracture Mechanics Data for the F-111 Aircraft" [71], contains the largest amount of crack growth data ever generated for any one material application.

For estimating flaw life with accuracy one can select appropriate data from the Damage Tolerant Design Handbook [50] or resort to laboratory tests to measure  $da/dN$  versus  $\Delta K$ , under the expected conditions of load ratio, environment, frequency, and temperature. A log-log plot of  $da/dN$  versus  $\Delta K$  then gives the basic crack behavior of the material. Numerical integration (See Reference [66]) or the report by Engle [72]) of the crack growth rate from the initial flaw size to the critical flaw size is then required to estimate the fatigue life of the structure.

### 5.5 Stress Corrosion Cracking

Under static load and the influence of an aggressive or corrosive environment, stable crack growth can occur at values of  $K_I$  considerably below the critical value. Such slow crack growth is referred to as subcritical crack growth. It can eventually lead to a critical flaw size and failure. Generally, two types of tests are conducted to assess the effects of an aggressive environment: (a) time-to-failure tests, and (b) sustained crack growth rate tests. Numerous types of specimens are used, including those already covered in this chapter. Details of specimens as well as data for several materials are included in Reference 50.

In time-to-failure tests, precracked specimens immersed in the corrosive environment are loaded at various levels of stress intensity and the time to failure is recorded. The stress intensity is reduced in steps until a threshold level of  $K_I$  is reached, below which no failure occurs. This  $K_I$  level is called  $K_{ISCC}$ . Values are tabulated in the Damage Tolerant Design Handbook.

The difference in the environmentally determined threshold stress intensity ( $K_{ISCC}$ ) and the plane-strain fracture toughness ( $K_{Ic}$ ) in air

provides a measure of the susceptibility of the material to stress corrosion cracking. The trend of data for such tests as indicated by Wilhelm [45] is shown in Figure 5.13. In high strength materials,  $K_{ISCC}$  may be small compared to  $K_{IC}$ , while in lower strength, tougher materials,  $K_{ISCC}$  may approach or equal  $K_{IC}$ .

Some  $K_{ISCC}$  data have been obtained in natural or simulated natural environments. Most  $K_{ISCC}$  data, though, have been obtained in aqueous solutions of 3.5 weight percent NaCl. This solution contains about the same percentage of salt as seawater. Other environments include distilled water and air at or near 100 percent relative humidity.

Environmentally sustained crack-growth rates ( $da/dt$ ) have been obtained with a variety of specimens. In general, results are obtained in most of the same environments as the  $K_{ISCC}$  data. Although other methods are used, crack extension is usually determined by optical measurements of the crack length as the crack propagates. An example set of results from a crack-growth-rate test is shown in Figure 5.14.

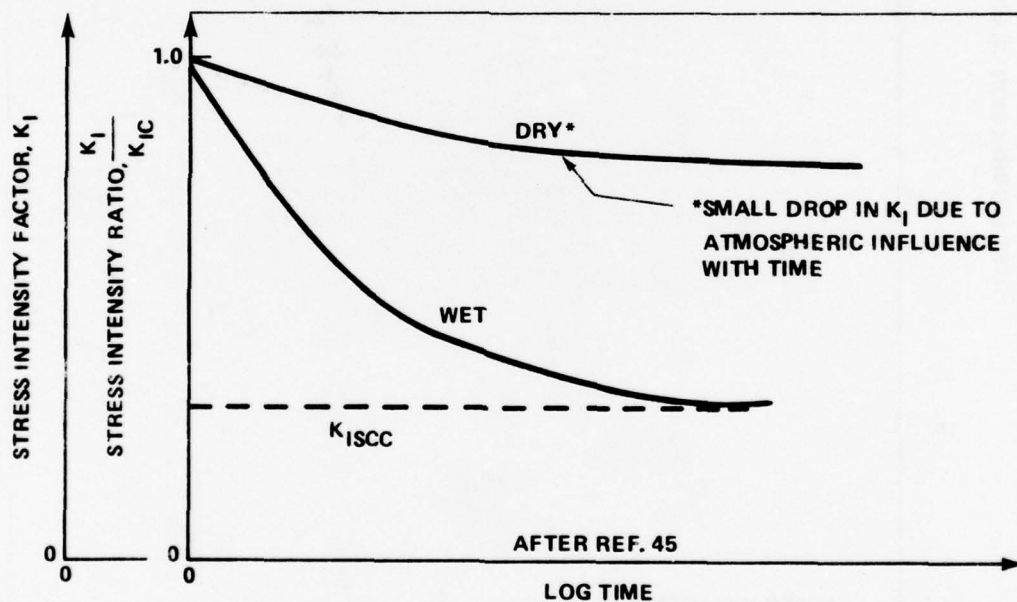


Figure 5.13. Delayed failure due to stress corrosion cracking in an aggressive environment.

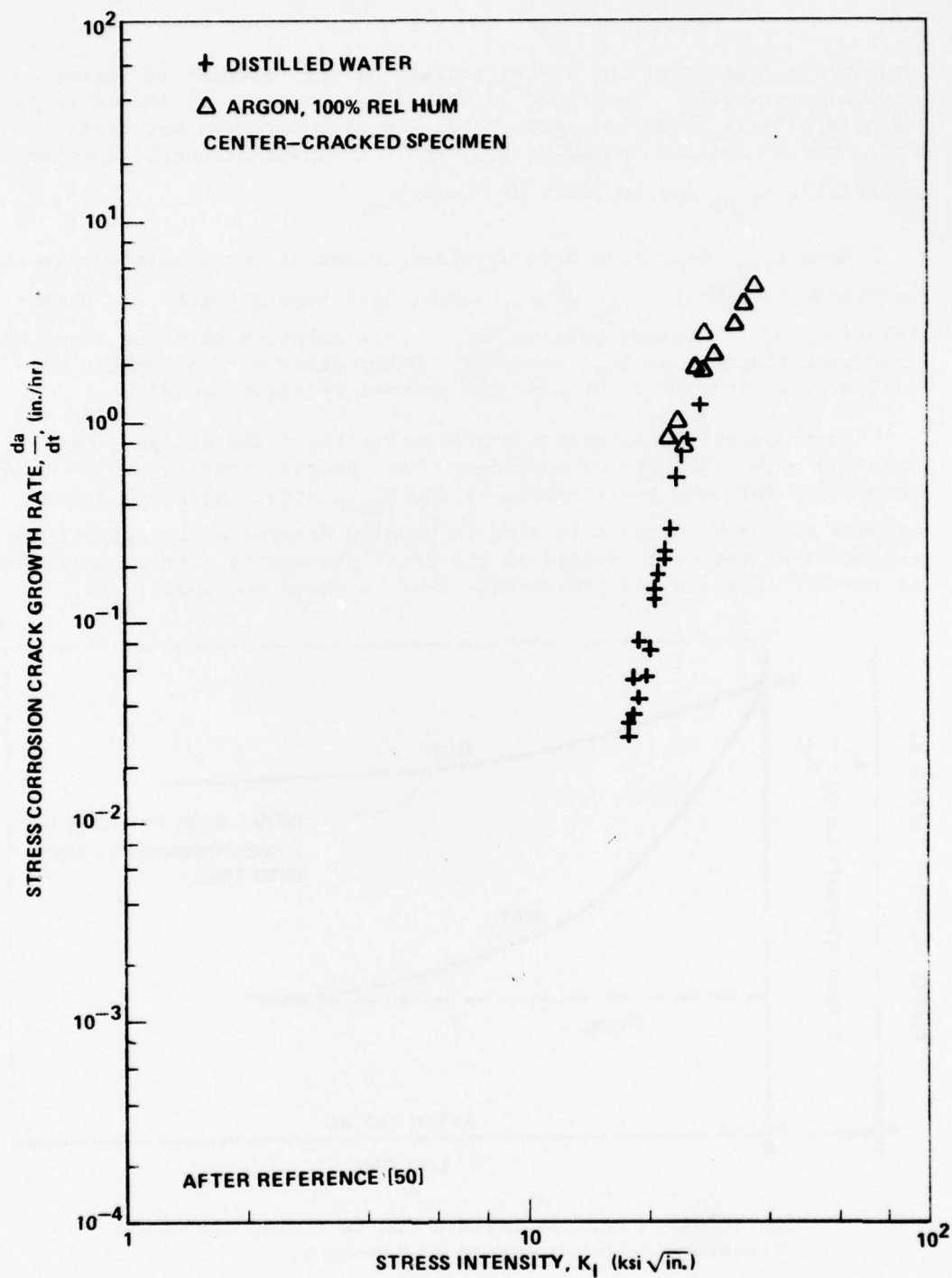


Figure 5.14. Sustained load crack growth rate data for H-11 steel in distilled water and humid argon.



## Chapter 6. DESIGN APPLICATIONS OF FRACTURE MECHANICS

In design, the fail safe philosophy requires that during the service life of a structure, any fatigue cracks, defects, or damage will not lead to failure prior to detection during regular inspection periods. This means that a structure containing readily detectable damage or cracks will retain sufficient residual strength to provide safe service upon subsequent load history. Thus, concern is for the remaining strength of a structural member in the presence of an existing crack. Fracture mechanics provides the technique for making such strength calculations. Coupled with nondestructive testing and reliable inspection techniques, fracture analysis can help ensure the integrity of an engineering structure.

Several example design problems follow. Some are concerned with only residual strength calculations; others involve fracture-resistance comparisons and selection of materials. In the illustrations, frequent use will be made of the crack solutions which appear in Chapter 7. Some of the problems have been selected from Wilhelm [45] and Wessel [73]; others have been devised under the guidance of these publications. The problems are for illustrative purposes only, and should be used only as guides. Each engineering problem will have its own unique features and solution. The values of fracture toughness used here may not correspond to the proper values required for a particular problem and environment. One should select the appropriate fracture toughness data such as  $K_{IC}$ ,  $K_C$ , and  $da/dn$  from the Damage Tolerant Design Handbook [50] or, if this is not possible, obtain the data from a testing program as outlined in Chapter 5.

### 6.1 Residual Strength of a Center-Cracked Panel [45]

It is assumed here that a simple rectangular aluminum panel uniformly loaded in tension across the width (Figure 6.1) will develop a central through-the-thickness crack 4 inches long before detection by the established inspection routine (it is noted that although this crack geometry occurs infrequently, it provides a good illustrative example). The material is 7075-T6 aluminum having a thickness,  $B$ , of 0.100 inch. The problem is to determine if the panel will fail at an operating stress of 45 ksi before crack detection. It is decided to analyze the panel using a plane-stress toughness value. Figure 5.3 indicates that for this thickness  $K_C \approx 85 \text{ ksi-}\sqrt{\text{in.}}$ .

The solution for the panel is

$$K_I = \sigma \sqrt{\pi a} f\left(\frac{a}{b}\right) \quad (6.1)$$



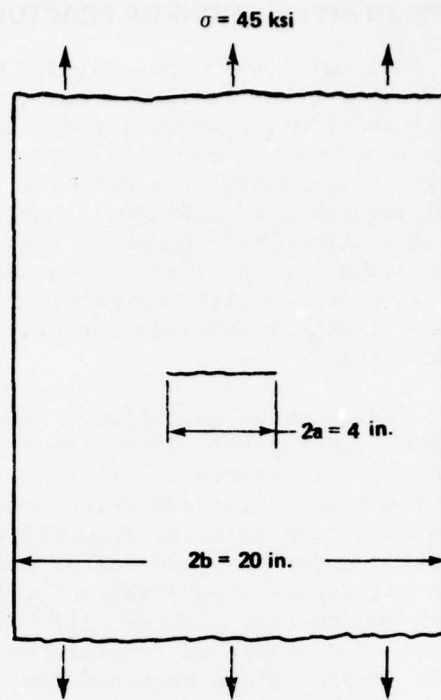


Figure 6.1. Center-cracked aluminum panel.

where  $f\left(\frac{a}{b}\right)$  is a finite width correction factor. Solving for stress,

$$\sigma = \frac{K_I}{\sqrt{\pi a} f\left(\frac{a}{b}\right)} .$$

Let critical conditions apply; i.e.,  $K_I \rightarrow K_c$ ,  $\sigma \rightarrow \sigma_c$ , and  $a \rightarrow a_c$ :

$$\sigma_c = \frac{K_c}{\sqrt{\pi a_c} f\left(\frac{a}{b}\right)} .$$

Determine  $f\left(\frac{a}{b}\right)$ . The crack aspect ratio is

$$\frac{a}{b} = \frac{2 \text{ in.}}{10 \text{ in.}} = 0.2 .$$

From Table 3.1,  $f\left(\frac{a}{b}\right) \approx 1.03$  for this aspect ratio. Then

$$\sigma_c = \frac{K_c}{\sqrt{\pi a_c} f\left(\frac{a}{b}\right)} = \frac{85 \text{ ksi} \sqrt{\text{in.}}}{\sqrt{\pi(2 \text{ in.})} 1.03} = 33 \text{ ksi}$$

This critical stress would be reduced by 20% to 30% if crack buckling takes place. Thus, the sheet can sustain a gross area stress which is less than 33 ksi in the presence of a 4-inch-long crack. Because this is 27% below the required operating stress (45 ksi), the requirements are not met.

From this illustration, a change in inspection schedule to detect a crack smaller than 4 inches or a reduction of operating stress level or both is indicated.

## 6.2 Strength of a Bracket with Cracks Emanating from a Hole

A proposed design for a bracket contains a 0.5-inch-diameter hole (Figure 6.2). It is anticipated that a fatigue crack will grow from the hole to a length of 0.25 inch before detection by inspection. The bracket is loaded with a remote stress of 52 ksi. The material data follow:

- a) Material: 4340, oil quenched, tempered at 500°F
- b) Material yield strength  $\sigma_{ys} = 238 \text{ ksi}$
- c) Material fracture toughness:  $K_{IC} = 46 \text{ ksi-in.}^{1/2}$

Can the design be considered to be a safe one? To answer this question the critical stress will be calculated. It will be conservative to assume that a crack develops from both sides of the hole. The problem then becomes the one shown in the inset of Figure 6.2.

Any stress intensity factor solution for this problem must reflect both the presence of the free surface of the hole and the finite width of the bracket. For cases such as this, an approximate solution can often be developed by applying separate correction factors for the various free surfaces. Let  $f_1\left(\frac{a}{R}\right)$  be the correction factor for the hole and  $f_2\left(\frac{a_e}{b}\right)$  be a correction factor for the finite width of the plate. The quantity  $a_e$  is an effective crack length for computing the finite width correction. Apply corrections for both effects by writing  $K_I$  in the form

$$K_I = \sigma \sqrt{\pi a} f_1\left(\frac{a}{R}\right) f_2\left(\frac{a_e}{b}\right) \quad (6.2)$$

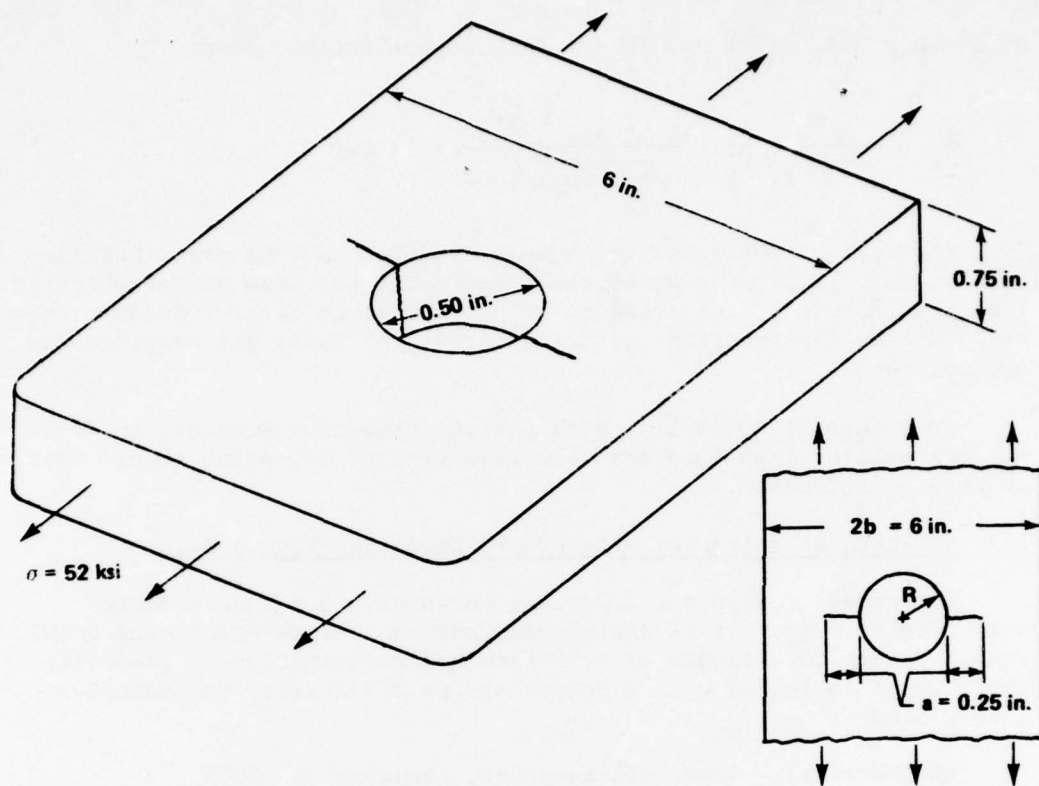


Figure 6.2. Bracket containing a hole.

This is clearly an approximation since it neglects any interaction of the two effects. Such a procedure is common practice and is normally sufficiently accurate for design calculations.

Returning to the problem at hand, compute the ratio  $\frac{a}{R}$

$$\frac{a}{R} = \frac{0.25 \text{ inch}}{0.25 \text{ inch}} = 1.0$$

From Bowie's solution (Figure 7.17)

$$f_1\left(\frac{a}{R}\right) = 1.45$$

For computing the finite width correction, an effective crack length  $a_e$  of  $a + R$  will be used. Thus,

$$\frac{a_e}{b} = \frac{a + R}{b} = \frac{0.25 \text{ in.} + 0.25 \text{ in.}}{3 \text{ in.}} = 0.167$$

From Table 3.1,

$$f_2\left(\frac{a_e}{b}\right) = 1.02$$

Solving Equation (6.2) for the stress and letting critical conditions apply, one has

$$\sigma_c = \frac{K_{IC}}{\sqrt{\pi a_c} f_1\left(\frac{a}{R}\right) f_2\left(\frac{a_e}{R}\right)}$$

$$\sigma_c = \frac{46 \text{ ksi} \sqrt{\text{in.}}}{\sqrt{\pi(0.25 \text{ in.})} (1.45)(1.02)} = 35 \text{ ksi}$$

Since the critical stress is well below the imposed load of 52 ksi, the design will not tolerate an inspectable crack.

It is interesting to investigate the maximum crack length which could be tolerated by this design. Solve Equation (6.2) for the crack size and assume critical conditions at the imposed stress of 52 ksi.

$$a_c = \frac{1}{\pi} \left[ \frac{K_{IC}}{\sigma_c f_1\left(\frac{a}{R}\right) f_2\left(\frac{a+R}{b}\right)} \right]^2$$

This gives the solution for the maximum crack length. However, the hole correction  $f_1$  and the width correction  $f_2$  are both a function of crack length. For this crack geometry, estimates can be made for  $f_1$  and  $f_2$ . As  $\frac{a+R}{b} \rightarrow 0$ ,  $f_2 \rightarrow 1.00$ . Assume  $f_2 \approx 1.00$ . For the hole correction factor,  $f_1$ , assume  $f_1 \approx 3.39$ , which corresponds to  $\frac{a}{R} = 0$ . After calculating  $a_c$  one can determine revised estimates for  $f_1$  and  $f_2$  and iterate:



$$a_c = \frac{1}{\pi} \left[ \frac{46 \text{ ksi} \sqrt{\text{in.}}}{(52 \text{ ksi})(3.39)(1.00)} \right]^2 = 0.0217 \text{ in.}$$

check

$$\frac{a}{R} = \frac{0.0217}{0.25} = 0.088$$

for which, from Figure 7.17,

$$f_1 = 2.81$$

Also

$$\frac{a + R}{b} = \frac{0.0217 + 0.25}{3} = 0.091$$

for which, from Table 3.1

$$f_2 = 1.00$$

Calculating  $a_c$  again

$$a_c = \frac{1}{\pi} \left[ \frac{46 \text{ ksi} \sqrt{\text{in.}}}{(52 \text{ ksi})(2.81)(1.00)} \right]^2 = 0.032 \text{ in.}$$

Three more such iterations finally lead to the following critical crack length:

$$a_c = 0.038 \text{ in.}$$

This is a very short crack length and could perhaps correspond to a nick caused by a tool at the hole edge; therefore, a re-evaluation of the design is inevitable.

In a situation similar to this, Wilhelm [45] lists four possible design modifications. They are:

- a) Reduce allowable operating stress.
- b) Reduce hole diameter.
- c) Use a different material (higher  $K_{IC}$ ).
- d) Reduce plate thickness and still meet stress criteria.



Functional constraints may prohibit reducing the hole diameter. The fourth alternative would be possible for some materials. By reducing the plate thickness, one takes advantage of the material's ability to deform plastically which results in higher values of fracture toughness. For the present material though, it is felt that a moderate reduction in thickness would not significantly improve the fracture toughness, and for a thickness reduction, a wider bracket would be required to meet stress criteria. In this case, probably, the best solution is to select a different material having a higher toughness, which also may have a lower operating stress due to a lower yield strength. This attacks the real weakness of the present design; i.e., a low toughness steel ( $K_{IC} = 46 \text{ ksi } \sqrt{\text{in.}}$ ) with a high yield strength ( $\sigma_{ys} = 238 \text{ ksi}$ ) which permitted a high operating stress.

### 6.3 Cracked Bar Loaded in Bending

An arm, loaded in bending as shown in Figure 6.3, is assumed to develop a crack as shown. A force P of either 2000 or 4000 pounds is applied at the center. Two aluminum alloys are being considered:

2219-T851 ( $K_{IC} = 35.8 \text{ ksi } \sqrt{\text{in.}}$ ) and 2124-T851 ( $K_{IC} = 28.8 \text{ ksi } \sqrt{\text{in.}}$ ).

If a 1/4-inch deep crack can be detected during inspection, which of the two materials would be the most fracture resistant for the two loads under consideration?

The stress-intensity factor solution for this problem is shown in Figure 7.46 for span length-to-depth ratios,  $s/b$ , of 4 and 8, and also for the case of pure bending. Also note that this solution is for a beam of unit thickness. The solution is (allowing for the thickness B):

$$K_I = \frac{6M}{Bb^2} \sqrt{\pi a} F\left(\frac{a}{b}\right) \quad (6.3)$$

where M is the bending moment. In this case

$$\frac{s}{b} = \frac{12 \text{ in.}}{2 \text{ in.}} = 6$$

$$\frac{a}{b} = \frac{0.25 \text{ in.}}{2 \text{ in.}} = 0.125$$

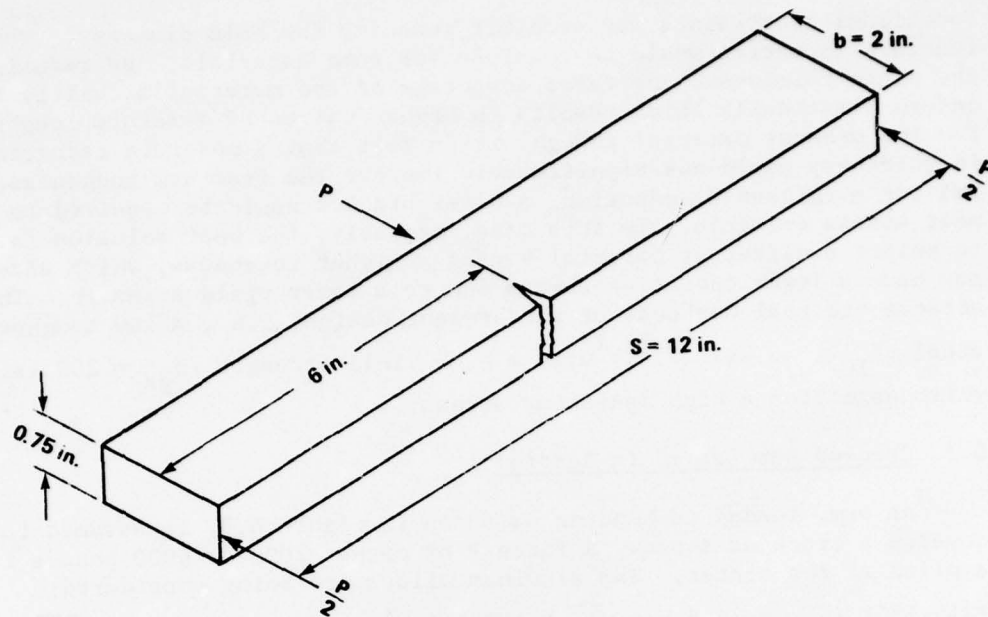


Figure 6.3. Cracked bar loaded in bending.

and the correction factor from Figure 7.46 is

$$F\left(\frac{a}{b}\right) = \frac{0.81}{\left(1 - \frac{a}{b}\right)^{3/2}} = \frac{0.81}{(1 - 0.125)^{3/2}} = 0.99$$

For the 2000-pound force,

$$M = \frac{Ps}{4} = \frac{(2000 \text{ lb})(12 \text{ in.})}{4} = 6000 \text{ in.-lb}$$

and for the 4000-pound force

$$M = 12,000 \text{ in.-lb}$$

Calculate  $K_I$

$$K_I = \frac{6 (6000 \text{ in.-lb})}{(0.75 \text{ in.})(2 \text{ in.})^2} \sqrt{\pi(0.25 \text{ in.})} (0.99)$$

$$= 10.53 \text{ ksi} - \sqrt{\text{in.}} \text{ (for } P = 2000 \text{ lb)}$$

and

$$K_I = 21.2 \text{ ksi} - \sqrt{\text{in.}} \text{ (for } P = 4000 \text{ lb)}$$

Compare these calculated values of the stress-intensity factor to the plane-strain fracture toughness values.

Material	$K_{IC}$ (ksi $\sqrt{\text{in.}}$ )	$\frac{K_I}{K_{IC}}$ (2000 lb)	$\frac{K_I}{K_{IC}}$ (4000 lb)
2219-T851	35.8	0.29	0.59
2124-T851	28.8	0.36	0.73

For the 2000-pound load, either of the two materials might be considered acceptable since the  $K_I/K_{IC}$  ratio is fairly low for both. For the 4000-pound load, a greater difference is apparent and the 2219-T851 alloy would be preferred.

#### 6.4 Evaluation of Materials Based on $K_{IC}$ Data and Design Requirements - Surface Flaw [73]

Three materials - a steel, aluminum, and titanium - are to be compared for a particular application. One of the primary considerations is minimum weight, and the yield strengths of the three materials have been chosen so that their strength-to-weight ratios are equivalent. The allowable stress is to be one-half of the yield stress. The material properties are as follows:

Alloy	Density (lb/in. <sup>3</sup> )	$\sigma_{ys}$ (ksi)	$\sigma_{ys}/\text{Density}$ (x 1000 in.)	$K_{IC}$ (ksi $\sqrt{\text{in.}}$ )
Steel	0.234	250	880	100
Aluminum	0.098	85	870	30
Titanium	0.163	140	860	80

A typical flaw is judged to be a semielliptical surface flaw (Figure 6.4) with a depth to half-length ratio  $\left(\frac{a}{c}\right)$  of 0.4.

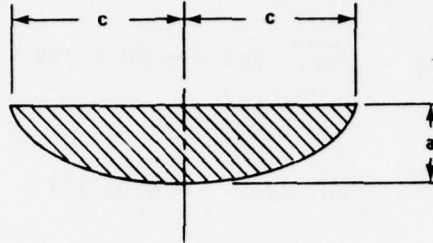


Figure 6.4. Semielliptical surface flaw to be used in a materials evaluation.

The basic solution for the surface flaw is the Irwin Solution Equation (3.33). This solution has been widely used, both for analysis and for fracture toughness testing. It does not contain a correction for the back-side free surface of the plate, and hence is not valid if the flaw is "deep;" i.e., if the flaw-depth-to-plate-thickness ratio is greater than 0.5. Consequently, numerous corrections to Equation (3.33) have been developed, some based on results of tests, others based on analytical solutions. The Shah-Kobayashi solution [74] (Figure 7.74) is an analytical solution which applies to a wide range of flaw aspect ratios  $\left(\frac{a}{c}\right)$  and flaw-depth-to-plate-thickness ratios. It essentially agrees with the Irwin Solution for long, shallow flaws. It should be noted that the Irwin solution classically contains a

plasticity correction (the  $0.212 \frac{\sigma^2}{\sigma_{ys}^2}$  term) which is not included in

Figure 7.74. For precision, one should use the Shah-Kobayashi solution; however, because of its simplicity, the Irwin solution will be used here for illustrative purposes. The Irwin solution is:

$$K_I = \frac{1.1 \sigma \sqrt{\pi a}}{\left[ E^2 - 0.212 \left( \frac{\sigma}{\sigma_{ys}} \right)^2 \right]^{1/2}} .$$

To calculate the critical flaw size, solve the above for  $a$  and let critical conditions apply:

$$a_c = \frac{K_{IC}^2 \left[ E^2 - 0.212 \left( \frac{\sigma}{\sigma_{ys}} \right)^2 \right]}{1.21 \pi \sigma^2}$$

or

$$a_c = \frac{K_{IC}^2 Q}{1.21 \pi \sigma^2} \quad (6.4)$$

where  $Q = E^2 - 0.212 \left( \frac{\sigma}{\sigma_{ys}} \right)^2$  is the flaw shape parameter. It is

recalled that  $E$  is the elliptic integral of the second kind. Values of  $E$  are given in Table 7.1. The quantity  $Q$  can be obtained from the graph of Figure 7.73 or calculated from the above equation. For illustrative purposes the latter method will be used. Calculate the modulus of the elliptic integral

$$k = \sqrt{1 - \left( \frac{c}{a} \right)^2}$$

$$k = \sqrt{1 - (0.4)^2} = 0.9165$$

From the Table 7.1,  $E = 1.15$  and  $E^2 = 1.32$ . Thus,  $Q = 1.32 - 0.212 \left( \frac{\sigma}{\sigma_{ys}} \right)^2$ .

The allowable stress is  $\sigma = 0.5 \sigma_{ys}$ . Therefore,

$$Q = 1.32 - 0.212 (0.5)^2 = 1.27$$

Substituting into Equation (6.4),

$$a_c = \frac{1.27 K_{IC}^2}{1.21 \pi \sigma^2}$$



The following results are tabulated for the three materials:

<u>Material</u>	$\sigma_{All} (= 0.5\sigma_{ys})$ (ksi)	$K_{IC}$ (ksi $\sqrt{\text{in.}}$ )	$a_{cr}$ (in.)	Length (in.)
Steel	125	100	0.212	1.06
Aluminum	42.5	30	0.165	0.83
Titanium	70	80	0.432	2.16

For the conditions imposed, the titanium alloy is the most fracture resistant. This conclusion could have been reached by considering the ratio  $K_{IC}/\sigma_{ys}$  for the following materials:

<u>Material</u>	$\frac{K_{IC}}{\sigma_{ys}}$	$\left(\frac{K_{IC}}{\sigma_{ys}}\right)^2$
Steel	0.400	0.160
Aluminum	0.353	0.125
Titanium	0.572	0.327

The titanium, having the highest  $K_{IC}/\sigma_{ys}$  ratio, could be expected to be the toughest material. Since the applied stress is a fixed percentage of  $\sigma_{ys}$  for all the materials, the critical defect size will be proportional to the ratio  $(K_{IC}/\sigma_{ys})^2$ . All other terms in Equation (6.4) are constant, therefore  $(K_{IC}/\sigma_{ys})^2$  provides a good index to the relative critical defect size.

Assume that with inspection techniques the minimum detectable flaw is 0.15-inch deep by 0.75-inch long. Calculate the critical stress for fracture from

$$\sigma = \frac{K_{IC} \left[ E^2 - 0.212 \left( \frac{\sigma}{\sigma_{ys}} \right)^2 \right]^{1/2}}{\sqrt{1.21 \pi a}}$$

This is conveniently done by iteration (because of the  $0.212 \sigma^2/\sigma_{ys}^2$  term), which converges very rapidly. The results are:

<u>Material</u>	<u><math>\sigma_c</math></u> <u>(ksi)</u>
Steel	148
Aluminum	45
Titanium	115

Note: These values differ slightly from those in Reference 73.

With this information, the designer can now re-evaluate his original choice of a design stress equivalent to one-half of the yield strength. With assurance that a defect of the type used in the foregoing can be reliably detected in the component, the designer can proceed to establish the safety factor in his design. The steel looks better at first since it requires the highest stress for fracture in the presence of a flaw. To assess the safety factor, however, one must consider the ratio of the critical stress to the design stress ( $1/2 \sigma_{ys}$ ). Results are:

<u>Material</u>	<u><math>\sigma_{ys}</math></u> <u>(ksi)</u>	<u><math>\sigma_{ALL}</math></u> <u>(ksi)</u>	<u><math>\sigma_c</math></u> <u>(ksi)</u>	<u><math>\frac{\sigma_c}{\sigma_{ALL}}</math></u>
Steel	250	125	148	1.18
Aluminum	85	42.5	45	1.06
Titanium	140	70	115	1.64

Thus, the titanium provides the greatest safety factor and resistance to fracture. Steel and aluminum are marginal. The designer could alter the design stress for each of the materials to provide whatever safety factor is desired. Any decrease in the design stress to raise the factor of safety, however, would result in an increase in weight.

#### 6.5 Eccentric Crack Growing from a Rivet Hole [45]

A crack, starting at the rivet hole (Figure 6.5) has grown to a length of 3 inches prior to being detected. The panel is made of 7075-T6 aluminum with a plane-stress fracture toughness of approximately  $85 \text{ ksi} \cdot \sqrt{\text{in}}$ . The operating stress is 30 ksi. What are the critical conditions for fracture for this crack geometry and loading and should the panel be replaced?

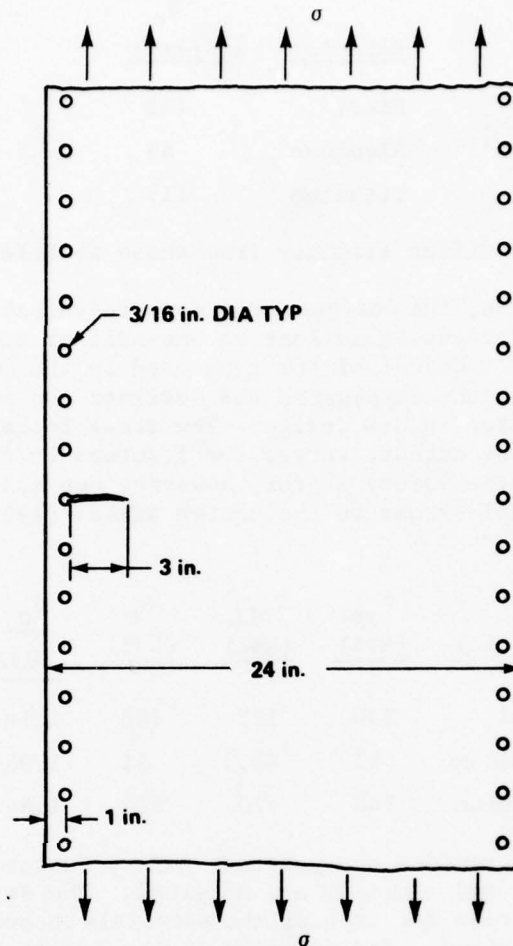


Figure 6.5. Crack growing from an edge rivet hole.

In solving this problem, the restraining effect of the adjoining panels or stiffeners to which the panel is riveted will be ignored. (Panels with stiffeners will be considered in the next example.) This problem can be treated in an appropriate manner by simplifying it to a panel containing an eccentric crack of length

$$2a_e \approx a + d = 3.1875 \text{ in.}$$

for a 3 16-inch rivet hole. Figure 7.39 provides the solution for this problem which includes both the eccentricity and finite plate width effect,

$$K_I = \sigma \sqrt{\pi a} F \left( \frac{a}{b_1}, \frac{e}{b} \right) \quad (6.5)$$

where  $b$  is plate half-width and  $e$  is eccentricity. A correction factor  $F$  is provided for both crack tips; however, in this problem it is assumed that the crack tip at the rivet hole will not grow through the hole; hence, only the inside tip must be considered. Determine the crack aspect ratio and the normalized eccentricity:

$$\frac{a_e}{b_1} = \frac{3.1875/2}{1.5 + 1 + 0.1875/2} = 0.61 = \frac{a_e}{a + 1 + \frac{d}{2}}$$

$$\frac{e}{b} = \frac{12.0 - 2.59}{12.0} = \frac{9.40}{12.0} = 0.78$$

From Figure 7.39, the correction factor  $F$  is

$$F = 1.11$$

Let critical conditions apply

$$K_I \rightarrow K_c, \sigma \rightarrow \sigma_c, a \rightarrow a_c$$

Then,

$$\sigma_c = \frac{K_c}{\sqrt{\pi a_c} F \left( \frac{a_c}{b_1}, \frac{e}{b} \right)}$$

$$\sigma_c = \frac{85 \text{ ksi } \sqrt{\text{in.}}}{\sqrt{\pi(1.594 \text{ in.})} 1.11}$$

$$\sigma_c = 34.2 \text{ ksi}$$

Hence, the panel is fracture-safe under the 30 ksi operating stress as long as the other end of the crack remains stopped at the rivet hole.

The easiest way to approach the second part of the problem is to plot the stress-crack length history; i.e., compute and plot the critical stress for a number of assumed crack lengths. The results are shown in Table 6.1 and Figure 6.6.

TABLE 6.1. CRITICAL STRESS FOR VARIOUS CRACK LENGTH FOR  
PANEL GEOMETRY OF FIGURE 6.5

$2a_e$ (in.)	$a_e$ (in.)	$b_1 = \frac{2a_e - 0.1875}{2} + 1$ (in.)	$\frac{a_e}{b_1}$	$e = 12 - b_1$ (in.)	$\frac{e}{b}$	F	$\sigma_c$ (ksi)
1	0.5	1.406	0.36	10.594	0.88	1.04	65.2
2	1.0	1.906	0.52	10.094	0.84	1.08	44.4
3	1.5	2.406	0.62	9.594	0.80	1.12	35.0
4	2.0	2.906	0.69	9.094	0.76	1.16	29.2
6	3.0	3.906	0.77	8.094	0.67	1.24	22.3
8	4.0	4.906	0.82	7.094	0.59	1.32	18.2
10	5.0	5.906	0.85	6.094	0.51	1.39	15.4
12	6.0	6.906	0.87	5.094	0.42	1.46	13.4
14	7.0	7.906	0.88	4.094	0.34	1.52	11.9
16	8.0	8.906	0.90	3.094	0.26	1.59	10.7

Figure 6.6 shows that up to a crack length of about 4.0 inches the panel would be fracture safe. An effective crack length of 4 inches corresponds to a physical crack length of 3.81 inches growing from the edge of the hole.



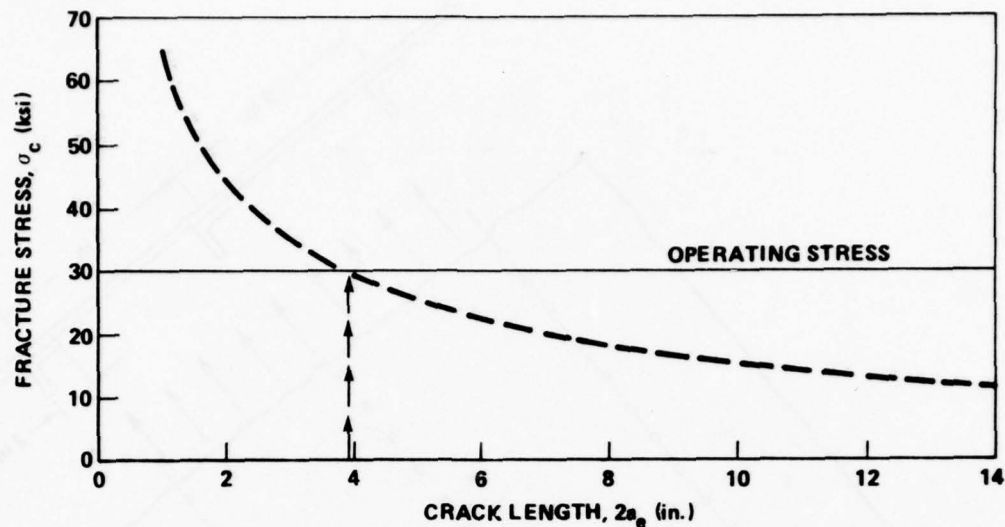


Figure 6.6. Critical fracture stress for panel geometry of Figure 6.5.

#### 6.6 Crack in a Stiffened Panel [45]

Figure 6.7 shows a built-up structure consisting of a skin stiffened by a number of stringers riveted to the skin. A crack grows from one of the rivet holes as shown. The fracture stress of the panel will be investigated for various assumed crack lengths. It is assumed that the 9-inch bars are repeated and that the crack grows in a symmetric manner. To solve this problem, it is necessary to separate it into two parts:

- a) A center-cracked, edge-stiffened sheet with the center stiffener removed.
- b) The effect of the center stiffener.

Consider the center-cracked, edge-stiffened problem. The geometry of Figure 6.8 applies. In the solutions of Figures 7.65 through 7.69, the edge stiffeners are considered as integral; however, it is felt that the rivets introduce negligible error for crack aspect ratios  $\leq 0.8$ . As the crack approaches the edge stiffeners, the influence of these stiffeners predominates and the crack geometry of Figure 6.9 applies.

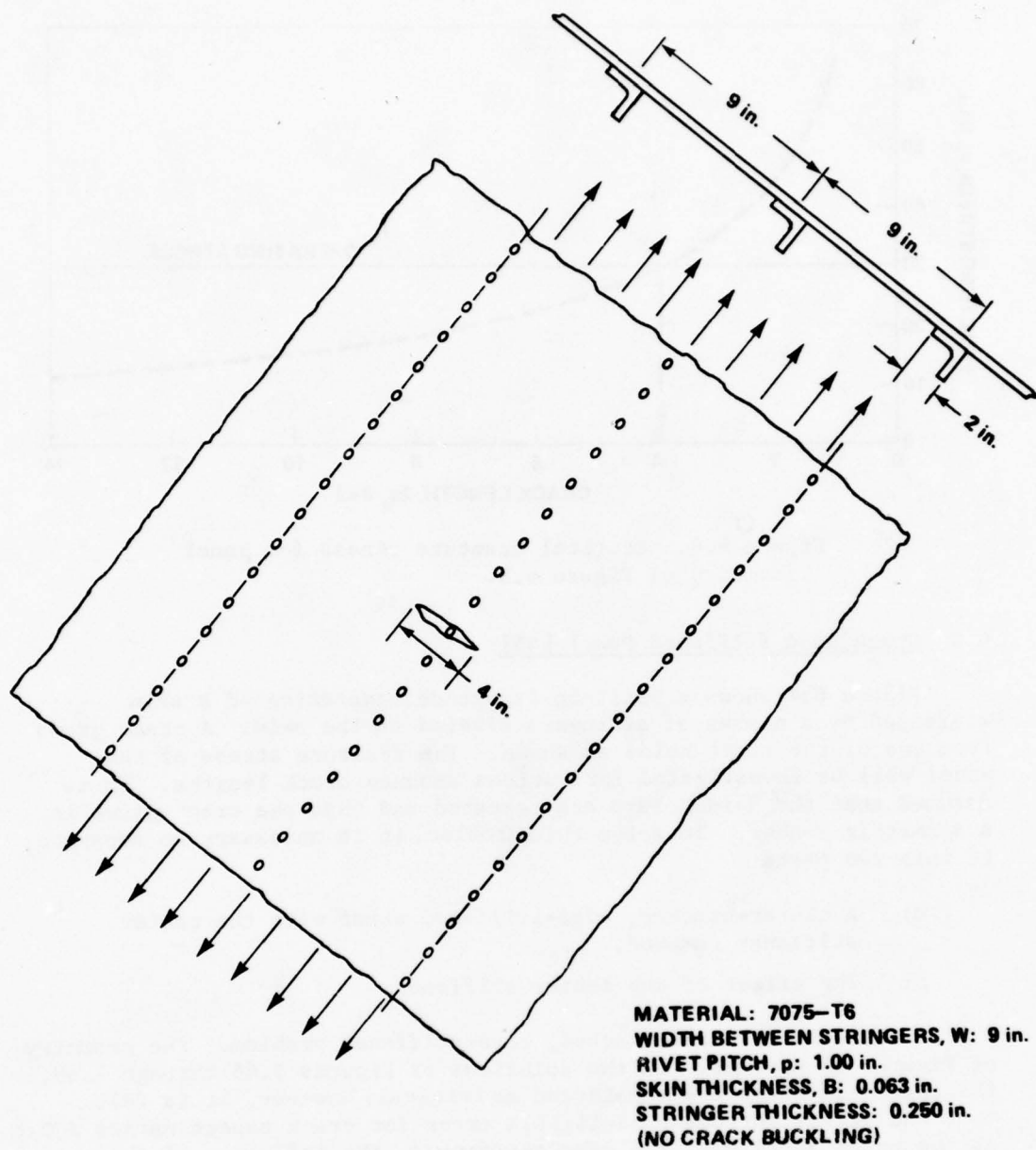


Figure 6.7. Stiffened panel with a crack.

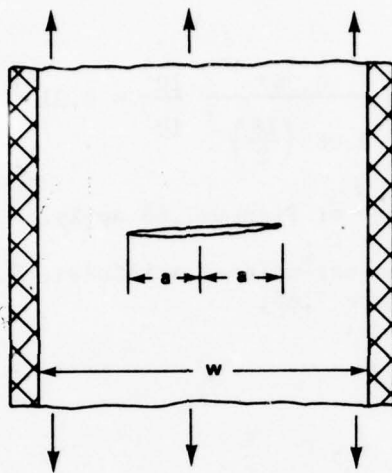


Figure 6.8. Center-cracked edge-stiffened panel.

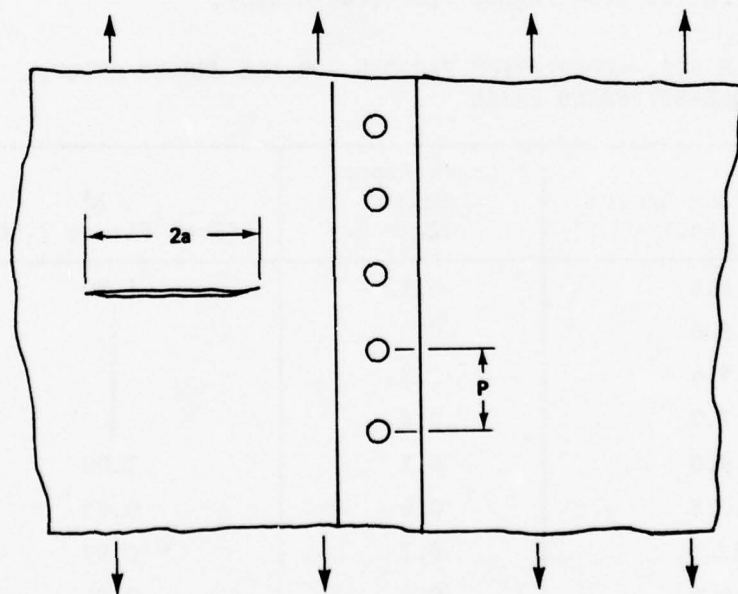


Figure 6.9. Crack tip approaching a stiffener.

Step 1: Determine  $\alpha$ , the nondimensional inertia parameter. In this case,  $I_z$ , the moment of inertia of the edge stiffener (2-inch angle, 1/4-inch thick) about the stringer neutral axis perpendicular to the plane of the skin, is

$$I_z = 0.347 \text{ in.}^4$$

$$\alpha = \frac{I_z}{B \left( \frac{w}{2} \right)^3} \frac{E_{\text{str}}}{E} = \frac{0.347}{0.063 \left( \frac{18}{2} \right)^3} \frac{10^7}{10^7} \approx 0.01$$

and the correction factors of Figure 7.66 apply.

Step 2: Compute the extensional stiffness,  $S$ , for the finite width, cracked strip. From Figure 7.66,

$$S = \frac{A_{\text{str}}}{B \left( \frac{w}{2} \right)} \frac{E_{\text{str}}}{E}$$

$$S = \frac{0.25 (2 + 1.75)}{0.063 \left( \frac{18}{2} \right)} \frac{10^7}{10^7} = 1.65$$

Step 3: Prepare a table of correction factors ( $\lambda'$ ) for various crack aspect ratios from Figure 7.66 (Table 6.2).

TABLE 6.2. CORRECTION FACTORS FOR THE CENTER-CRACK, EDGE-STIFFENED PANEL

Total Crack Length 2a (in.)	Crack Aspect Ratio 2a/w	$\lambda'$ (From Figure 7.66)
1.8	0.1	1.00
3.6	0.2	↓
5.4	0.3	
7.2	0.4	
9.0	0.5	
10.8	0.6	0.98
12.6	0.7	0.97
14.4	0.8	0.91

As the crack approaches the edge stiffeners,  $2a/w > 0.8$ , Figure 7.66 does not apply. The problem, however, approximates that of a non-symmetric crack approaching a riveted stiffener, the geometry of Figure 6.9.

Step 4: Determine the correction factors as the crack goes through the edge stringer areas and beyond (Figures 7.63 and 7.64). Compute the stiffness ratio  $S'$  and the ratio of crack length to rivet pitch for crack aspect ratios  $> 0.8$  (Table 6.3).

TABLE 6.3. CORRECTION FACTORS FOR A CRACK TIP PASSING THROUGH A STIFFENER AREA

$\frac{2a}{w}$	$S' = \frac{2a}{A_{str}} \frac{B}{E_{str}}$	$\left(\frac{a}{p'}\right)$ (Note 1)	$\lambda''$ (Note 2)
0.9	1.09	4.05	0.7
1.0	1.21	4.50	0.45
1.1	1.33	4.95	0.28
1.2	1.45	5.40	0.32

Note 1: The crack is assumed to grow through a rivet hole, thus effectively doubling the rivet pitch,  $p' = 2p$ .

Note 2: From Figures 7.63 and 7.64.

Figure 6.10 shows the correction factors for various values of  $2a/w$ . It is apparent that the stiffening effect of the edge stringers decreases the stress intensity factor sharply as the crack tip passes through the stiffener area.

Step 5: The second part of this problem involves accounting for the effect of the center stringer on the stress intensity factor. This can be done by using the solution of either Figure 7.61 or Figure 7.62, depending on whether the crack passes through a rivet hole. Figures 7.61 and 7.62 were computed for a Poisson's ratio of 0.33 and a rivet-diameter-to-rivet-pitch ratio of  $d/2p = 0.1$ . The correction factor, however, is insensitive to variations in this ratio. Since it is here assumed that the crack grows from a rivet hole, Figure 7.62 will be used. The resulting correction factors are shown in Table 6.4.

Step 6: Multiply the correction factors in Tables 6.2 and 6.3 with those in Table 6.4 to obtain combined correction factors,  $\lambda^*$  or  $\lambda^{**}$ . These are shown in Table 6.5.



TABLE 6.4. CORRECTION FACTORS FOR CENTER STRINGER

$\frac{2a}{w}$	$S = \frac{2(a B)}{A_{str}} \frac{E}{E_{str}}$	$\frac{a}{P}$	$\lambda'''$
0.1	0.12	0.9	0.73
0.2	0.24	1.8	0.68
0.3	0.36	2.7	0.68
0.4	0.48	3.6	0.675
0.5	0.60	4.5	0.67
0.6	0.73	5.4	0.67
0.7	0.85	6.3	0.67
0.8	0.97	7.2	0.675
0.9	1.09	8.1	0.67
1.0	1.21	9.0	0.68
1.1	1.33	9.9	0.68
1.2	1.45	10.8	0.68

TABLE 6.5. COMBINED CORRECTION FACTORS

$\frac{2a}{w}$	$\lambda^* = \lambda' \times \lambda'''$	$\lambda^{**} = \lambda'' \times \lambda'''$
0.1	0.73	-
0.2	0.68	-
0.3	0.68	-
0.4	0.675	-
0.5	0.67	-
0.6	0.66	-
0.7	0.65	-
0.8	0.61	-
0.9	-	0.47
1.0	-	0.31
1.1	-	0.19
1.2	-	0.22

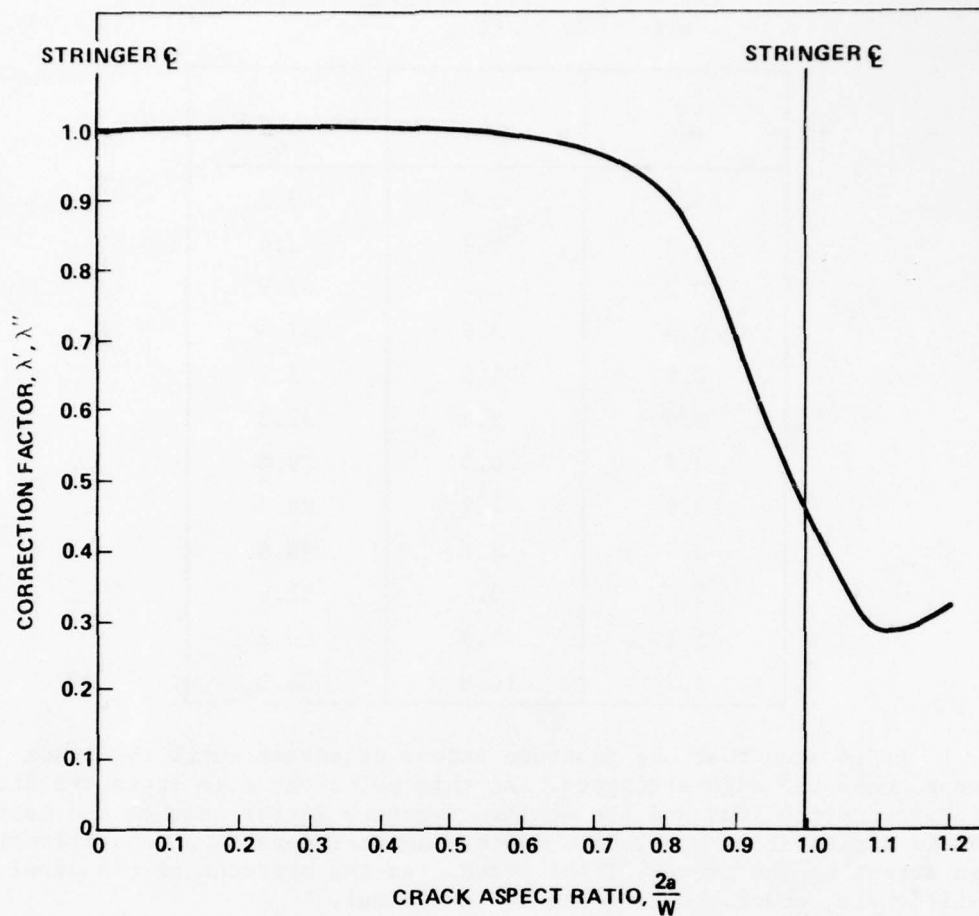


Figure 6.10. Correction factors for symmetrically cracked plate with stiffened edges.

Step 7: With the correction factors known, it is now possible to solve for the critical stress. One must have a value of  $K_c$  for the particular material and thickness under consideration. For illustration purposes, a value of  $K_c = 85 \text{ ksi} - \sqrt{\text{in.}}$  will be used. The critical stress is computed from

$$\sigma_c = \frac{K_c}{\sqrt{\pi a_c} (\lambda^* \text{ or } \lambda^{**})}$$

Results are shown in Table 6.6 and in graphical form on Figure 6.11.

TABLE 6.6. CRITICAL STRESS FOR A STIFFENED PANEL

$\frac{2a}{w}$	a	$\sigma_c$
0.1	0.9	69.2
0.2	1.8	52.6
0.3	2.7	42.9
0.4	3.6	37.4
0.5	4.5	33.7
0.6	5.4	31.3
0.7	6.3	29.4
0.8	7.2	29.3
0.9	8.1	35.8
1.0	9.0	51.6
1.1	9.9	80.2
1.2	10.8	66.3

It is seen that the fracture stress decreases until the crack approaches the edge stringers. At this point the edge stringers start to pick up the load and the maximum fracture stress reaches the material yield stress at  $2a/w \approx 1.05$ . Hence, the stringers should be effective in arresting the growth of the crack. In the presence of the panel stiffeners, crack buckling should be minimal.

#### 6.7 Fatigue Life of an Edge Crack

An edge crack of 1-inch length has developed in the 20-inch-wide panel as shown in Figure 6.12. The plate thickness is 0.100 inch and the material is 7075-T6 aluminum. In this example the plane-stress fracture toughness  $K_{Ic}$  for this thickness is assumed to be 68 ksi-in.<sup>1/2</sup>.

The operating cyclic stress of the part is sinusoidal with a maximum stress of 25 ksi and a minimum of 7.5 ksi (R of 0.3). How many cycles will be allowed before critical conditions prevail?

Write the stress intensity factor as

$$K_I = \lambda \sigma \sqrt{\pi a} \quad .$$

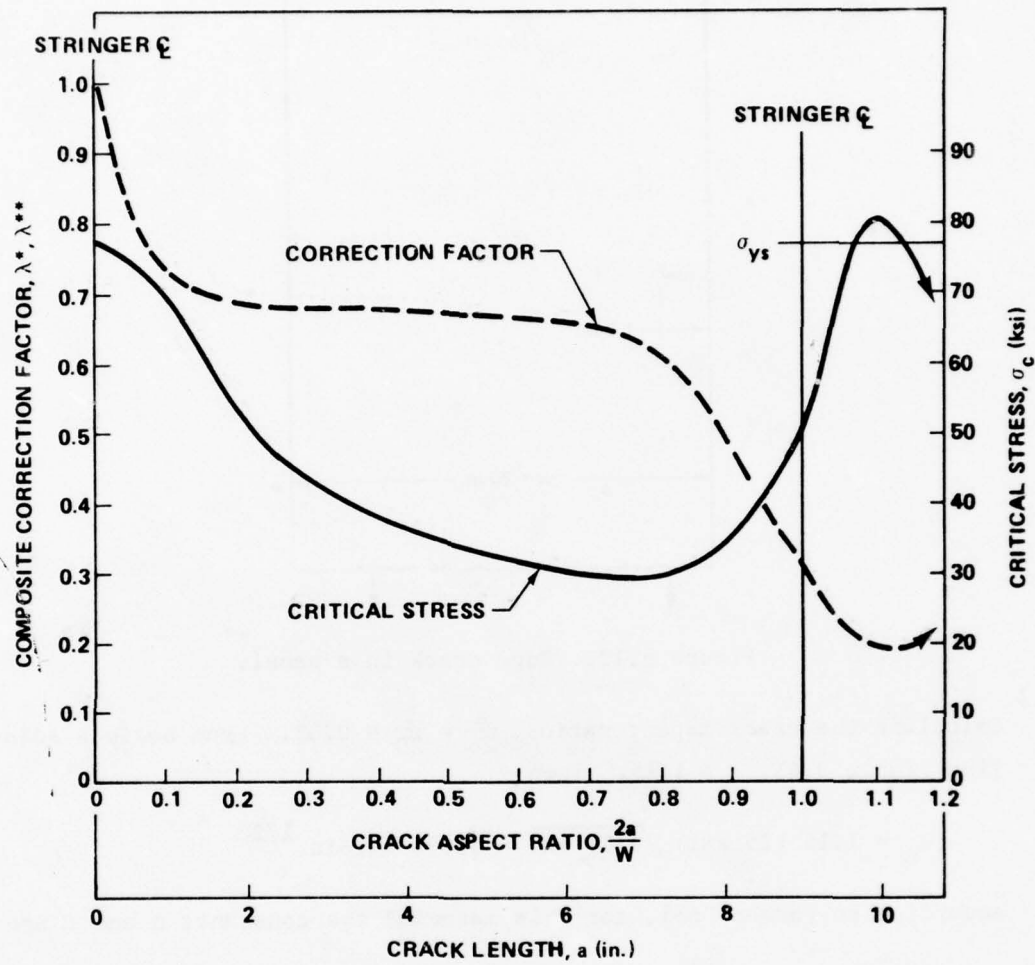


Figure 6.11. Composite correction factors and critical stress for problem of Figure 6.7 (no crack buckling).

Assume that  $\lambda$ , the finite width correction factor, is a constant during the crack propagation. Then, Equation (5.16), which was for  $\lambda = 1$ , is modified slightly to

$$N_c - N_o = \frac{2}{\lambda^2 \pi C (1 - R)^2 \sigma^2} \left[ \frac{K_c}{K_o} - 1 - \ln \frac{K_c}{K_o} \right] \quad (6.6)$$

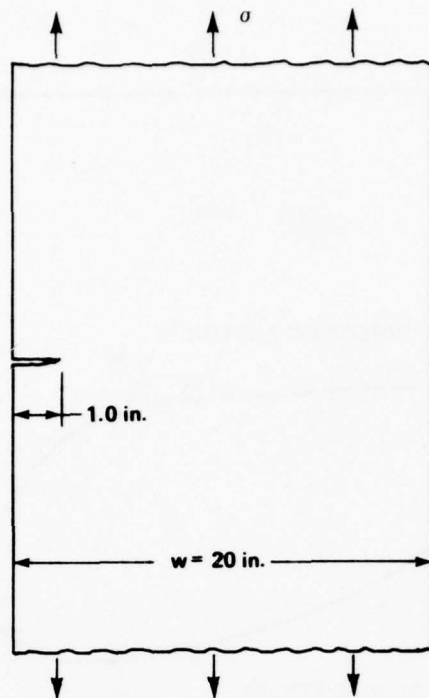


Figure 6.12. Edge crack in a panel.

Calculate the crack aspect ratio:  $\frac{a}{2b} = \frac{1}{20} = 0.05$ . From Bowie's solution (Table 3.4),  $\lambda = 1.15$ . Then

$$K_o = 1.15 (25 \text{ ksi}) \sqrt{\pi(1) \text{ in.}} = 50.95 \text{ ksi-in.}^{1/2}$$

According to Forman [66], for this material the constants  $n$  and  $C$  are:

$$n = 3$$

$$C = 5 \times 10^{-13}$$

From Equation (6.6),

$$N_c - N_o = \frac{2}{(1.15)^2 \pi (5 \times 10^{-13}) (1 - 0.3)^2 (25,000)^2}$$

$$\left[ \frac{68,000}{50,950} - 1 - \ln \frac{68,000}{50,950} \right]$$

$$N_c - N_o = 144 \text{ cycles.}$$



Thus, for a sinusoidal loading of 25 ksi maximum, the 1.0-inch crack will approach critical conditions in approximately 144 cycles. This is a rather low remaining life. A low value is not unexpected since  $K_0 = 50.95 \text{ ksi} \cdot \sqrt{\text{in.}}$  approaches the critical value of  $68.0 \text{ ksi} \cdot \sqrt{\text{in.}}$

The above is only an estimate, since the geometric correction factor  $\lambda$  changes slightly as the crack grows, and the above applies only if  $\lambda$  is a constant.

Estimate the change in  $\lambda$  during the fatigue crack growth by estimating  $\lambda$  when the crack reaches the critical length  $a_c$ .

$$K_c = \beta \sigma \sqrt{\pi a_c}$$

or

$$a_c = \frac{K_c^2}{\lambda^2 \sigma^2 \pi}$$

$$a_c = \frac{(68,000)^2}{(1.15)^2 (25,000)^2 \pi} = 1.78 \text{ in.}$$

Crack aspect ratio  $\frac{a}{2b} = \frac{1.78}{20} = 0.089$ . From Bowie's solution (Table 3.4),  $\lambda \approx 1.19$ . Therefore,  $\lambda$  changes only slightly (from 1.15 to 1.19) during the crack growth from  $a_0$  to  $a_c$ . In light of material variability, the noted results of 144 cycles are probably sufficiently accurate for an engineering estimate. For estimating the fatigue life of flaws in specimens of more complex geometry, one should use a computer-assisted numerical integration as in the report by Engle [72].

## Chapter 7. COMPENDIUM OF STRESS INTENSITY FACTORS

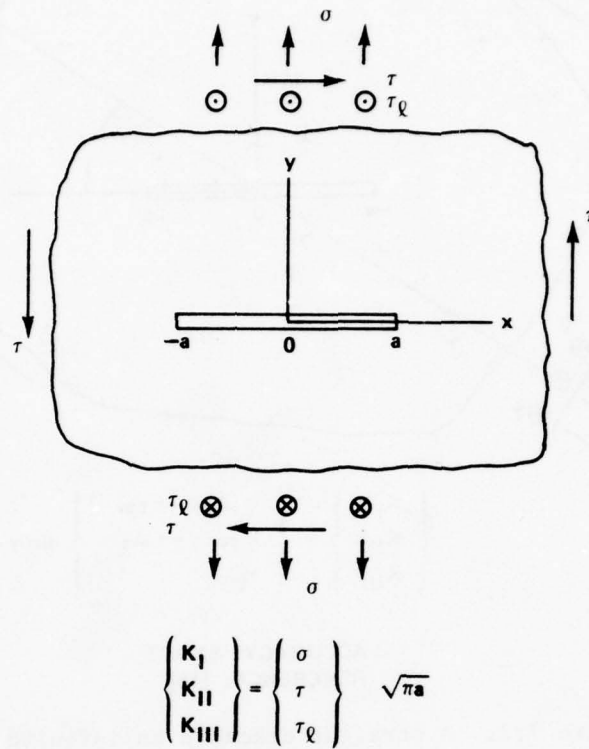
The following is a collection of stress intensity factor solutions. It is not a comprehensive collection. In the interest of brevity, solutions are limited only to those judged to be of potential usefulness to the designer. Thus, many solutions, though elegant and ingenious, thought primarily to be of academic or research interest, are not included here.

Solutions included are from several sources; however, most of them have been included in other collections. Sources of stress intensity factors which may be of additional usefulness to the designer are ASTM STP 381 [11], the handbook by Tada [15], the book on three-dimensional solutions by Parmeter [75], and the design manual by Wilhelm [45]. Most of the solutions included here have been included in one of the above. Therefore, most of the references given in the following will refer to one of the above source books rather than the original paper which contained the solution.

Because the solutions included here were taken from several sources, the notation may occasionally vary from that of the other chapters. Where departures occur, an attempt has been made to include sketches and explanations with the solutions explaining the meanings of the various symbols.

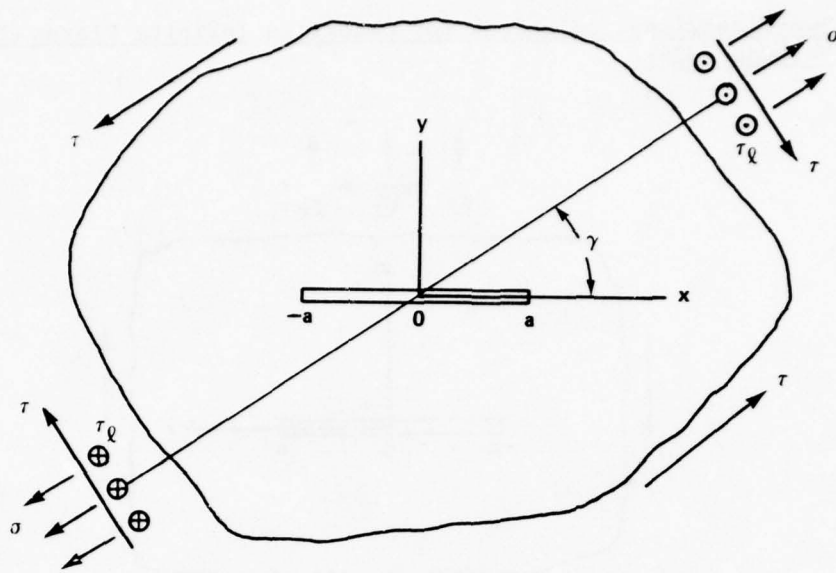
It should be noted that in two-dimensional solutions when a concentrated force appears in the solution, the force should be taken to be force per unit thickness, i.e., lb/in. Similarly, a concentrated in-plane moment means moment per unit thickness, i.e., inch-lb/inch.

7.1 Two-Dimensional Solutions for Cracks in Infinite Plates (Figures 7.1 Through 7.24)



ACCURACY: EXACT  
REFERENCES: [11, 15]

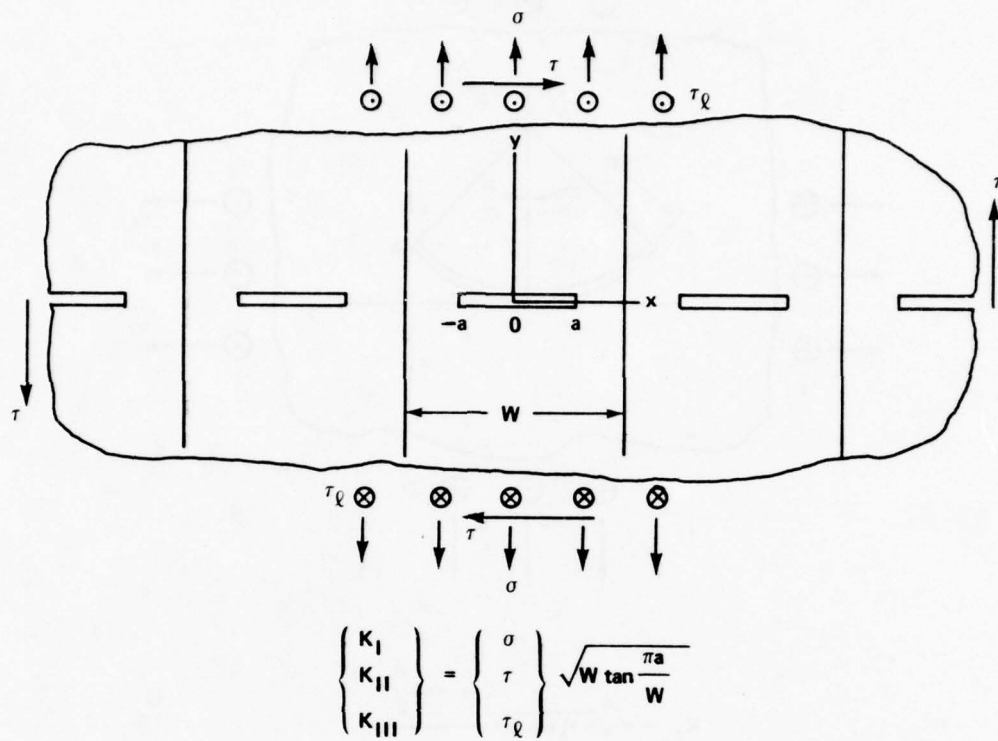
Figure 7.1. A straight crack in an infinite plate.



$$\begin{Bmatrix} K_I \\ K_{II} \\ K_{III} \end{Bmatrix} = \begin{Bmatrix} \sigma \sin \gamma - \tau \cos \gamma \\ \sigma \cos \gamma + \tau \sin \gamma \\ \tau \end{Bmatrix} \sin \gamma \cdot \sqrt{\pi a}$$

ACCURACY: EXACT  
REFERENCE: [15]

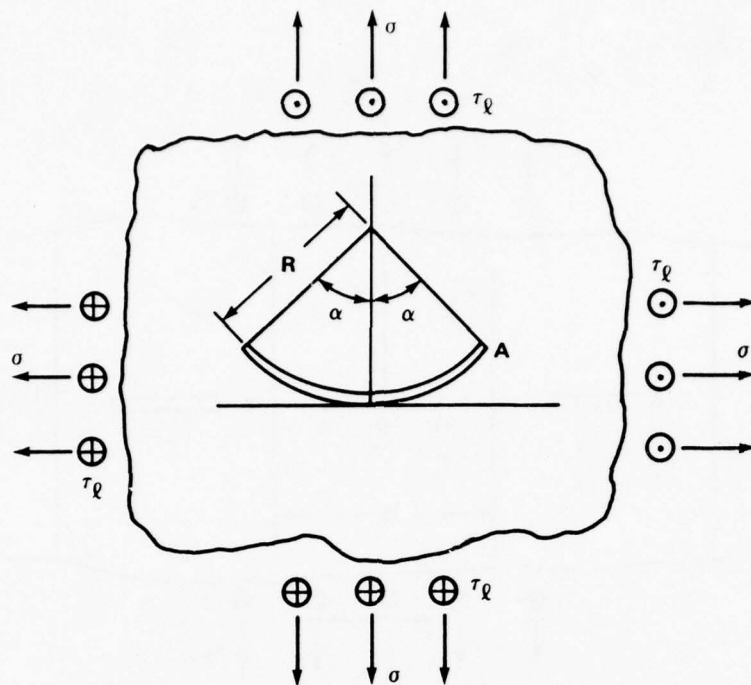
Figure 7.2. A straight crack in an infinite plate with skew loading.



ACCURACY: EXACT  
REFERENCES: [11, 15]

Figure 7.3. An infinite array of collinear cracks in an infinite plate.





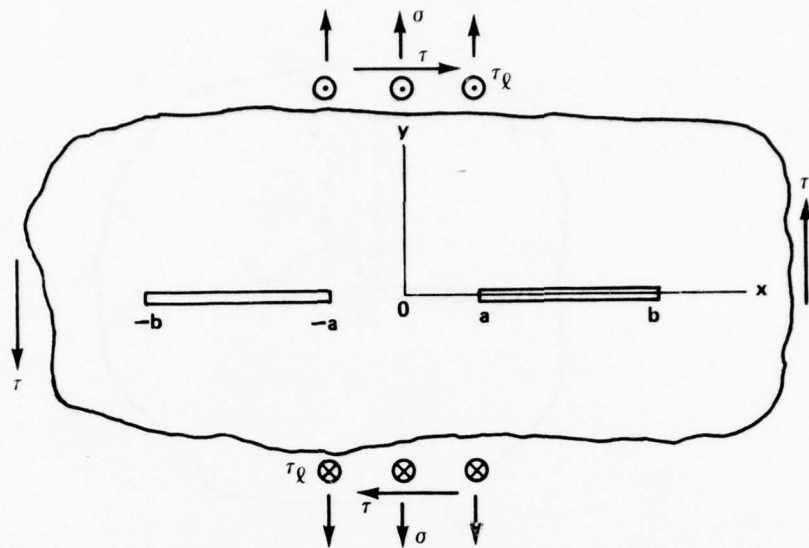
$$K_{I A} = \sigma \sqrt{\pi R \sin \alpha} \cdot \frac{\cos \frac{\alpha}{2}}{1 + \sin^2 \frac{\alpha}{2}}$$

$$K_{II A} = \sigma \sqrt{\pi R \sin \alpha} \cdot \frac{\sin \frac{\alpha}{2}}{1 + \sin^2 \frac{\alpha}{2}}$$

$$\begin{aligned} K_{III A} &= \tau_{\ell} \sqrt{\pi R \sin \alpha} \cdot \left( \cos \frac{\alpha}{2} - \sin \frac{\alpha}{2} \right) \\ &= (\sqrt{2} \tau_{\ell}) \sqrt{\pi R \sin \alpha} \cdot \sin \left( \frac{\pi}{4} - \frac{\alpha}{2} \right) \end{aligned}$$

**ACCURACY: EXACT**  
**REFERENCE [15]**

Figure 7.4. A circular-arc crack in an infinite plate.



$$\begin{aligned} \begin{Bmatrix} K_I \\ K_{II} \\ K_{III} \end{Bmatrix}_{\pm a} &= \begin{Bmatrix} \sigma \\ \tau \\ \tau_Q \end{Bmatrix} \sqrt{\pi a} \frac{b^2 \frac{E(k)}{K(k)} - a^2}{a \sqrt{b^2 - a^2}} \\ \begin{Bmatrix} K_I \\ K_{II} \\ K_{III} \end{Bmatrix}_{\pm b} &= \begin{Bmatrix} \sigma \\ \tau \\ \tau_Q \end{Bmatrix} \sqrt{\pi b} \frac{1}{k} \left\{ 1 - \frac{E(k)}{K(k)} \right\} \end{aligned}$$

WHERE  $k = \sqrt{1 - a^2/b^2}$

$$K(k) = \int_0^{\pi/2} \frac{d\varphi}{\sqrt{1 - k^2 \sin^2 \varphi}}$$

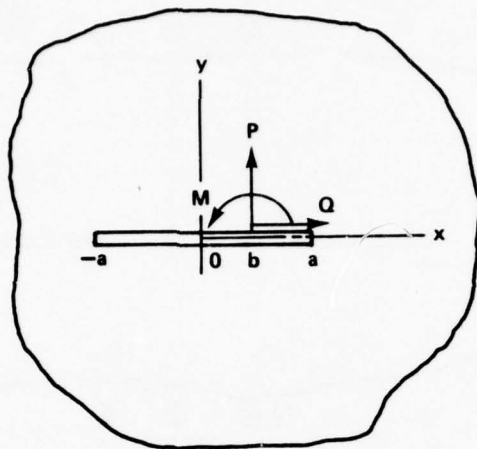
$$E(k) = \int_0^{\pi/2} \sqrt{1 - k^2 \sin^2 \varphi} d\varphi$$

(SEE TABLE 7.1, p. 193 FOR VALUES OF  $K(k)$  AND  $E(k)$ )

ACCURACY: EXACT

REFERENCES: [11, 15]

Figure 7.5. Two equal collinear cracks in an infinite plate.



$$K_I = \frac{1}{2\sqrt{\pi a}} \left\{ P \sqrt{\frac{a+b}{a-b}} + \left( \frac{\kappa-1}{\kappa+1} \right) Q + \frac{Ma}{(a-b)\sqrt{a^2-b^2}} \right\}$$

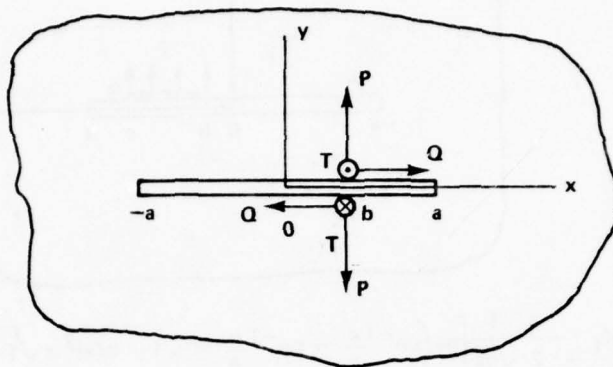
$$K_{II} = \frac{1}{2\sqrt{\pi a}} \left\{ Q \sqrt{\frac{a+b}{a-b}} - \left( \frac{\kappa-1}{\kappa+1} \right) P \right\}$$

WHERE

$$\kappa = \begin{cases} \frac{3-\nu}{1+\nu} & \text{PLANE STRESS} \\ 3-4\nu & \text{PLANE STRAIN} \end{cases}$$

ACCURACY: EXACT  
REFERENCE: [15]

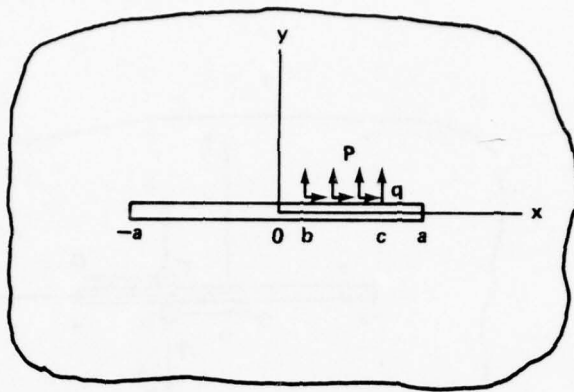
Figure 7.6. A straight crack in an infinite plate with concentrated force and concentrated moment applied to one surface.



$$\begin{pmatrix} K_I \\ K_{II} \\ K_{III} \end{pmatrix} = \frac{1}{\sqrt{\pi a}} \begin{pmatrix} P \\ Q \\ T \end{pmatrix} \sqrt{\frac{a \pm b}{a \mp b}}$$

ACCURACY: EXACT  
REFERENCE: [15]

Figure 7.7. A straight crack in an infinite plate with opposing forces applied to the two crack surfaces.



$$K_{I \pm a} = \frac{1}{2} \frac{1}{\sqrt{\pi a}} \left[ pa \left( \sin^{-1} \frac{c}{a} - \sin^{-1} \frac{b}{a} \mp \sqrt{1 - (c/a)^2} \pm \sqrt{1 - (b/a)^2} \right) + \left( \frac{\kappa - 1}{\kappa + 1} \right) q (c - b) \right]$$

$$K_{II \pm a} = \frac{1}{2} \frac{1}{\sqrt{\pi a}} \left[ qa \left( \sin^{-1} \frac{c}{a} - \sin^{-1} \frac{b}{a} \mp \sqrt{1 - (c/a)^2} \pm \sqrt{1 - (b/a)^2} \right) - \left( \frac{\kappa - 1}{\kappa + 1} \right) p (c - b) \right]$$

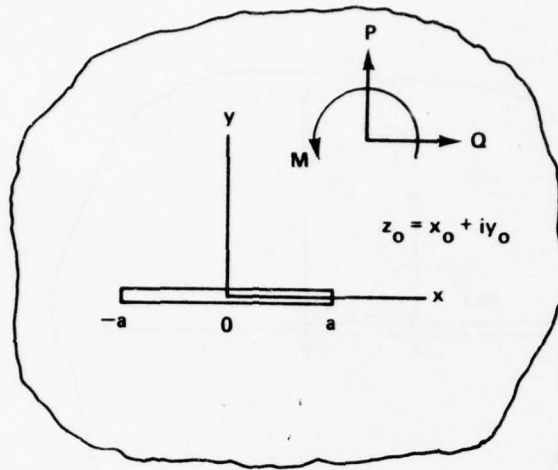
WHERE  $\kappa = \begin{cases} \frac{3 - \nu}{1 + \nu} & \text{PLANE STRESS} \\ 3 - 4\nu & \text{PLANE STRAIN} \end{cases}$

ACCURACY: EXACT

REFERENCES: [11, 15]

Figure 7.8. A straight crack in an infinite plate with distributed forces applied to one surface.





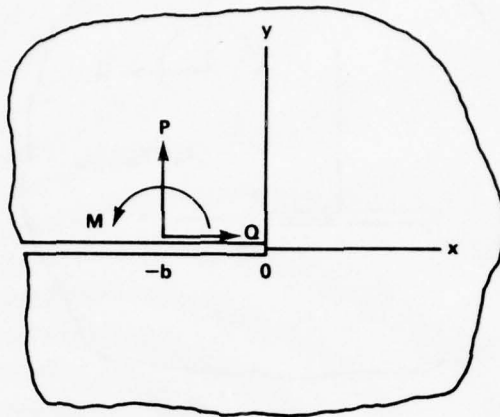
$$\begin{aligned}
 K_{+a} &= (K_I - iK_{II})_{+a} \\
 &= \frac{1}{2\sqrt{\pi a}} \frac{1}{\kappa + 1} \left\{ (Q + iP) \left[ \left( \frac{a + z_0}{\sqrt{z_0^2 - a^2}} - 1 \right) - \kappa \left( \frac{a + \bar{z}_0}{\sqrt{\bar{z}_0^2 - a^2}} - 1 \right) \right] \right. \\
 &\quad \left. + \frac{a [(Q - iP)(\bar{z}_0 - z_0) + i(1 + \kappa)M]}{(\bar{z}_0 - a)\sqrt{\bar{z}_0^2 - a^2}} \right\}
 \end{aligned}$$

WHERE

$$\kappa = \begin{cases} \frac{3 - \nu}{1 + \nu} & \text{PLANE STRESS} \\ 3 - 4\nu & \text{PLANE STRAIN} \end{cases}$$

ACCURACY: EXACT  
REFERENCES: [11, 15]

Figure 7.9. A straight crack in an infinite plate with remote concentrated moment and concentrated forces.

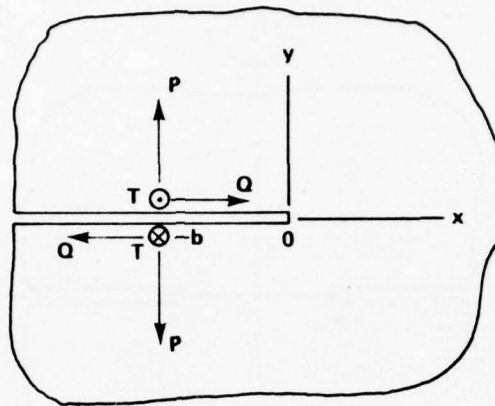


$$K_I = \frac{1}{\sqrt{2\pi b}} \left( P + \frac{M}{2b} \right)$$

$$K_{II} = \frac{1}{\sqrt{2\pi b}} Q$$

ACCURACY: EXACT  
REFERENCE: [15]

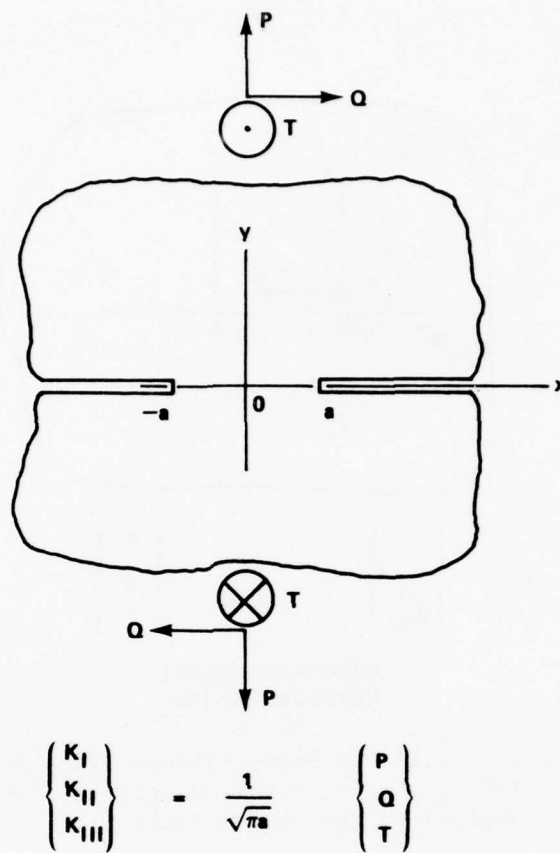
Figure 7.10. A semi-infinite crack in an infinite plate with concentrated forces and a concentrated couple applied to one surface.



$$\begin{Bmatrix} K_I \\ K_{II} \\ K_{III} \end{Bmatrix} = \frac{2}{\sqrt{2\pi b}} \begin{Bmatrix} P \\ Q \\ T \end{Bmatrix}$$

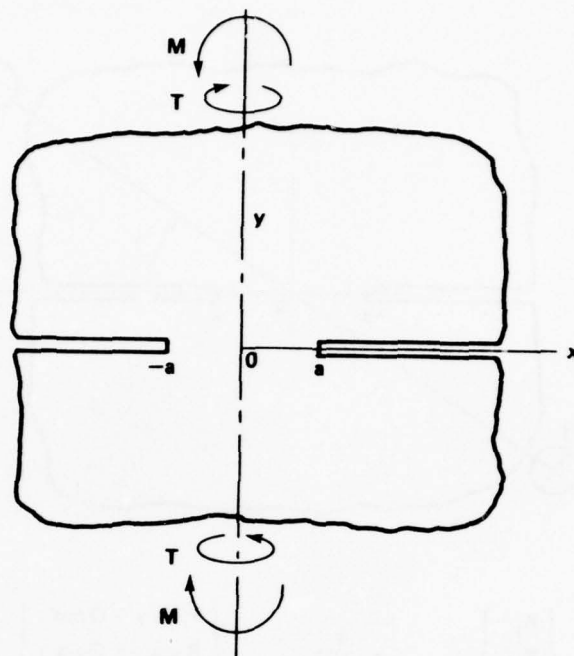
ACCURACY: EXACT  
REFERENCES: [15]

Figure 7.11. A semi-infinite crack in an infinite plate with concentrated forces applied to the two surfaces.



ACCURACY: EXACT  
REFERENCE: [15]

Figure 7.12. Two semi-infinite cracks in an infinite plate.

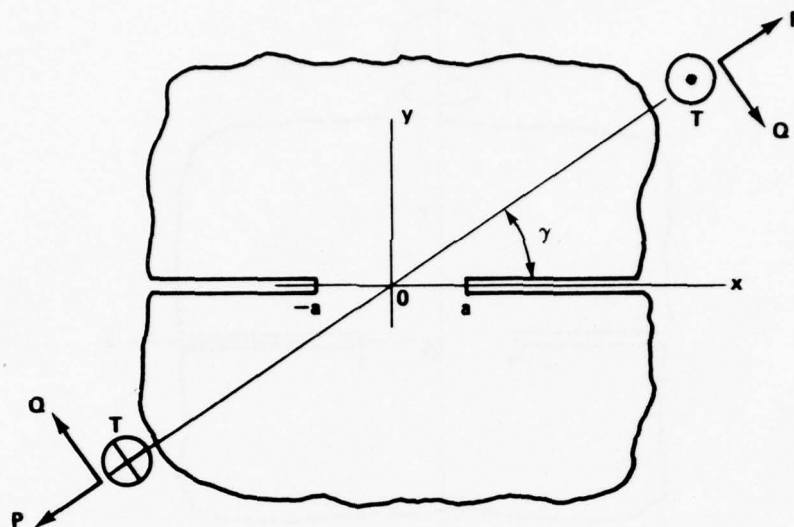


$$\begin{Bmatrix} K_I \\ K_{III} \end{Bmatrix}_{+a} = \frac{2}{a\sqrt{\pi a}} \begin{Bmatrix} M \\ T \end{Bmatrix}$$

ACCURACY: EXACT  
REFERENCE: [15]

Figure 7.13. Two semi-infinite cracks in an infinite plate with remote moments.

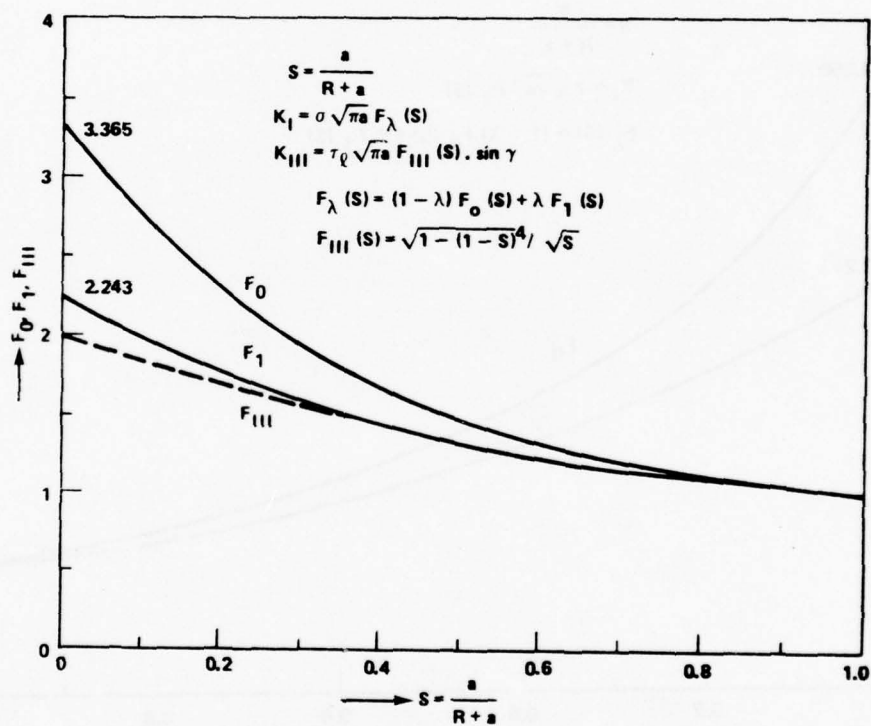
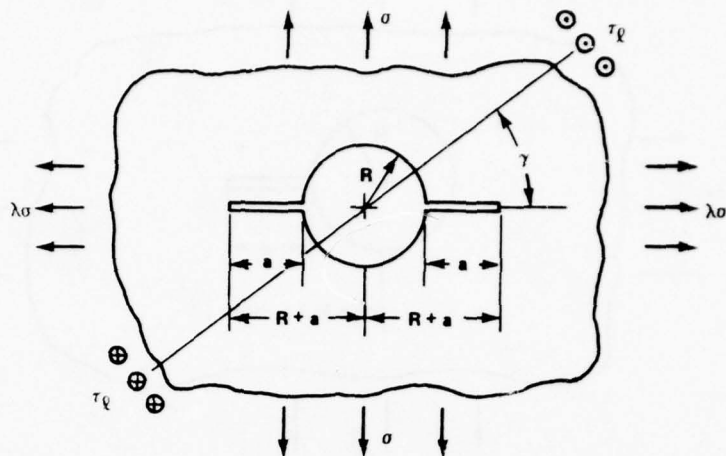




$$\begin{Bmatrix} K_I \\ K_{II} \\ K_{III} \end{Bmatrix} = \frac{1}{\sqrt{\pi a}} \begin{Bmatrix} P \sin \gamma - Q \cos \gamma \\ P \cos \gamma + Q \sin \gamma \\ T \end{Bmatrix}$$

ACCURACY: EXACT  
REFERENCE: [15]

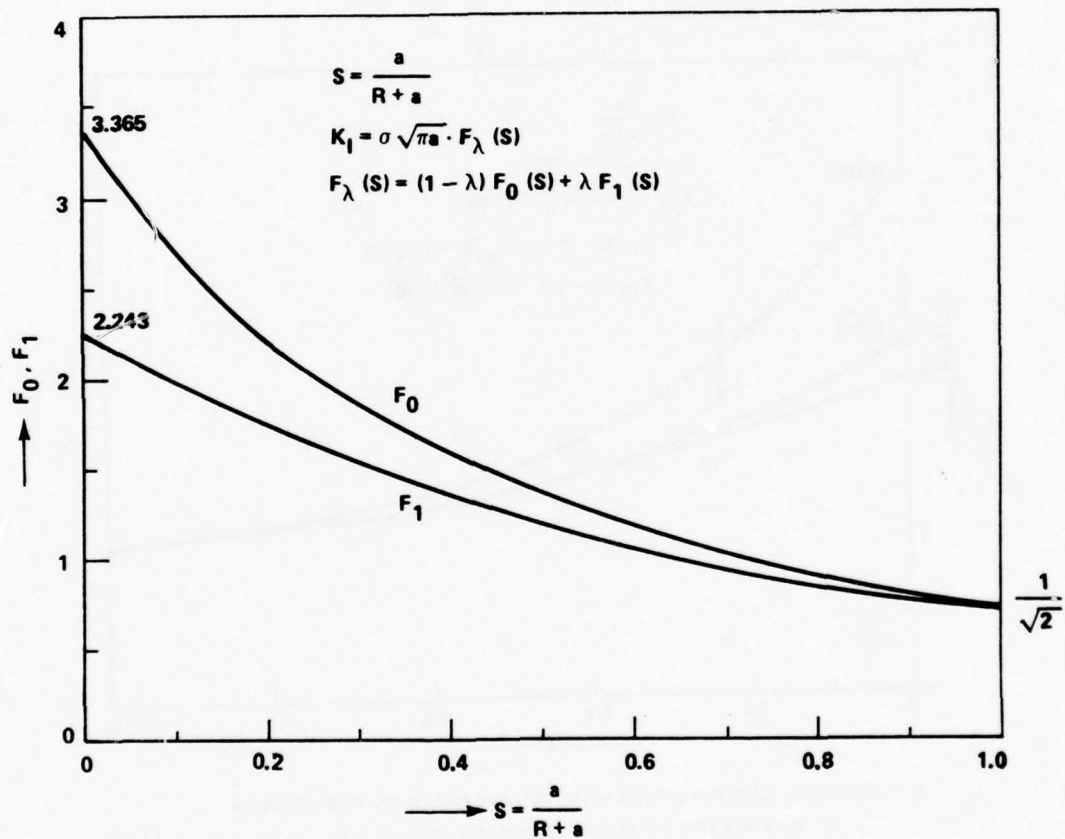
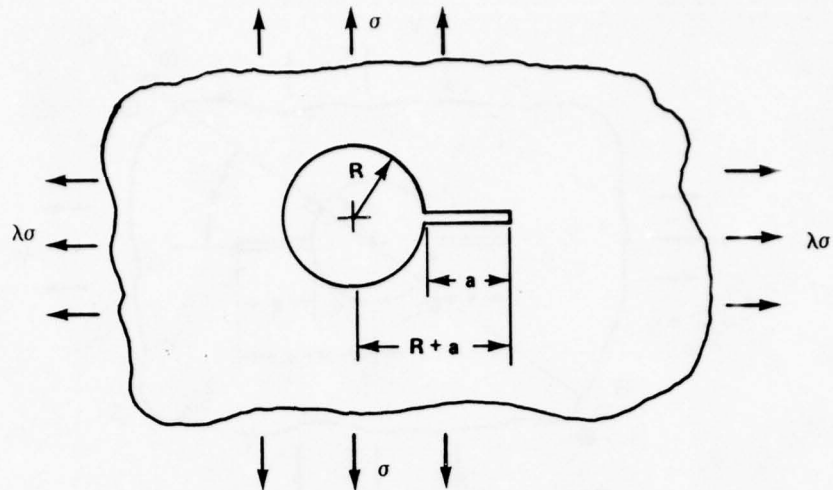
Figure 7.14. Two semi-infinite cracks in an infinite plate with skew loading.



ACCURACY:  $F_0$  AND  $F_1$  CURVES WERE DRAWN BASED ON THE RESULTS  
 HAVING THE EXPECTED ACCURACY OF 0.1% [15]  
 $F_{III}$ : EXACT [15]

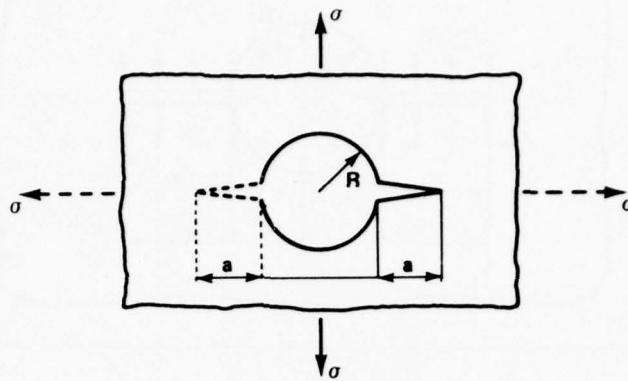
REFERENCE: [15]

Figure 7.15. Two cracks growing out of a hole in an infinite plate.



ACCURACY:  $\pm 1\%$  [15]  
 REFERENCE: [15]

Figure 7.16. A single crack growing out of a hole in an infinite plate.

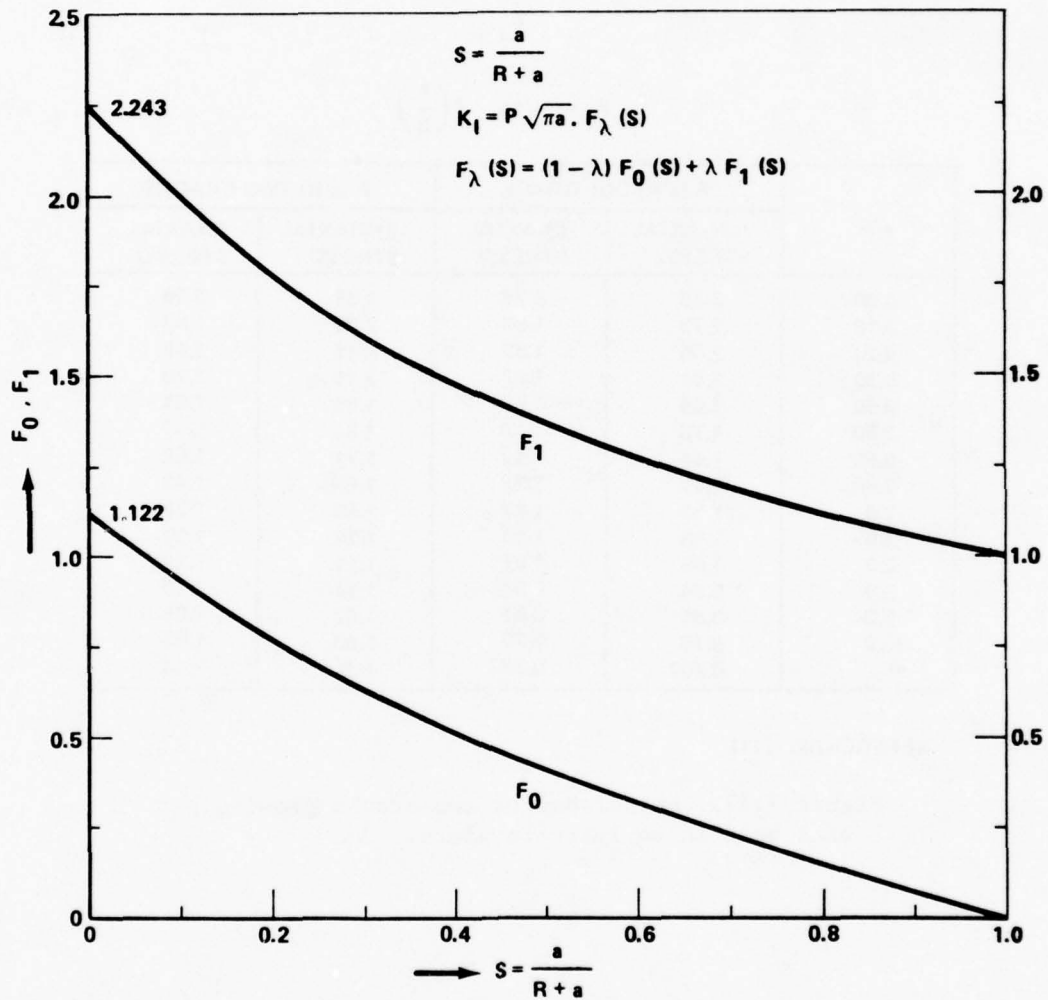
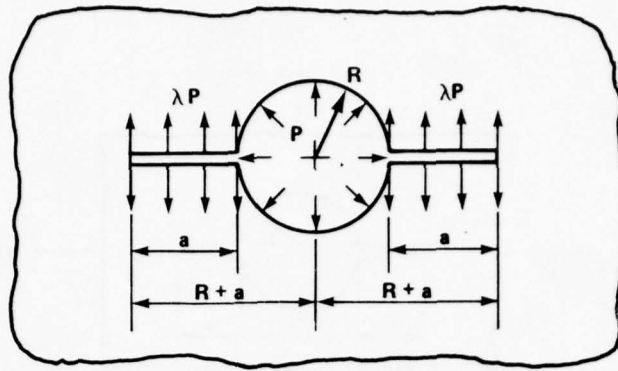


$$K_I = \sigma \sqrt{\pi a} F\left(\frac{a}{R}\right)$$

a/R	F (a/R) ONE CRACK		F (a/R) TWO CRACKS	
	(UNIAXIAL STRESS)	(BIAXIAL STRESS)	(UNIAXIAL STRESS)	(BIAXIAL STRESS)
0.00	3.39	2.26	3.39	2.26
0.10	2.73	1.98	2.73	1.98
0.20	2.30	1.82	2.41	1.83
0.30	2.04	1.67	2.15	1.70
0.40	1.86	1.58	1.96	1.61
0.50	1.73	1.49	1.83	1.57
0.60	1.64	1.42	1.71	1.52
0.80	1.47	1.32	1.58	1.43
1.0	1.37	1.22	1.45	1.38
1.5	1.18	1.06	1.29	1.26
2.0	1.06	1.01	1.21	1.20
3.0	0.94	0.93	1.14	1.13
5.0	0.81	0.81	1.07	1.06
10.0	0.75	0.75	1.03	1.03
$\infty$	0.707	0.707	1.00	1.00

REFERENCE: [11]

Figure 7.17. Either one or two cracks growing out of a hole in an infinite plate.

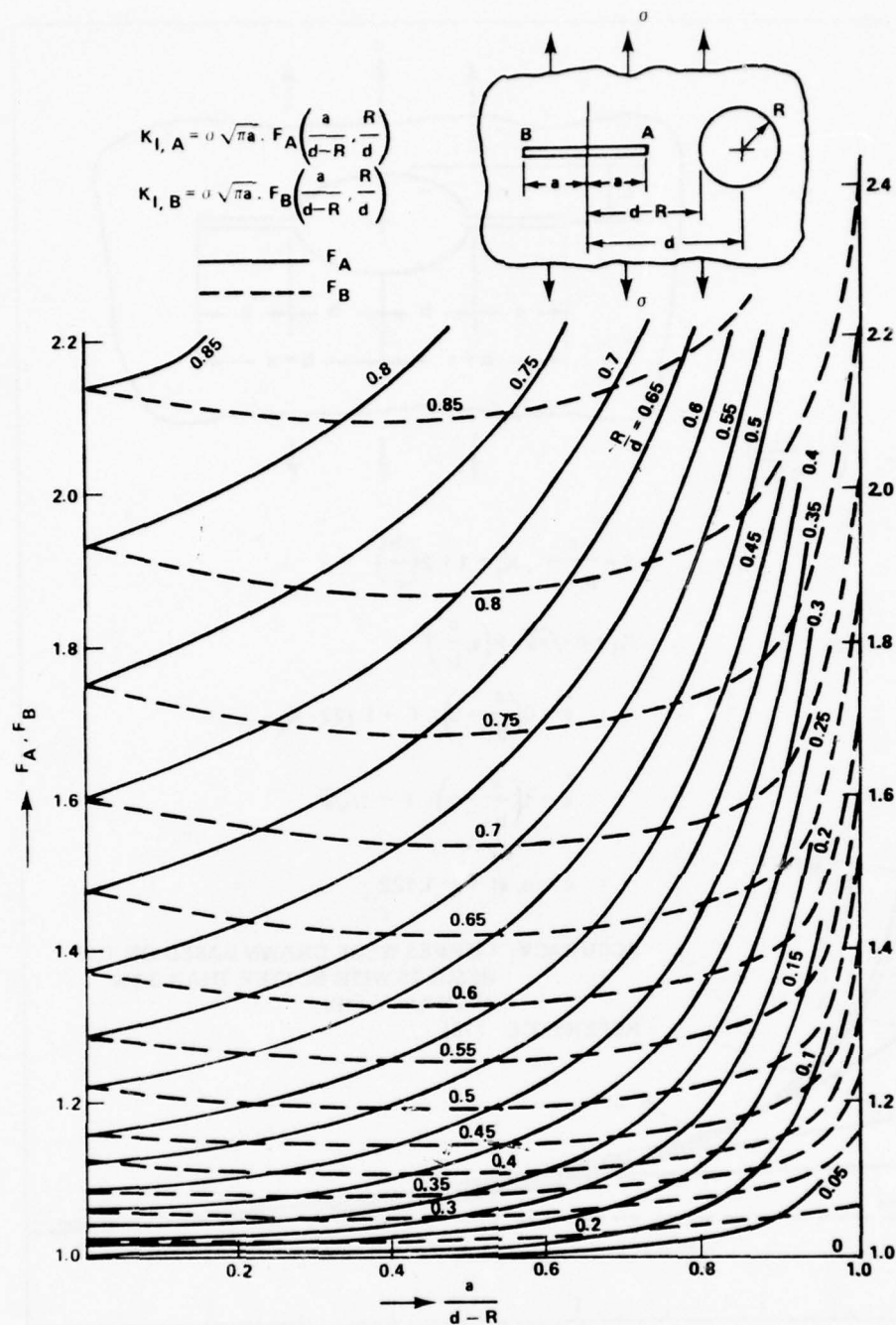


ACCURACY: CURVES WERE DRAWN BASED ON THE RESULTS HAVING  
BETTER THAN 0.1% ACCURACY [15]

REFERENCE: [15]

Figure 7.18. Pressurized hole and cracks in an infinite plate.





ACCURACY: CURVES WERE DRAWN BASED ON THE RESULTS HAVING 0.1%  
 ACCURACY (THICK SOLID AND DASHED LINES) [15].  
 REFERENCE: [15]

Figure 7.19. Crack near a hole in an infinite plate.

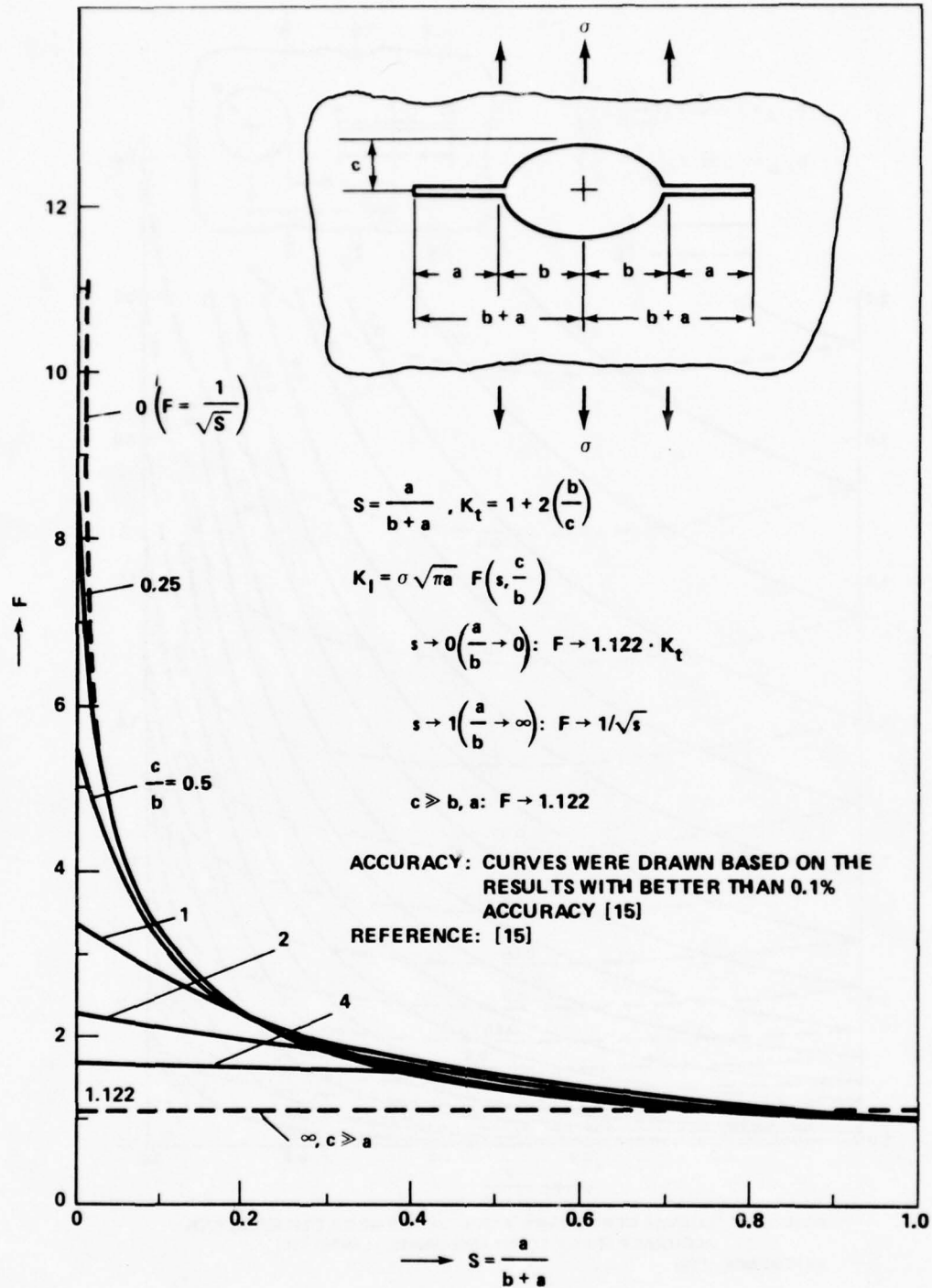


Figure 7.20. Crack growing from an elliptical hole in an infinite plate.

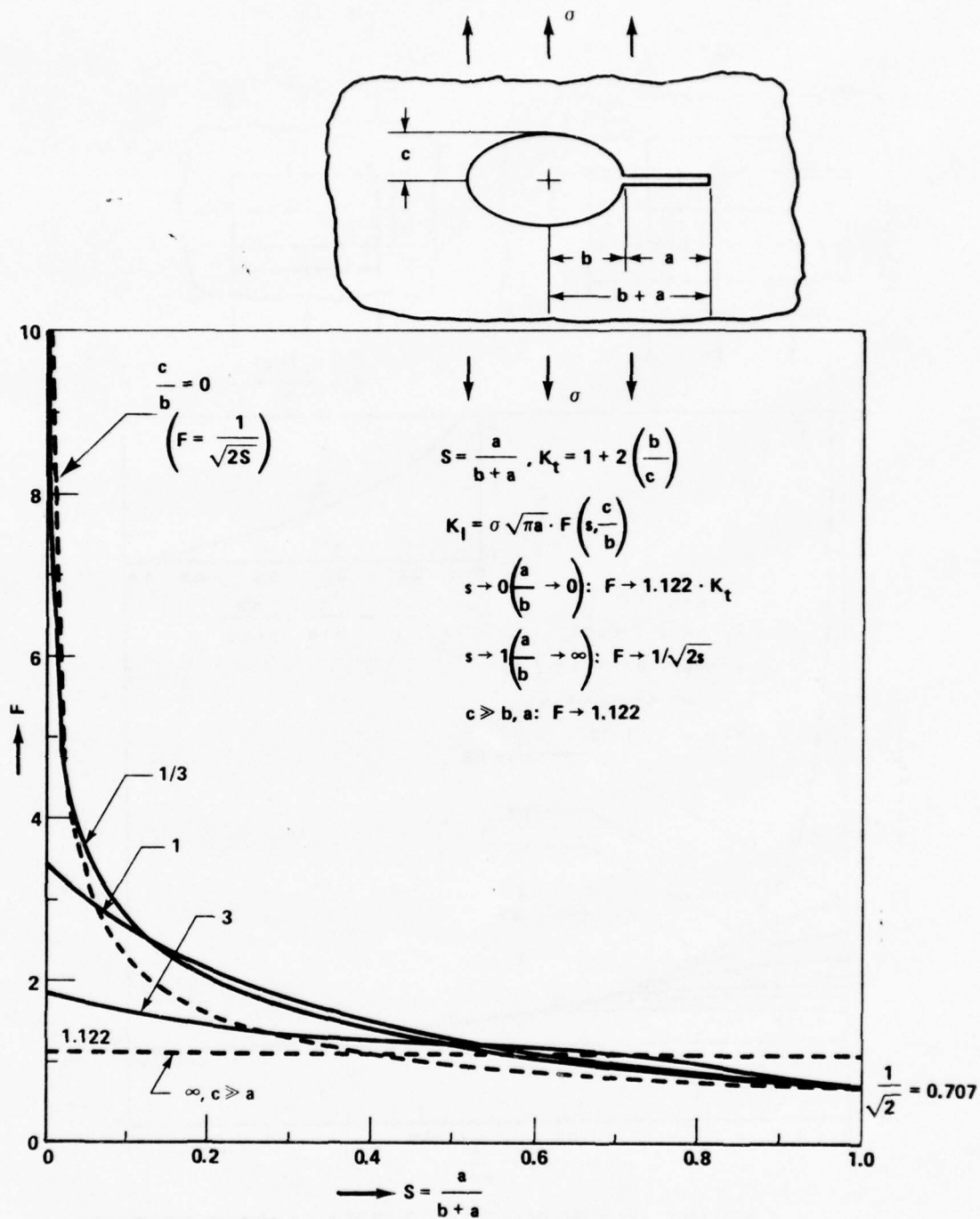
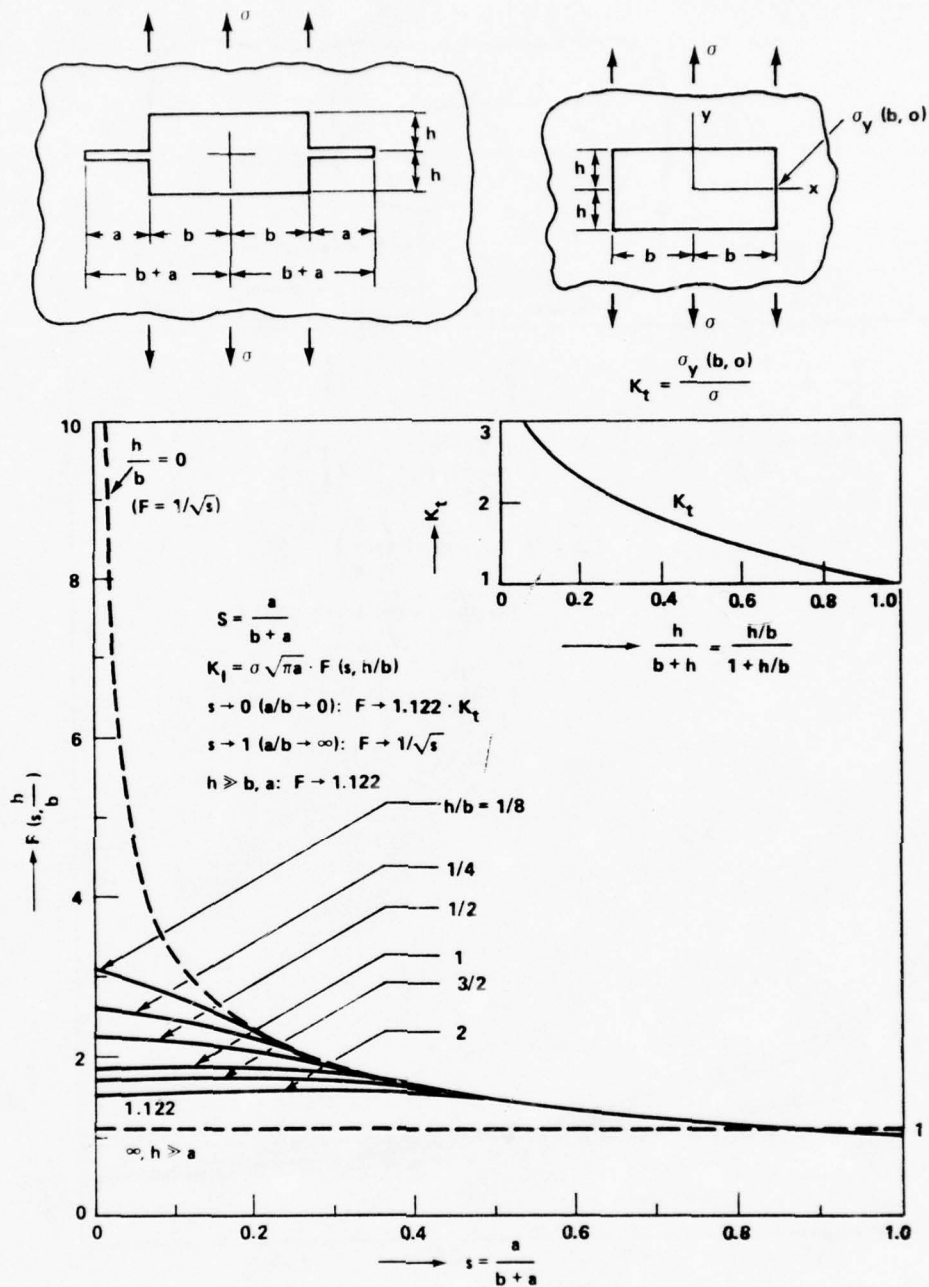
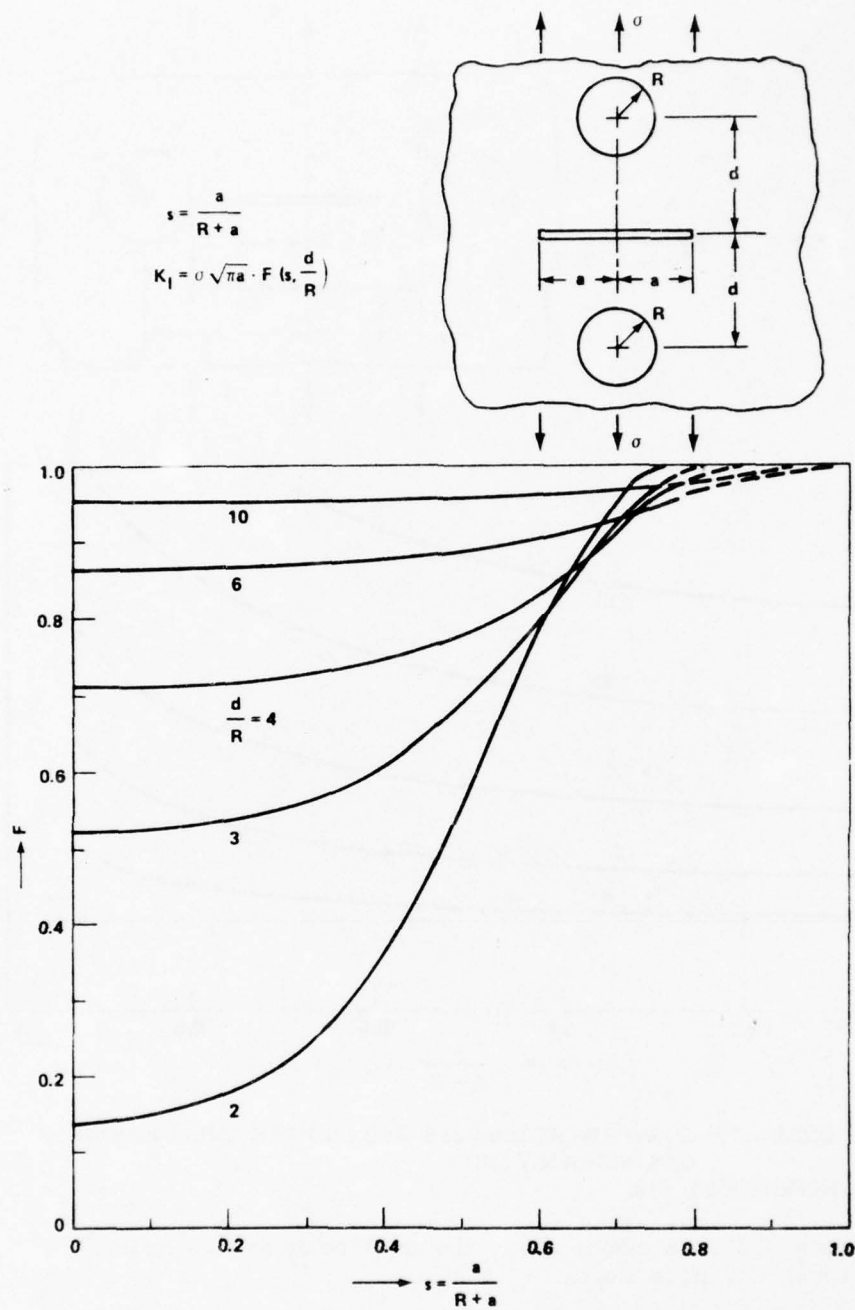


Figure 7.21. A single crack growing from an elliptical hole in an infinite plate.



ACCURACY: EXPECTED TO BE BETTER THAN 5% FOR  $s < 0.25$ ,  
 BETTER THAN 2% FOR  $s \geq 0.25$  [15]  
 REFERENCE: [15]

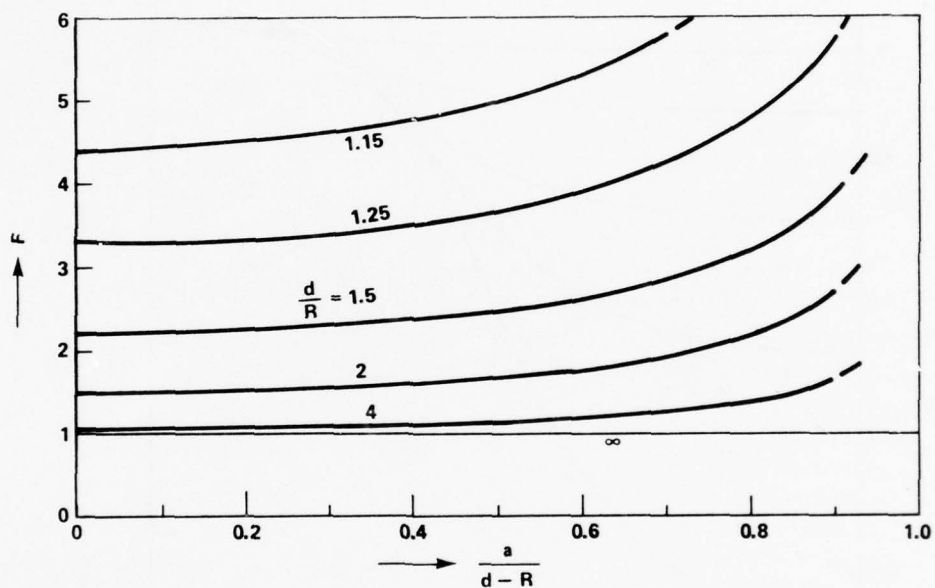
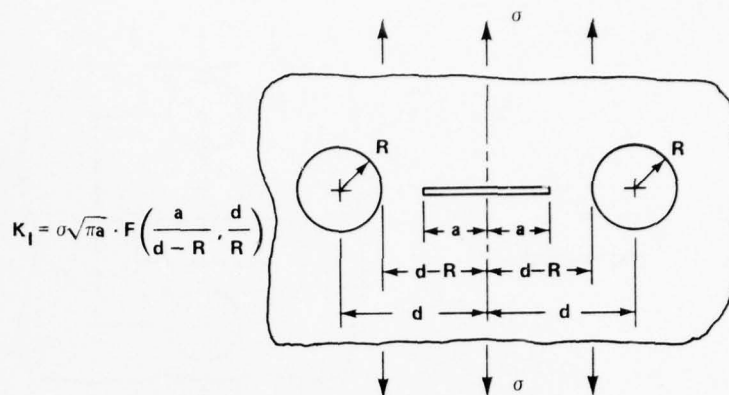
Figure 7.22. Cracks growing from a rectangular hole in an infinite plate.



ACCURACY: CURVES (SOLID LINES) WERE DRAWN BASED ON THE  
RESULTS HAVING 0.1% ACCURACY [15]  
REFERENCE: [15]

Figure 7.23. A crack perpendicular to the axis between two holes in an infinite plate.

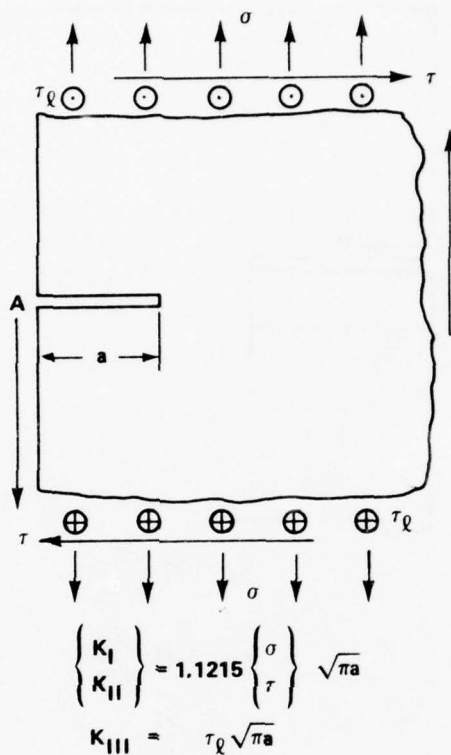




ACCURACY: CURVES WERE DRAWN BASED ON THE RESULTS HAVING  
0.1% ACCURACY [15]  
REFERENCES: [15]

Figure 7.24. A crack along the axis between two holes in an infinite plate.

7.2 Two-Dimensional Solutions for Cracks in Semiinfinite Plates  
(Figures 7.25 through 7.31)

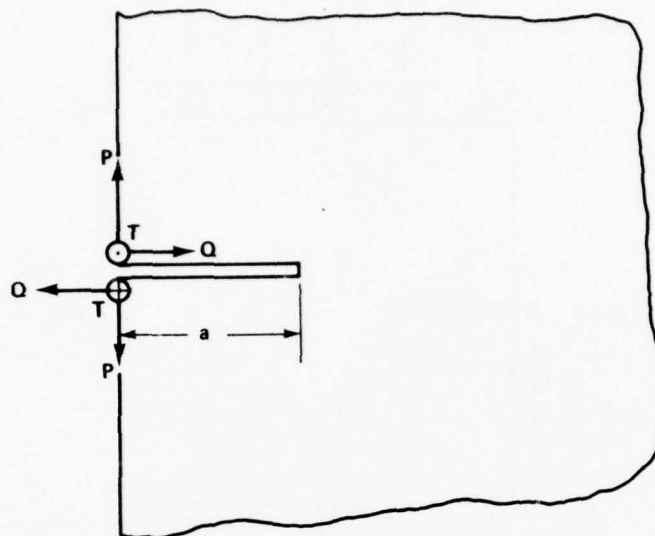


ACCURACY:  $K_I, K_{II}$  WITHIN ONE UNIT OF LAST DIGIT

$K_{III}$  EXACT [15]

REFERENCES: [11, 15]

Figure 7.25. Edge crack in a semi-infinite plate.



$$K_I = 1.30 \cdot \frac{2P}{\sqrt{\pi a}}$$

$$K_{II} = 1.30 \cdot \frac{2Q}{\sqrt{\pi a}}$$

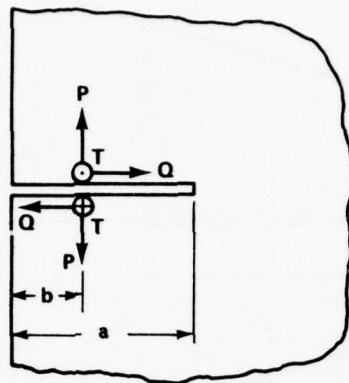
$$K_{III} = \frac{2T}{\sqrt{\pi a}}$$

ACCURACY:  $K_I, K_{II}$  BETTER THAN 0.5%

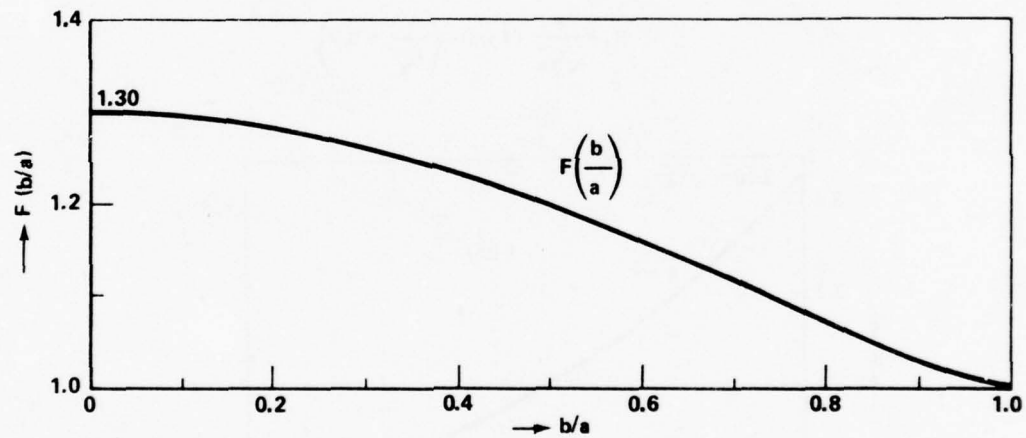
$K_{III}$  EXACT [15]

REFERENCE: [15]

Figure 7.26. Edge crack in a semi-infinite plate with concentrated forces at the crack mouth.



$$\begin{pmatrix} K_I \\ K_{II} \\ K_{III} \end{pmatrix} = \frac{2}{\sqrt{\pi a}} \begin{pmatrix} P \\ Q \\ T \end{pmatrix} \frac{1}{\sqrt{1 - (b/a)^2}} \begin{pmatrix} F(b/a) \\ F(b/a) \\ 1 \end{pmatrix}$$

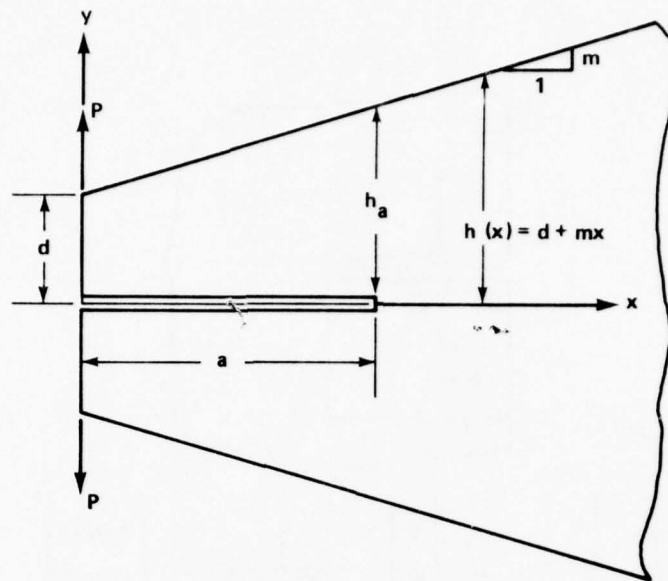


ACCURACY:  $K_I$ ,  $K_{II}$  ESTIMATED AT BETTER THAN 2%

$K_{III}$  EXACT [15]

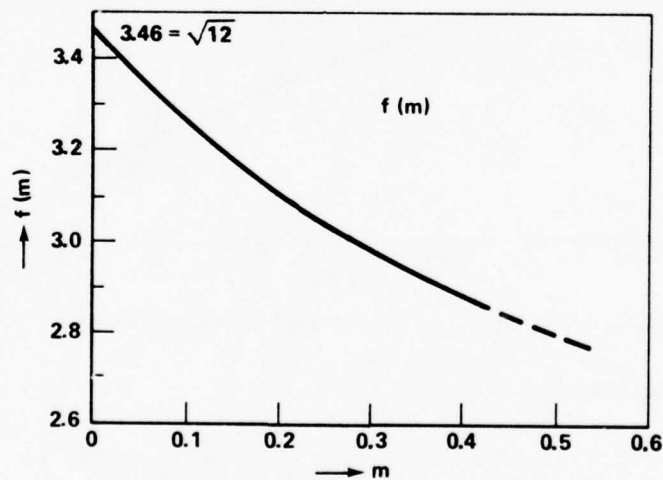
REFERENCE: [15]

Figure 7.27. Edge crack in a semi-infinite plate with concentrated crack forces arbitrarily placed.



$$h_a = h(a) = d + ma$$

$$K_I = \frac{P}{\sqrt{h_a}} \cdot f(m) \cdot \left( \frac{a}{h_a} + 0.7 \right)$$

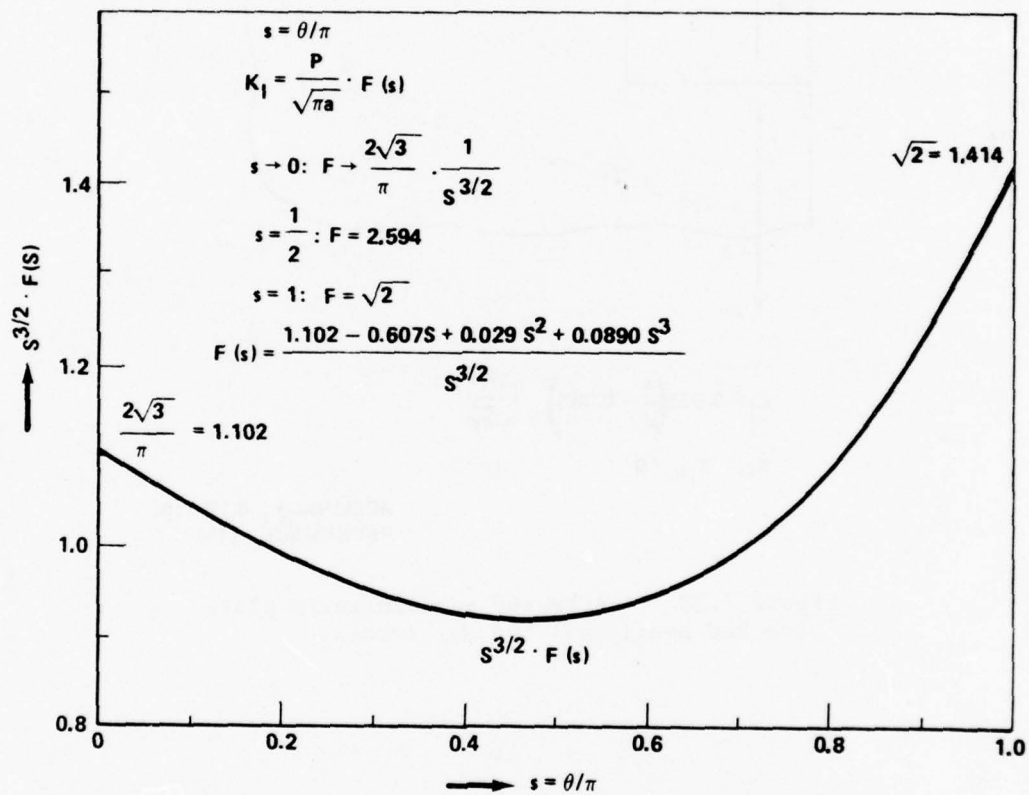
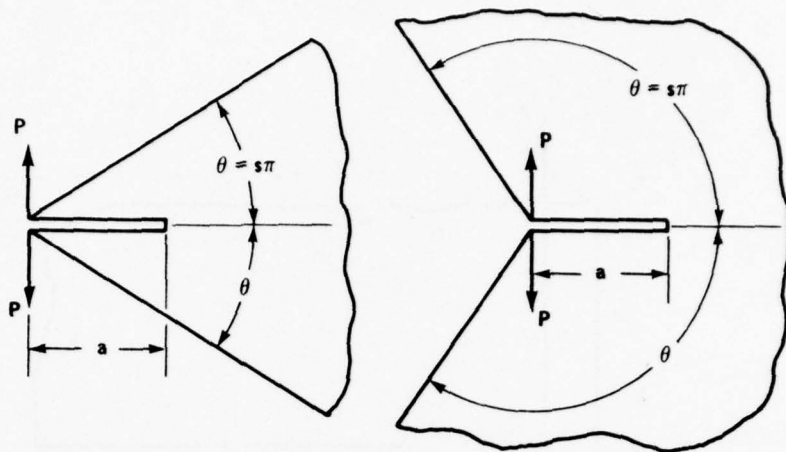


ACCURACY: ORDER OF 1% FOR  $a/h_a > 1$  [15]

REFERENCE: [15]

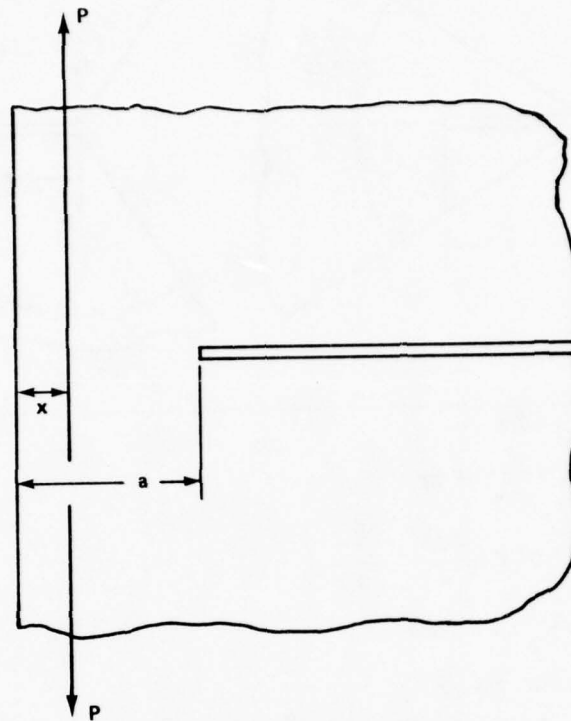
Figure 7.28. Edge crack in a semi-infinite wedge-strip with concentrated opening forces at the end.





ACCURACY: EXPECTED TO BE BETTER THAN 2% FOR ANY  $s$ .  
 (EXACT FOR  $s \rightarrow 0$  AND  $s \rightarrow 1$ ; ACCURATE FOR  $s = 1/2$  [15])  
 REFERENCE: [15]

Figure 7.29. Crack at the intersection of two straight boundaries of a semi-infinite plate.

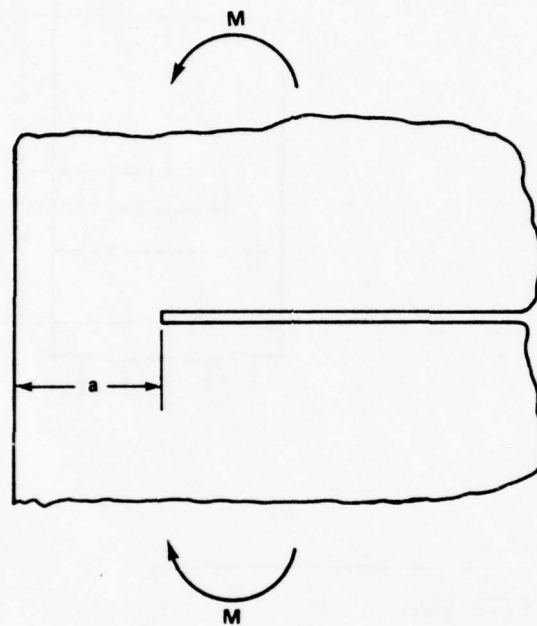


$$K_I = 3.522 \left( \frac{x}{a} - 0.368 \right) \frac{2P}{\sqrt{\pi a}}$$

$$K_{II} = K_{III} = 0$$

ACCURACY: 0.1% [15]  
REFERENCE: [15]

Figure 7.30. A stressed semi-infinite plate cracked nearly all the way across.



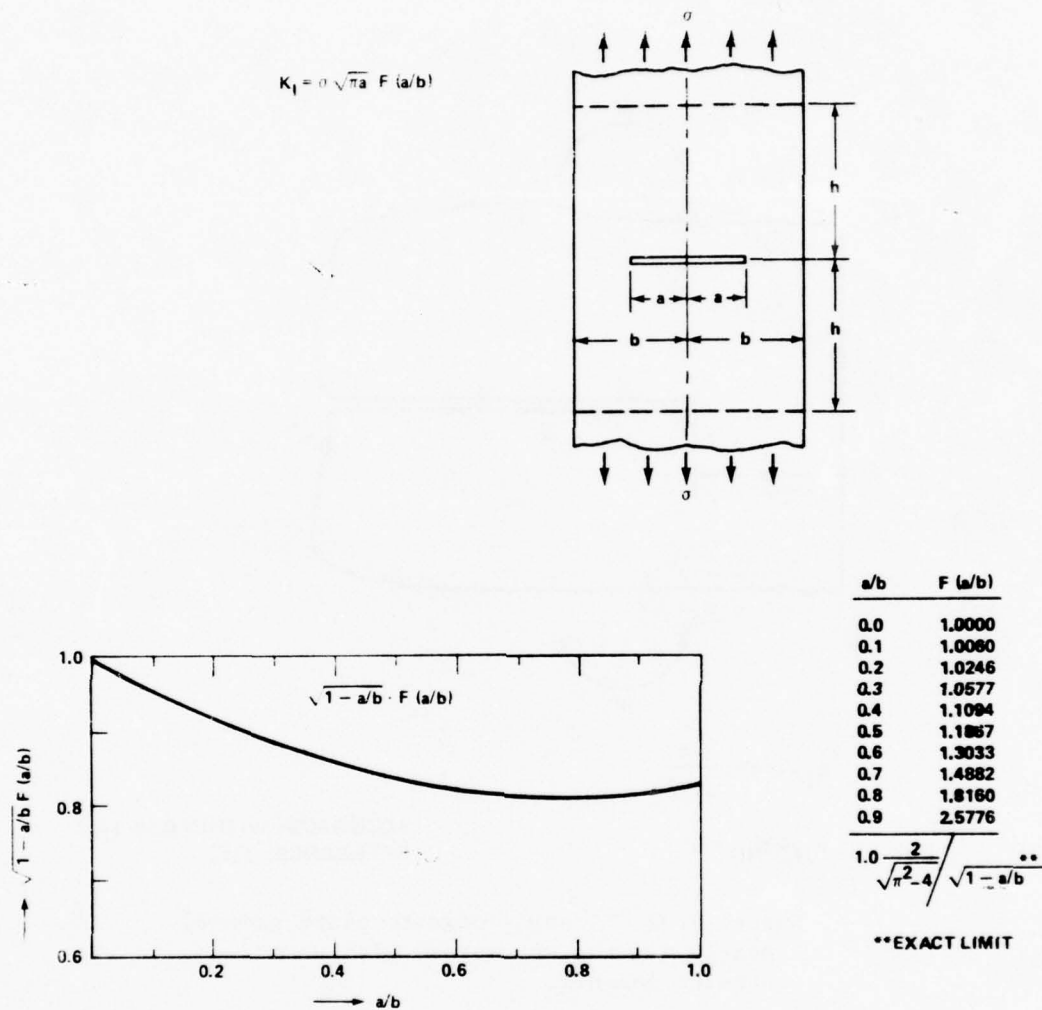
$$K_I = 3.975 \frac{M}{a \sqrt{a}}$$

$$K_{II} = K_{III} = 0$$

ACCURACY: WITHIN 0.1% [15]  
REFERENCE: [15]

Figure 7.31. A semi-infinite plate cracked nearly all the way across with remote bending moments.

7.3 Two-Dimensional Solutions for Cracks in Long Strips (Figures 7.32 through 7.45)



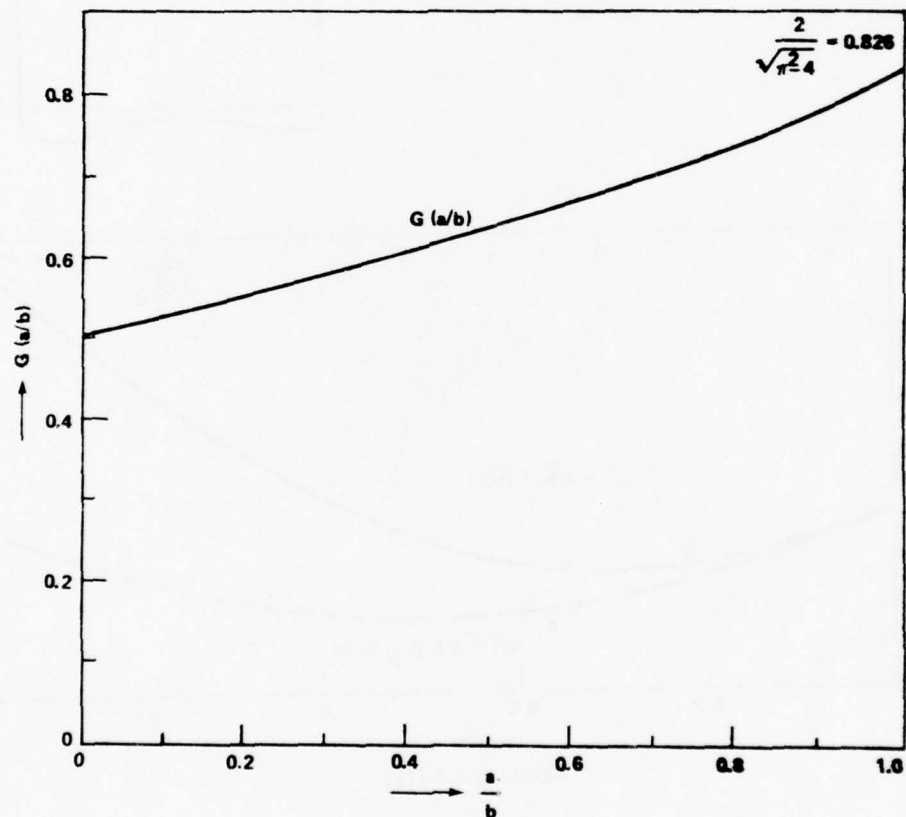
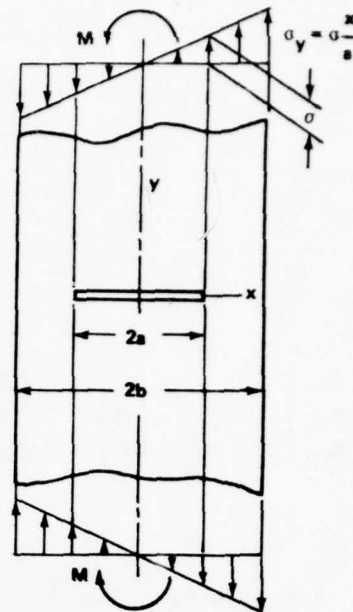
REFERENCES. [11, 15]

Figure 7.32. A center cracked strip loaded in tension.

$$\sigma = \frac{3Ma}{2b^3}$$

$$K_1 = \sigma \sqrt{\pi a} \cdot F_1(a/b)$$

$$G(a/b) = \frac{\{1 - (a/b)^3\} F_1(a/b)}{\sqrt{1 - a/b}}$$



ACCURACY: BETTER THAN 1% [15]  
REFERENCE: [15]

Figure 7.33. A center cracked strip loaded in bending.



$$\begin{Bmatrix} K_I \\ K_{II} \\ K_{III} \end{Bmatrix} = \frac{1}{\sqrt{\pi a}} \begin{Bmatrix} P \\ Q \\ T \end{Bmatrix} \begin{Bmatrix} F(a/b) \\ F(a/b) \\ F_{III}(a/b) \end{Bmatrix}$$

$$F_{III}(a/b) = \sqrt{\frac{\pi a}{b} / \sin \frac{\pi a}{b}}$$

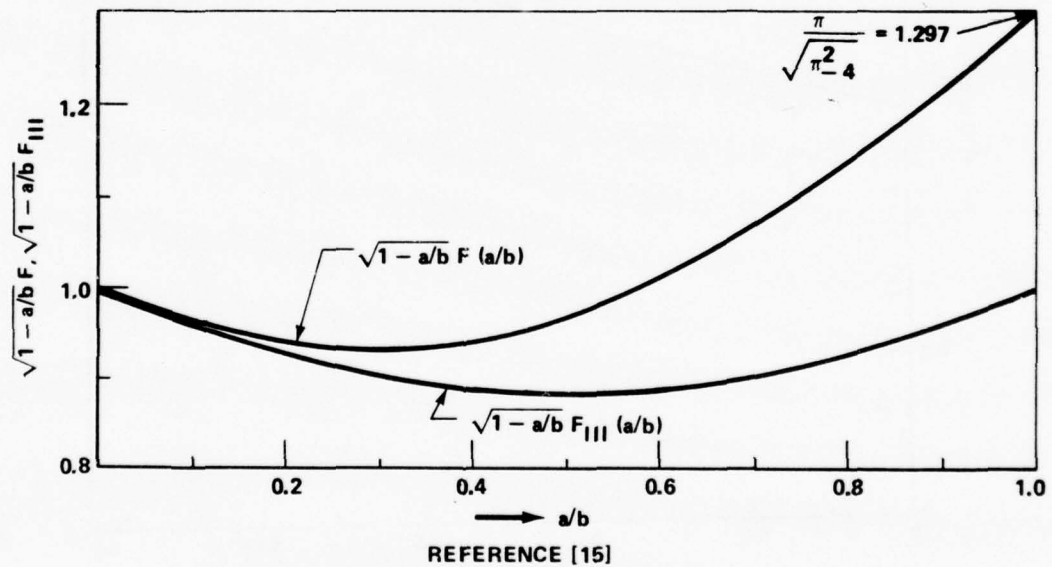
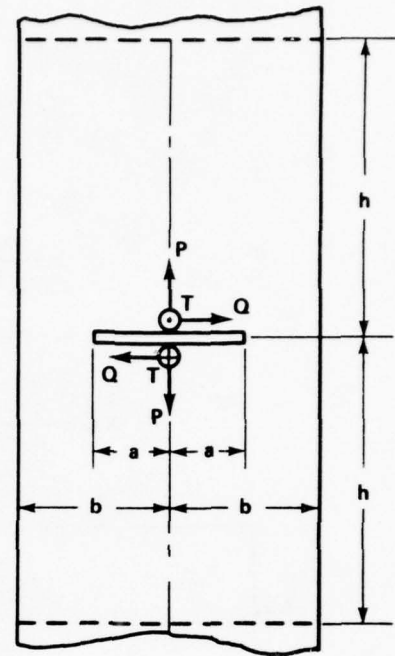
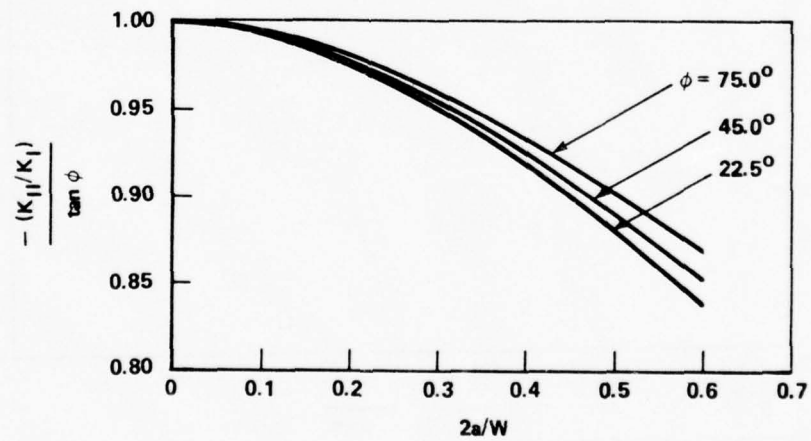
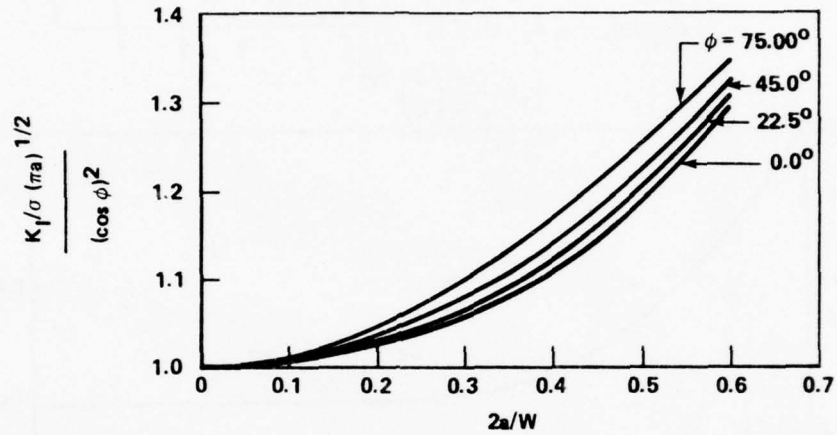
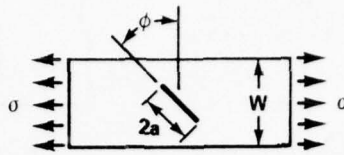


Figure 7.34. A center cracked strip loaded with concentrated forces on the crack surface.



REFERENCE: [33]

Figure 7.35. A skewed crack in a strip loaded in tension.

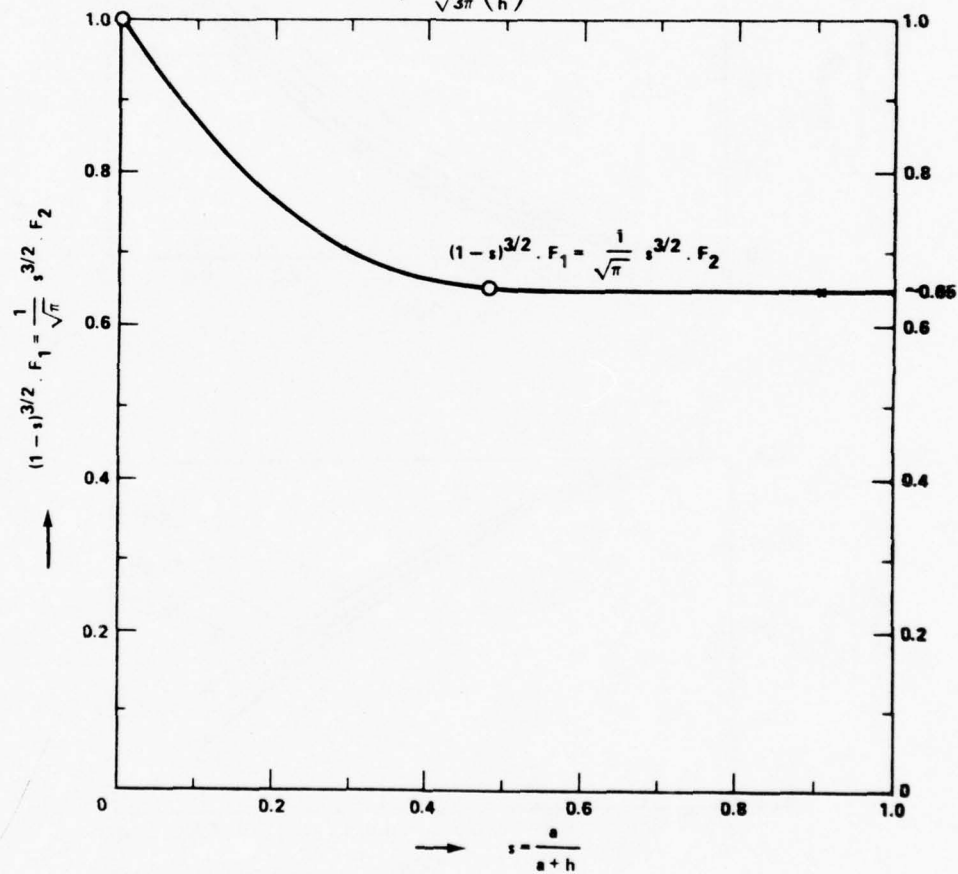
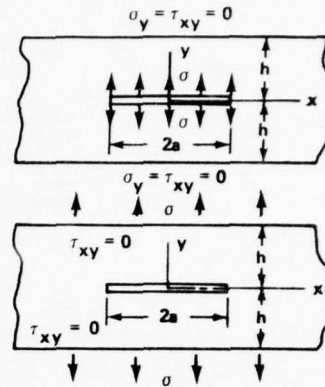
$$s = \frac{a}{a+h} = \frac{a/h}{1+a/h} = \frac{1}{1+h/a}$$

$$K_I = \sigma \sqrt{\pi a} \cdot F_1(s) \\ = \sigma \sqrt{\pi} \left(\frac{a}{h}\right)^{3/2} \cdot F_2(s)$$

$$s \rightarrow 0 \ (a/h \rightarrow 0): F_1 = 1 \\ F_2 \rightarrow \sqrt{\pi} \left(\frac{h}{a}\right)^{3/2}$$

$$s \rightarrow 1 \ (a/h \rightarrow \infty): F_2 = 2/\sqrt{3}$$

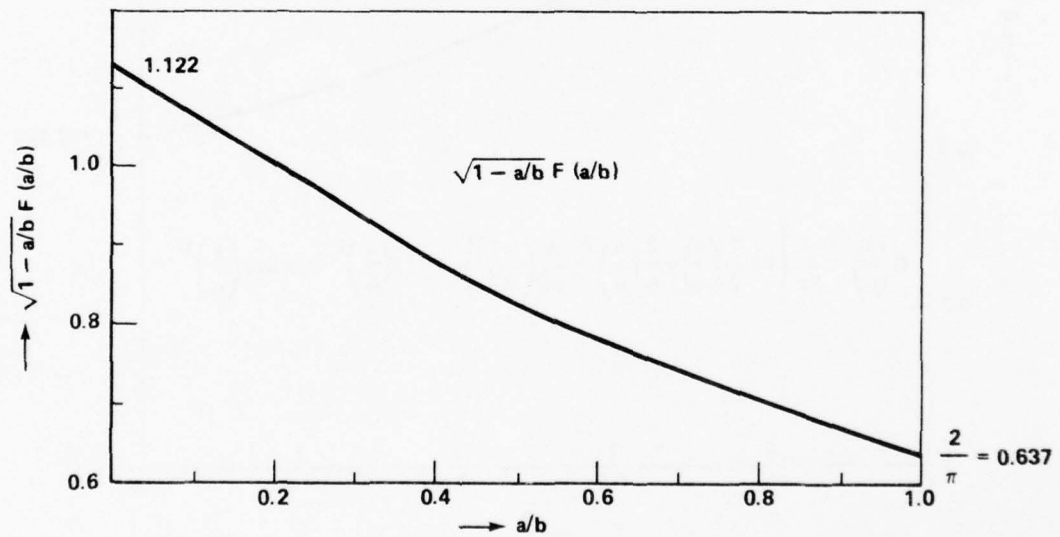
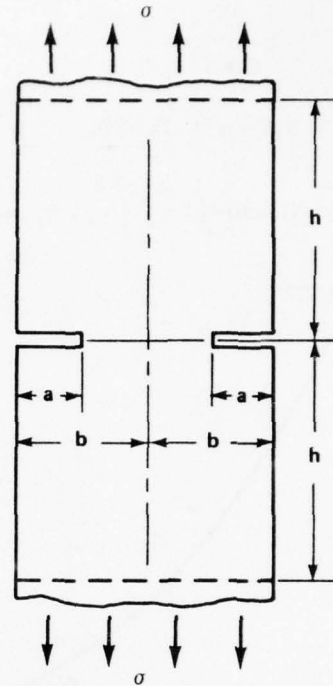
$$F_1 \rightarrow \frac{2}{\sqrt{3\pi}} \left(\frac{a}{h}\right)^{3/2}$$



ACCURACY: ORDER OF 1% [15]  
REFERENCE: [15]

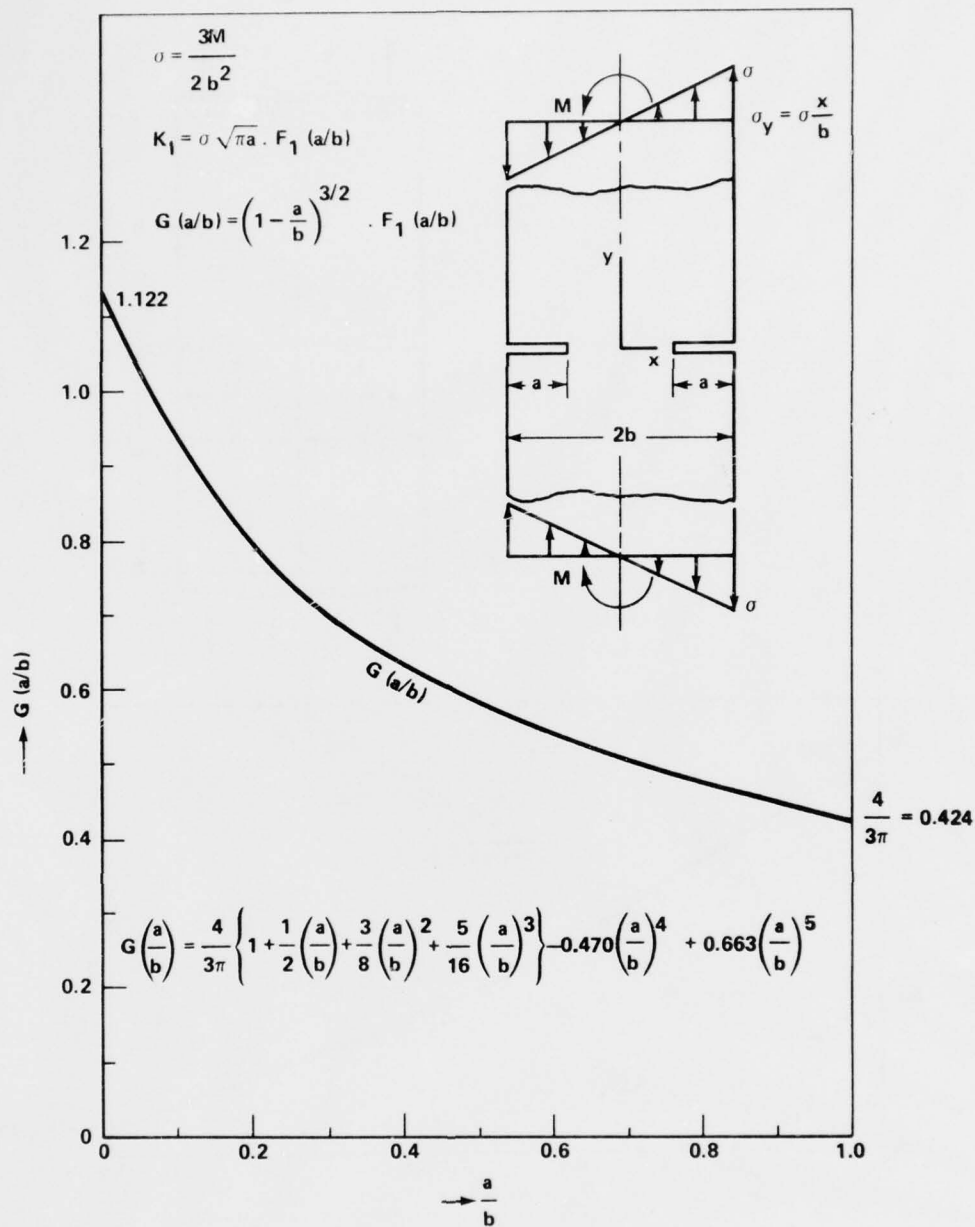
Figure 7.36. A crack parallel to the boundaries of an infinite strip.

$$K_I = \sigma \sqrt{\pi a} F(a/b)$$



REFERENCES: [11, 15]

Figure 7.37. A double-edge cracked strip loaded in tension.



ACCURACY: BETTER THAN 1% [15]  
 REFERENCE: [15]

Figure 7.38. A double-edge cracked strip loaded in bending.



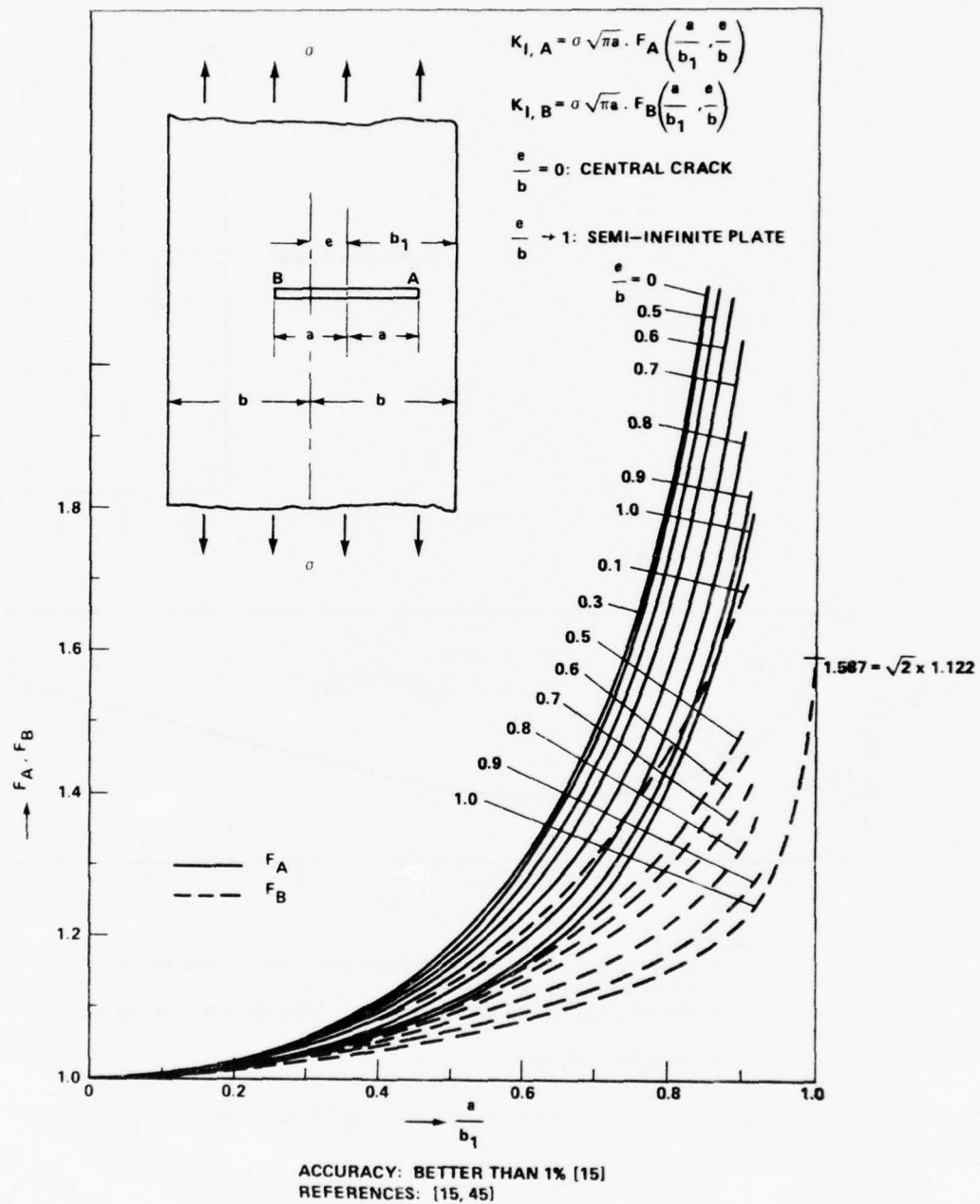
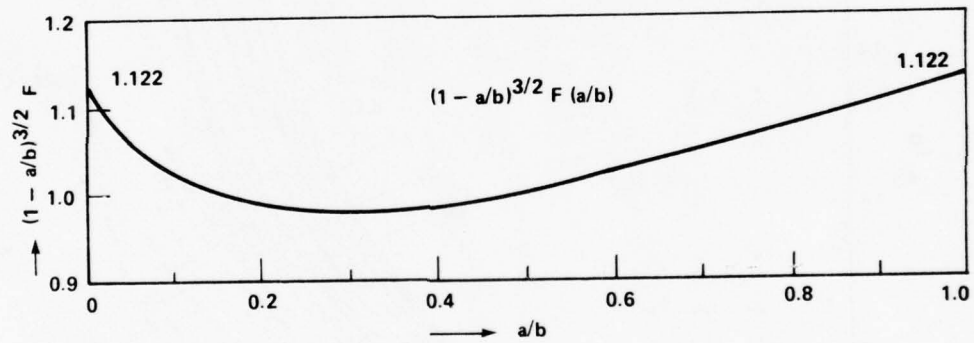
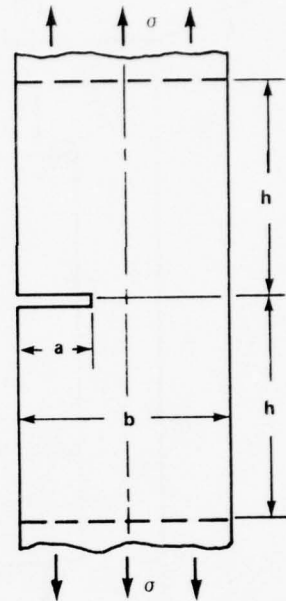


Figure 7.39. An eccentric crack in a strip.

$$K_I = \sigma \sqrt{\pi a} F(a/b)$$



NOTES:

1. LOAD IS APPLIED ALONG THE CENTER LINE OF THE STRIP AT THE CRACK LOCATION.
2. THE EFFECT OF  $h/b$  IS PRACTICALLY NEGLIGIBLE FOR  $h/b \geq 1.0$

REFERENCES: [11, 15]

Figure 7.40. An edge-cracked strip loaded in tension.

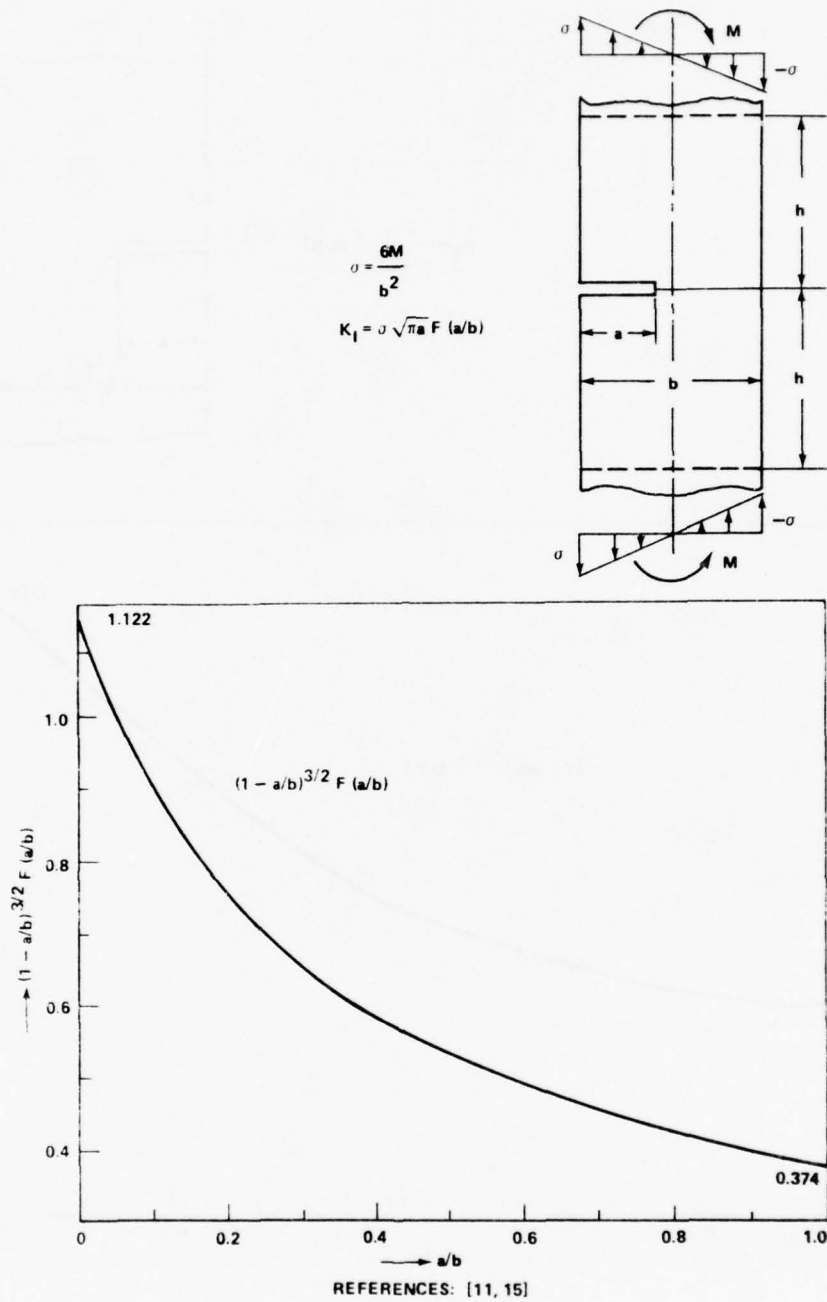
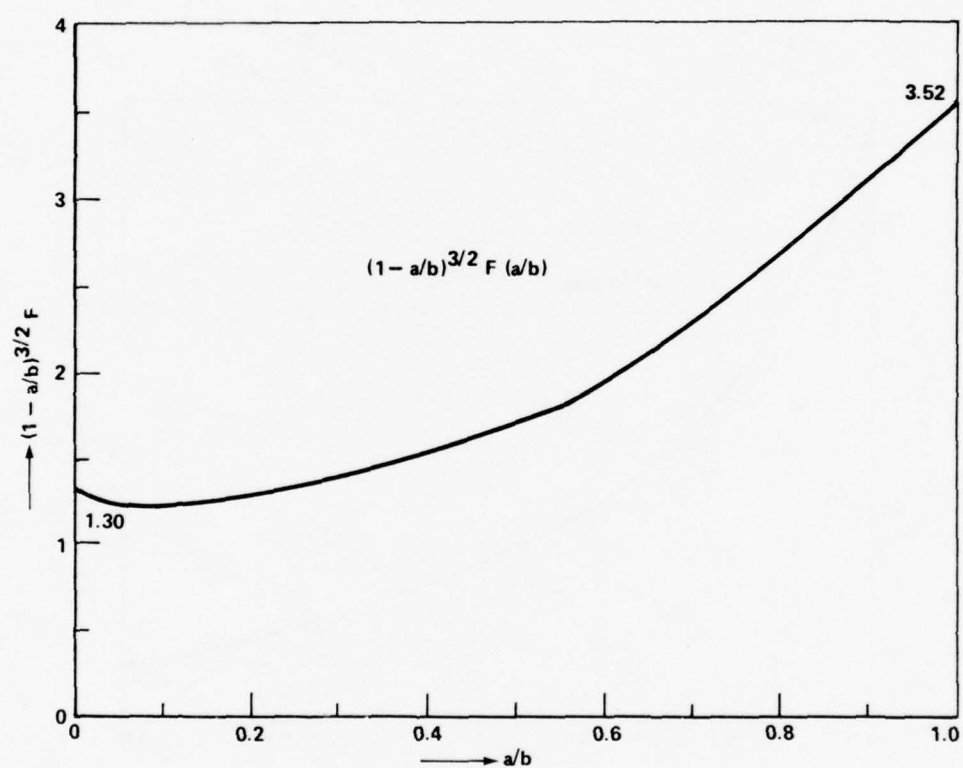
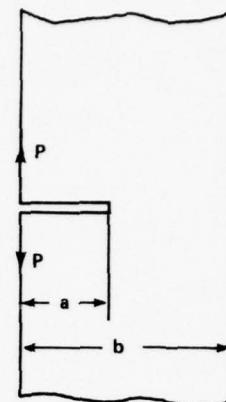


Figure 7.41. An edge-cracked strip loaded in tension.

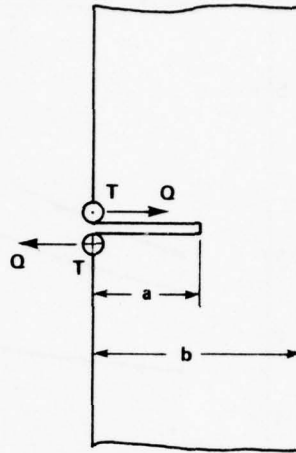
$$K_I = \frac{2P}{\sqrt{\pi a}} F(a/b)$$



REFERENCE: [15]

Figure 7.42. An edge-cracked strip with opening forces at the crack mouth.

$$\begin{Bmatrix} K_{II} \\ K_{III} \end{Bmatrix} = \frac{2}{\sqrt{\pi a}} \begin{Bmatrix} Q \\ T \end{Bmatrix} \begin{Bmatrix} F_{II}(a/b) \\ F_{III}(a/b) \end{Bmatrix}$$



$$F_{II}(a/b) = \frac{1.30 - 0.65(a/b) + 0.37(a/b)^2 + 0.28(a/b)^3}{\sqrt{1 - a/b}}$$

$$F_{III}(a/b) = \sqrt{\frac{\pi a}{b}} \sin \frac{\pi a}{b}$$

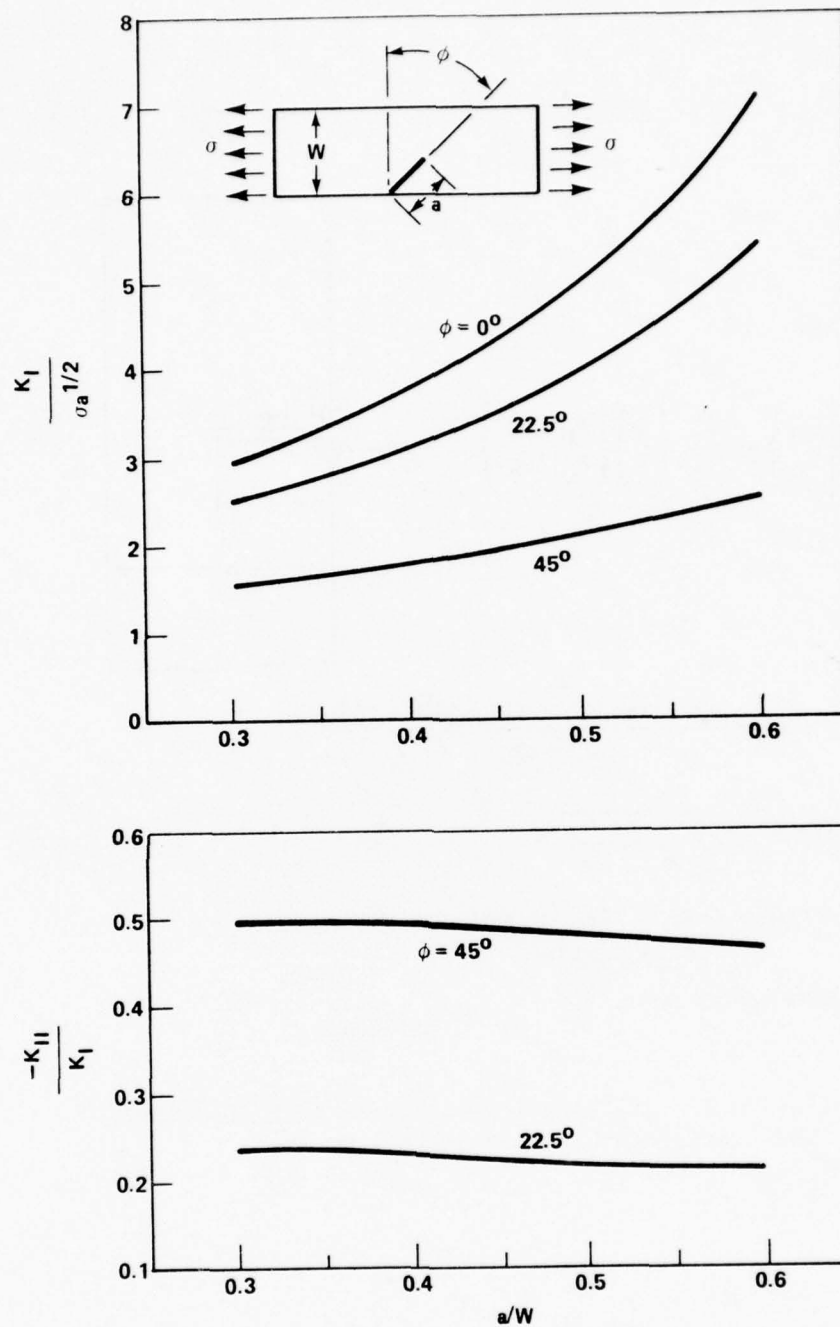
ACCURACY:  $F_{II}$  BETTER THAN 1% FOR ANY  $a/b$

$F_{III}$  EXACT [15]

REFERENCE: [15]

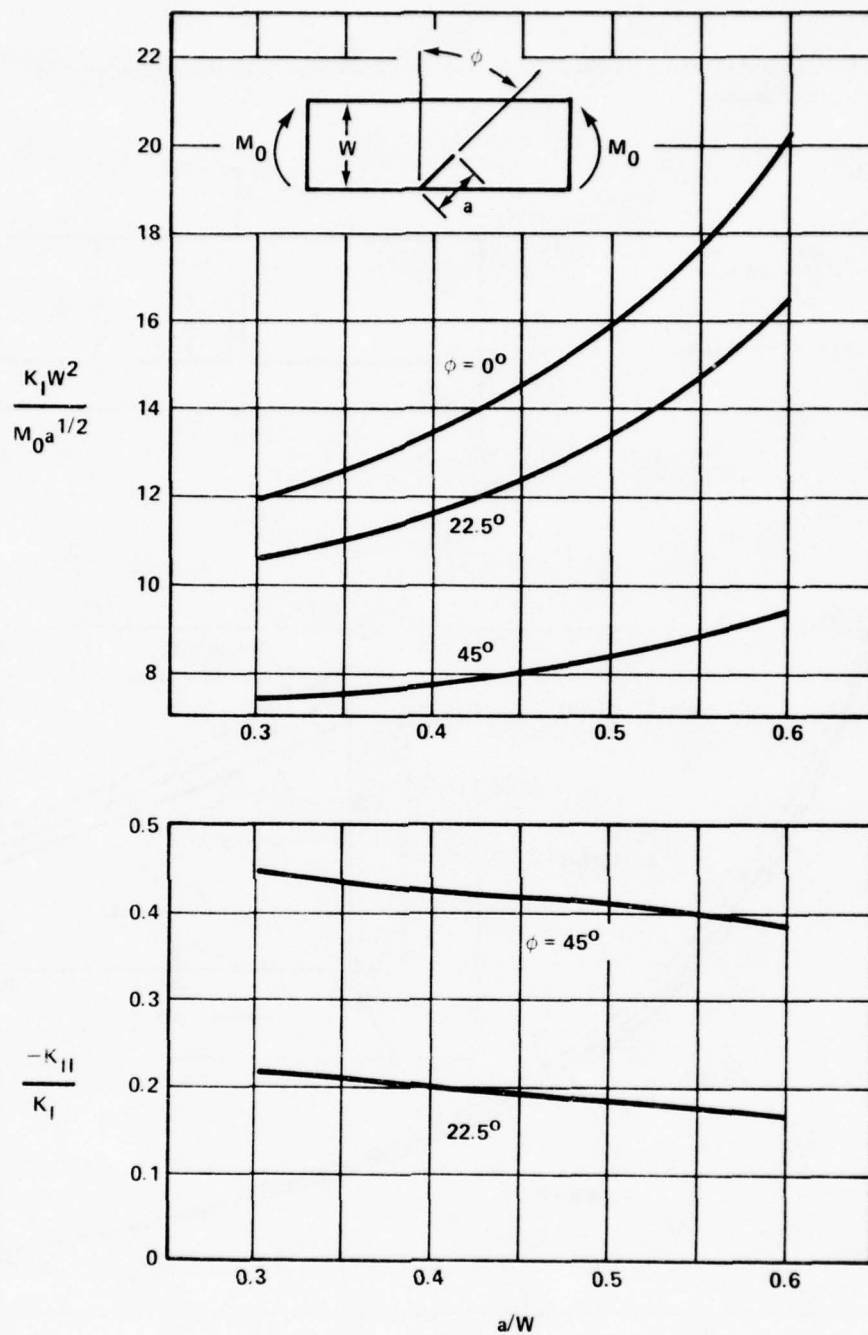
Figure 7.43. An edge-cracked strip with shearing and tearing forces at the crack mouth.





REFERENCE: [33]

Figure 7.44. A strip with a slanted edge-crack loaded in tension.



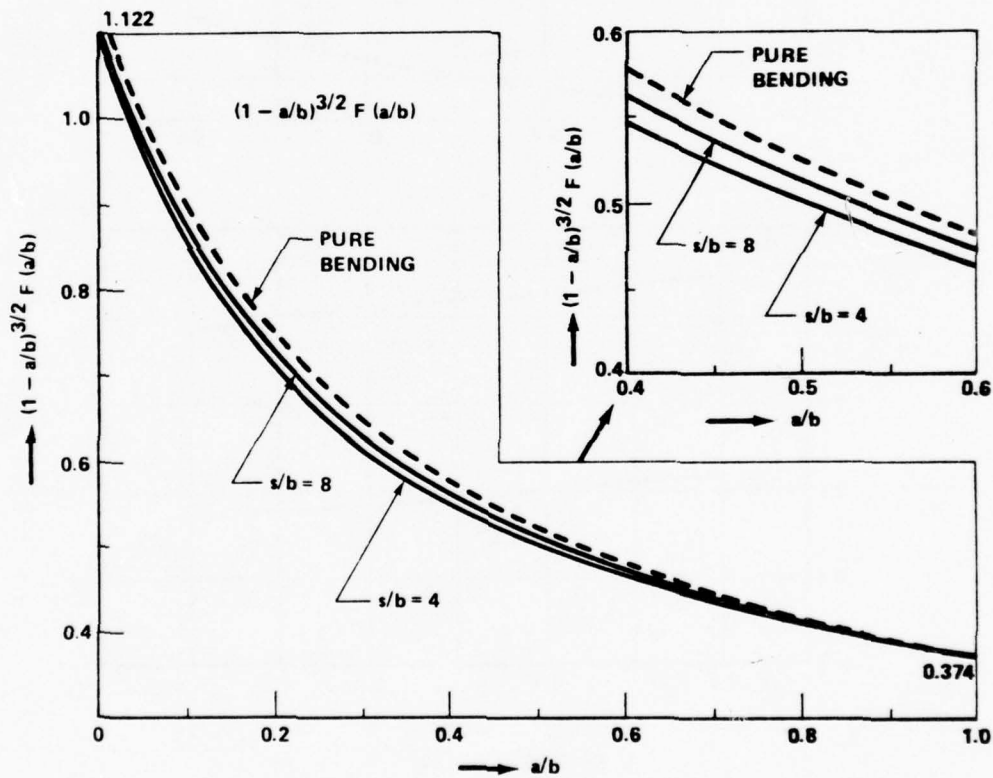
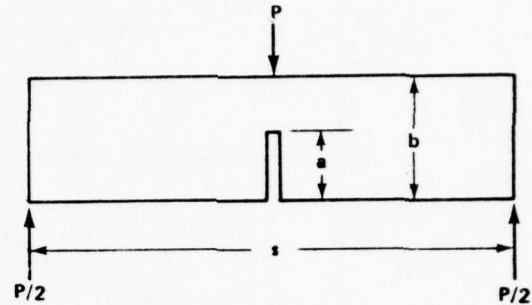
REFERENCE: [33]

Figure 7.45. A strip with a slanted edge-crack loaded in bending.

7.4 Two-Dimensional Solutions for Finite Specimens (Figures 7.46 Through 7.57)

$$\sigma = \frac{6M}{b^2} \left( M = \frac{Ps}{4} \right)$$

$$K_I = 3\sqrt{\pi a} F(a/b)$$



ACCURACY: THE CURVES HAVE 1% ACCURACY.  
REFERENCES: [15, 51]

$$K_I = \sigma \sqrt{a} F_1(a/b, h/b, d/h)$$

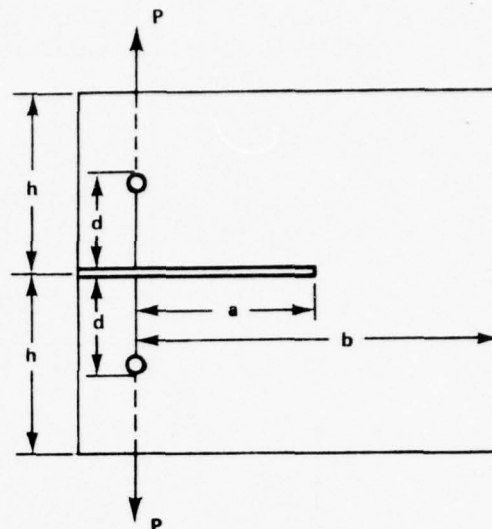
WHERE  $\sigma = P/b$

OR  $K_I = \sigma_N \sqrt{b-a} F_2(a/b, h/b, d/h)$

WHERE  $\sigma_N = \sigma_N^{\text{TENSION}} + \sigma_N^{\text{BENDING}}$

$$= \frac{P}{b-a} + \frac{6P \left( a + \frac{b-a}{2} \right)}{(b-a)^2}$$

$$= \frac{2P(2b+a)}{(b-a)^2}$$



NUMERICAL VALUES OF  $F_2$  (NOTE:  $F_1 \frac{2(2+a/b)}{(1-a/b)^{3/2}} \cdot \frac{1}{\sqrt{a/b}} \cdot F_2$ )

THE CURVES IN THE FOLLOWING FIGURE HAVE BETTER THAN 1% ACCURACY [15].

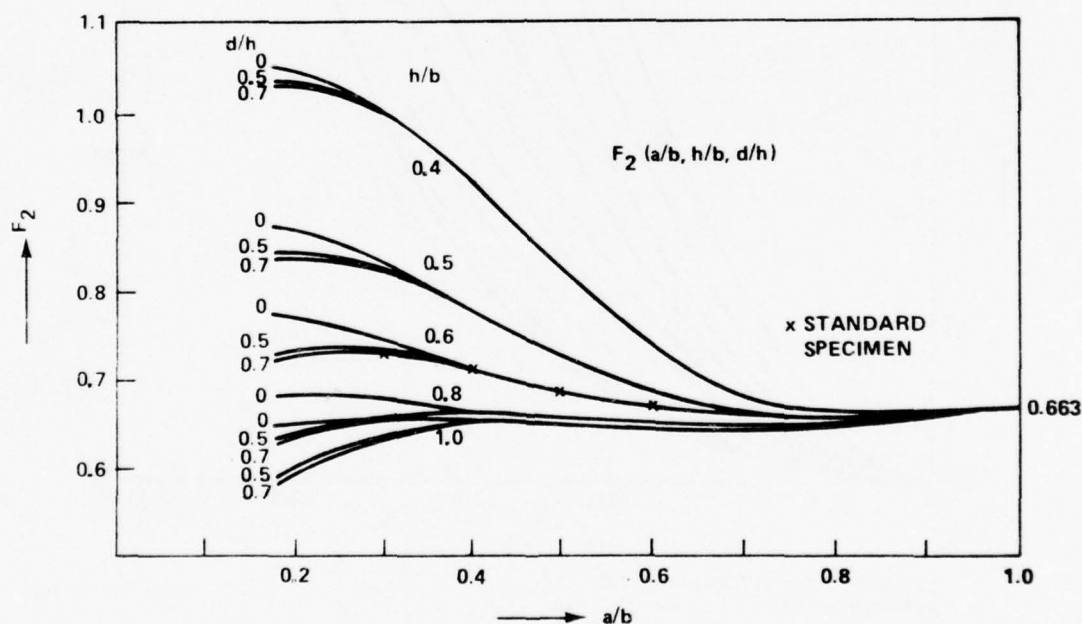


Figure 7.47. The compact tension specimen.

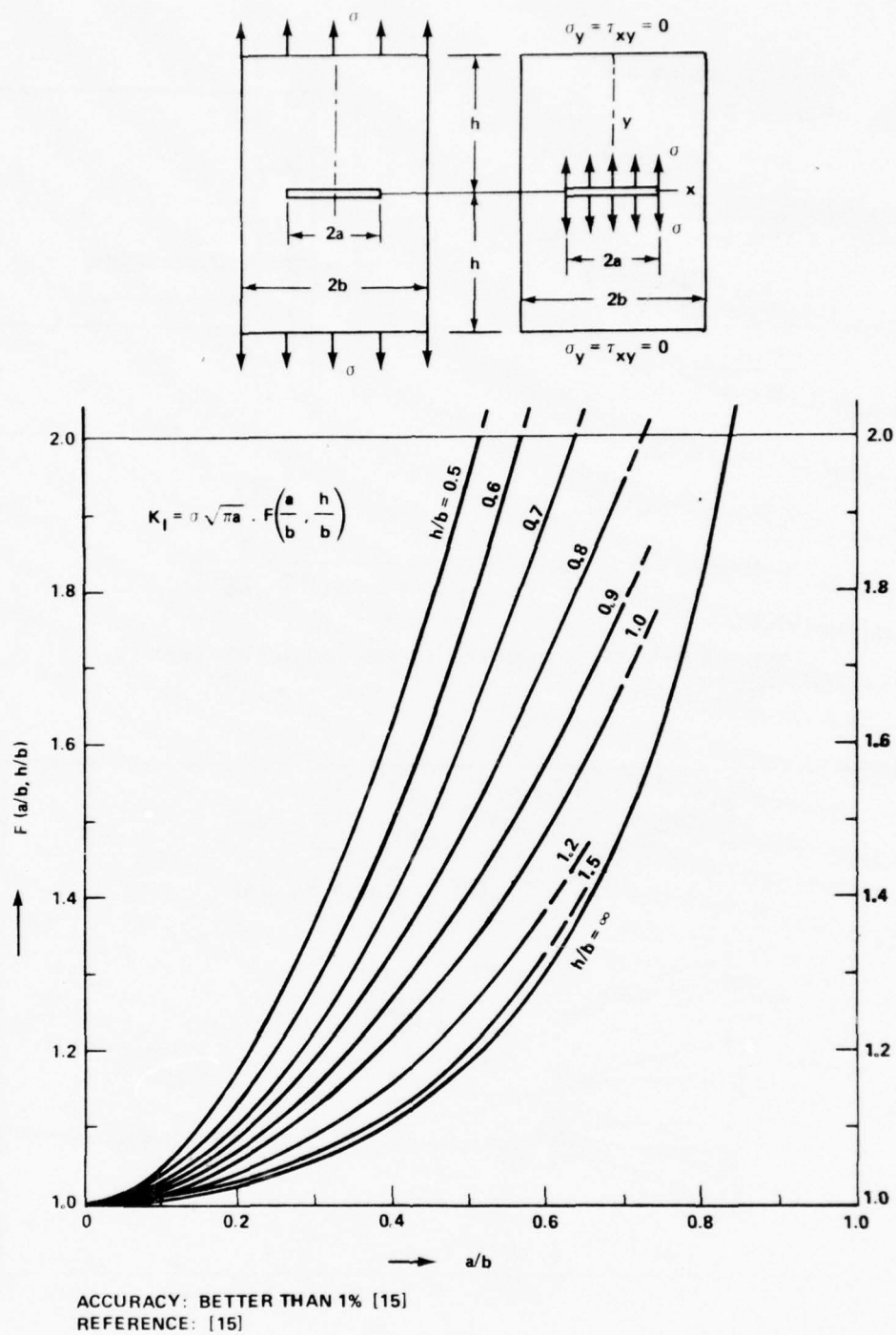
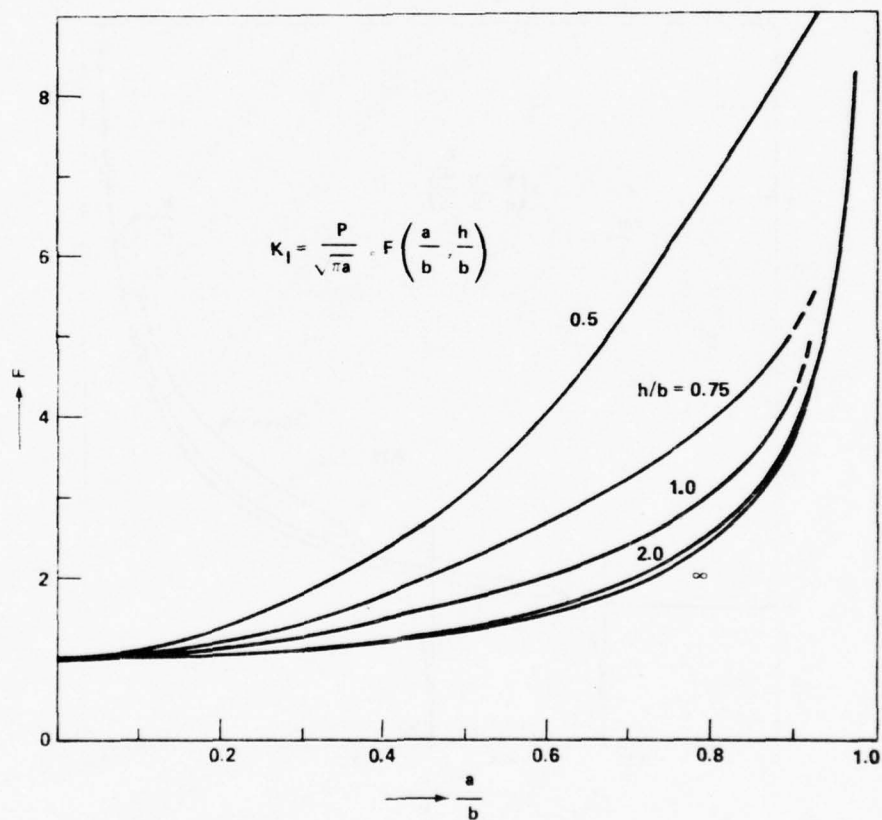
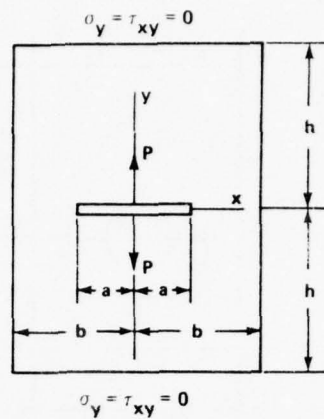


Figure 7.48. The center-cracked tension specimen.





ACCURACY: CURVES WERE DRAWN BASED ON THE RESULTS WHICH  
HAVE BETTER THAN 0.1% ACCURACY [15]

REFERENCE: [15]

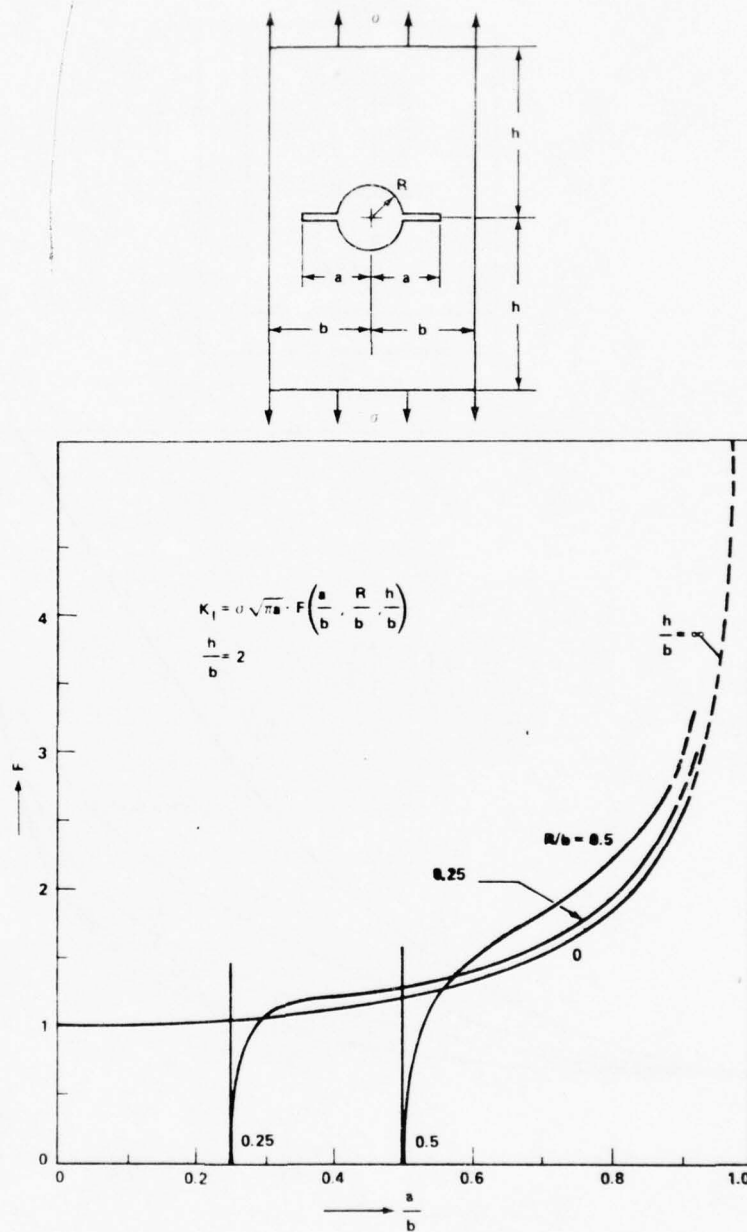


Figure 7.50. A plate containing a hole with two cracks.

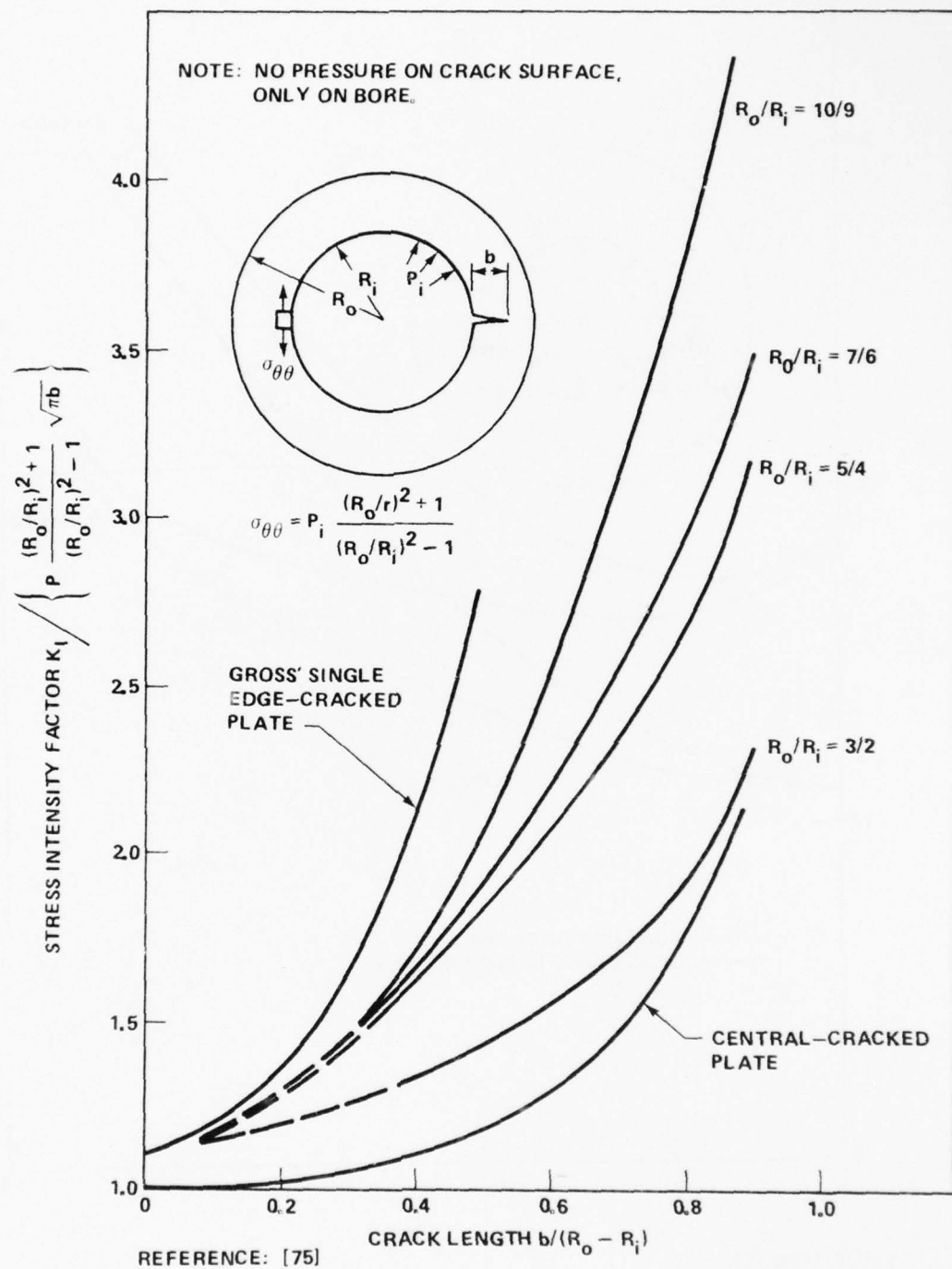
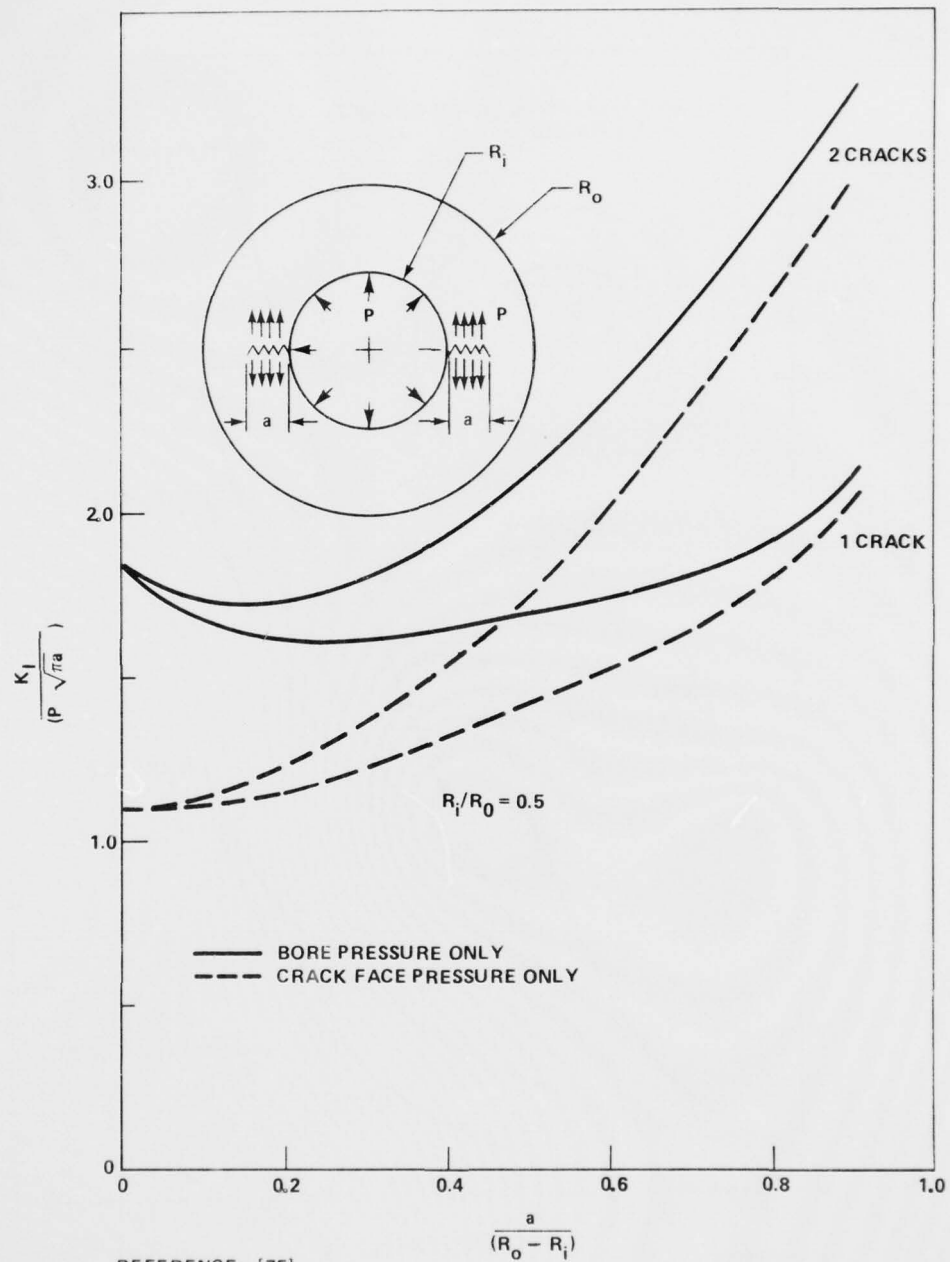


Figure 7.51. A cylindrical pressure vessel with an internal longitudinal crack.



REFERENCE: [75]

Figure 7.52. Two internal cracks in a cylindrical pressure vessel ( $R_i/R_o = 0.5$ ).

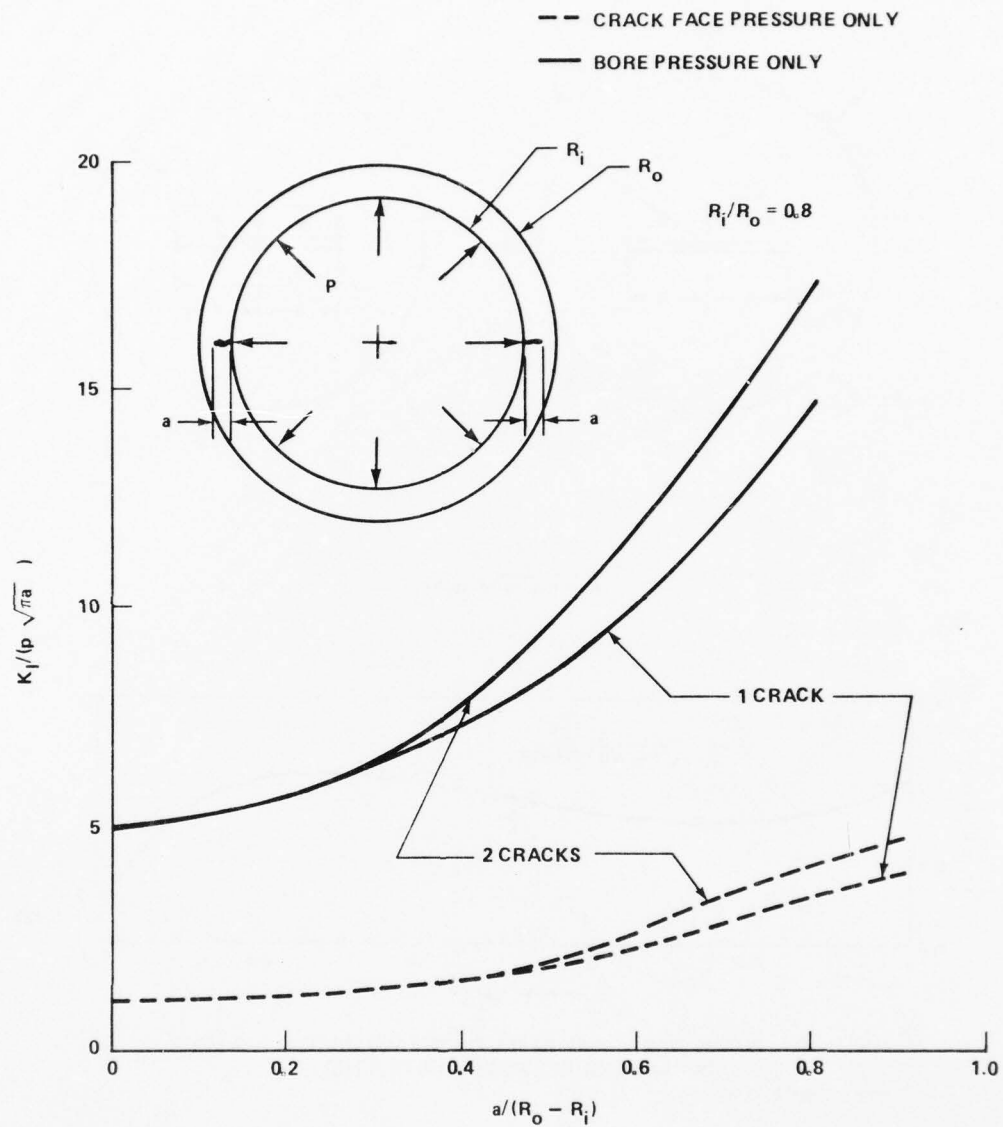
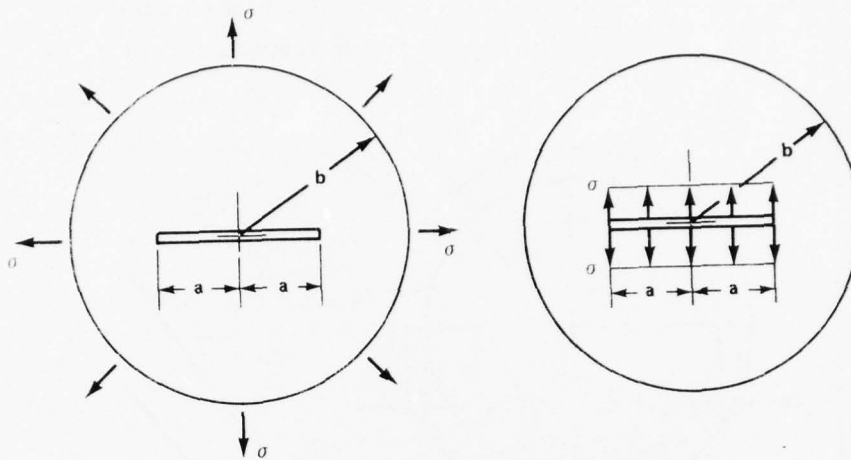
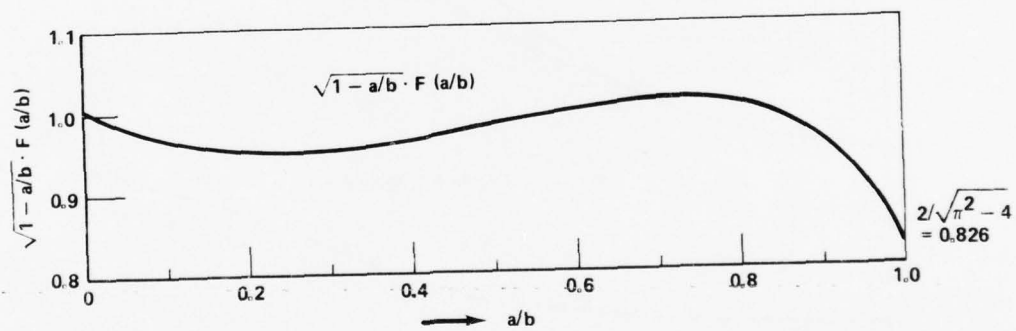


Figure 7.53. Two internal cracks in a cylindrical pressure vessel ( $R_i/R_o = 0.8$ ).



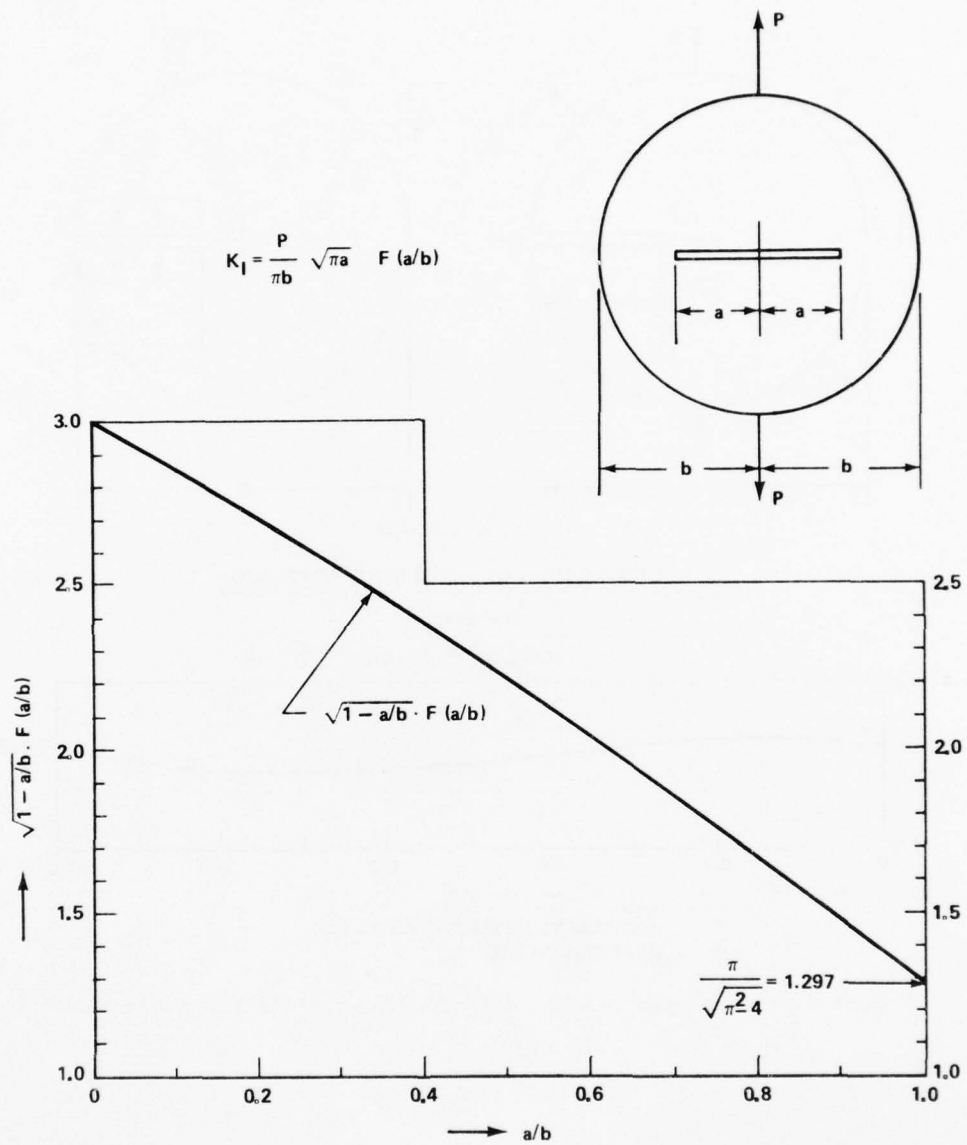


$$K_I = \sigma \sqrt{\pi a} \cdot F(a/b)$$



ACCURACY: CURVE WAS DRAWN BASED ON THE VALUES HAVING FOUR  
SIGNIFICANT FIGURES FOR  $0 \leq a/b \leq 0.9$  [15]  
REFERENCE: [15]

Figure 7.54. A center-cracked disk loaded with all-around tension.



ACCURACY: BETTER THAN 1% [15]  
REFERENCE: [15]

Figure 7.55. A center-cracked disk loaded with two tension forces.

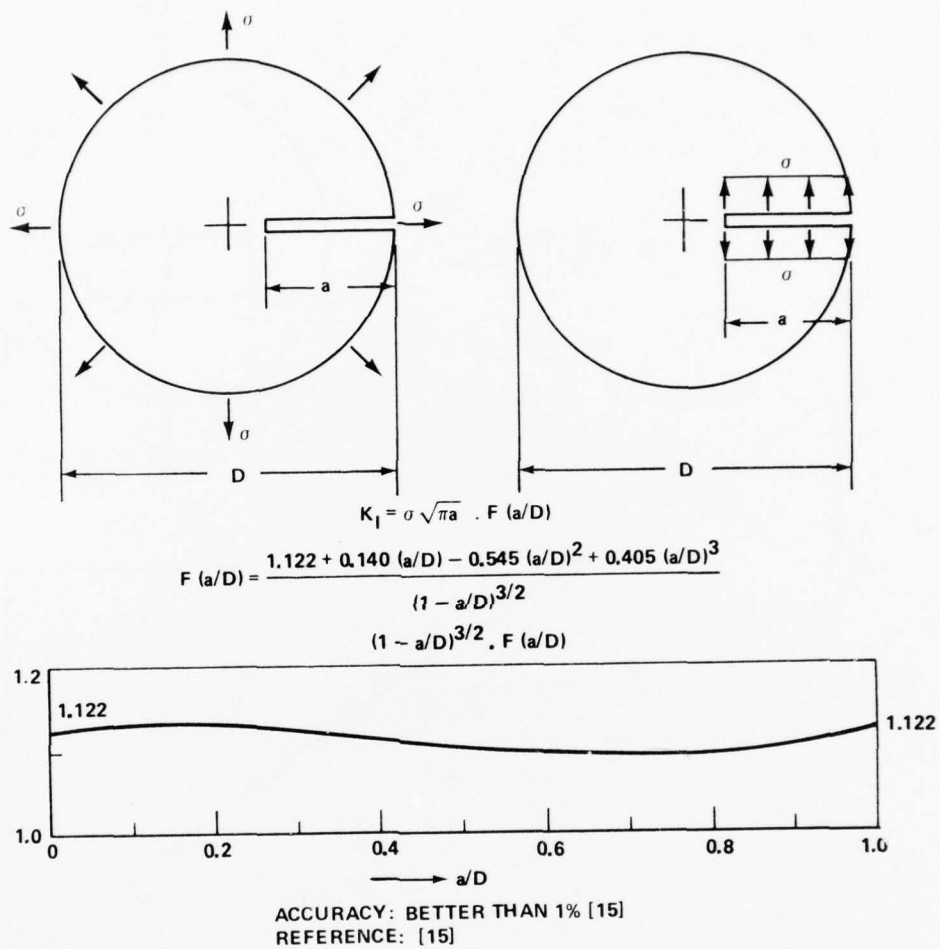
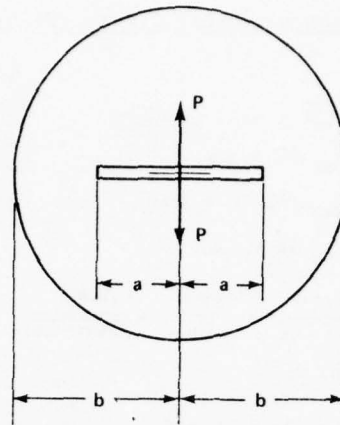
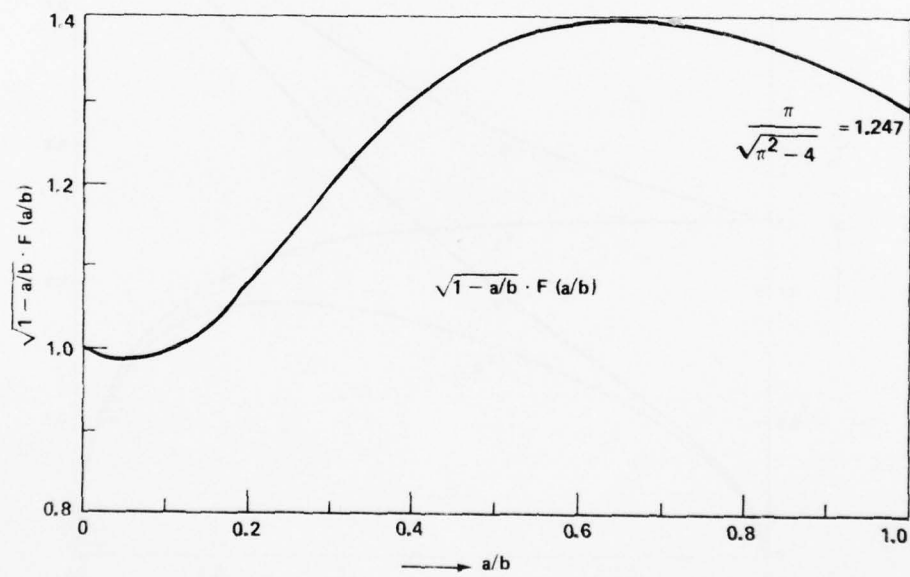


Figure 7.56. An edge-cracked disk loaded with all-around tension.



$$K_I = \frac{P}{\sqrt{\pi a}} \cdot F(a/b)$$



ACCURACY: EXPECTED TO BE BETTER THAN 2% [15]  
REFERENCE: [15]

Figure 7.57. A center-cracked disk loaded with two crack-opening forces.

7.5 Shafts with Circumferential Cracks (Figures 7.58, 7.59, and 7.60)

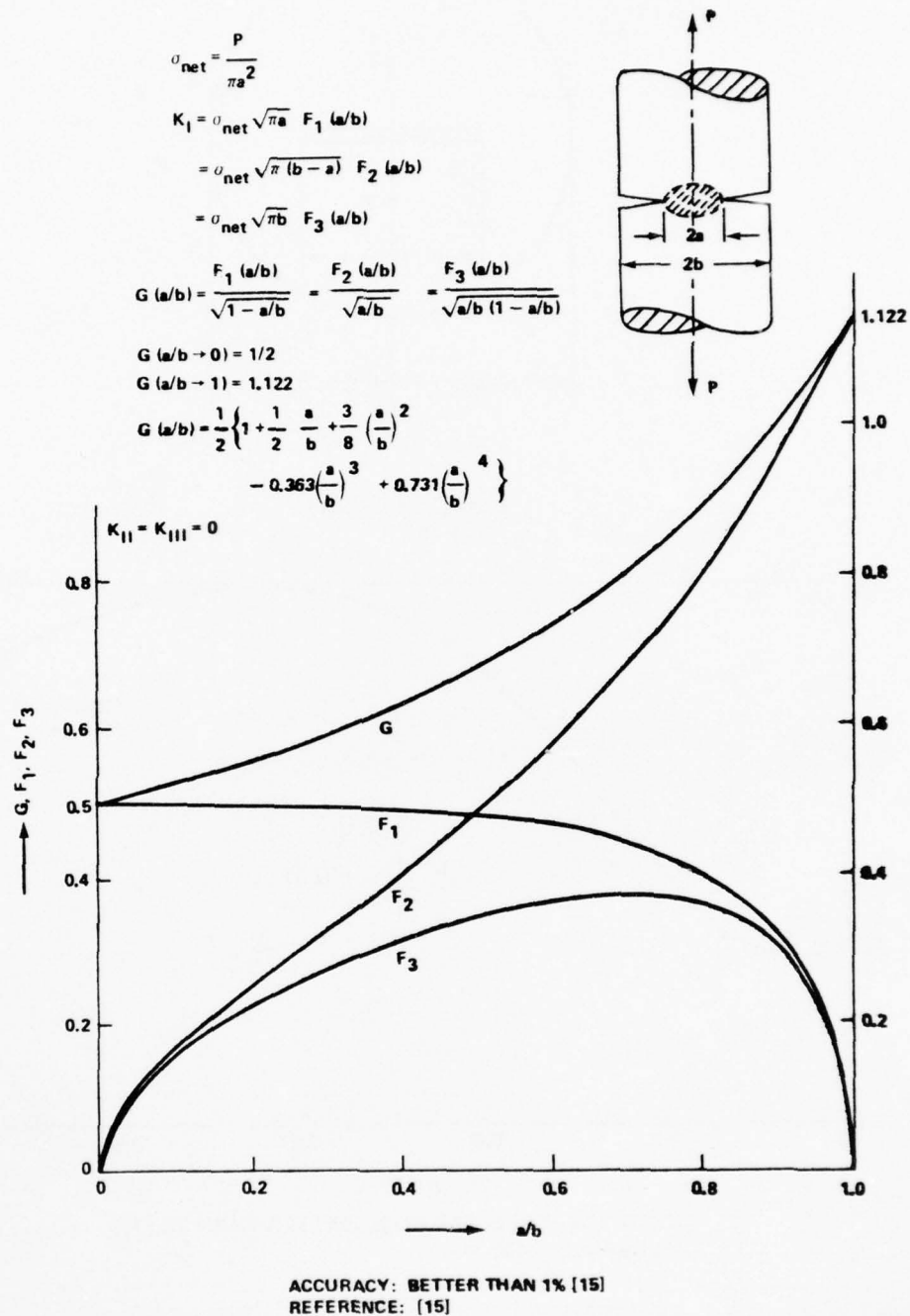
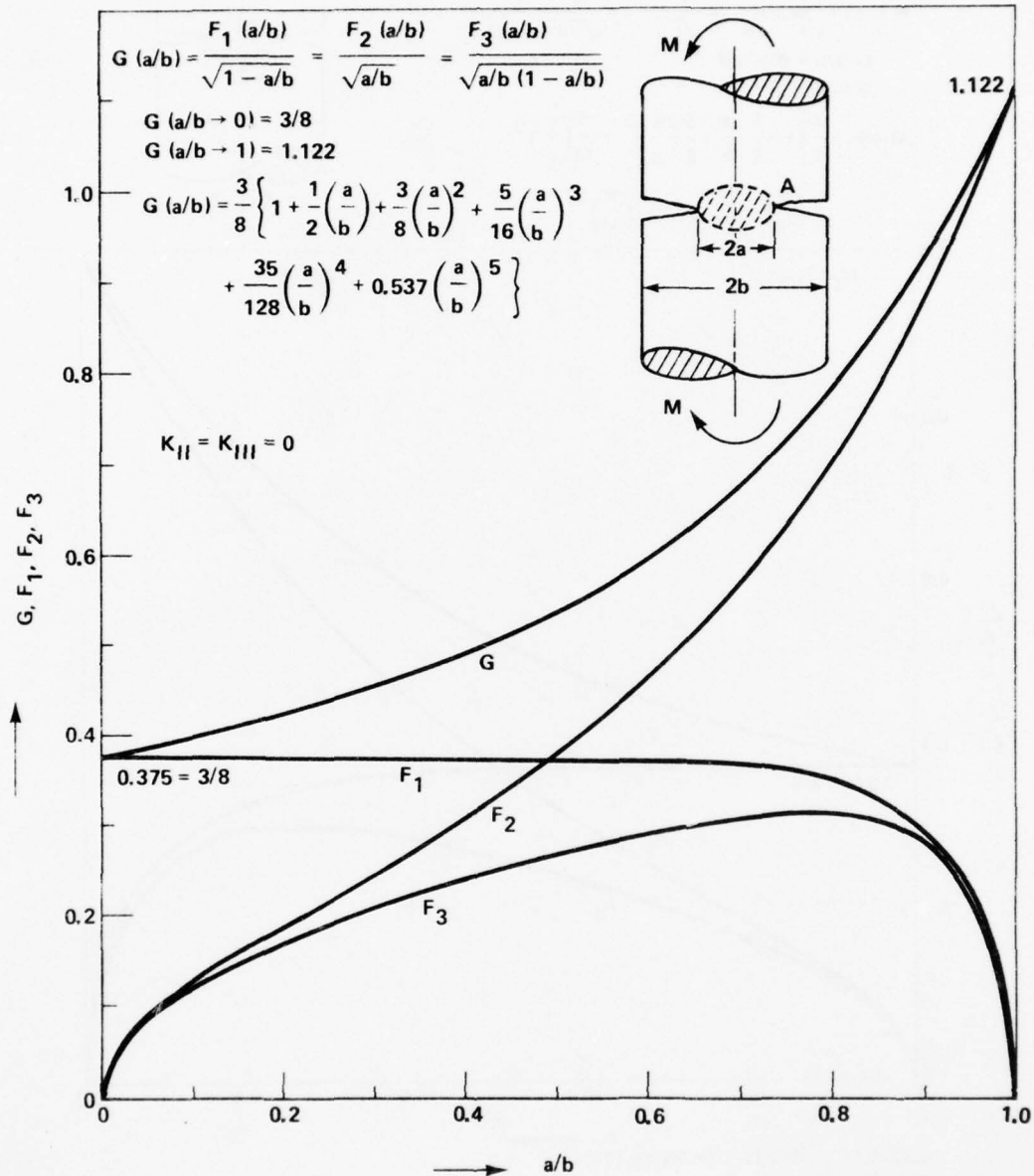


Figure 7.58. A circumferentially-cracked round bar loaded in tension.



$$\sigma_N = \frac{4M}{\pi a^3}$$

$$K_{IA} = \sigma_N \sqrt{\pi a} F_1(a/b) = \sigma_N \sqrt{\pi(b-a)} F_2(a/b) = \sigma_N \sqrt{\pi b} F_3(a/b)$$



ACCURACY: BETTER THAN 1% [15]

REFERENCE: [15]

Figure 7.59. A circumferentially-cracked round bar loaded in bending.

$$\tau_N = \frac{2T}{\pi a^3}$$

$$K_{III} = \tau_N \sqrt{\pi a} F_1(a/b) = \tau_N \sqrt{\pi(b-a)} F_2(a/b)$$

$$= \tau_N \sqrt{\pi b} F_3(a/b)$$

$$G(a/b) = \frac{F_1(a/b)}{\sqrt{1-a/b}} = \frac{F_2(a/b)}{\sqrt{a/b}} = \frac{F_3(a/b)}{\sqrt{a/b(1-a/b)}}$$

$$G(a/b \rightarrow 0) = 3/8$$

$$G(a/b \rightarrow 1) = 1$$

$$G(a/b) = \frac{3}{8} \left\{ 1 + \frac{1}{2} \frac{a}{b} + \frac{3}{8} \left( \frac{a}{b} \right)^2 + \frac{5}{16} \left( \frac{a}{b} \right)^3 + \frac{35}{128} \left( \frac{a}{b} \right)^4 + 0.208 \left( \frac{a}{b} \right)^5 \right\}$$

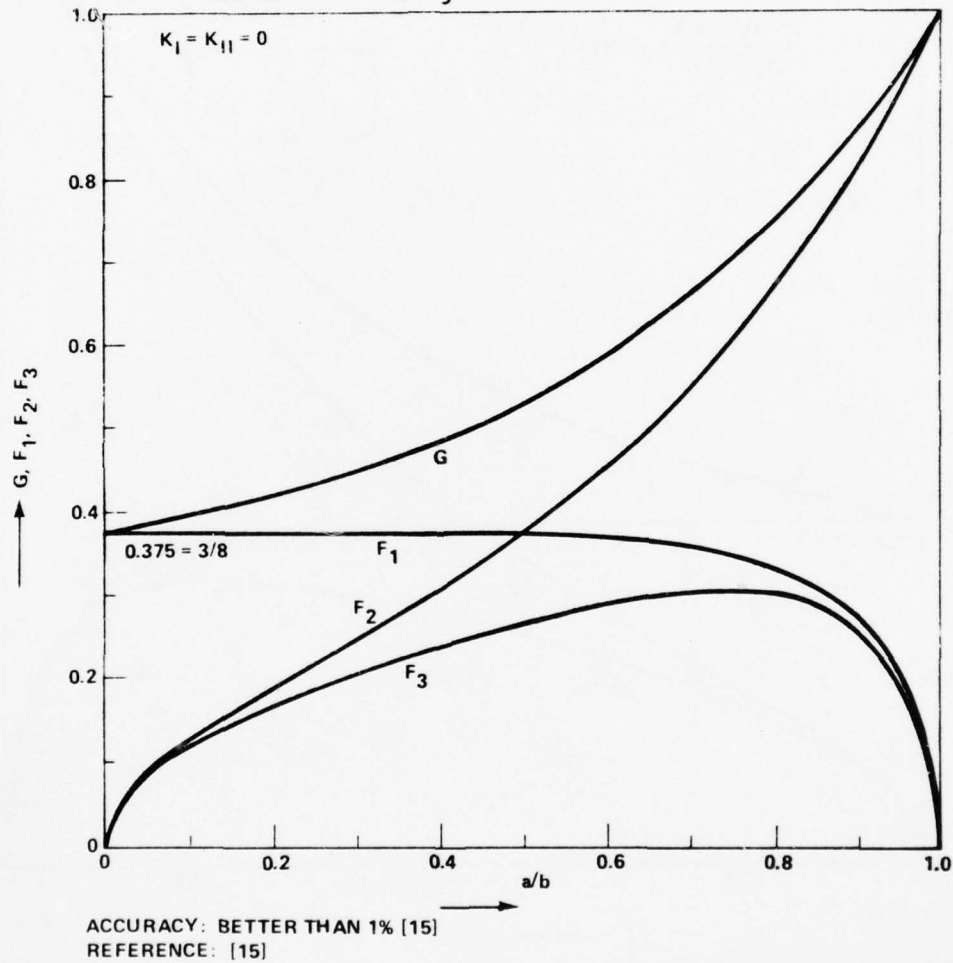
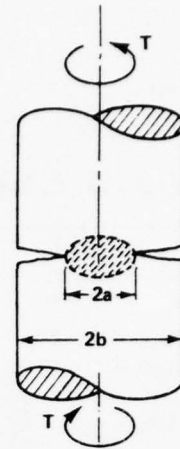


Figure 7.60. A circumferentially-cracked round bar loaded in torsion.

7.6 Large Stiffened Plates with Cracks (Figures 7.61 through 7.70)

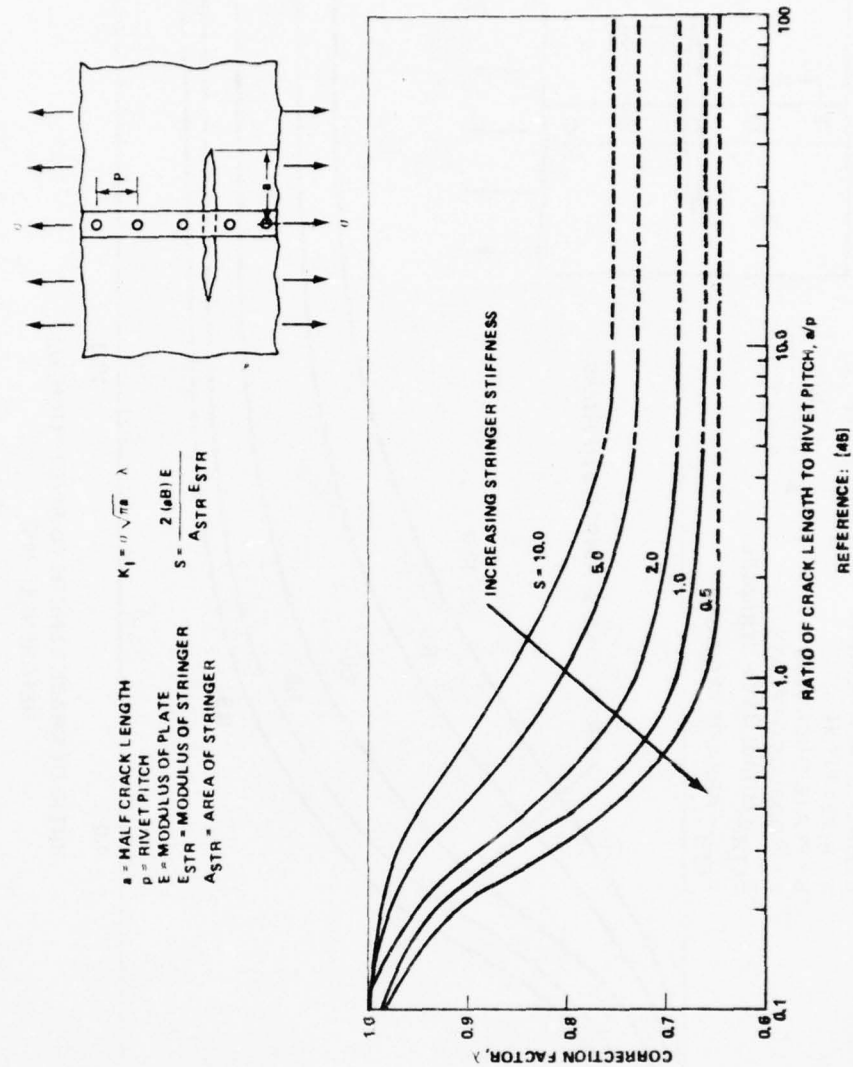


Figure 7.61. A symmetric crack in a plate under a riveted stringer - crack between rivets.

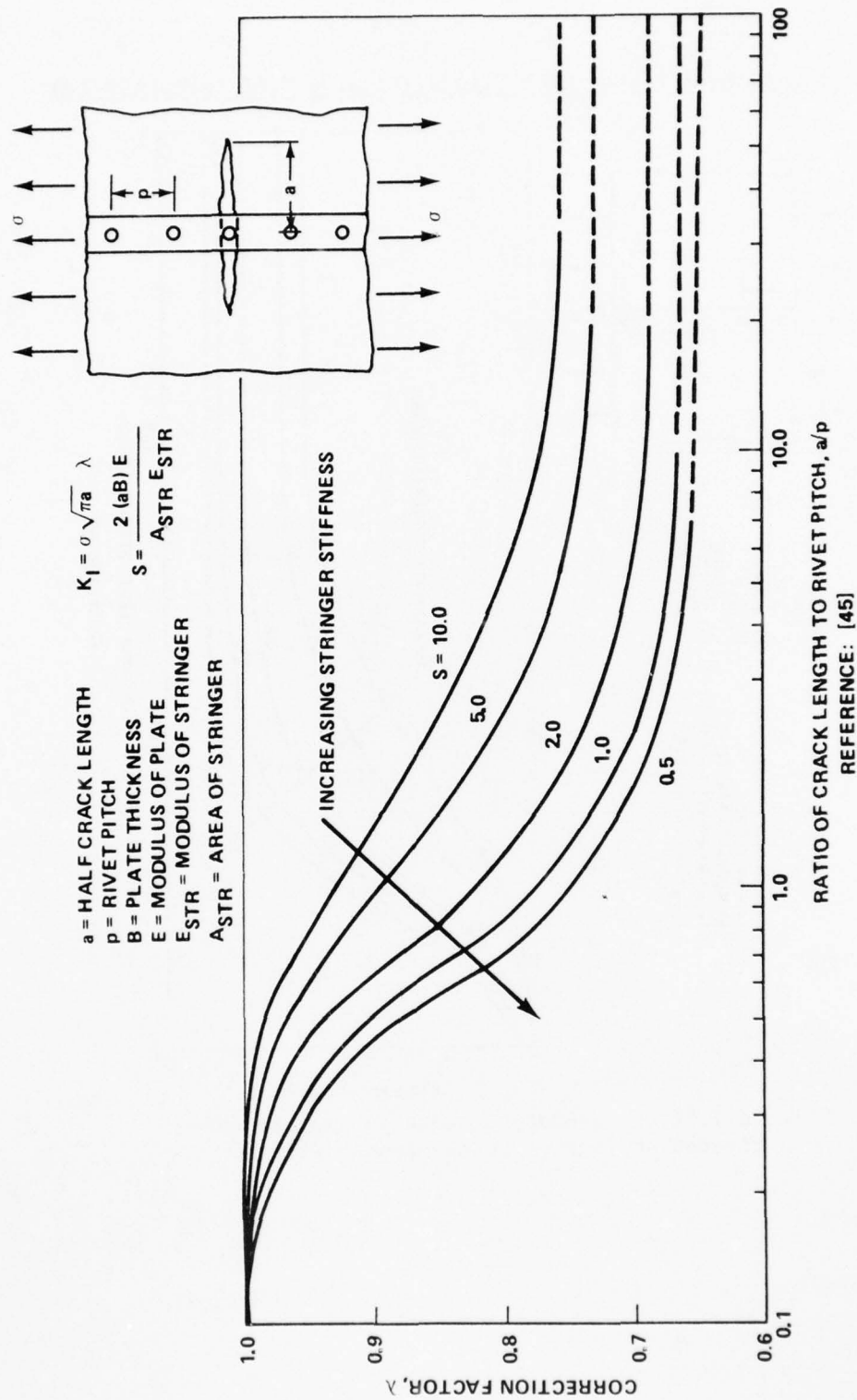


Figure 7.62. A symmetric crack in a plate under a riveted stringer - crack through a rivet hole.

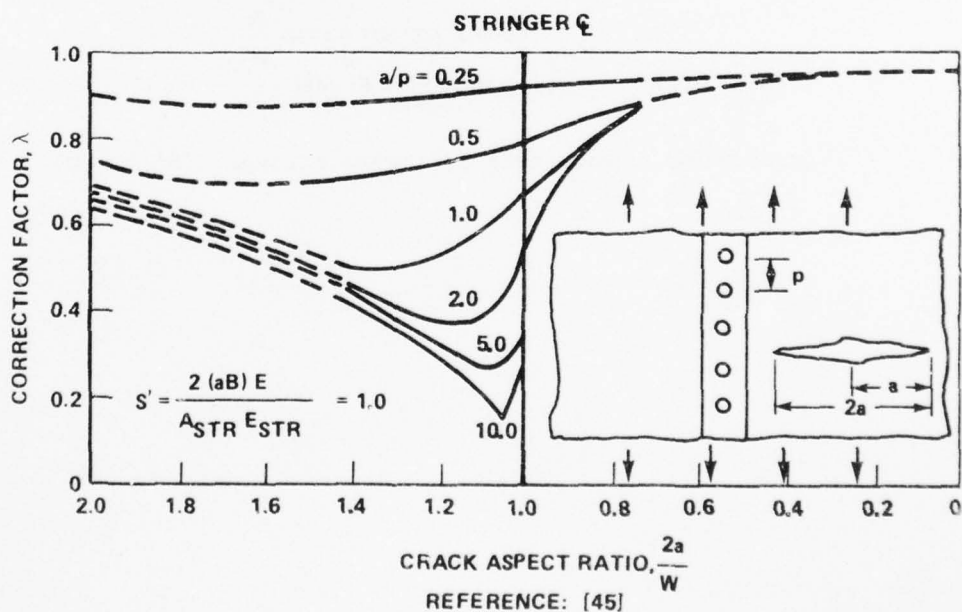
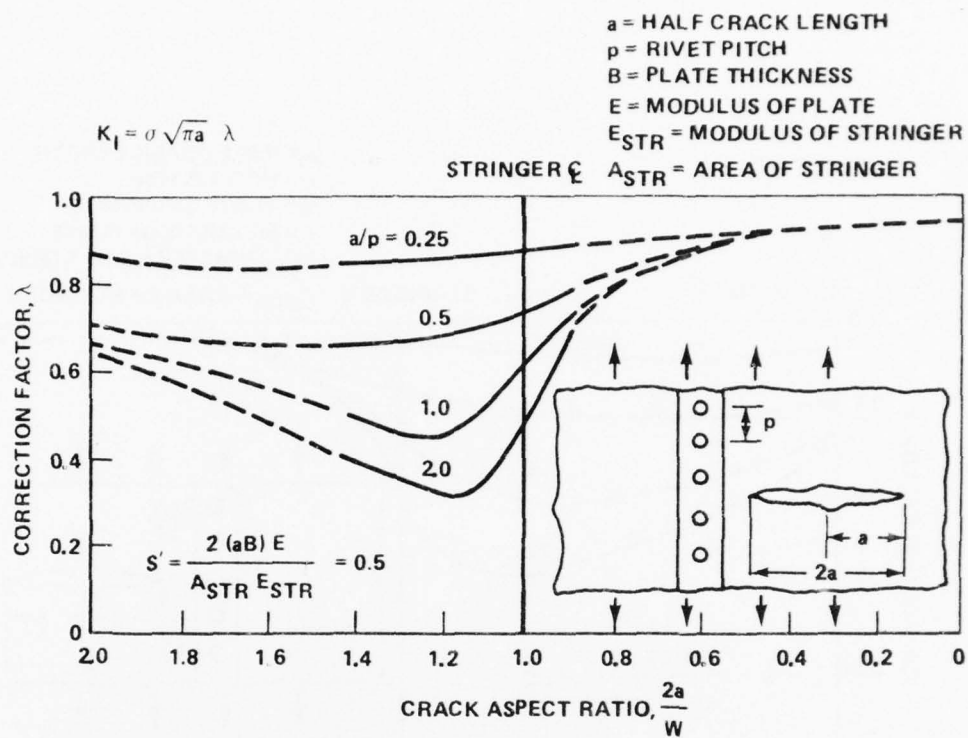


Figure 7.63. Crack near a riveted stringer ( $S' = 0.5$  and  $1.0$ ).



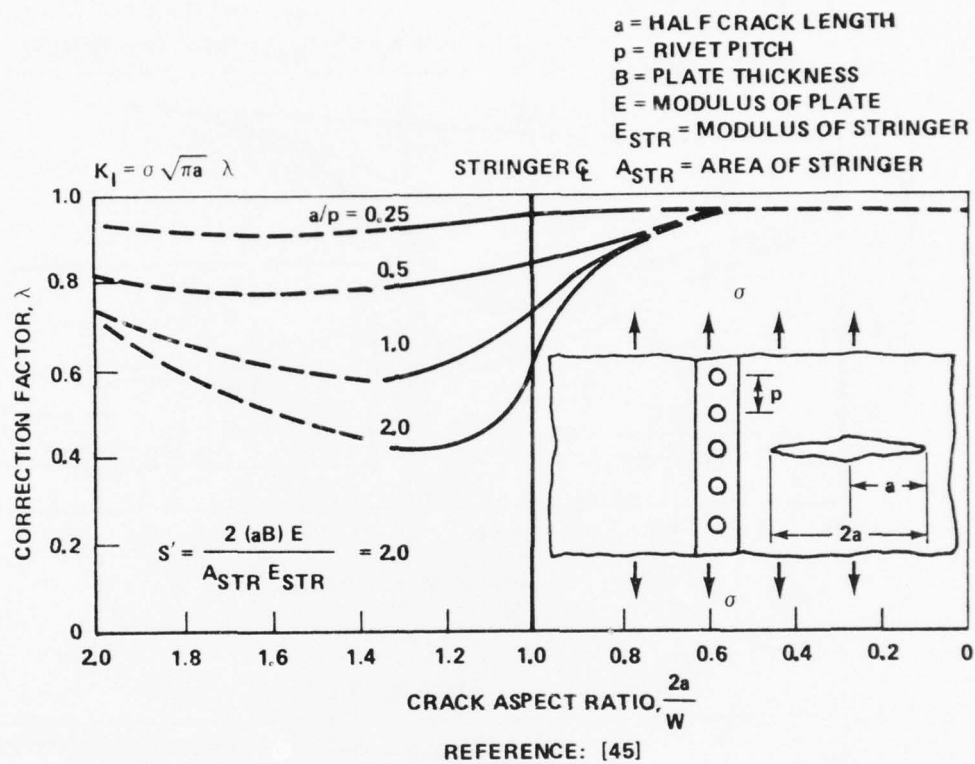


Figure 7.64. Crack near a riveted stringer ( $S' = 2.0$ ).

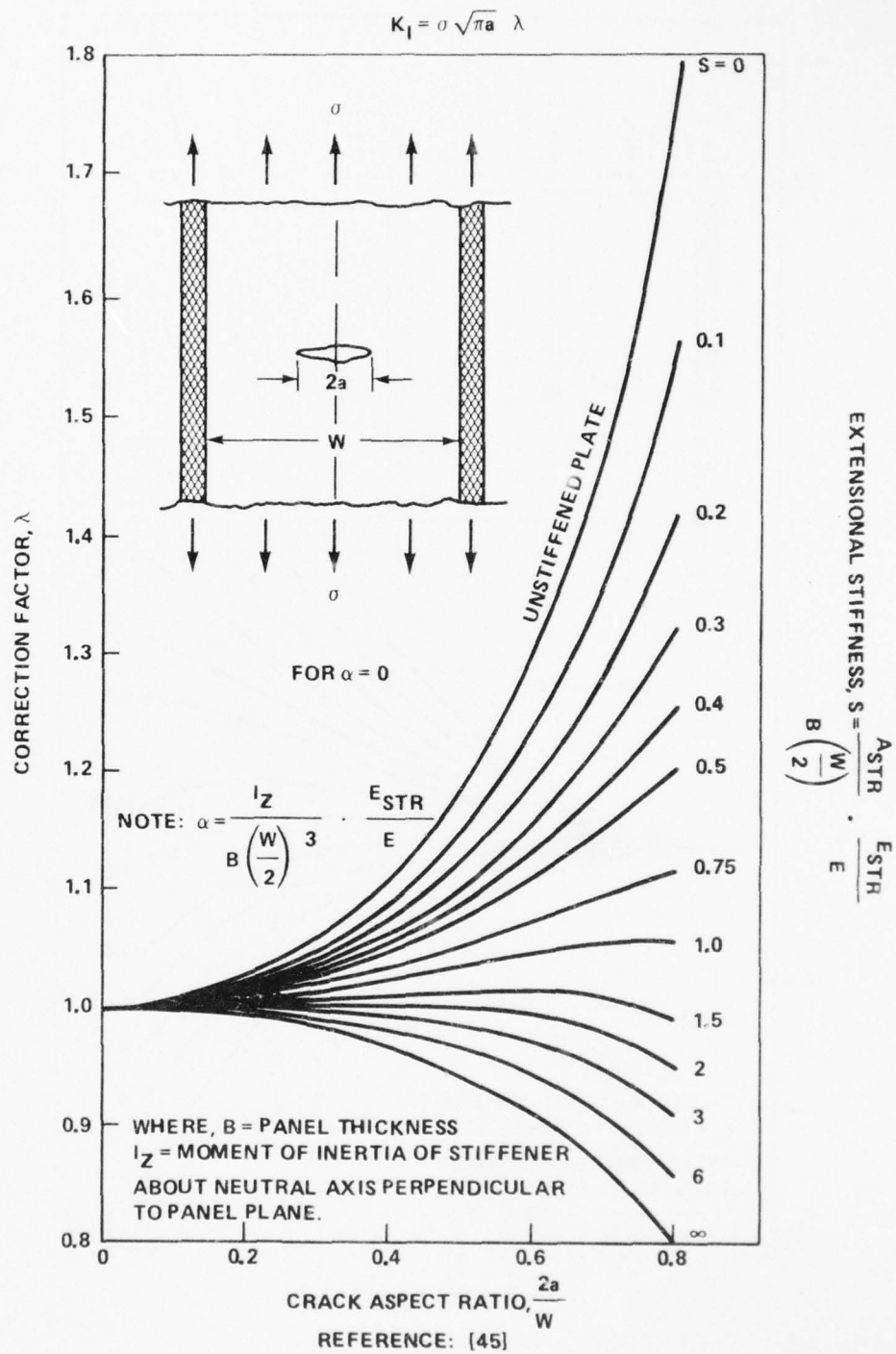


Figure 7.65. Edge-stiffened center-cracked plate ( $\alpha = 0$ ).

A038 457

ARMY MISSILE RESEARCH DEVELOPMENT AND ENGINEERING LAB--ETC F/G 20/11  
FRACTURE MECHANICS DESIGN HANDBOOK.(U)

DEC 76 D G SMITH, B R MULLINIX  
RL-77-5

CLASSIFIED

3 OF 3

AD  
A038457

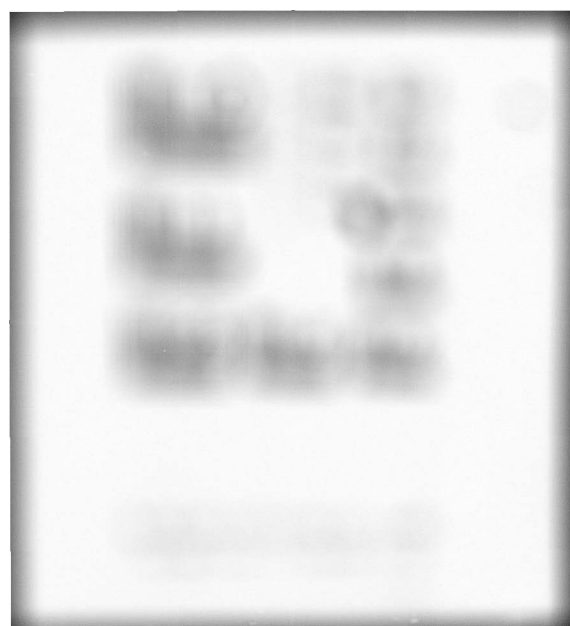
NL

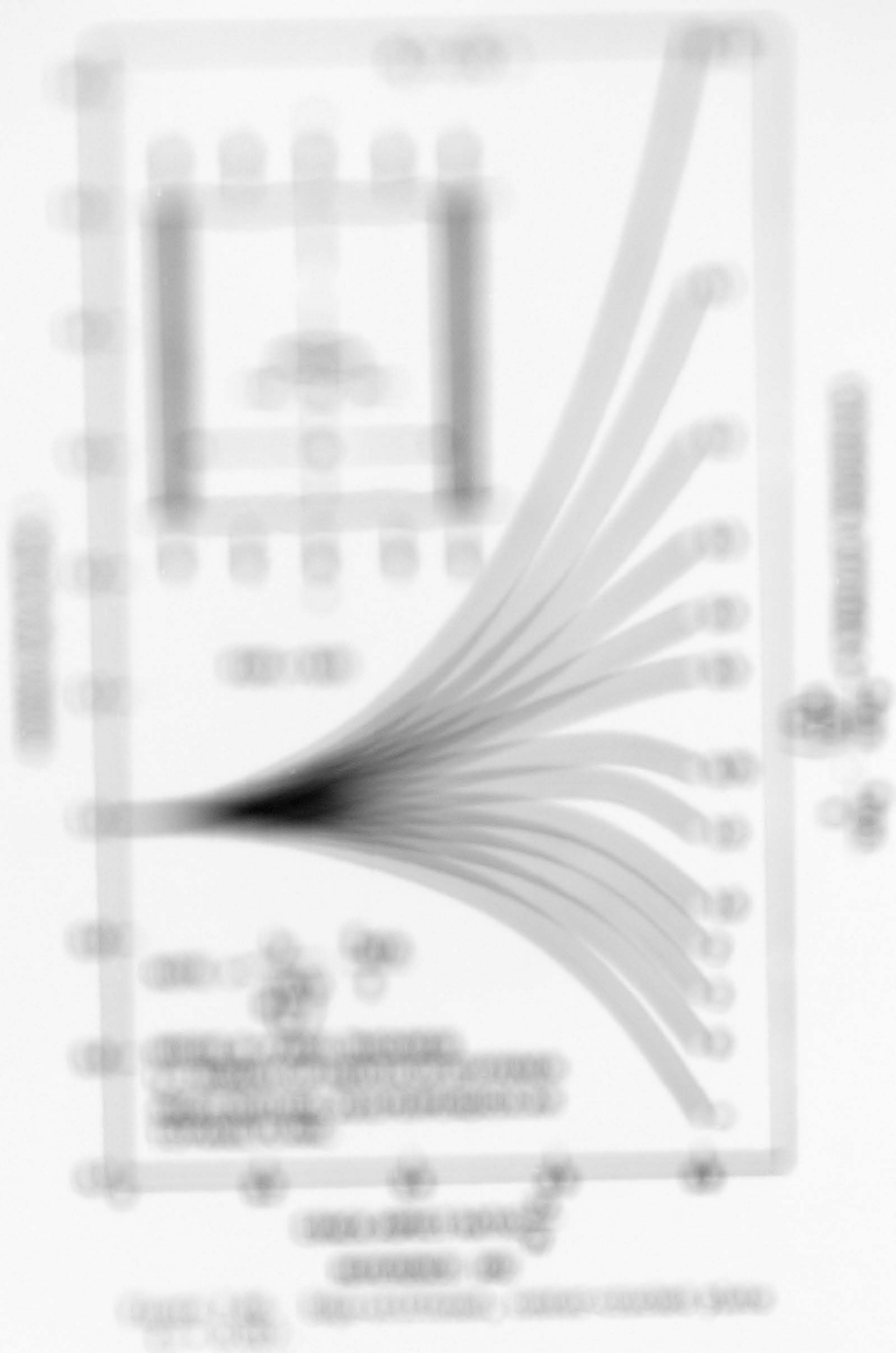


END

DATE  
FILMED

5-77







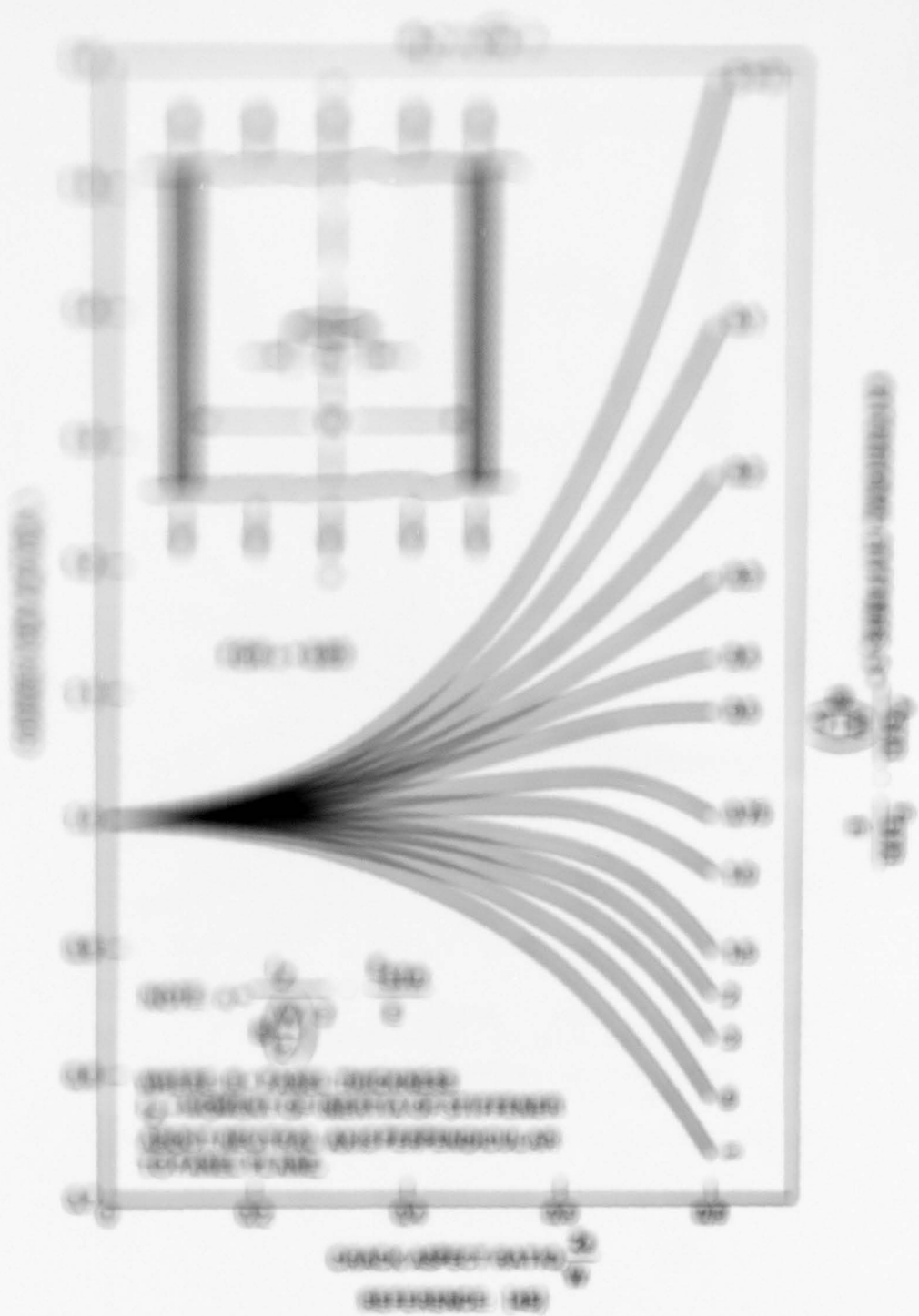


Figure 1. (a) Dependence of the coordinate  $y$  on the coordinate  $x$  ( $\alpha = 0.05$ ).

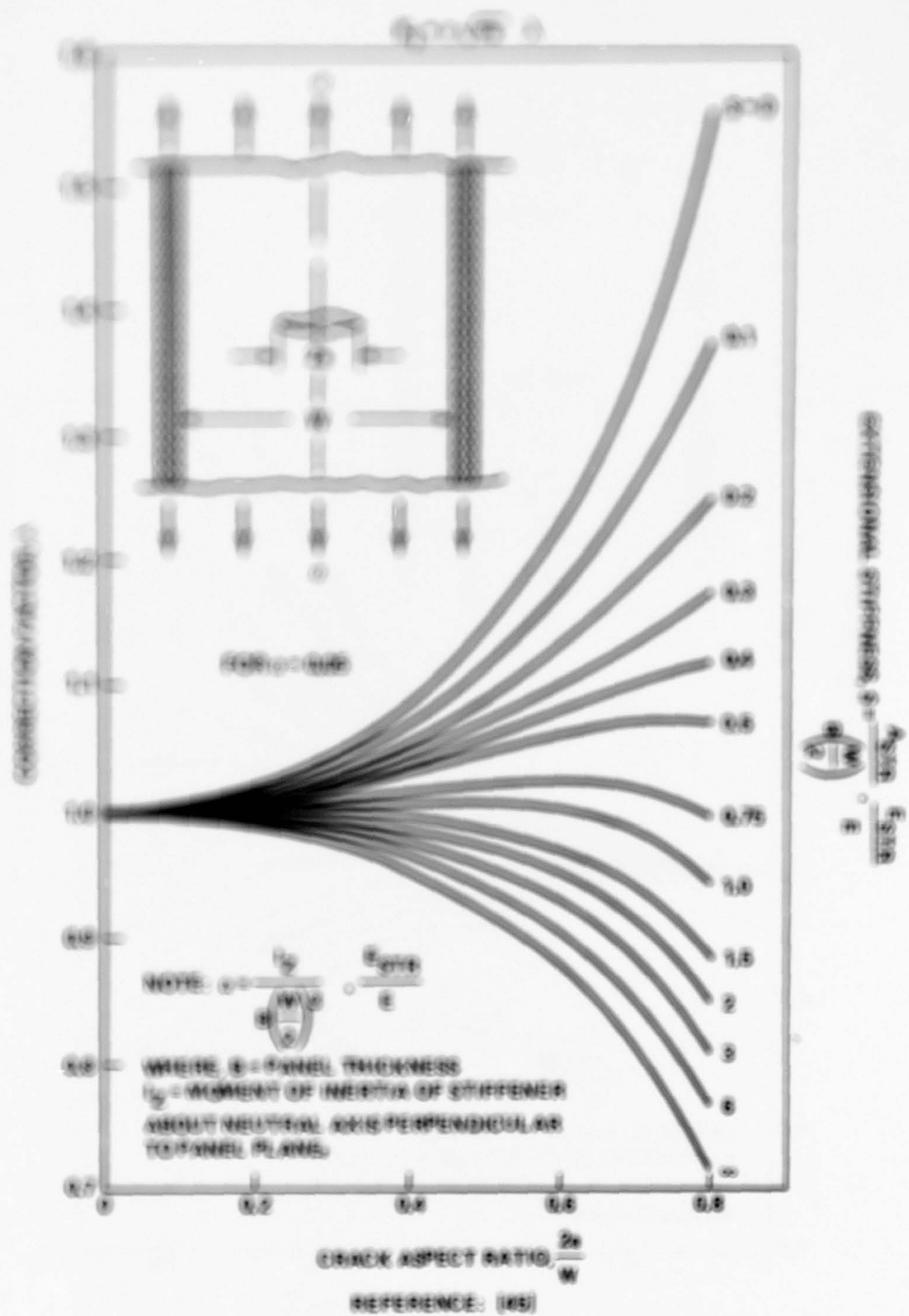


Figure 7.68. Edge-stiffened, center-cracked plate ( $\alpha = 0.05$ ).

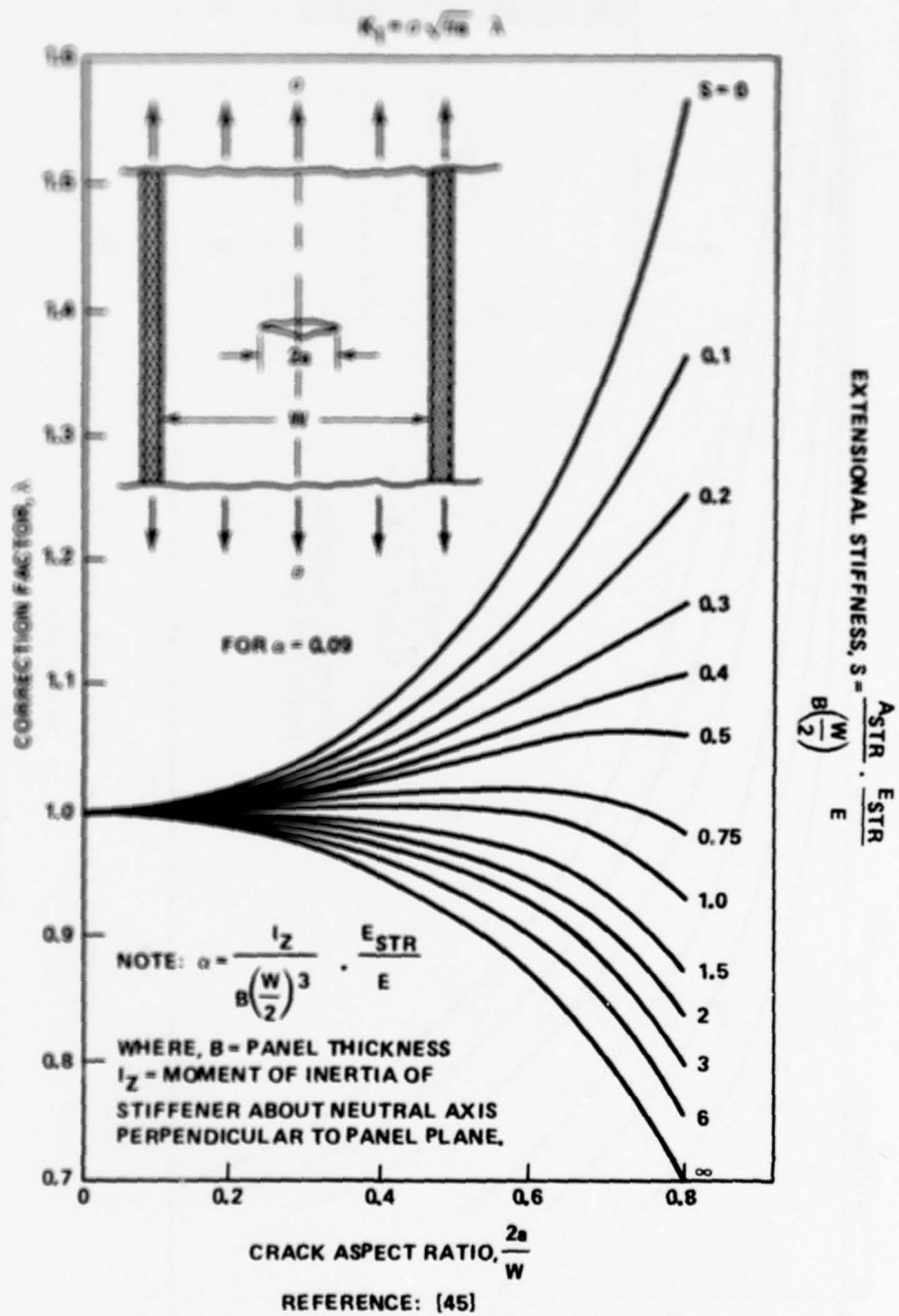


Figure 7.69. Edge-stiffened, center-cracked plate ( $\alpha = 0.09$ ).

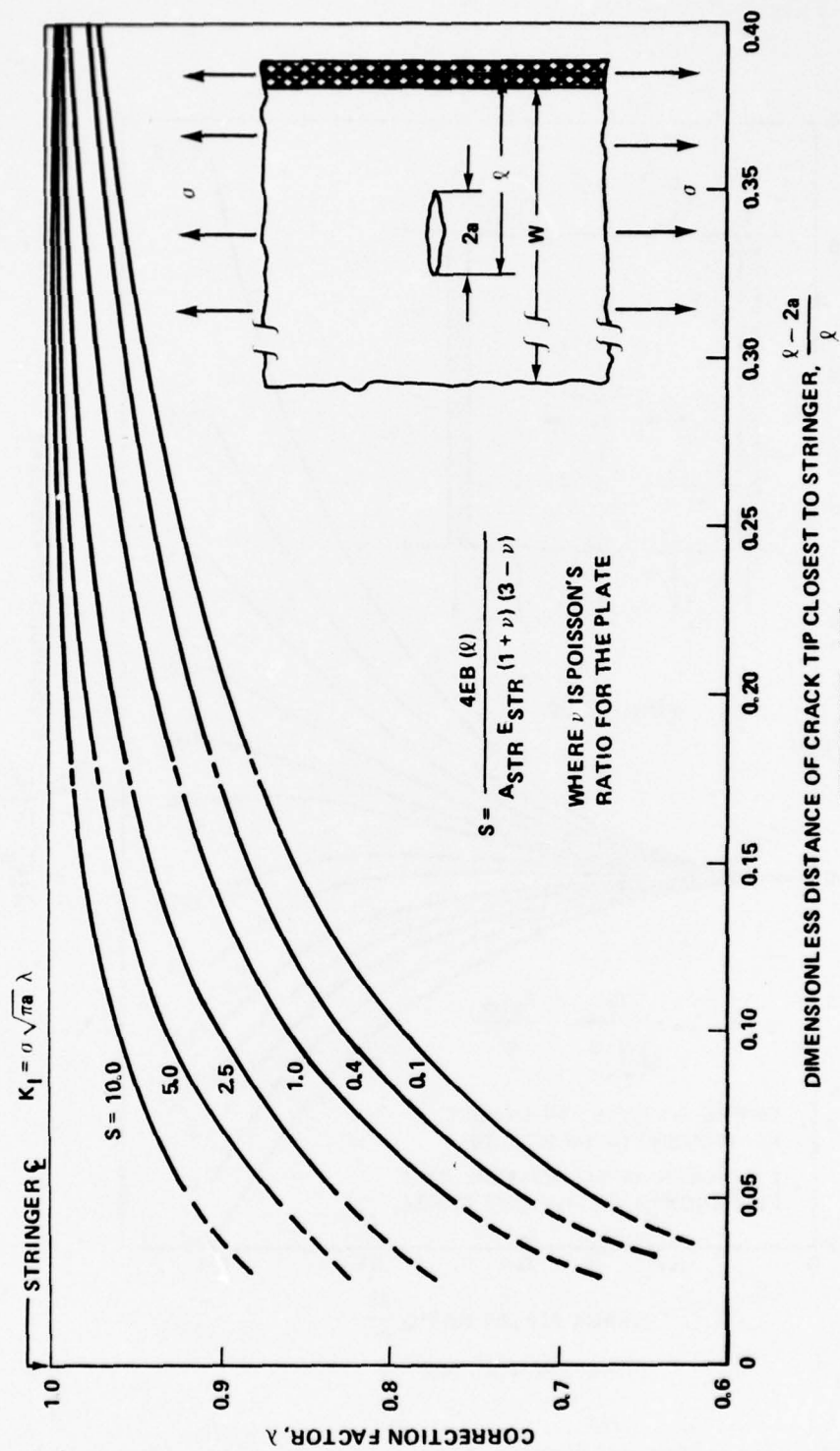
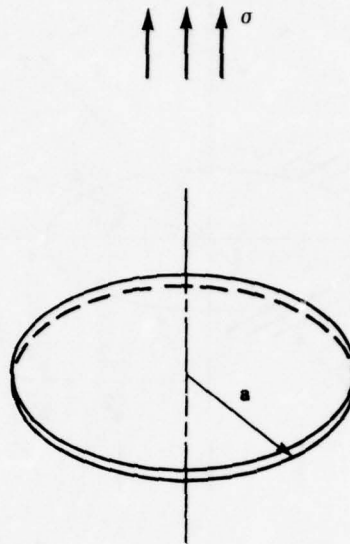


Figure 7.70. Nonsymmetric crack in an edge-stiffened plate.

7.7 Three-Dimensional Solutions for Surface Flaws, Embedded Flaws, and Through Flaws (Figures 7.71 and 7.91)



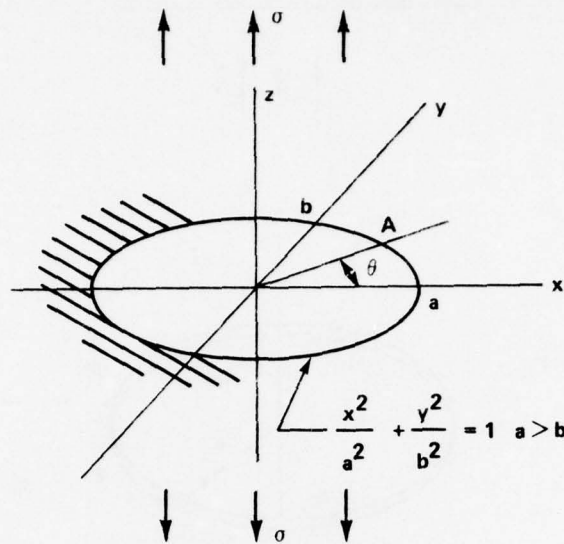
$$K_I = \frac{2}{\pi} \sigma \sqrt{\pi a}$$

$$K_{II} = K_{III} = 0$$

ACCURACY: EXACT  
REFERENCES: [11, 15]

Figure 7.71. Penny-shaped crack.





$$K_{I,A} = \frac{\sigma \sqrt{\pi b}}{E(k)} \left\{ \sin^2 \theta + \frac{b^2}{a^2} \cos^2 \theta \right\}^{1/4}$$

$$E(k) = \int_0^{\pi/2} \sqrt{1 - k^2 \sin^2 \varphi} \, d\varphi$$

$$k^2 = 1 - b^2/a^2$$

$$K_{I,MAX} = K_I(\theta = \pm \pi/2) = \frac{\sigma \sqrt{\pi b}}{E(k)}$$

$$K_I(a=b) = \frac{2\sigma}{\pi} \sqrt{\pi a}$$

$$K_I(a \rightarrow \infty) = \sigma \sqrt{\pi b}$$

NOTE: SEE TABLE 7.1 FOR VALUES OF E (k)

ACCURACY: EXACT

REFERENCES: [15, 45]

Figure 7.72. Elliptical crack loaded in tension.

TABLE 7.1. ELLIPTIC INTEGRALS, E(k) AND K(k)

k	K(k)	E(k)
0	1.5708	1.5708
0.0871	1.5738	1.5678
0.1736	1.5828	1.5589
0.2588	1.5981	1.5442
0.3420	1.6200	1.5238
0.4226	1.6490	1.4981
0.5000	1.6858	1.4675
0.5736	1.7312	1.4323
0.6428	1.7868	1.3931
0.7071	1.8541	1.3506
0.7660	1.9356	1.3055
0.8192	2.0347	1.2587
0.8660	2.1565	1.2111
0.9063	2.3088	1.1638
0.9397	2.5046	1.1184
0.9659	2.7681	1.0764
0.9848	3.1525	1.0401
0.9903	3.6519	1.0278
0.9945	4.0528	1.0172
0.9976	4.7427	1.0087
0.9994		1.0026
1.0000	$\infty$	1.0000

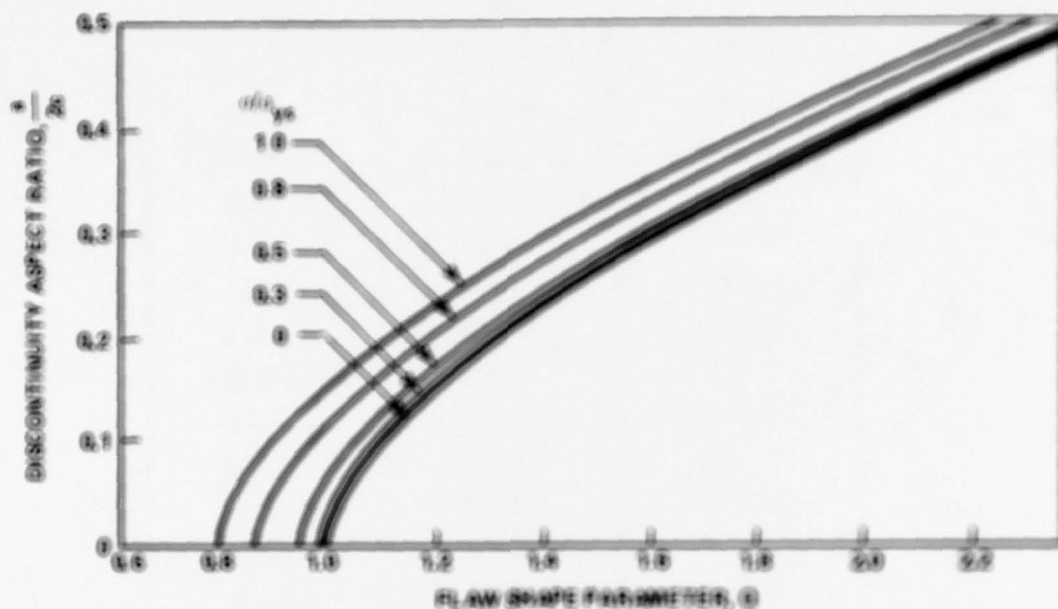
Note: The definition of integrals in the above tabulation are:

$$K(k) = \int_0^{\pi/2} \frac{d\phi}{\sqrt{1 - k^2 \sin^2 \phi}}, \text{ the complete}$$

elliptic integral of the first kind and

$$E(k) = \int_0^{\pi/2} \sqrt{1 - k^2 \sin^2 \phi} d\phi, \text{ the complete}$$

elliptic integral of the second kind.



SURFACE FLOW

$$h_{1, \text{max}} = 1.17 \sqrt{\frac{h}{\phi}}$$

$$\phi = \left[ \frac{E(h)}{E(0)} \right]^2 = 0.212 \left( \frac{h}{v_{yp}} \right)^2$$

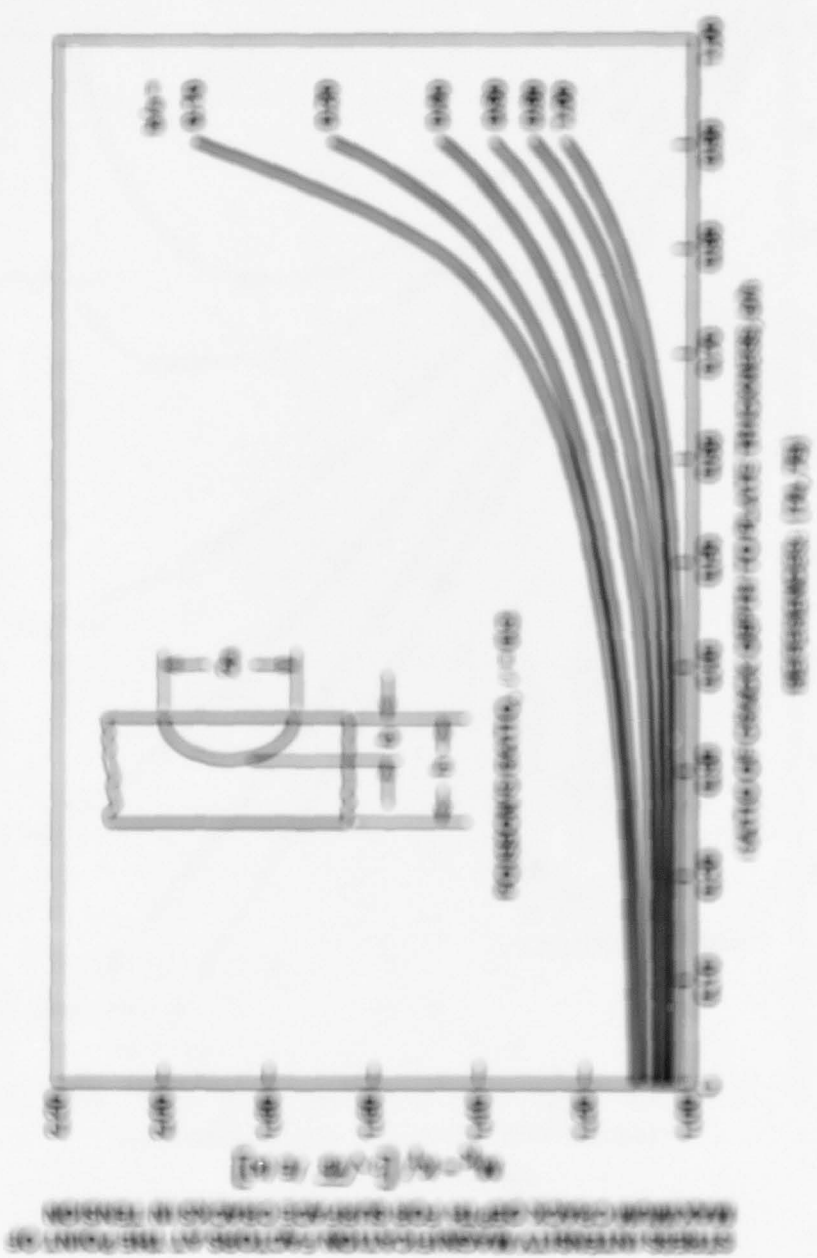
$$\psi^2 = 1 - \psi_{10}^2$$

NOTE:  $\phi$  CONTAINS A PLACEDITY CORRECTION, FOR THE CASE OF  $u/v_{yp} = 0$ , THE PARAMETER,  $\sqrt{\phi}$  BECOMES  $E(h)$  THE COMPLETE ELLIPTIC INTEGRAL OF THE SECOND KIND (VALUES GIVEN IN TABLE 7.1)

REFERENCE: (10)

Figure 7.73. The free solution for the surface flow loaded at tension.

Figure 1. Comparison of the calculated and experimental results for the case of the flow of water in the pipe.



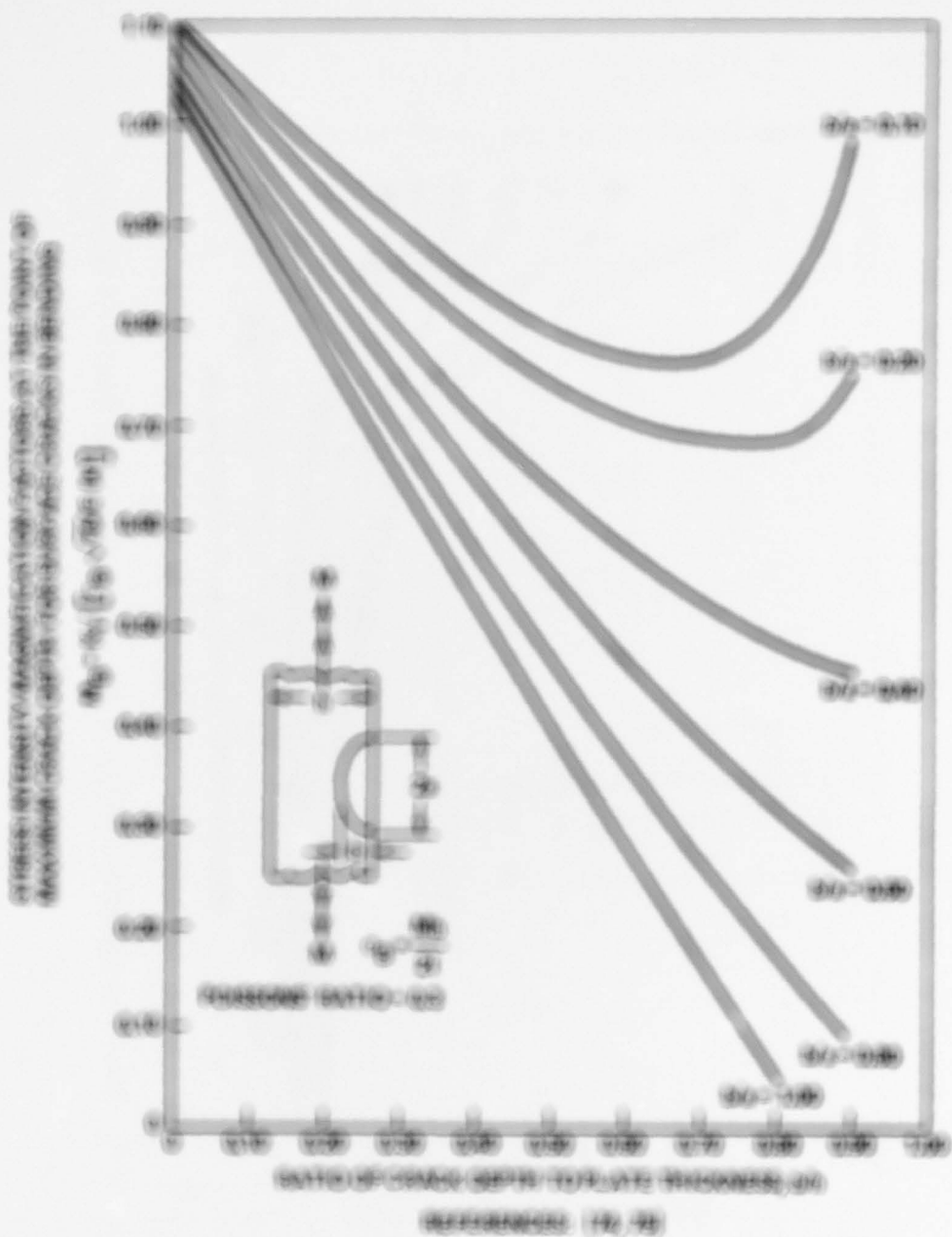


Figure 7.5. The relationship between the ratio of the maximum to the minimum value of the function.



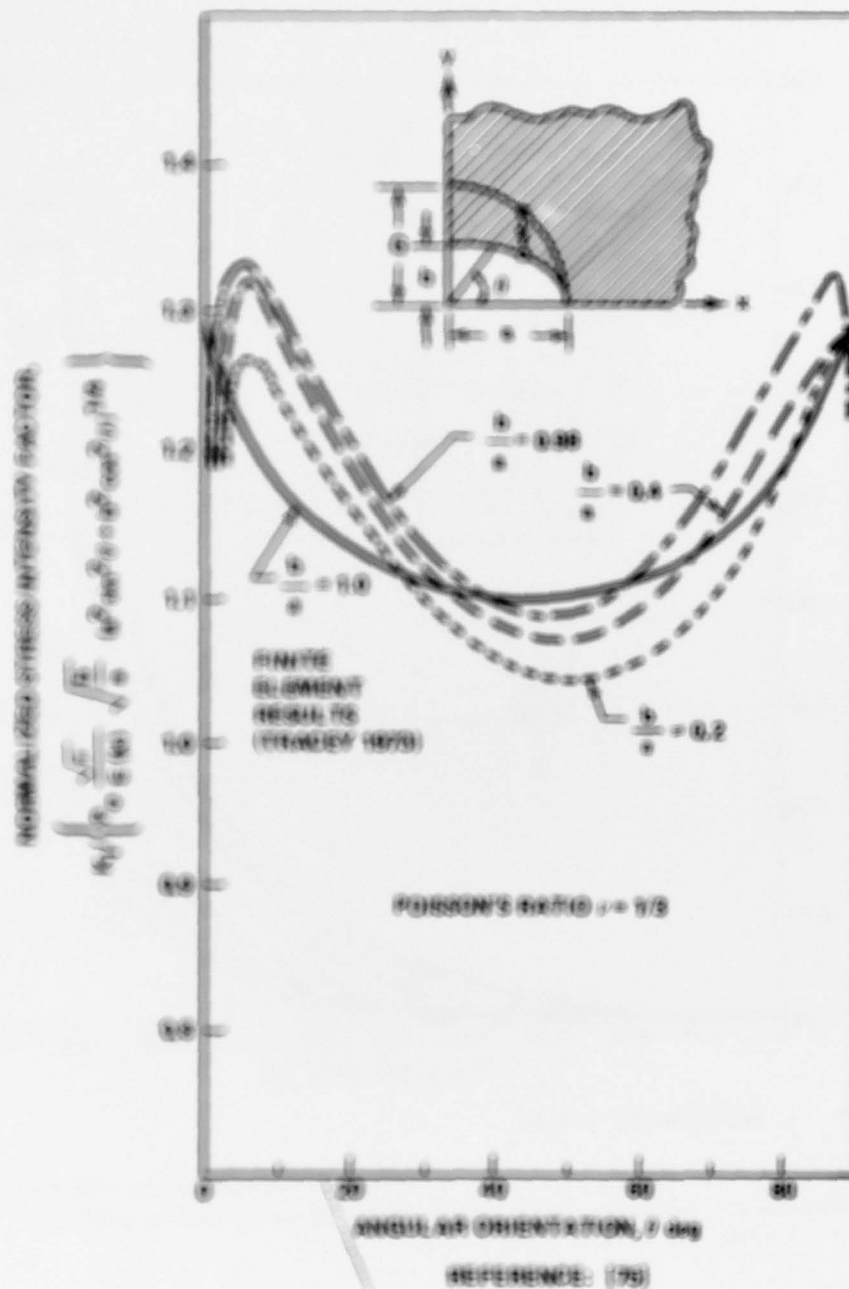


Figure 7.76. A corner flaw in a quarter infinite solid subjected to uniaxial tension.

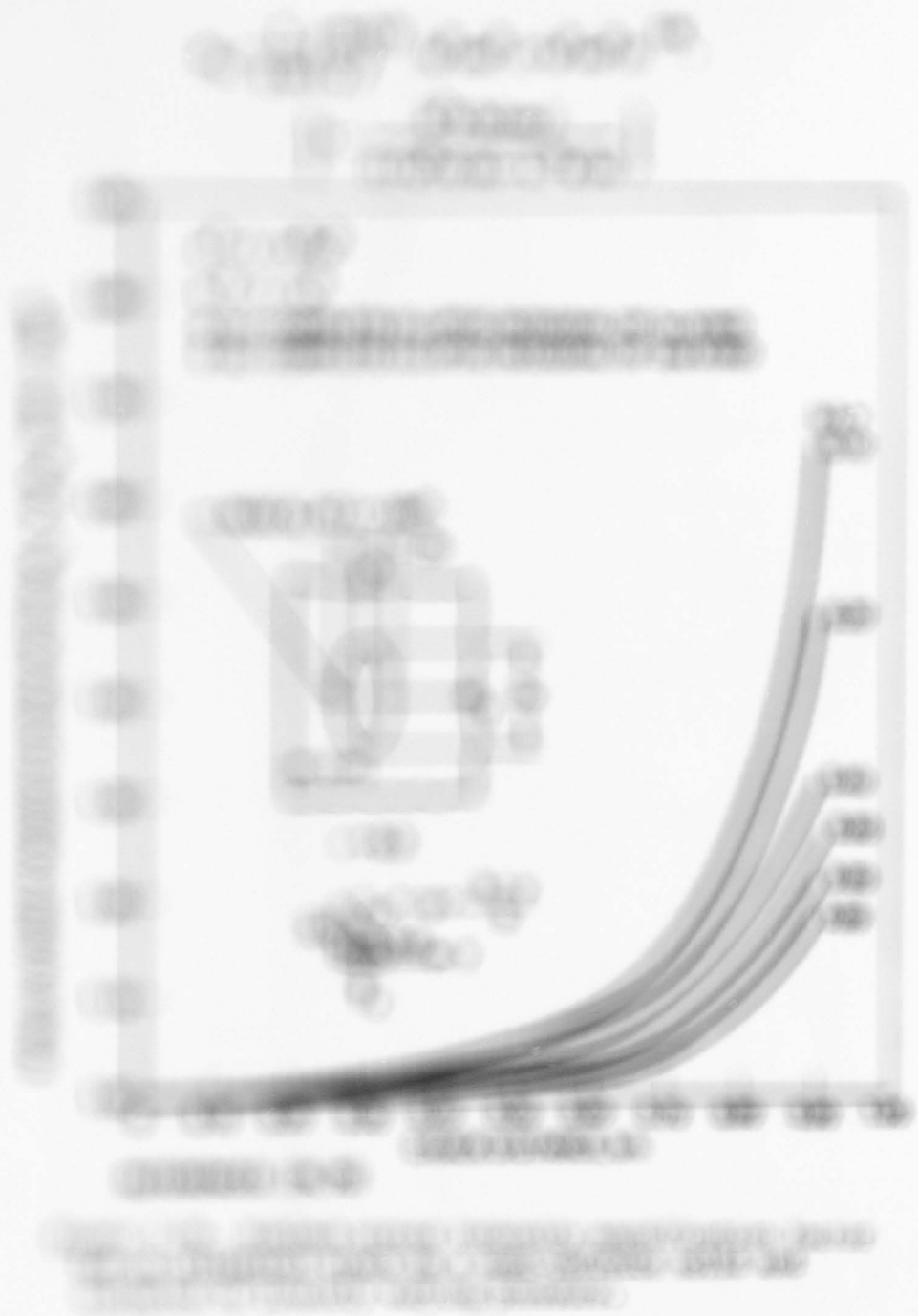




Figure 1.1. A graph showing the relationship between the rate of change of the function,  $dy/dx$ , and the function value,  $y$ .

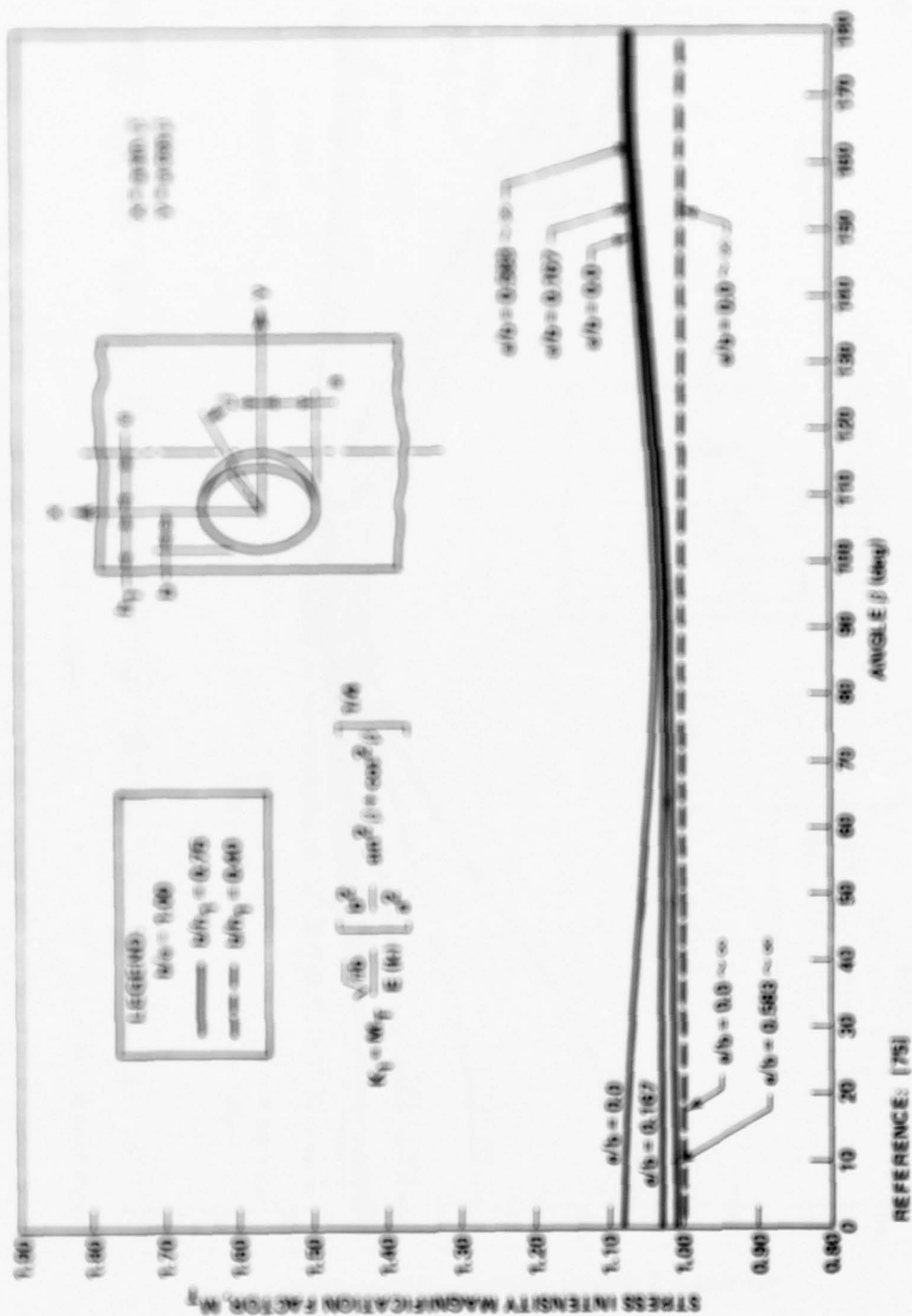


Figure 7.80. An elliptical crack in a plate subjected to uniaxial tension ( $b/a = 1.00$ ).

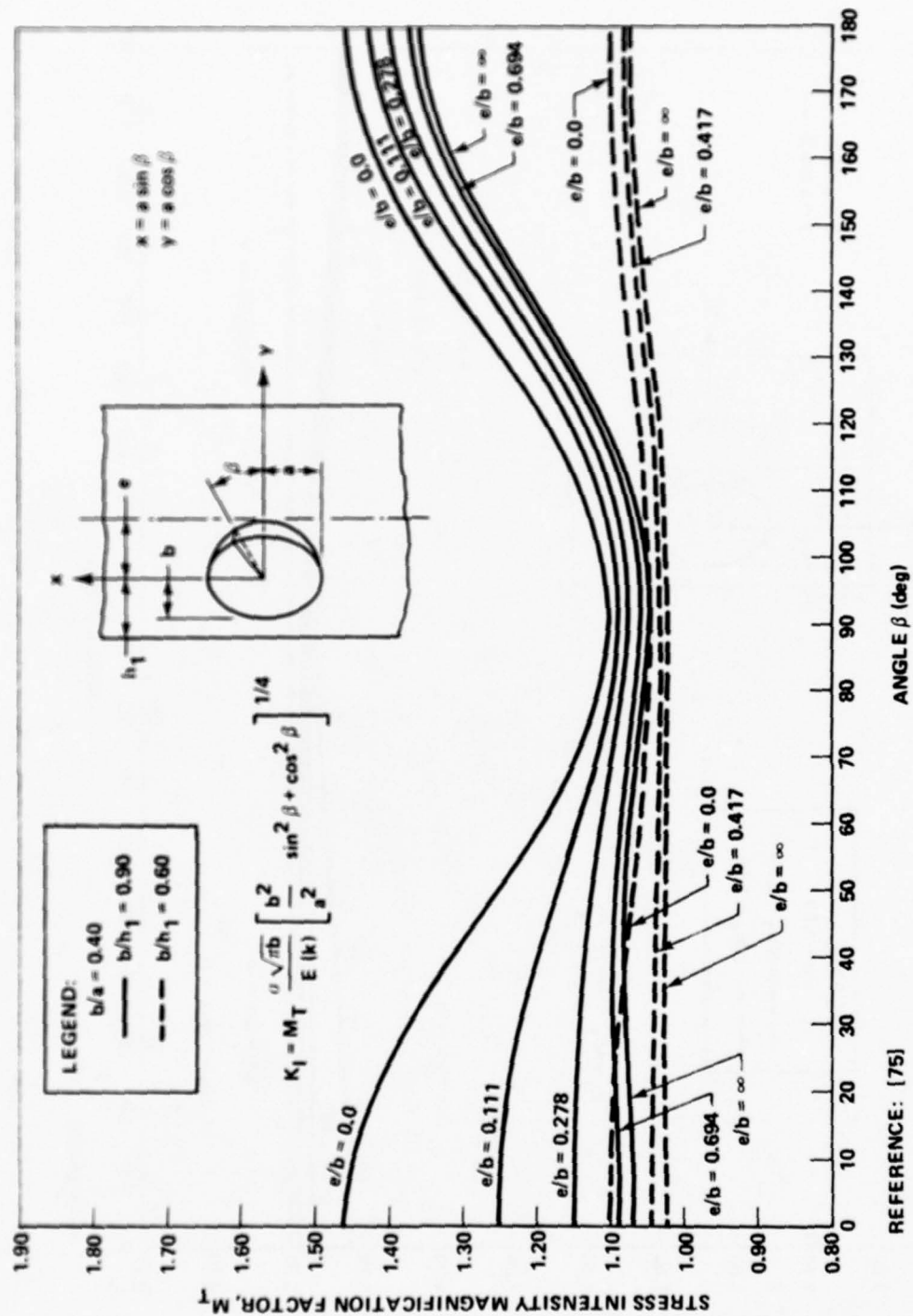


Figure 7.81. An elliptical crack in a plate subjected to uniaxial tension ( $b/a = 0.40$ ).



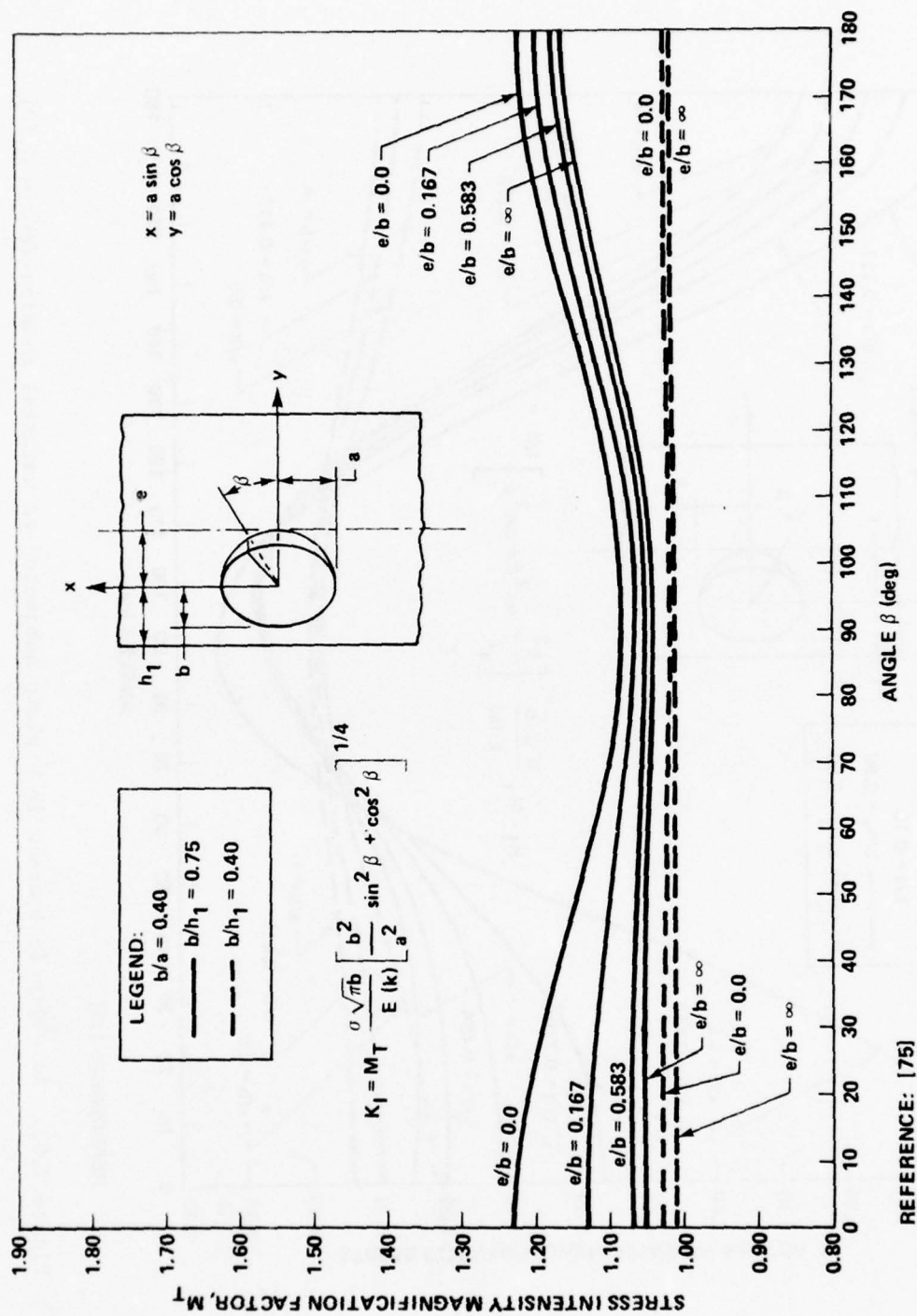
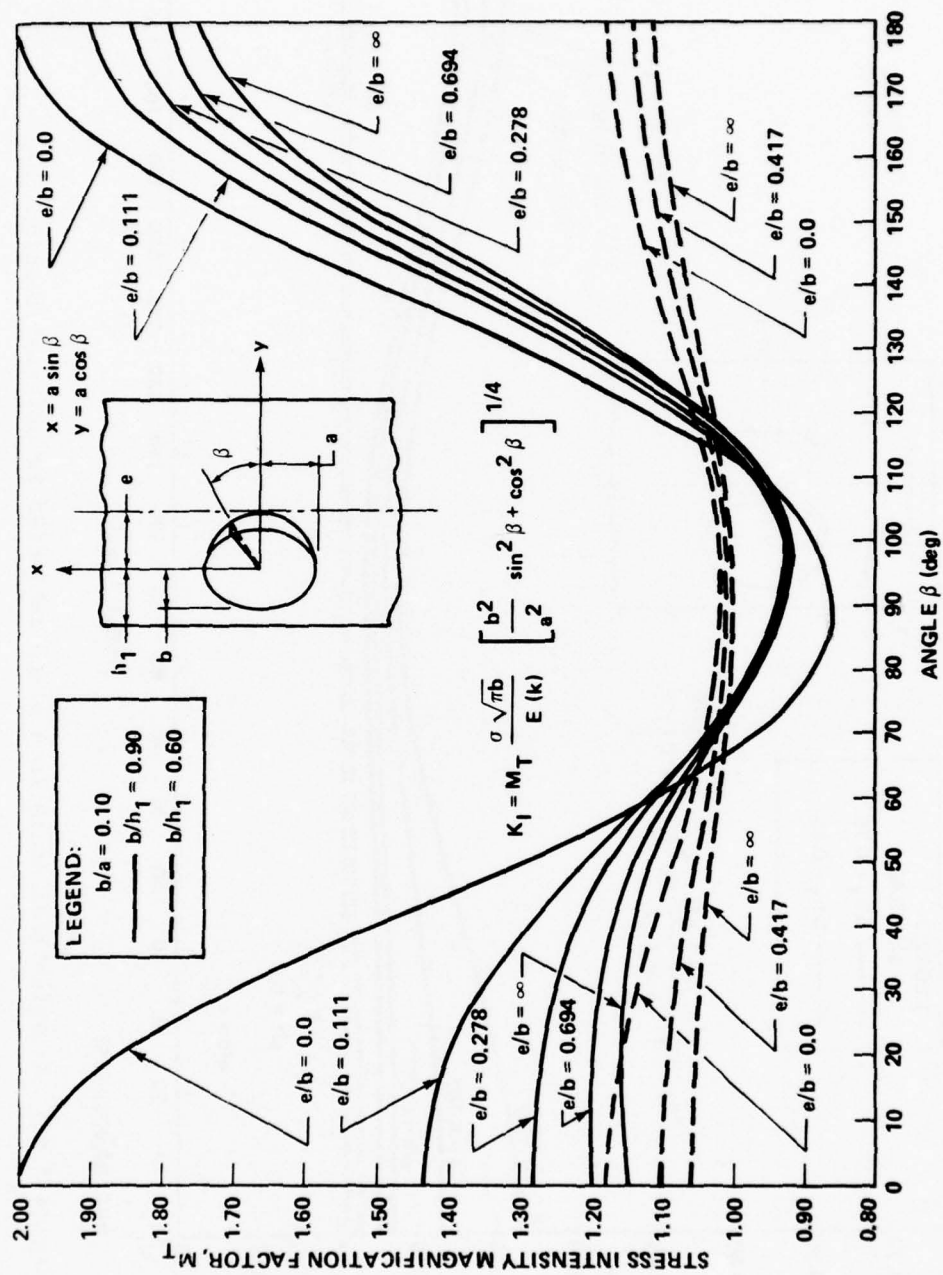


Figure 7.82. An elliptical crack in a plate subjected to uniaxial tension ( $b/a = 0.40$ ).



REFERENCE: [75]

Figure 7.83. An elliptical crack in a plate subjected to uniaxial tension ( $b/a = 0.10$ ).

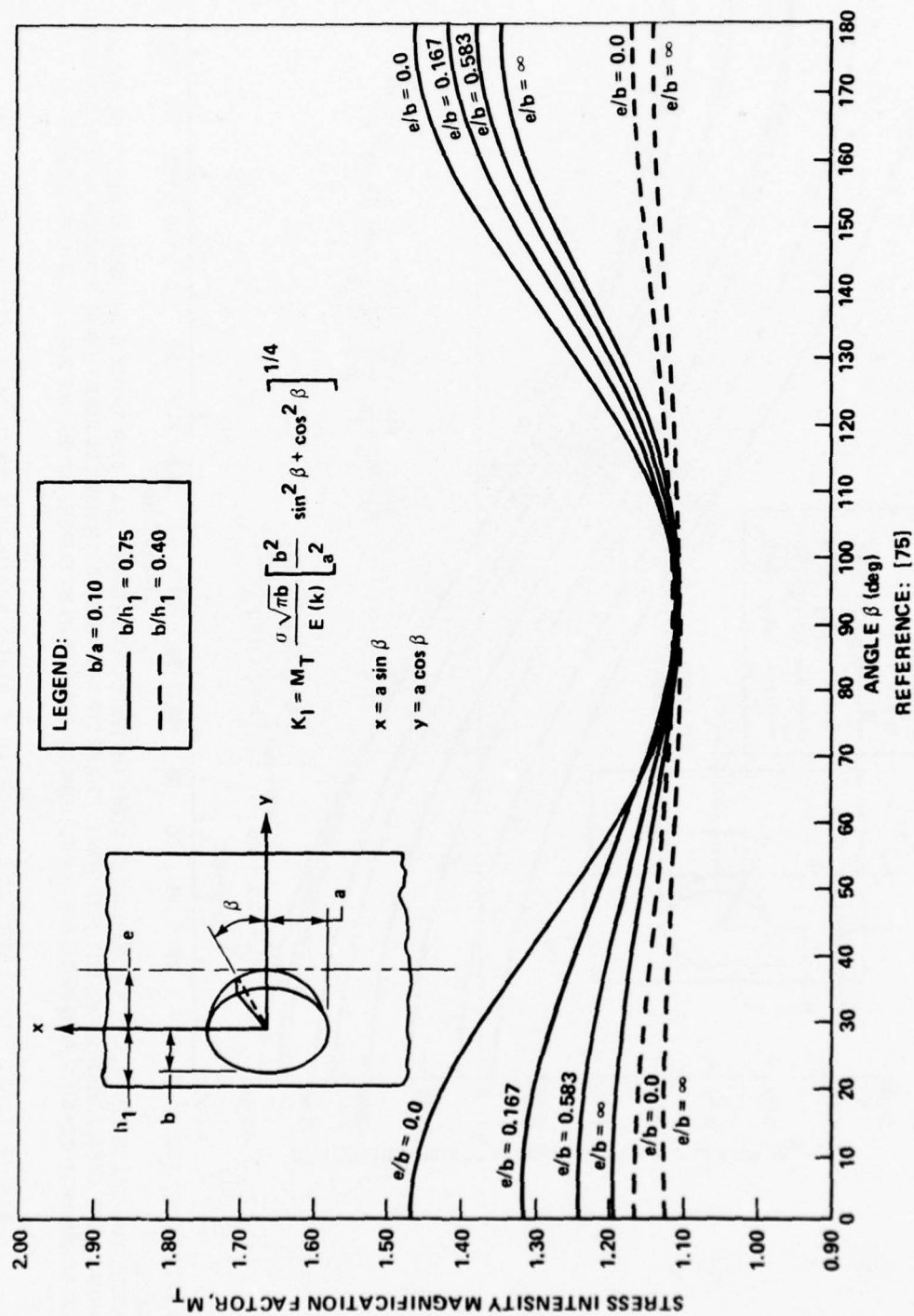


Figure 7.84. An elliptical crack in a plate subjected to uniaxial tension ( $b/a = 0.10$ ).

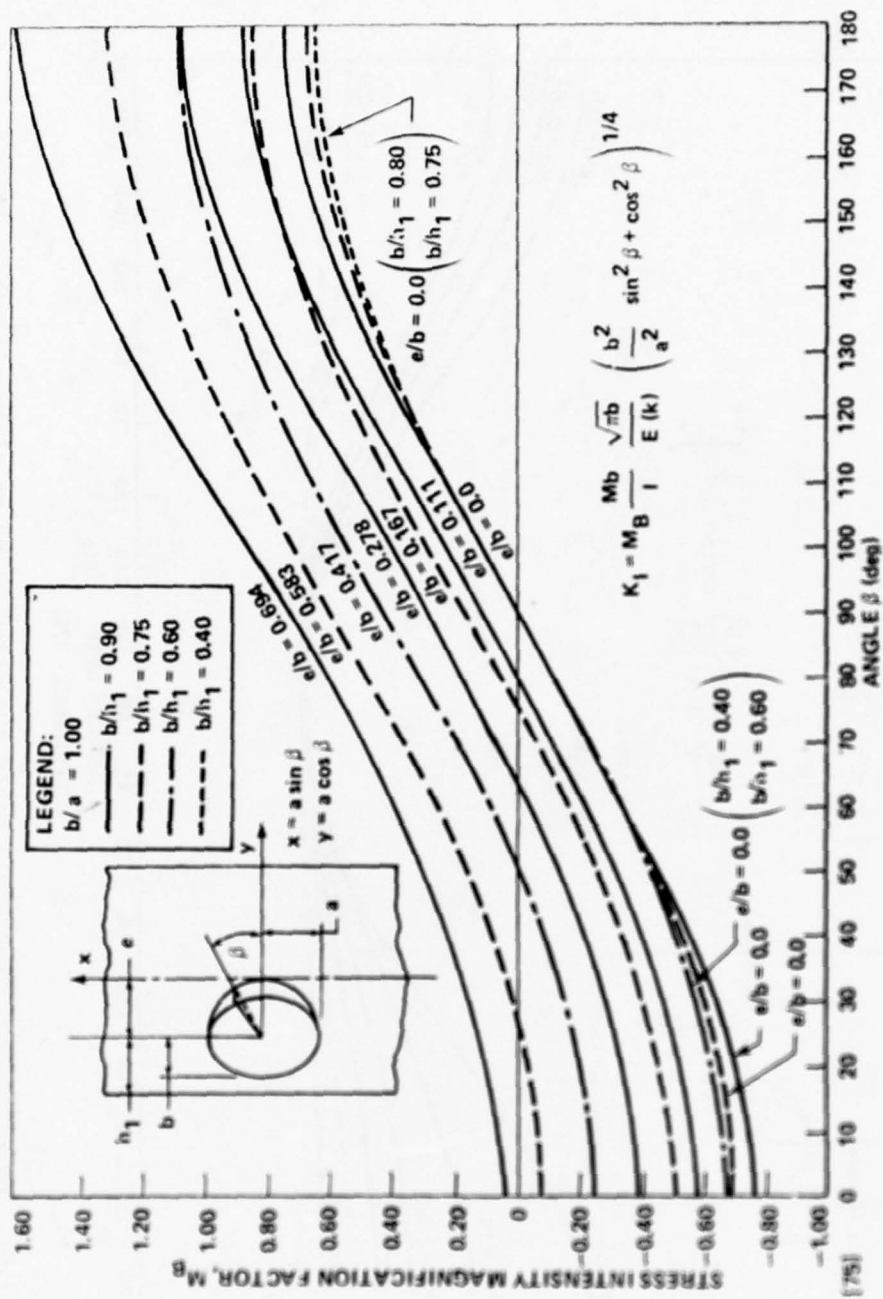
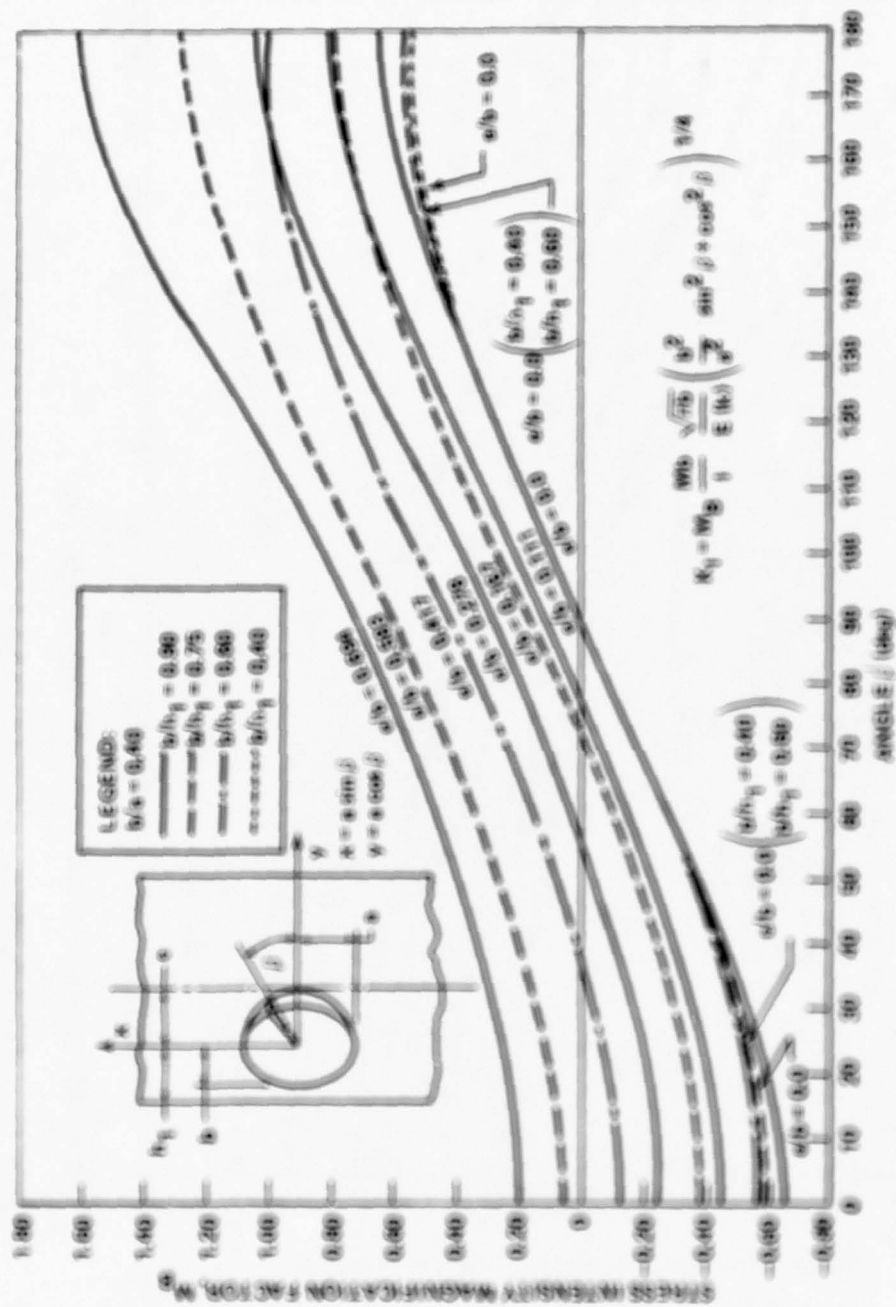


Figure 7.85. An elliptical crack in a plate subjected to pure bending ( $b/a = 1.00$ ).



REFERENCE: (76)  
NOTE: SEE NOTE ON FIG. 7.8B

Figure 7.8c. An elliptical crack in a plate subjected to pure bending ( $b/a = 0.40$ ).



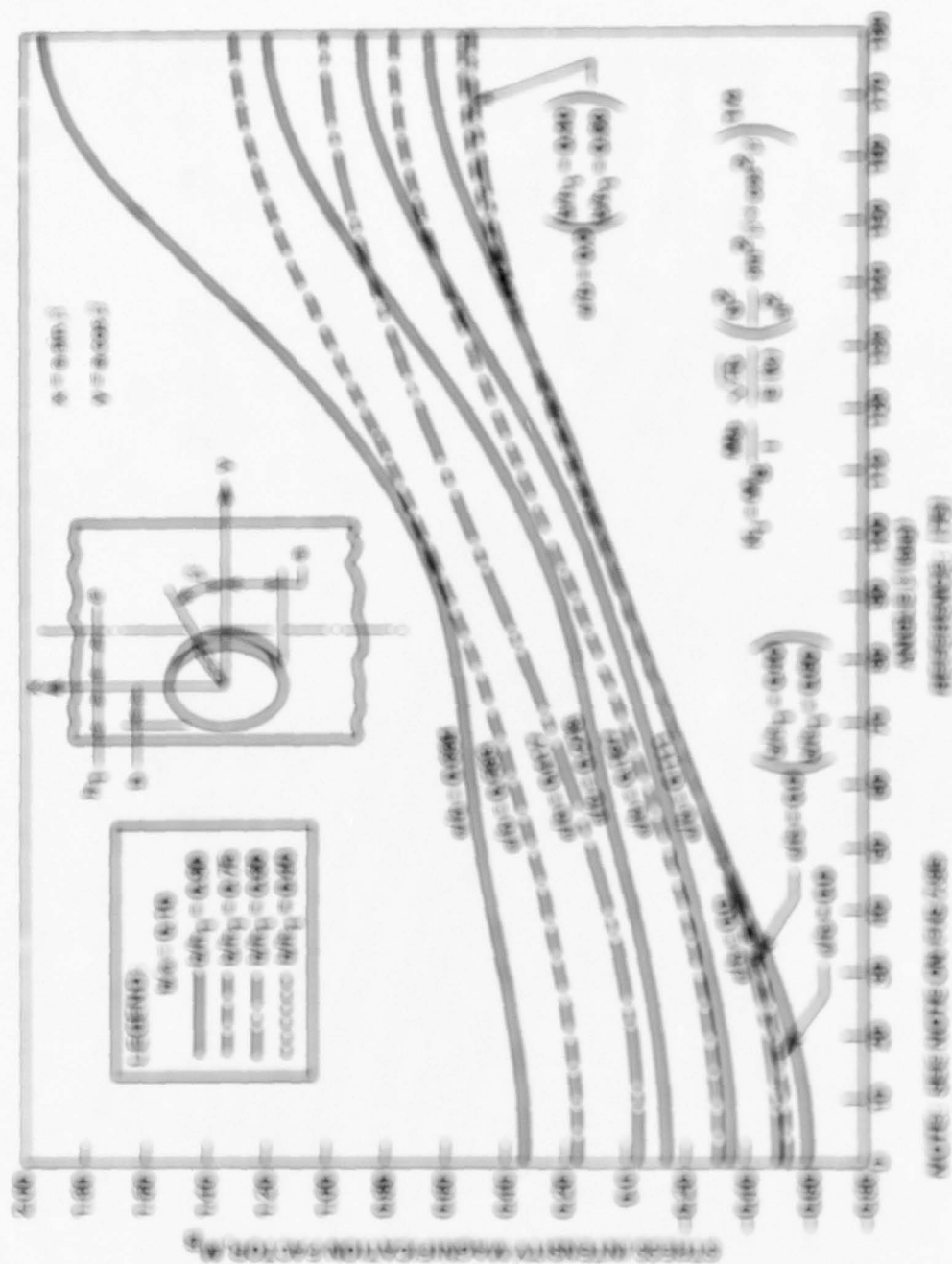


Figure 7.5. Stress intensification factors for plates subjected to pure bending ( $\sigma/\sigma_0 = 0.10$ ).

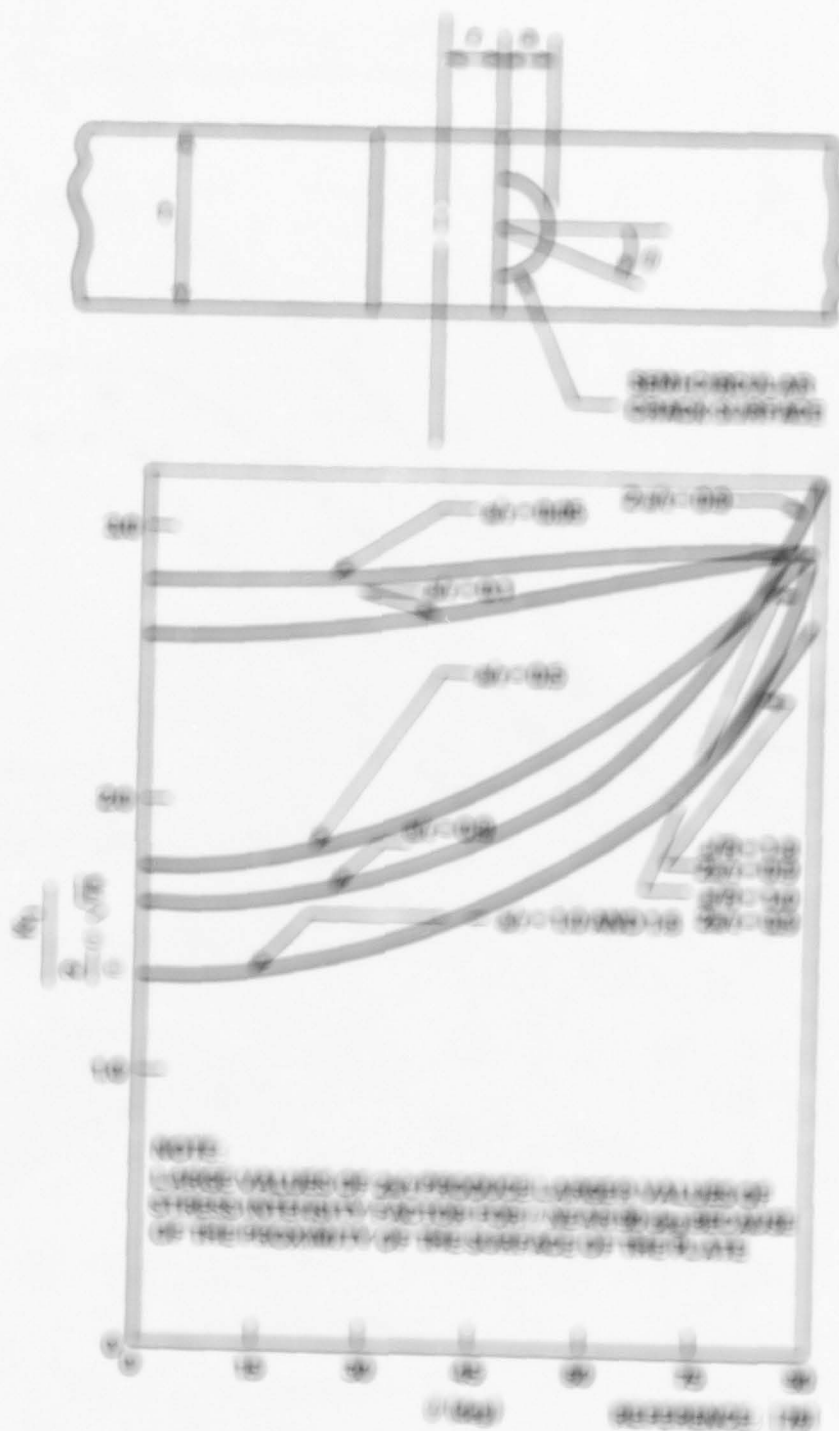


Figure 7. Normalized velocity  $U/V_0$  versus normalized time  $t/t_0$  for various values of the parameter  $\alpha$ .

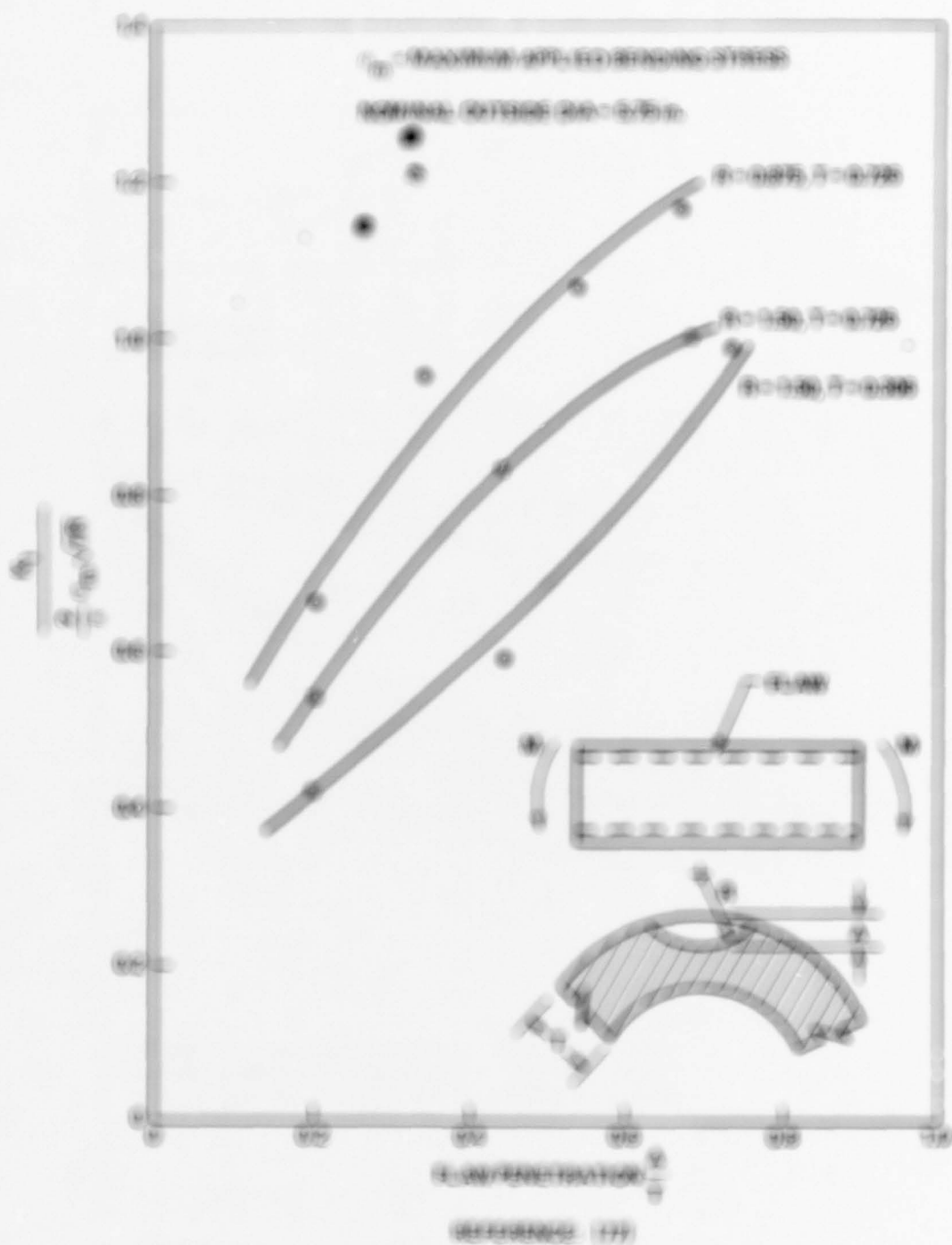
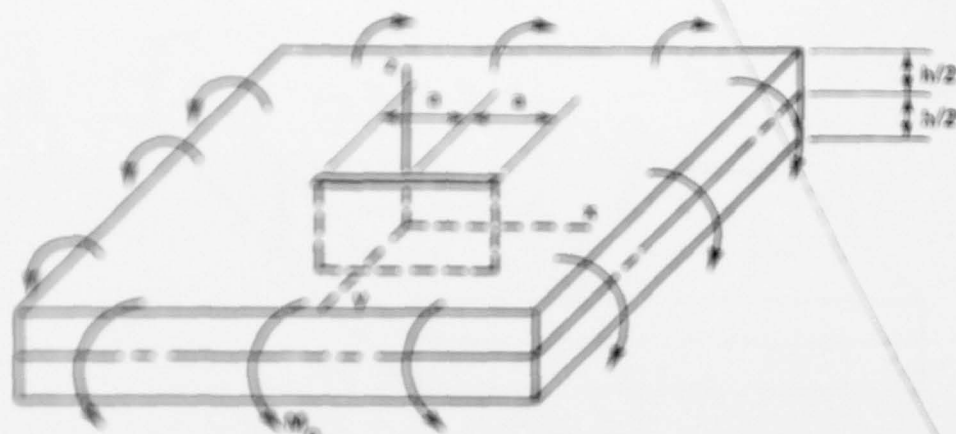
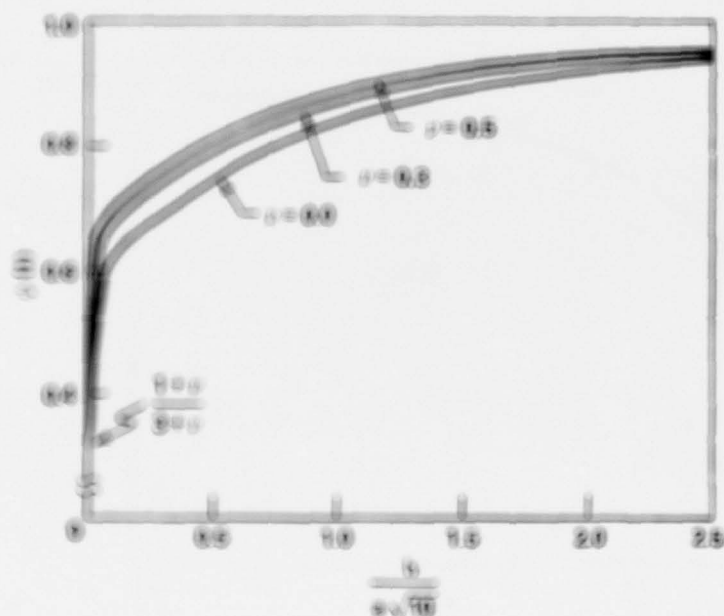


Figure 177. Variation of the ratio of the rate of reaction to the rate of diffusion,  $\left(\frac{k_p}{k_d}\right)^{1/2}$ , versus the concentration of the reactant,  $C_A$ , for different values of the rate of reaction,  $k_p$ , and the rate of diffusion,  $k_d$ .



$$\phi_1(z) = \left( \frac{1.65}{1.5} \right) \left( \frac{M_x}{W_x} \right) \sqrt{z/a}$$

$M_x$  IS THE BENDING MOMENT PER UNIT LENGTH,  $m \cdot lb/m$ .



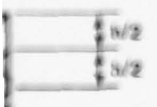
NOTE: NEGATIVE VALUES OF  $\phi$  ON THE COMPRESSIVE SIDE OF THE PLATE MEANS THAT THE CRACK CLOSURES UNLESS SUFFICIENT TENSION IS SUPERAPPLIED. REF. 80 INDICATES THAT CRACK CLOSURE INCREASES THE  $\phi$  ON THE TENSION SIDE BY APPROXIMATELY 40 PERCENT.

REFERENCE: [76, 80]

Figure 7.38. A center-cracked plate loaded in out-of-plane bending.



solid





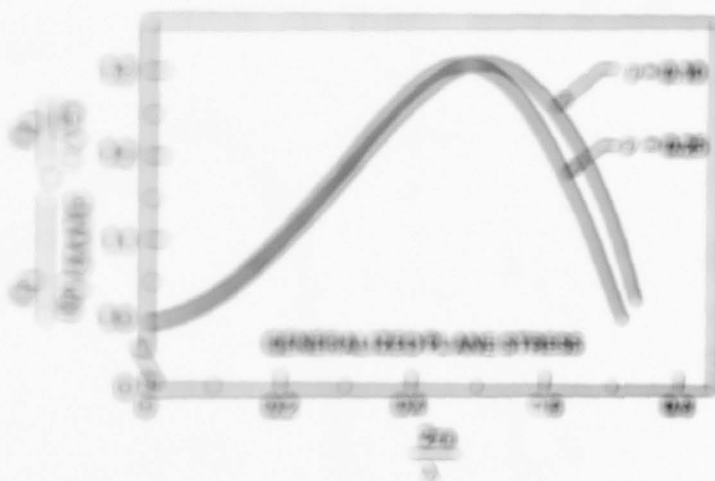
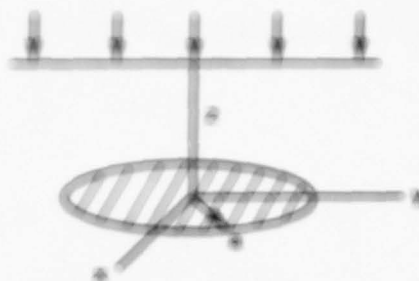
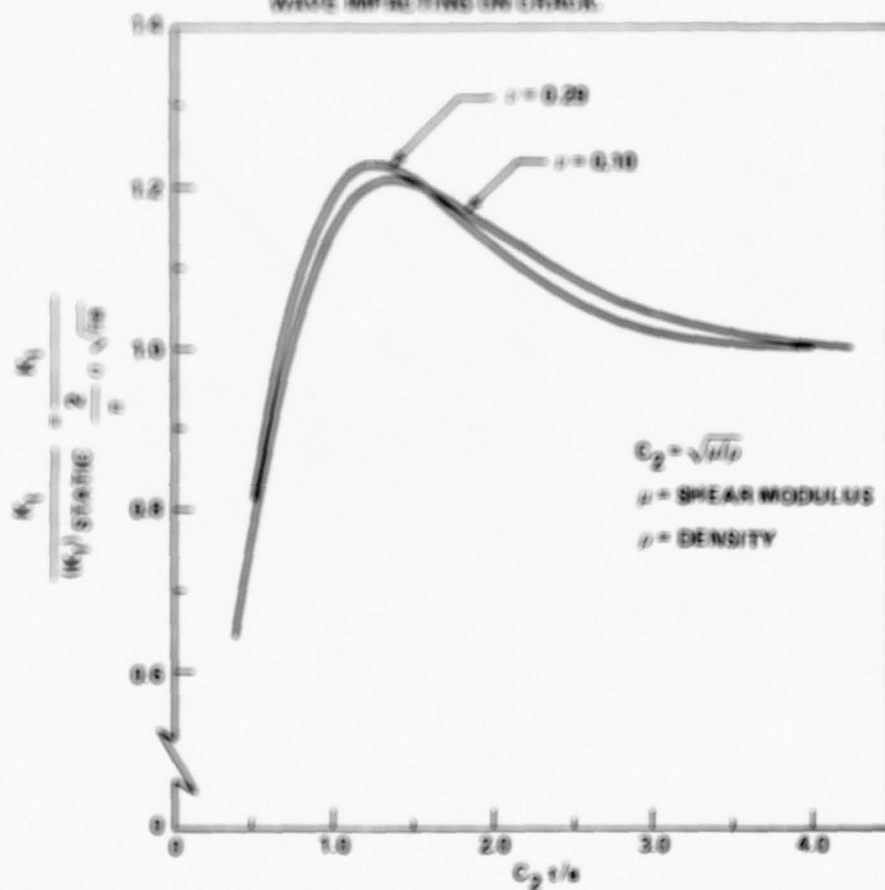


FIGURE 1

FIGURE 1. A graph showing the relationship between the amount of work done and the time taken to do it. The curve shows that the amount of work done increases with time, but at a decreasing rate.



LOAD  $\sigma_0 = \sigma$  APPLIED SUDDENLY BY STRESS WAVE IMPACTING ON CRACK.



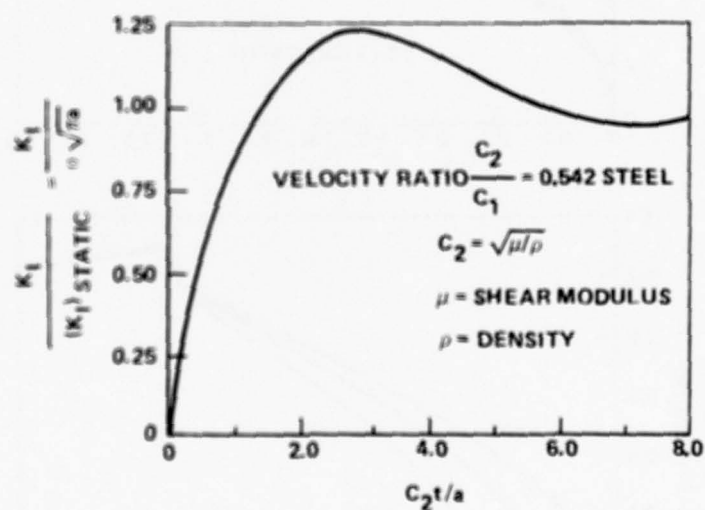
NOTE: SOLUTION IS THE SAME AS FOR THE SUDDEN APPEARANCE OF A PENNY-SHAPED CRACK IN A MEDIUM UNDER UNIFORM TENSILE STRESS  $\sigma_0$ .

REFERENCE: [82]

Figure 7.93. Transient stress intensity factor for dilatational stress wave impact on a penny-shaped crack.



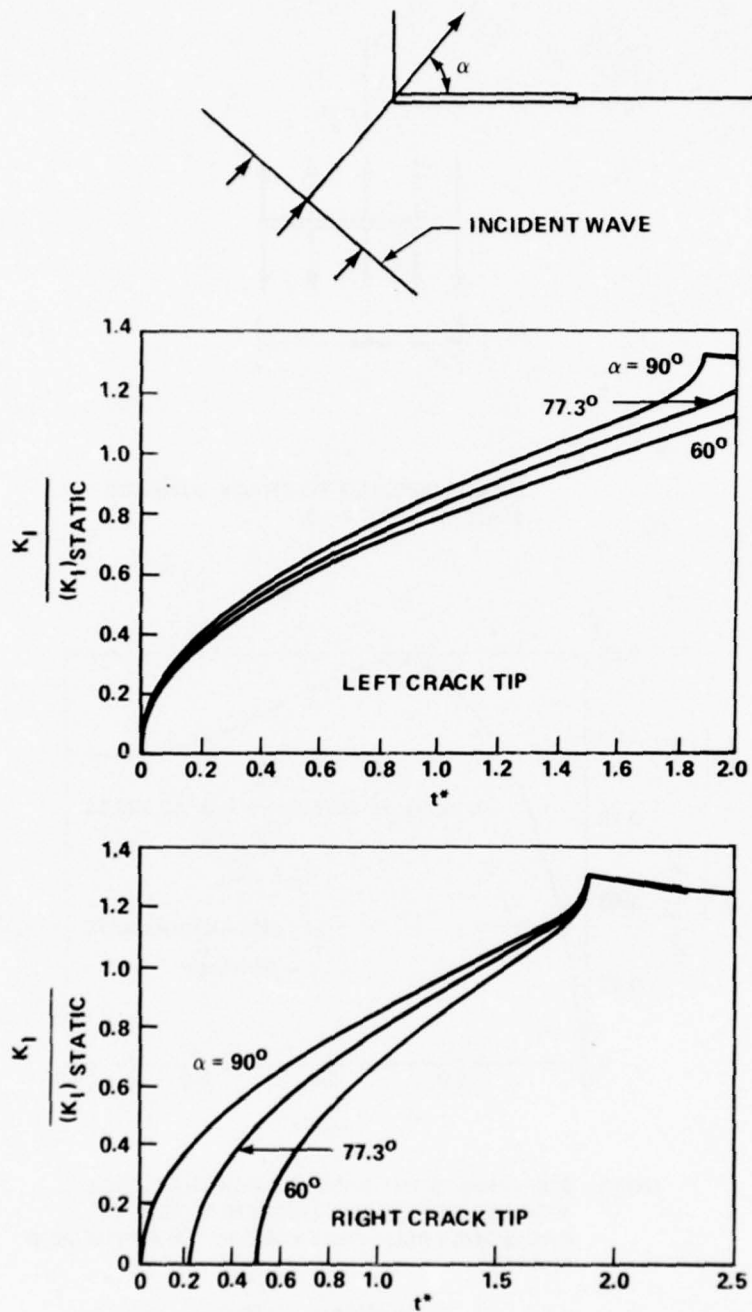
LOAD  $\sigma$  APPLIED TO CRACK SURFACE  
SUDDENLY AT  $t = 0$ .



NOTE: SOLUTION IS THE SAME AS FOR THE CASE OF  
A CRACK APPEARING SUDDENLY (DUE TO  
PROJECTILE PENETRATION, SAY) IN A STRESSED  
PLATE.

REFERENCE: [83]

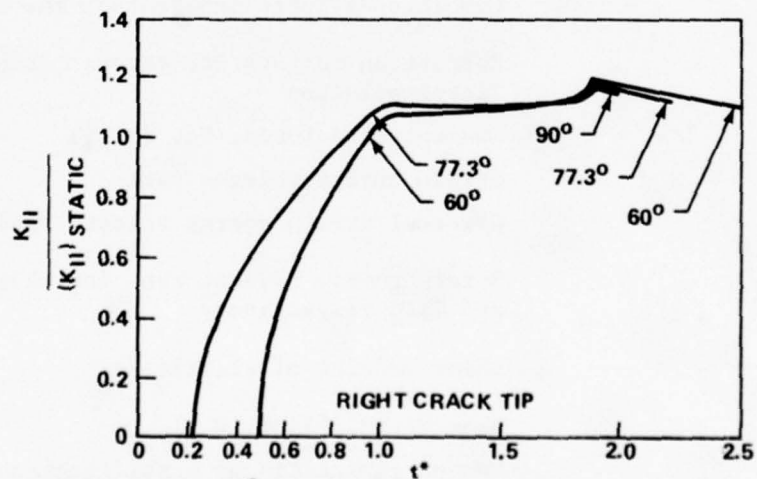
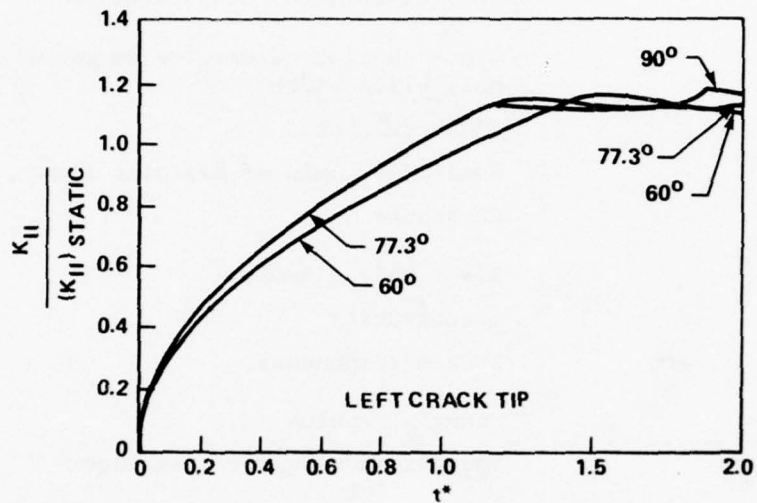
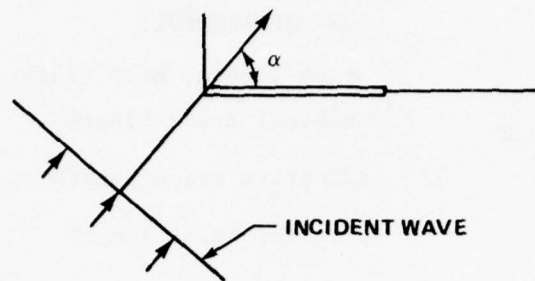
Figure 7.94. Transient stress intensity factor  
for sudden impact load applied to crack  
surface.



\*TIME NORMALIZED WITH RESPECT TO TIME REQUIRED FOR A DILATATIONAL WAVE TO TRAVEL ONE CRACK LENGTH.

REFERENCE [84]

Figure 7.95. Transient SIF due to oblique impact of a dilatational stress wave.



NOTE: FOR  $\alpha = 90^\circ$   $K_{II} \approx 0$

\*TIME NORMALIZED WITH RESPECT TO TIME REQUIRED FOR A DILATATIONAL WAVE TO TRAVEL ONE CRACK LENGTH.

REFERENCE: [84]

Figure 7.95. (Concluded).



# LIST OF SYMBOLS

$a$	Crack length; half crack length
$a_c$	Critical crack length
$a_e$	Effective crack length
$a_o$	Original crack length
$A_{str}$	Area of stringer cross section
$b$	Crack spacing; dimension on crack surface; half plate width
$B$	Plate thickness
$c$	Semi-major axis of elliptic flaw
$C, C_I, C'$	Constants
$d$	Rivet hole diameter
$e$	Eccentricity
$e_{xx}, e_{yy}, e_{xy}, \text{ etc}$	Strain components
$E$	Young's modulus
$E_{str}$	Young's modulus for a stringer
$E(k)$	Complete elliptic integral of the second kind
$f(\frac{a}{b}), F(\frac{a}{b})$	Correction factors for stress intensity factor solution
$F = P - iQ$	Concentrated force, Eq. (3.21)
$g$	Strain energy release rate
$g_c$	Critical strain energy release rate
$g_I, g_{II}, g_{III}$	Strain energy release rate for Modes I, II, and III, respectively
$G = \frac{E}{2(1 + \nu)}$	Shear modulus of elasticity
$h$	Beam depth, Fig 3.10
$I_z$	Moment of inertia of a stiffener about the stringer neutral axis perpendicular to the plane of the panel
$k = \sqrt{1 - b^2/a^2}$	Parameter in elliptic integral

K	Stress intensity factor
K*	Obsolete definition of stress intensity factor, $K^* = K/\sqrt{\pi}$
K <sub>c</sub>	Critical stress intensity factor
K <sub>f</sub>	Final stress intensity factor in fatigue analysis
K <sub>o</sub>	Original stress intensity factor in fatigue analysis
K <sub>Q</sub>	Conditioned stress intensity factor
K <sub>I</sub> , K <sub>II</sub> , K <sub>III</sub>	Stress intensity factors for modes I, II, and III, respectively
K <sub>IC</sub>	Plane strain critical stress intensity factor
K <sub>ISCC</sub>	Threshold stress intensity factor for stress corrosion cracking
L	Length of center cracked and double edge cracked specimens
M	Moment
n	Constant in fatigue equations
N	Number of cycles in fatigue analysis
N <sub>f</sub>	Number of cycles at fatigue
N <sub>o</sub>	Original number of cycles
P	Rivet pitch
P	Concentrated force; percent square fracture
P <sub>Q</sub>	Load used to calculate K <sub>Q</sub>
q	Shear stress load, Fig. 3.16
Q	Surface flaw shape parameter, $[E(k)]^2 = 0.212 (c/c_{ys})^2$
r, $\theta$	Polar coordinates centered at the crack tip
R	Plastic zone size; hole radius; load ratio
$R = \sigma_{min}/\sigma_{max}$	Load ratio, $\frac{2\gamma - 1}{2\gamma + 1}$
R <sub>o</sub>	Diameter of plastic zone for Mode III solution

$R_y$	Plastic zone radius ahead of crack tip
$S$	Span length of bending specimen
$S = \frac{A_{str}}{B(\frac{W}{2})} \cdot \frac{E_{str}}{E}$	Extensional stiffness of stiffened panel
$S^* = \frac{2\pi B}{A_{str}} \frac{E}{E_{str}}$	Stiffness ratio for stiffened panel
SIF	Stress intensity factor
$t$	Time
$T$	Surface tension
$U$	Surface energy per unit area
$u_x, u_y, u_z$	Displacement components
$V$	Strain energy
$w$	Plastic zone length for strip yield model
$W$	Length or width of fracture toughness specimens; panel width
$x, y, z$	Rectangular coordinates
$z = x + iy$	Complex coordinate
$\bar{z}, \bar{z}, z, z^*$	Westergaard stress function and its derivatives, Eq. (2.3)
$\phi = -\frac{iz}{2} \frac{E_{str}}{E}$	Nondimensional inertia parameter for stiffened panel
$\theta$	Crack angle, Fig. 3.5; elliptic flow angle, Fig. 3.15; $(K_e/\sigma_{ys})^2/B$ , Eq. (5.6)
$\gamma = \frac{e_{mean}}{f_{max}}$	Relative mean load = $\frac{1+R}{2(1-R)}$
$\Delta$	Displacement
$\zeta$	Complex coordinate located at the crack tip
$\eta = u + iv$	Complex coordinate in a mapped plane
$\rho, r$	Polar coordinates located at crack tip
$\nu$	elastic constant, Eq. (3.21)
$\lambda$	Compliance; correction factor for the stress intensity factor

$\nu$	Poisson's ratio
$\zeta = \frac{\sigma}{\sigma_{yp}} = \frac{\epsilon}{\epsilon_{yp}}$	Complex variable in stress plane
$\sigma$	Stress, usually tensile load on a specimen
$\sigma_{yp}$	Stress at initial yield
$\sigma_{xx}^0, \sigma_{yy}^0, \sigma_{zz}^0$ etc	Stress components, Fig. 3.14
$\sigma_{xy}^0, \sigma_{yz}^0, \sigma_{zx}^0$ etc	Stress components, Fig. 2.1
$\sigma_{ye}$	Tensile stress
$\sigma$	Stressing stress, usually tensile load on a specimen
$\sigma_{yp}$	Tensile stress in steel
$\sigma$	Angle to point on elliptic line, Fig. 3.16
$\sigma$	Any stress function
$\sigma_0$	Constant stress functions
$\sigma_1, \sigma_2, \sigma_3$	Principal functions
$\sigma$	Angle of shear load, Fig. 3.16
$\sigma(\cdot)$	Stressing function

# REFERENCES

1. GARDINER, G. G. "The Economic Aspects of Capitalism and Socialism," International Journal of Economics and Statistics, Vol. 1, No. 1, 1952, pp. 1-10.
2. GARDINER, G. G. "Economic Aspects of Socialism and Capitalism," International Journal of Economics and Statistics, Vol. 1, No. 1, 1952, pp. 11-20.
3. GARDINER, G. G. "Economic Aspects of Socialism and Capitalism," International Journal of Economics and Statistics, Vol. 1, No. 1, 1952, pp. 21-30.
4. GARDINER, G. G. "Economic Aspects of Socialism and Capitalism," International Journal of Economics and Statistics, Vol. 1, No. 1, 1952, pp. 31-40.
5. GARDINER, G. G. "Economic Aspects of Socialism and Capitalism," International Journal of Economics and Statistics, Vol. 1, No. 1, 1952, pp. 41-50.
6. GARDINER, G. G. "Economic Aspects of Socialism and Capitalism," International Journal of Economics and Statistics, Vol. 1, No. 1, 1952, pp. 51-60.
7. GARDINER, G. G. "Economic Aspects of Socialism and Capitalism," International Journal of Economics and Statistics, Vol. 1, No. 1, 1952, pp. 61-70.
8. GARDINER, G. G. "Economic Aspects of Socialism and Capitalism," International Journal of Economics and Statistics, Vol. 1, No. 1, 1952, pp. 71-80.
9. GARDINER, G. G. "Economic Aspects of Socialism and Capitalism," International Journal of Economics and Statistics, Vol. 1, No. 1, 1952, pp. 81-90.
10. GARDINER, G. G. "Economic Aspects of Socialism and Capitalism," International Journal of Economics and Statistics, Vol. 1, No. 1, 1952, pp. 91-100.
11. GARDINER, G. G. "Economic Aspects of Socialism and Capitalism," International Journal of Economics and Statistics, Vol. 1, No. 1, 1952, pp. 101-110.
12. GARDINER, G. G. "Economic Aspects of Socialism and Capitalism," International Journal of Economics and Statistics, Vol. 1, No. 1, 1952, pp. 111-120.
13. GARDINER, G. G. "Economic Aspects of Socialism and Capitalism," International Journal of Economics and Statistics, Vol. 1, No. 1, 1952, pp. 121-130.
14. GARDINER, G. G. "Economic Aspects of Socialism and Capitalism," International Journal of Economics and Statistics, Vol. 1, No. 1, 1952, pp. 131-140.
15. GARDINER, G. G. "Economic Aspects of Socialism and Capitalism," International Journal of Economics and Statistics, Vol. 1, No. 1, 1952, pp. 141-150.



- [illegible]

- [illegible]

17. Schwesky, F. A. and Haseburg, E. C., "Stress Concentration Around a Rectangular Elliptical Crack," Transactions, American Society of Mechanical Engineers, Journal of Applied Mechanics, 1949.
18. Green, A. E. and Snelton, I. E., "The Stress Distribution in the Neighborhood of a Flat Elliptical Crack in an Elastic Solid," Proceedings, Cambridge Philosophical Society, Vol. 46, 1950.
19. Smith, C. E., "Crack Extension Force for a Part Through Crack in a Plate," Transactions, American Society of Mechanical Engineers Vol. 80, December 1958, pp. 651-654.
20. The Surface Crack: Physical Features and Computational Solutions, E. E. Sneddon - Ed., The American Society of Mechanical Engineers, New York, 1972.
21. Leven, R. M., "Stress Distribution in the 90° Biaxial Fracture Specimen", Westinghouse Research Laboratory, Pittsburgh, Pennsylvania, March 1965, Research Report No. 65-137-STRS-81.
22. Green, F. A. and Venturini, R., "Three-Dimensional Elastic Stress Analysis of a Fracture Specimen with an Edge Crack," International Journal of Fracture Mechanics, Vol. 7, No. 1, March 1971, pp. 1-13.
23. Lee, E. W., Discussion to Proceedings of the Crack Propagation Symposium, Cambridge, Vol. II, 1961.
24. Kahn, E. T. and Rosenfield, A. E., "Sources of Fracture Toughness: The Relation between  $K_{IC}$  and the Ordinary Tensile Properties of Metals," Proceedings of American Society for Testing and Materials, Applications Related Phenomena in Titanium and its Alloys, April 1967.
25. Williams, D. F., Fracture Mechanics Guidelines for Aircraft Structural Analysis, Air Force Flight Dynamics Laboratory, Air Force Systems Command, Wright-Patterson Air Force Base, Ohio, January 1970, Technical Report No. AFFDL-TR-69-111.
26. Smith, C. E., Discussion of "Elastic-Plastic Deformation of a Single Crooved Flat Plate under Longitudinal Shear," M. F. Cockcroft, Journal of Basic Engineering, December 1963, pp. 585-594.
27. Rice, J. R., "Mathematical Analysis in the Mechanics of Fracture," Fracture - An Advanced Treatise, Vol. II, Mathematical Fundamentals, E. E. Gdoutos - Ed., Academic Press, New York, 1968.
28. Cockcroft, M. F., "Elastic-Plastic Deformation of a Single Crooved Flat Plate under Longitudinal Shear," Journal of Basic Engineering, December 1963, pp. 585-594.

RE  
PERCENT.

e bending.

ion Around  
ociety of

e in the  
lid,"  
1950.

track in  
ngineers

solutions,  
ngineers,

ture  
Pennsyl-

e Stress  
national  
pp. 1-15.

ation

- (17) Paris, P. C. and Erdogan, F., "A Critical Analysis of Crack Propagation Theory," Journal of Basic Engineering, Transactions of American Society of Mechanical Engineers, Series B, Vol. 85, 1963, pp. 528-533.
- (18) Paris, P. C. and Erdogan, F. C., "Fundamental Aspects of Crack Growth and Fatigue," Fracture - An Advanced Treatise, Vol. 3, Engineering Fundamentals and Environmental Effects, H. L. Liebowitz - Ed., Academic Press, New York, 1971.
- (19) Paris, P. C., "The Dependence of Fatigue Crack Propagation on Stress Intensity, Strain Rate and Crack Opening Displacement," Damage Tolerance in Aircraft Structures, American Society for Testing and Materials, 1971, pp. 1-15, ASTM STP 486.
- (20) Paris, P. C., Budd, R. J. and Little, C. D., "Fatigue Crack Propagation of Hot Steel in Air and Distilled Water," Stress Analysis and Growth of Cracks, Proceedings of the 1971 National Symposium on Fracture Mechanics, American Society for Testing and Materials, 1972, pp. 196-217, ASTM STP 513.
- (21) Paris, P. C., Discussion of "The Fracture Mechanics Approach to Fatigue," Fracture - An Interdisciplinary Approach, Syracuse University Press, Syracuse, New York, 1963.
- (22) Paris, P. C., Ramsey, V. E., and Engle, R. M., "Numerical Analysis of Crack Propagation in Cyclic-Loaded Structures," Transactions of American Society for Mechanical Engineers, Series B, Journal of Basic Engineering, Vol. 89, No. 3, September 1967, pp. 400-406.
- (23) Paris, P. C., Effect of Stress Ratio on Fatigue-Crack Growth in 7075-T6 and 2024-T3 Aluminum-Alloy Specimens, August 1969, NACA TN 3534.
- (24) Paris, P. C., Budd, R. J., Vessel, E. T., Clark, W. G., and Engle, R. M., "Extensive Study of Low Fatigue Crack Growth Rates in 7075 and 2024 Steels," Stress Analysis and Growth of Cracks, Proceedings of the 1971 National Symposium on Fracture Mechanics, American Society for Testing and Materials, 1972, pp. 141-176, ASTM STP 513.
- (25) Paris, P. C., "The Significance of Fatigue Crack Closure," Damage Tolerance in Aircraft Structures, American Society for Testing and Materials, 1971, pp. 230-242, ASTM STP 486.
- (26) Damage Tolerance in Aircraft Structures, American Society for Testing and Materials, 1971, ASTM STP 486.



71. "Crack Behavior in D6ac Steel," An Evaluation of Fracture Mechanics Data for the F-111 Aircraft, Metals and Ceramics Information Center and Air Force Materials Laboratory, January 1972, MCLC-72-04.
72. Engle, R. M., Jr., Cracks, A Fortran IV Digital Computer Program for Crack Propagation Analysis, Air Force Flight Dynamics Laboratory, Air Force Systems Command, Wright-Patterson Air Force Base, Ohio, October 1970, AFFDL-TR-70-107.
73. Wessel, E. T., Clark, W. G., and Wilson, W. K., Engineering Methods for the Design and Selection of Materials Against Fracture, Westinghouse Research Laboratories, Pittsburgh, Pennsylvania, June 1966, Technical Report.
74. Shah, R. C. and Kobayashi, A. S., "On the Surface Flaw Problem," The Surface Crack: Physical Problems and Computational Solutions, J. L. Swedlow - Ed., The American Society of Mechanical Engineers, New York, 1972, pp. 79-124.
75. Parmerter, R. R., Stress Intensity Factors for Three-Dimensional Problems, United Technologies Chemical Systems Division, Sunnyvale, California, April 1976, Prepared for Air Force Rocket Propulsion Laboratory, Director of Science and Technology, Air Force Systems Command, Edwards Air Force Base, California, Technical Report RPL-TR-76-30.
76. Browning, W. M., and Smith, F. W., "An Analysis Technique for Complex Three-Dimensional Crack Problems," Developments in Theoretical and Applied Mechanics - Volume 8, Proceedings of Eight Southeastern Conference on Theoretical and Applied Mechanics, April 1976, pp. 141-150.
77. Mullinix, B. R. and Smith, D. G., An Experimental Determination of the Stress Intensity Around Surface Flaws Embedded in Hollow Cylinders Subjected to Bending, US Army Missile Command, Redstone Arsenal, Alabama, February 1974, Technical Report RL-74-7.
78. Hartranft, R. J. and Sih, G. C., "Effect of Plate Thickness on the Bending Stress Distribution Around Through Cracks," Journal of Mathematics and Physics, Vol. 47, No. 3, September 1968, pp. 276-291.
79. Sih, G. C., "Three-Dimensional Stress-State in a Cracked Plate," International Journal of Fracture Mechanics, Vol. 7, March 1971, pp. 39-61.

80. Smith, D. G. and Smith, C. W., "A Photoelastic Evaluation of the Influence of Closure and Other Effects upon the Local Bending Stresses in Cracked Plates," International Journal of Fracture Mechanics, Vol. 6, No. 3, September 1970, pp. 305-317.
81. Sih, G. C. and Loeber, J. F., "Wave Propagation in an Elastic Solid with a Line of Discontinuity or Finite Crack," Quarterly of Applied Mathematics, Vol. 27, No. 2, July 1969, pp. 193-213.
82. Embley, G. T. and Sih, G. C., "Response of a Penny-Shaped Crack to Impact Waves", Developments in Mechanics, Vol. 6, Proceedings of the 12th Midwestern Conference, 1971, pp. 473-487.
83. Sih, G. C., Embley, G. T., and Ravera, R. S., "Impact Response of a Finite Crack in Plane Extension," International Journal of Solids and Structures, Vol. 8, 1972, pp. 977-993.
84. Thau, S. A. and Lu, T. H., "Transient Stress Intensity Factors for a Finite Crack in an Elastic Solid Caused by a Dilatational Wave", International Journal of Solids and Structures, Vol. 7, 1971, pp. 731-750.

## RECOMMENDED BIBLIOGRAPHY

The following list represents the core of a good library for "applied" fracture mechanics. The list is intended to be brief rather than complete. There are many other references which are as valuable as those presented here. Each of the following is a book (or of book length); together they represent a broad cross section of the various applied aspects of fracture mechanics.

Brown, W. F., Jr. - Ed., Review of Developments in Plane Strain Fracture Toughness Testing, American Society for Testing and Materials, Philadelphia, Pennsylvania, 1970, ASTM STP 463.

"Damage Tolerance in Aircraft Structures," American Society for Testing and Materials, Philadelphia, Pennsylvania, 1971, ASTM STP 486.

Damage Tolerant Design Handbook, Metals and Ceramics Information Center, Battelle, Columbus Laboratories, Columbus, Ohio, January 1975.

Fracture Toughness, American Society for Testing and Materials, Philadelphia, Pennsylvania, 1972, ASTM STP 514.

Fracture Toughness Testing and Its Applications, American Society for Testing and Materials, Philadelphia, Pennsylvania, 1965, ASTM STP 381.

Kobayashi, A. S. - Ed., Experimental Techniques in Fracture Mechanics, Society for Experimental Stress Analysis, Wesport, Connecticut, Vol. 1, 1973, SESA Monograph No. 1.

Kobayashi, A. S. - Ed., Experimental Techniques in Fracture Mechanics, Society for Experimental Stress Analysis, Wesport, Connecticut, Vol. 2, 1975, SESA Monograph No. 2.

Parmeter, R. R., Stress Intensity Factors for Three-Dimensional Problems, United Technologies Chemical Systems Division, Sunnyvale, California, April 1976, Prepared for Air Force Rocket Propulsion Laboratory, Director of Science and Technology Air Force Systems Command, Edwards Air Force Base, California, Technical Report RPL-TR-76-30.

"Stress Analysis and Growth of Cracks," American Society for Testing and Materials, Philadelphia, Pennsylvania, 1972, ASTM STP 513.

Swedlow, J. L., Ed., "The Surface Crack: Physical Problems and Computational Solutions," The American Society of Mechanical Engineers, New York, 1972.

Tada, H., The Stress Analysis of Cracks Handbook, Del Research Corporation, Hellertown, Pennsylvania, 1973.

Wilhem, D. P., Fracture Mechanics Guidelines for Aircraft Structural Applications, Air Force Flight Dynamics Laboratory, Air Force Systems Command, Wright-Patterson Air Force Base, Ohio, February 1970, Technical Report AFFDL-TR-69-111.

# DISTRIBUTION

	No. of Copies
Defense Documentation Center Cameron Station Alexandria, Virginia 22314	2
Commander US Army Materiel Development and Readiness Command Attn: DRCRD	1
DRCDL 5001 Eisenhower Avenue Alexandria, Virginia 22333	1
Dallas G. Smith Department of Engineering Science Tennessee Technological University Cookeville, Tennessee 38501	5
DRSML-FR, Mr. Strickland	1
-LP, Mr. Voigt	1
-R, Dr. McDaniel	1
Dr. Kobler	1
-RL, Mr. Lewis	1
Dr. Mullinix	45
-RBD	3
-RPR (Record Set)	1
(Reference Copy)	1



iners,

re  
ansyl-

Stress  
ational  
p. 1-15.

ion

ghness:  
s of  
rials,

fy,  
Ohio,

a

585-594.

ature,"  
mentals,

rooved  
seeing,

